PROCEEDINGS

of the

MASTER

8TH

RARE EARTH RESEARCH CONFERENCE
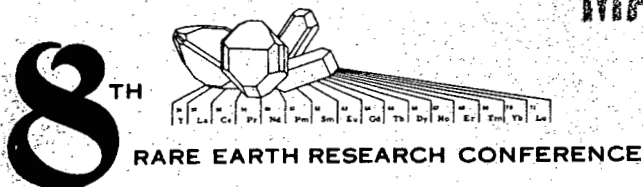
April 19 – 22, 1970

Volume I

Sessions A through H

Reno, Nevada

PROCEEDINGS

of the

8TH

RARE EARTH RESEARCH CONFERENCE
APRIL 19 - 22, 1970   RENO, NEVADA
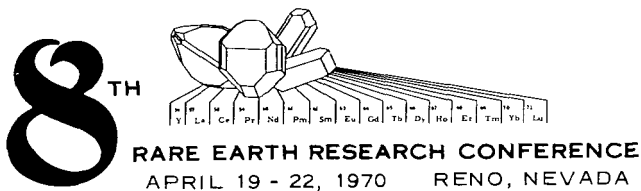
Volume I
Sessions A through H

Edited by THOMAS A. HENRIE
Reno Metallurgy Research Center

and

R. E. LINDSTROM
Reno Metallurgy Research Center

DISCLAIMER

This report was prepared as an account of work sponsored by an agency of the United States Government. Neither the United States Government nor any agency Thereof, nor any of their employees, makes any warranty, express or implied, or assumes any legal liability or responsibility for the accuracy, completeness, or usefulness of any information, apparatus, product, or process disclosed, or represents that its use would not infringe privately owned rights. Reference herein to any specific commercial product, process, or service by trade name, trademark, manufacturer, or otherwise does not necessarily constitute or imply its endorsement, recommendation, or favoring by the United States Government or any agency thereof. The views and opinions of authors expressed herein do not necessarily state or reflect those of the United States Government or any agency thereof.

DISCLAIMER

Portions of this document may be illegible in electronic image products. Images are produced from the best available original document.

FOREWORD

The Eighth Rare Earth Research Conference was held at the Pioneer Theatre Auditorium in Reno, Nevada, April 19-22, 1970. The Conference preprints contained in this book were prepared for the convenience of the Conferees and, as such, do not constitute a formal publication. Accordingly, authors are at liberty to publish their papers in scientific journals of their choice.

The Conference included research papers and discussions on the latest developments in the field of rare earth and related metals. Research topics were interdisciplinary and included the fields of physics, chemistry, ceramics, and metallurgy of the elements, their compounds, and alloys. Also included was a session on industrial processes and geochemistry.

Approximately 93 papers were scheduled for presentation, reflecting nearly 10-percent growth over the previous Conference -- a most gratifying response and very real evidence of continuing increase in use paterns for the rare earths.

Our gratitude is expressed to the Bureau of Mines for providing personnel and facilities for the Conference and for assuming responsibility for hosting the Conference. Further thanks are due the Bureau for making this publication available to the Conferees.

To the individual members of the Conference Committee, who gave unstintingly of their time, we express our sincere appreciation.

We also gratefully acknowlege the support of the following members of the rare-earth industry, who helped to make the Conference a more pleasant and enjoyable occasion:

American Potash and Chemical Corporation
Molybdenum Corporation of America
Ronson Metals Corporation
W. R. Grace and Company, Davison Chemical Division
Research Chemicals

Finally, we thank all who contributed to the success of the Conference: Professor Henry Eyring for a comprehensive and challenging introductory speech, the hard working Session Chairmen who kept the Conference moving smoothly, the interesting and informative speakers, and the Conferees themselves to whom this collection of papers is dedicated.

Chairman

T. A. HENRIE
Reno Metallurgy Research Center
U. S. Bureau of Mines
Reno, Nevada

Program Chairmen

R. E. LINDSTROM
Reno Metallurgy Research Center
U. S. Bureau of Mines
Reno, Nevada

D. J. BAUER
Reno Metallurgy Research Center
U. S. Bureau of Mines
Reno, Nevada

Committee

J. F. NACHMAN, Ex-Officio
Research Laboratories
Solar Division of International
Harvester, San Diego, California

K. A. GSCHNEIDNER, JR.
Iowa State University
Ames Laboratory
Ames, Iowa

A. F. CLIFFORD
Virginia Polytechnic Institute
Blacksburg, Virginia

W. C. KOEHLER
Oak Ridge National Laboratory
Oak Ridge, Tennessee

C. E. LUNDIN
Metallurgy Division
Denver Research Institute
University of Denver
Denver, Colorado

TABLE OF CONTENTS

i

TABLE OF CONTENTS

SESSION D - CHEMISTRY I

Chairman: L. EYRING, Arizona State University

TABLE OF CONTENTS

iii

TABLE OF CONTENTS

iv

TABLE OF CONTENTS

TABLE OF CONTENTS

SESSION H - CHEMISTRY IV

Chairman: A. F. CLIFFORD, Virginia Polytechnic Institute

TABLE OF CONTENTS

vii

TABLE OF CONTENTS

viii

TABLE OF CONTENTS

TABLE OF CONTENTS

SESSION K - SOLID STATE IV

Chairman: H. A. EICK, Michigan State University

x

TABLE OF CONTENTS

xi

TABLE OF CONTENTS

xii

TABLE OF CONTENTS

xiii

Introductory Address. Professor Henry Eyring,
University of Utah.

SPIN WAVE SPECTRUM FOR HOLMIUM METAL[*]

R. M. Nicklow, J. C. G. Houmann[+], H. A. Mook and M. K. Wilkinson
Solid State Division, Oak Ridge National Laboratory
Oak Ridge, Tennessee 37830

ABSTRACT

The dispersion relation, $E(\vec{q})$, for spin waves propagating in the c-direction of holmium metal in its plane-spiral magnetic phase has been studied by coherent inelastic scattering of thermal neutrons. Extensive measurements were made at 50° and 78°K. Incident neutrons with energies as low as 3.5 meV were used in order to measure $E(\vec{q})$ at small $\vec{q}$, where spin waves with energies down to 0.25 meV have been observed. The shape of this part of the dispersion relation is quite sensitive to the anisotropy properties of holmium. At both temperatures $E(\vec{q})$ increases linearly with increasing $\vec{q}$ and then levels-off near $\vec{q} = \vec{k}_o$, the wave vector of the spiral structure, before increasing further to maximum energies of 3 meV at 50°K and 2.6 meV at 78°K near the Brillouin Zone boundary. Analysis of these data, neglecting magneto-elastic and six-fold anisotropy effects, shows that the uniaxial anisotropy parameter is .022 ± .003 meV/ion at both temperatures and that the exchange interaction extends at least to the fifth-nearest neighbor plane in the c-direction. The parameters describing the exchange interaction between nearest neighbor planes are relatively independent of the range assumed for the interaction and are approximately 0.10 meV at 50°K and 0.09 meV at 78°K. Analysis of these data including magneto-elastic and six-fold anisotropy contributions to the Hamiltonian will be discussed. The energy width of the measured spin waves increased markedly with increasing $\vec{q}$.

PERMANENT MAGNET PROPERTIES OF $PrCo_5$ ALLOY POWDERS

Karl Strnat and James Tsui

Department of Electrical Engineering
University of Dayton, Dayton, Ohio 45409

ABSTRACT

The intermetallic compound $PrCo_5$ holds the promise of
permanent magnets having energy products up to 36 MGOe, yet it has
been neglected in favor of $SmCo_5$ in the recent efforts to develop rare
earth-cobalt-based magnets. This paper reports the particle-size
dependence of coercivity and hysteresis loop shape of mortar-ground
powders, results of ballmilling experiments, and two ways to improve
the properties by surface treatment of the particles. Intrinsic
coercive forces up to $_MH_c$ = 5750 oersted were obtained by ballmilling.
Mortar-ground powders of <10μm had $_MH_c$ = 3350 Oe. This could
be improved to nearly 8000 Oe by metallizing the particles with zinc.
Chemical surface polishing with 1% HNO_3 is another effective method
to increase the coercivity.

-3-10

INTRODUCTION

In the research work on the permanent-magnet alloys of the type RCo_5, the compound promising the highest values of the energy product,[1] $PrCo_5$, has so far been somewhat neglected. The emphasis has been on $SmCo_5$ which allows one to produce powders having extraordinarily high intrinsic coercive forces by simple mechanical grinding. For $PrCo_5$, only the relatively modest values of $_M H_c =$ 3500 Oe[2] and 5750 Oe[3] could be obtained by different methods of vibration grinding. With the powder having 3500 Oe coercivity, the respectable energy product of 4.35 MGOe was achieved readily in a compact of only 63.5% density.[4] But if one hopes to approach the theoretical limit of 36 MGOe and get high $_B H_c$-coercivity by using the special pressing or sintering techniques now being developed for $SmCo_5$,[5,6,7] minimum values of $_M H_c$ in the range of 6000 to 12000 Oe. are required. The desired value depends on the hysteresis loop shape, the density and the intended application of the magnet.

In this paper we report on the permanent magnet properties of $PrCo_5$ powders made by mechanical comminution in a mortar or with an attritor mill, and about successful attempts to improve these properties by surface treatment of the particles.

PARTICLE-SIZE DEPENDENCE OF $_M H_c$ FOR MORTAR-GROUND POWDERS

A single-phase $PrCo_5$ alloy, prepared from the elemental metals by arcmelting and homogenization for 65 hours at $1050^\circ C$, was pulverized with mortar and pestle. The particle sizes were classified by sifting, aided by a permanent magnet for the finest fractions as recommended by Becker.[8] Samples for hysteresis-loop measurements were prepared by premagnetizing the powders with 26 kOe,

-4-

potting $\sim$ 250 mg in epoxy resin and curing at temperatures between 45 and 70°C in a 4. 5 kOe aligning field.

Fig. 1 shows the particle-size dependence of the intrinsic coercive force, $_MH_c$, and the residual-to-peak magnetization ratio ("loop squareness"), M_r/M_p, measured with a peak field of 22. 4 kOe in the alignment direction. The curve exhibits the expected size dependence of the properties. The best value of $_MH_c$ = 3350 Oe, combined with a good loop squareness M_r/M_p = 0.9, is found for the < 10 μ fraction. The coercivities observed are about twice those of the corresponding fractions of mischmetal-cobalt powders,[1] but much less than those reported for $SmCo_5$.[7]

IMPROVEMENTS BY TREATING THE PARTICLE SURFACES

One factor that limits the coercive force of RCo_5 powders to values far below the anisotropy field is the existence of easy domain-nucleation or wall-trapping sites on the particle surfaces from which the magnetization reversal can be initiated at relatively low opposing fields. Becker and Cech[7,8] have demonstrated on YCo_5 and $SmCo_5$ that the coercivity of particles can be increased many times when the granules are smoothed and rounded by immersing them in a chemical polishing solution. As an alternative, the powder may be heated with a small amount of zinc powder.[7] Under proper conditions, the Zn reacts with the RCo_5 compound, apparently forming a thin nonmagnetic shell, and thus deactivating the disturbed surface layer and leaving the magnetic core underneath geometrically rounder and smoother.

We have tried to adapt both techniques to $PrCo_5$. The upper curves in Fig. 1(a) and (b) show the changes in the properties of mortar-ground powders when they are intimately mixed with 5 w/o of Zn dust, outgassed in quartz tubes which are then pumped down to

-5-

2×10^{-6} Torr, valved off and heated to 450°C for 10 minutes. This treatment increases the coercivity after magnetization in 22.4 kOe by a factor 2 to 4 for the various size fractions. The highest value is 7900 Oe for powder of $< 10 \mu$m. The loop squareness is generally also improved except for the finest fraction for which M_r/M_p declined from 0.9 to 0.79. The conditions for this treatment are likely to depend strongly on the surface-to-volume ratio of the powder and must yet be optimized for these small particle sizes.

Fig. 2 shows the effects of immersing mortar-ground particles of 37 to 44 μm diameter in an aqueous solution of 1 % HNO_3 at room temperature. The coercivity is approximately doubled after 8 to 16 minutes of this polishing treatment. The hysteresis loop shape is also slightly improved. On prolonged etching, $_M H_c$ declines again. The weight loss of the powders in the acid was $\sim 18\%$ after 16 minutes, the diameter reduction consequently $\sim 6\%$, so that the increase in coercivity cannot be attributed to reduced particle size.

BALLMILLING EXPERIMENTS

To produce larger quantities of powders for magnet fabrication, one must use some form of commercial grinding device. We ground $PrCo_5$ in a vertical ball mill with a stationary jar, a Szegevary Attritor Mill, Model BS-01 of the Union Process Corporation. The initially $< 105\mu$m granules are ground with ~ 2.5 kg of 3mm-diameter stainless-steel balls in a 800 ml jar under tetrachloroethyiene. In two different milling runs, charges of 30 g and 60 g of $PrCo_5$ were ground. Samples of ~ 300 mg were withdrawn at regular time intervals, magnetically aligned and bonded as described, and hysteresis loops measured. The material used in these experiments was prepared from Pr-Co master alloys received from the U.S. Bureau of Mines in Reno, Nev. These

-6-

alloys, made by a fused-salt electrolysis process,[9] were remelted in the arcmelting furnace under addition of cobalt. The ingots used for ballmilling contained approximately 7% of a second phase.

Fig. 3 presents the results of this attrition grinding. The general features of the curves are those seen previously in experiments with other materials. Initially, both $_M H_c$ and $^M r/M_p$ increase rapidly. The loop squareness reaches a flat peak between 20 and 60 minutes grinding time, then begins to decline, while the coercivity continues to increase slowly. The amount of material ground has some, although not a very important, influence on these properties and the grinding speed. A final coercivity of $_M H_c \simeq 5750$ Oe was attained - the same value which Buschow et al. got with vibration grinding[3] - but a somewhat higher peak would have been reached had the grinding been continued. The loop squareness had dropped to 0.67 at this point. For magnet fabrication, the properties of the powder after 60 min. of grinding the 60 g-lot would be better: $_M H_c = 4800$ Oe, $^M r/M_p = 0.95$.

SUMMARY

The particle size dependence of the intrinsic coercive force and hysteresis-loop squareness as well as the properties attainable by attrition grinding of $PrCo_5$ are reported. With the best attritor-ground material produced, magnets with a static energy product up to 25 MGOe should be possible if a packing density of at least 90% can be achieved and good particle alignment retained, as has been done with $SmCo_5$. The coercivity of $< 10\,\mu m$ powder was raised to nearly 8000 Oe by coating the particles with a zinc alloy.

REFERENCES

(1) K. Strnat, Proc. 7th Rare Earth Research Conf., p.17, Coronado, Calif. (1968); also: Proc. 2nd Europ. Conf. on Hardmagnetic Materials, in press: IEEE Trans. Mag. (1970).

(2) K. Strnat, Cobalt No. 36 (1967), 133.

(3) K. H. J. Buschow and W. A. J. J. Velge, Z. angew. Physik 26 (1969), 157.

(4) U.S. Air Force Materials Laboratory, unpublished results (1966).

(5) K. H. J. Buschow, et al., Philips Tech. Rev. 29 (1968), 336.

(6) D. K. Das, IEEE Trans. Mag. 5 (1969), 214.

(7) J. J. Becker and R. E. Cech, Tech. Report AFML-TR-69-46 on Contract No. F33615-68-C-1248 with the USAF Materials Laboratory; also: J. J. Becker, J. Appl. Physics (March 1970), in press.

(8) J. J. Becker, IEEE Trans. Mag. 5 (1969), 211.

(9) E. Morrice, E. S. Shedd, M. M. Wong and T. A. Henrie, J. Metals 21 (1969), 34.
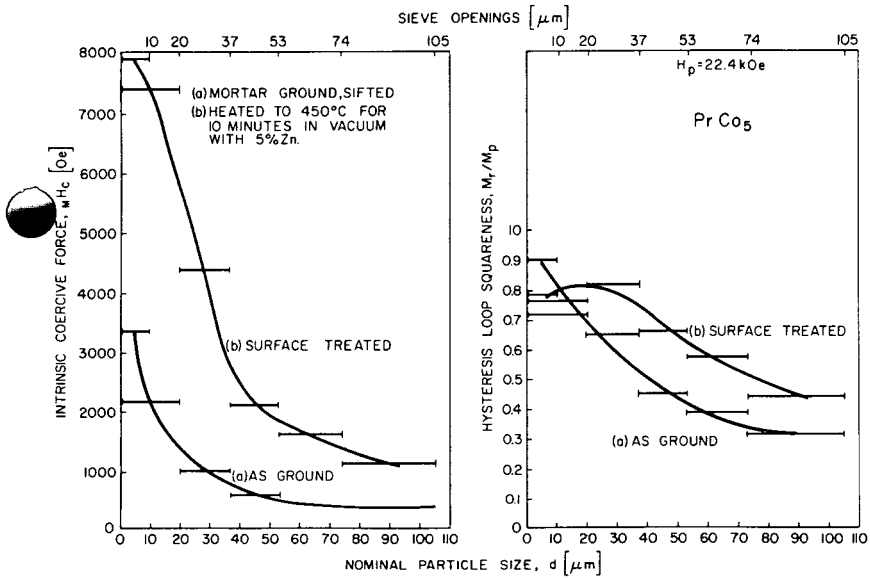
Figure 1: Particle-size dependence of the intrinsic coercive force and the residual-to-peak magnetization ratio for mortar-ground and zinc-treated powders. Particles premagnetized with 26 kOe, field-aligned, bonded with epoxy resin at low packing density. Properties after magnetizing with $H_p = 22.4$ kOe.
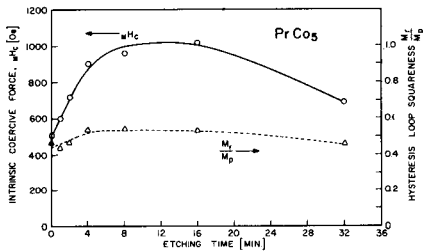
Figure 2: Effect of chemical surface polishing on the coercive force and the hysteresis loop squareness of mortar-ground powder after magnetization in 22.4 kOe. Particle size: 37-44μm. Etching solution: 1% HNO_3 in H_2O. Particles aligned in field.
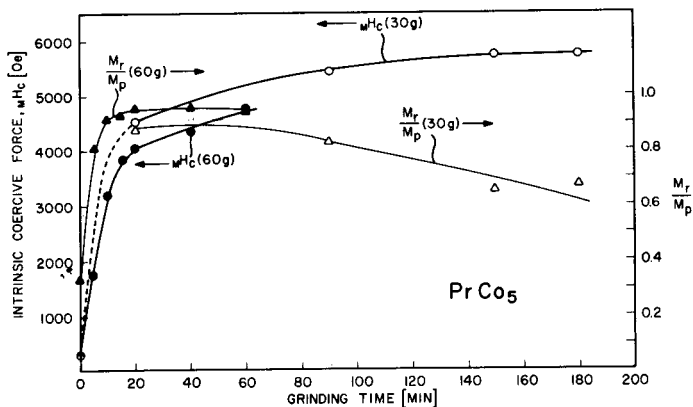
Figure 3: Attrition grinding of $PrCo_5$: Dependence of the coercive force and hysteresis-loop squareness on grinding time. Aligned particles. Magnetizing field H_p = 22.4 kOe.

STRUCTURAL AND MAGNETIC PROPERTIES OF INTERMETALLIC
COMPOUNDS IN THE TERNARY SYSTEM Y-Fe-Co

Hans R. Kirchmayr
Institut für Experimentalphysik
Ruhr-Universität, BOCHUM, Germany

Abstract

Samples of the composition $Y(Fe_{1-v}Co_v)_2$, $Y_6(Fe_{1-x}Co_x)_{23}$, $Y(Fe_{1-y}Co_y)_5$, and $Y_2(Fe_{1-z}Co_z)_{17}$ have been prepared by high frequency melting and by arc-melting. By X-ray diffraction and X-ray fluorescence analysis the crystal structure, lattice spacings, and the actual composition have been determined.

Solid solubility is observed for $v = 0.0$ to 0.4 and $v = 0.7$ to 1.0; for $x = 0.0$ to 0.2; for $y = 0.7$ to 1.0 and for $z = 0.0$ to 1.0.

The magnetic measurements show a marked dependence of the magnetization of YCo_2 on the mechanical treatment of the samples. The magnetization σ and the hyperfine field at the Fe-nuclei reach a maximum for $v = 0.3$ to 0.4.

In the $Y_6(Fe,Co)_{23}$ samples the Curie temperature T_c increases with x. With increasing y-values T_c and σ decrease.

In Y_6Fe_{23} the crystallographic different lattice sites, occupied by Fe-atoms, are also magnetically non-equivalent as is shown by Mössbauer measurements.

1. Indroduction

The phase diagrams of rare earth metals (RE) with transition metals, especially 3d-metals, the intermetallic compounds present in these systems, and especially the magnetic

properties of these compounds have been the object of
many investigations in the last years (1,2). This is due
mainly to the fact that in such compounds the interaction
between the magnetic moments of 4f- and 3d-atoms can be
studied. By diluting either the 4f-atoms by a nonmagnetic
RE-atom, e.g. Y or by substituting one 3d-atom by another
3d-atom, very often the magnetic properties are changed
drastically, while the crystal structure remains the same.
This is for instance true for compounds of the general
formula $RE(Mn, Fe)_2$ and $RE_6(Mn,Fe)_{23}$ (RE = Y, Gd, Er) (3).

In this paper we want to present preliminary results of
investigations on intermetallic compounds of the ternary
system Y-Fe-Co ($Y(Fe,Co)_2$, $Y(Fe,Co)_5$ resp. $Y_6(Fe,Co)_{23}$,
and $Y_2(Fe,Co)_{17}$). This system has been chosen because Y
has no magnetic moment, while Fe and Co have usually a
non-zero magnetic moment. In subsequent investigations we
want to replace Y by RE-atoms with a magnetic moment and
want to study the interaction between the 4f- and the
3d-moments.

2. The boundary systems of the ternary system Y-Fe-Co

Y-Fe-system:

The phase diagram of Y-Fe has been given schematically
by DOMAGALA et al. in 1961 (4). In the meantime additional
phases and intermetallic compounds have been detected by
X-ray methods. At least the following compounds seem to
be stable at room temperature: YFe_2, YFe_3, Y_6Fe_{23},
Y_2Fe_{17} (1). The compound YFe_5 ($CaCu_5$ structure-type) has
been reported by different authors; whether or not it is
stable at room temperature is not sure.

Y-Co-system:

The phase diagram of the Y-Co system has been investigated more recently (5,6). At least the following compounds seem to be stable (1):

Y_3Co, Y_4Co_3, YCo_2, YCo_3, Y_2Co_7, YCo_5, Y_2Co_{17}.

Fe-Co system:

The phase diagram of this system is well known (7). At high temperatures complete solid solubility exists (γ-iron phase, austenite), at low temperatures an extended α-iron (ferrite) mixed crystal region and a narrow region of c.p. hexagonal-cobalt exist.

3. Experimental techniques

The samples (5 - 7 g) were prepared by induction melting mixtures of yttrium (nuclear grade 99.9 %), electrolytic cobalt (99.9 %) and iron (soft, carbonfree iron 99.9 %) in an alumina crucible ("morganite"). An excess of 3 - 15 % Y was used in order to compensate the loss of Y by vaporization, although argon of normal pressure was used as protective atmosphere. Temperatures up to 1800^oC were necessary to obtain homogeneous samples. The cooling rate was 15^oC/minute. An additional tempering procedure was not performed. Some samples were also prepared by arc-melting. All samples were checked for their composition by X-ray fluorescence (8), using watery solutions of the alloys. A part of each sample was crushed in a mortar under kerosene and the alloy powder was investigated by X-ray Debye-Scherrer photographs, using CrK -radiation. Some samples were also examined by high-temperature X-ray diffraction.

The remaining part of each sample was used for

differential thermal analysis, micrographs and especially
for magnetic measurements including Mössbauer measurements.
The DTA-apparatus (9) and the magnetic balance (10) have
been described earlier. The Mössbauer equipment, utilizing
a 1024 channel analyzer, was of a conventional type.

4. Experimental results

Lattice spacings and structures:

Samples of three pseudobinary cuts, corresponding to
the compositions $Y(Fe_{1-x}Co_x)_2$, $Y(Fe_{1-x}Co_x)_z$ (z: 23/6 = 3.83
to 5), and $Y_2(Fe_{1-x}Co_x)_{17}$ have been prepared over the
whole concentration region x = 0.0 to 1.0.

In contrast to earlier investigations (11) we have not
been able to obtain single phased samples of $Y(Fe,Co)_2$ in
the whole concentration region, at least with our prepara-
tion procedure. From the X-ray diffraction patterns and
from the change of the lattice spacings only for x = 0.0
to 0.4, and x = 0.7 to 1.0 a single phase could be observed.
The reason for these results, are not clear yet since
actually YFe_2 and YCo_2 have both the same structure
($MgCu_2$-type).

By preparing samples of the nominal compositions
$Y_6(Fe,Co)_{23}$ and $Y(Fe,Co)_5$ the solid solubility of Co in
Y_6Fe_{23} (Th_6Mn_{23}-type) and of Fe in YCo_5 ($CaCu_5$-type) was
investigated.

When the composition was approximately $Y(Fe_{1-x}Co_x)_5$
(x = 0.2 to 0.7), then three phases were co-existing,
namely $Y_6(Fe,Co)_{23}$, $Y(Fe,Co)_5$, and $Y_2(Fe,Co)_{17}$.

It could not be determined to what extend the Fe:Co
ratio was different in these 3 phases. At high temperatures
near the solidus line, complete solid solution for all

-14-

Fe:Co ratios seems to exist in the compound $Y(Fe,Co)_5$.

The alloys of the composition $Y_2(Fe_{1-x}Co_x)_{17}$ show complete solid solubility for any x-value. The structure is of the rhomboedral Th_2Zn_{17}-type.

If a hexagonal unit cell is chosen, the a- and the c-values show a positive deviation from Vegard's rule.

Magnetic measurements:

The susceptibility and the magnetization have been measured from 80 K to 1200 K in fields up to 12 kOe.

First several samples of YCo_2 have been investigated because of the controversial results of earlier investigations. For YCo_2 a Curie-temperature near 300 K and a small saturation magnetization has been reported (11,12). However, also antiferromagnetic (13) and Pauli-paramagnetic behavior (14) has been reported. By neutron-diffraction studies (14) no magnetic lines resp. no magnetic ordering could be observed.

We have found that the properties of YCo_2 samples are very sensitive to any mechanical treatment. Grinding e.g. may change the magnetic character of the samples completely. Measurements on bulk samples of YCo_2 showed a very small variation of the magnetization of less than 0.1 Gauß cm^3 g^{-1}. The susceptibility does not follow a Curie-Weiss-law and is smaller than 0.285 Gauß cm^3g^{-1}.

The same sample showed the same X-ray diffraction lines after grinding in a mortar under kerosene. The magnetization at 80 K and 10 kOe increased, however, to 0.748 Gauß cm^3g^{-1}. The temperature variation of the magnetization between 77 K and 500 K increased to 0.45 Gauß cm^3g^{-1}.

When the same sample was ball milled for 12 hours

under n-pentane (dried with sodium metal), the X-ray
diffraction lines became diffuse and broad. This fact must
be attributed to lattice distortions, but not to grain
size effects. The temperature dependence of the magnetiza-
tion of this sample is raised to the 10 fold value of the
original sample. The magnetization at 80 K and 10 kOe is
now 14.5 Gauß $cm^3 g^{-1}$.

The results of the magnetic measurements on the series
$Y(Fe_{1-x}Co_x)_2$ in general agree with the results by ABEL
and CRAIG (11). For x = 0.3 a maximum of the magnetization
is observed. Then the magnetization decreases with in-
creasing x. Also the Curie-temperatures increase from 530 K
for YFe_2 to 640 K for $Y(Fe_{0.6}Co_{0.4})_2$. After that they
remain more or less constant and decrease for x = 0.9 to
525 K.

The Mössbauer Fe^{57}-measurements, performed at 300 K,
yield a single well resolved spectrum for all specimens
investigated (x = 0.0 to 0.8). For YFe_2 a hyperfine field
of 190 kOe is measured, which agrees with earlier
measurements (2). For x = 0.1 195 kOe, x = 0.2 200 kOe
and x = 0.3 203 kOe have been detected.

The samples with the composition $Y_6(Fe_{1-x}Co_x)_{23}$ showed
Curie-temperatures for x = 0.0, x = 0.1 and x = 0.2 of
481 K, 485 K and 640 K, respectively. The magnetization
at 80 K and 10 kOe for these 3 samples was nearly the
same (120 Gauß $cm^3 g^{-1}$).

The samples with the composition $Y(Fe_{1-x}Co_x)_5$ showed
Curie temperatures of 1085 K and 935 K, for x = 0.9
and x = 1.0 respectively. The corresponding σ-values
were 98 and 83.

The temperatures dependence of the susceptibility of
the series $Y(Fe,Co)_2$ and $Y(Fe,Co)_{23}$ resp. $Y(Fe,Co)_5$

shows more or less normal Curie-Weiss behavior. A detailed
analysis and the calculation of the effective Bohr-magneton
numbers is now being performed.

The magnetic properties of the mixed crystal series
$Y_2(Fe,Co)_{17}$ are presently under investigation.

Mössbauer-measurements on Y_6Fe_{23} showed that in this
compound the Fe-atoms at the different lattice sites are
magnetically non-equivalent. This results from the fact
that the spectrum shows more than the usual 6 lines and is
non-symmetric. Therefore, also an isomer shift seems to be
present indicating different valence states of the iron-
atoms. Mössbauer measurements on other members of the
series $Y_6(Fe,Co)_{23}$ are also now being performed.

5. Discussion

Because of the different number and crystal structures
of the compounds in the binary systems Y-Fe and Y-Co,
complete solid solubility can only be possible for the
series YFe_2-YCo_2, $Y_2Fe_{17}-Y_2Co_{17}$, and probably for
YFe_3-YCo_3, (this latter series has not been investigated).

For $Y_2(Fe,Co)_{17}$ such a complete solid solubility range
has been observed. For the series $Y(Fe,Co)_2$ we could
observe only limited solubility. The reason is obviously
the different method of sample preparation and tempering
procedure we have used in contrast to (11).

For the compound $Y_6(Fe_{1-x}Co_x)_{23}$ a homogeneity region
seems to exist for x = 0.0 to 0.2 and for $Y(Fe_{1-x}Co_x)_5$
for x = 0.7 to 1.0. Although it was attempted to establish
the phase relations, liquidus and solidus lines and the
nature of the transition from the $Y_6(Fe,Co)_{23}$ phase to
the $Y(Fe,Co)_5$ phase by differential thermal analysis and
by micrographs, additional investigations are necessary.

Nevertheless the fact that an appreciable amount of Co resp. Fe can be solved in Y_6Fe_{23} resp. YCo_5 seems to be well established.

The results of the magnetic measurements reflect the phase relations just discussed.

YCo_2 has magnetic properties which depend mainly on the mechanical treatment performed. If stacking faults and dislocations are produced e.g. by ball milling, the magnetization increases by several orders of magnitude. Such a behavior may be explained by the fact that stacking faults in the $MgCu_2$ structure can bring Co-atoms close together, which are otherwise well separated. This can result in a magnetic ordering which is otherwise impossible. A similar behavior has been observed with cold worked $Sc(Ni_{1-x}Co_x)_2$ (15) and Fe-Al (16) samples. By tempering a cold worked YCo_2 sample at $150^{\circ}C$ for 4 hours a continuous decrease of the susceptibility by 10 % could be observed, which can be interpreted as a recovery of the distorted lattice.

We think, however, that final conclusions about the magnetic nature of YCo_2 can only be drawn if a single crystal is investigated.

The results of the magnetic measurements on the series $Y(Fe,Co)_2$ show that the mean value of the magnetic moments increases with the Co content in a similar manner as in the Fe-Co system. The increase in the magnetization resp. the moment is reflected in a similar increase of the hyperfine field, which is uniform for all Fe-atoms, irrespective of the number of Co-atoms at nearest neighbor sites. This is in contrast to measurements of the hyperfine field at the Fe-nuclei in compounds of the composition $Y(Fe,Mn)_2$ (2).

Also the magnetic properties of the compounds
$Y_6(Fe,Co)_5$ can be understood if one considers the limited
solid solubility of Fe and Co in these compounds and the
fact that Fe and Co are very probably distributed
statistically on the 3d-atom lattice sites. In the
Y_6Fe_{23} structure, however, 4 different lattice sites are
present, which are occupied by Fe. This is reflected in
the Mössbauer pattern.

After concluding the investigations on the compounds
of the ternary system Y-Fe-Co, the next step of our
investigations will be studies of RE-Fe-Co systems, where
RE is a magnetic rare earth element, because then all
magnetic properties of a specific $RE(Fe,Co)_z$ compound
which differ from the magnetic properties of the
isostructural $Y(Fe,Co)_z$ compound can be attributed to the
presence of a localized magnetic moment at the RE-site.

References

1) H.R. Kirchmayr, Zeitschrift für Metallkunde 60, 699,
      60, 778 (1969)
2) H.R. Kirchmayr, Zeitschrift für Angewandte Physik 27,
      18 (1969)
3) H.R.Kirchmayr, J.Appl. Physics 39, 1088 (1968)

4) R.F. Domagala, J.J. Rausch, D.W. Levinson, Trans.
    ASM 53, 137 (1961)

5) K.J. Strnat, W. Ostertag, N.J. Adams, J.C. Olson,
    Proceed. 5th Rare Earth Research Conf. Ames,
    Iowa, 5, 67 (1965)

6) J. Pelleg, O.N. Carlson, J. Less-Common Metals 9,
    281 (1965)

7) M. Hansen, K. Anderko, Constitution of binary alloys,
    McGraw-Hill, N.Y. 1958, p. 471

8) H.R. Kirchmayr, D. Mach, Zeitschrift für Metallkunde
    55, 247 (1964)

9) W. Lugscheider, Berichte d. Bunsengesellschaft f.Phys.
    Chem. 71, 228 (1967)

10) H.R. Kirchmayr, K.-H. Schindl, Zeitschrift für Ange-
    wandte Physik, 19, 517 (1965)

11) A.W. Abel and R.S. Craig, J. Less-Common Metals 16,
    77 (1968)

12) J. Farrell, W.E. Wallace, Inorganic Chemistry 5,
    105 (1966)

13) K.N.R. Taylor, H.D. Ellis, M.I. Darby, Physics Letters
    20, 327 (1966)

14) R. Lemaire, J. Schweizer, Physics Letters 21, 366 (1966)

15) E.W. Collings, R.D. Smith, R.G. Lecander, J. Less-Common
    Metals 18, 251 (1969)

16) G.P. Huffman, R.M. Fisher, J. Appl. Physics 38, 735
    (1967)

MAGNETIC AFTEREFFECT AND AGING OF Sm(Co, Cu, Fe)$_5$

PERMANENT MAGNET ALLOYS

H. Mildrum, A. E. Ray

245 3000   Dayton Univ., Ohio. Research Inst.

~~University of Dayton Research Institute~~

and

K. Strnat

Department of Electrical Engineering
University of Dayton, Dayton, Ohio 45409

ABSTRACT

Alloys of this type can be magnetically hardened by precipita-
tion of a nonmagnetic phase. Magnets made from them show a very
pronounced magnetic aftereffect: Once the magnetization reversal has
started, the intrinsic induction continues to drop slowly - at constant
field strength - for several minutes and in increments up to 50% of the
saturation. This undesirable phenomenon has been studied for
R(Co, Cu, Fe)$_5$ alloys in different stages of heat treatment and for
SmCo$_5$.

R-Co alloy powders are subject to a degradation of their
permanent-magnet properties by aging. Air-aging experiments were
performed at room temperature and 125°C with powders of SmCo$_5$,
SmCo$_{3.5}$Cu$_{1.5}$ and SmCo$_{3.5}$ Cu$_{1.35}$ Fe$_{0.4}$ subjected to various treat-
ments. The degradation is very severe for SmCo$_5$ and for poorly heat-
treated alloys with copper and iron substitution, while properly
precipitation-hardened samples of the latter type are rather stable.
The results are discussed in terms of the metallurgical phase structure
and models of the magnetization-reversal mechanisms.

INTRODUCTION

Permanent magnets containing as their magnetically active
constituent a rare earth-cobalt intermetallic phase of the type RCo$_5$
or a modification thereof, can be made by powdering the alloy, then

bonding or pressing the powder, and, if desired, sintering it. [1]
Nesbitt et al [2] and Tawara and Senno [3] have also demonstrated an
alternative approach which allows one to achieve high intrinsic coercive
forces in the bulk without the necessity of comminution. The present
paper is concerned with magnets of the latter type.

Alloys with a two-phase microstructure can be produced by
replacing a part of the cobalt by copper. If they are given an appropriate
heat treatment, very high coercive forces can be achieved. This has
so far been done successfully with alloys based on Sm-Co, Ce-Co and
mischmetal-cobalt. The addition of nonmagnetic copper also lowers
the saturation magnetication and, consequently, the energy product
possible for magnets made from such alloys. This undesirable side
effect can be counteracted to some degree by the simultaneous addition
of iron in amounts that are accommodated by the AB_5 lattice. On the
basis of recent further investigations, [4, 5, 6, 7] a clearer concept of
the mechanism of the magnetic hardening has begun to evolve: At
high temperatures, near the peritectic reaction, extensive solid
solubility of copper (and iron, if used) in the "RCo_5"-crystal appears
to exist. But on cooling, the alloy decomposes into two phases, the
one rich in Co and strongly magnetic at room temperature, the other
rich in Cu and nonmagnetic. (At least, it has a much lower saturation
and Curie point than the first phase.)

Near the center of the miscibility gap, i.e., near $x \approx 1.5-2$
in the $SmCo_{5-x}Cu_x$ system, spinodal decomposition occurs on cooling. [4]
This yields an extremely fine-grained structure in which the magnetic
phase ("$SmCo_5$") is present in the form of more or less isolated
particles which act like the granules in ground powders, except that
they are rather perfect crystallites with a roundish shape and a smooth
surface and consequently can have extremely high domain-nucleation
coercivity.

However, for alloys with low copper content on the Co side of the immiscibility region, where the solvus line falls off steeply, annealing at only a few hundred °C following homogenization produces an intragranular, nonmagnetic precipitate in a magnetic "SmCo$_5$" matrix. [7] This precipitate impedes the motion of magnetic domain walls through the material, thus creating coercive force in the classical manner, so that a subdivision of the magnet into fine particles is not required. The alloys investigated by us are in the latter category.

AGING EXPERIMENTS

a.   Description of the Phenomenon

SmCo$_5$ powders prepared by mechanical grinding, and to a lesser extent the magnets made by compacting these, lose much of their high initial coercive force upon prolonged exposure to air. [8] This aging process, which is considerably accelerated by heating to 100-150°C, has been attributed to the creation of low-energy domain nucleation sites on the particle surfaces by selective oxidation. In the alloys which are magnetically hardened by precipitation of a nonmagnetic phase, however, surface nucleation of domains plays no role, if our concept of the causes of magnetic hardness is correct. Consequently, their permanent-magnet properties should not deteriorate upon aging. (The same might be expected of the spinodally-decomposed alloys. While domain nucleation processes may be important in these, the particles are completely imbedded in the solid and not exposed to air.) For massive pieces of such two -phase alloys, no aging problem should therefore exist - at least not at the low temperatures mentioned - and this expectation appears to be borne out by our experiments.

However, in the production of magnets from these alloys, it may be necessary to work with powders after all. The difficulties of controlling simultaneously the chemical homogeneity, the matrix-crystal

-23-

orientation, and the precipitation process during the casting of magnets of practical sizes and shapes may prove prohibitive. Powder-metallurgical processing allows a better homogenization and the imposition of a texture by means of magnetic particle alignment before pressing. Production casting of any but the simplest and smallest shapes may also prove quite difficult in view of the brittleness of the alloys. If the copper-containing alloys are to go through a particulate state during processing, it is important to know how their magnetic properties depend on particle size, and in what manner the properties may change because of the reaction of powders or compacts with the atmosphere. The first set of experiments reported here was designed to shed some light on these questions.

b.   Experimental Procedures

The alloys were prepared by arcemelting from the elemental metals as described previously. Then they were annealed with intent to homogenize, for the times and temperatures noted in the figure captions, and water-quenched to preserve the solid solution. The ternary and quaternary alloys were then annealed for 4 hours at various lower temperatures to develop the precipitate. Figure 1 shows the microstructures found in $SmCo_{3.5}CuFe_{0.5}$ for the various stages of heat treatment. The material was then ground with mortar and pestle and classified by sifting, all in air and at room temperature. For the magnetic measurements, 250 mg of the loose powder were premagnetized in a field of 26 kOe and mixed with an epoxy resin which was cured at temperatures between 45° and $70^{\circ}C$ in 4.5 kOe. Hysteresis loops were measured with a peak field strength of H_p = 22.4 kOe and the reported data for the intrinsic coercive force, $_MH_c$, determined from these. The loops were symmetric and generally nicely square as shown in Figure 3c. For the air-aging studies, several grams of the powder

-24-

were spread thin in a flat aluminum dish and either kept at 125°C in a heated "desiccator" with the lid left open, or merely at room temperature in a cabinet. Samples of 250mg were withdrawn, potted and measured as described.

c.   Results of Forced-Aging Experiments

In Figure 2 we show how the intrinsic coercive force changes during aging at 125°C for periods up to 72 hours. A control sample of $SmCo_5$ powder (Curve a) was aged alongside the two-phase alloys and exhibited the previously observed severe degradation. From an initial value of $_MH_c$ = 10, 200 oersted, the coercivity dropped to 7, 000 Oe during the first two hours and continued to decrease, although at a much slower rate, to values below 6, 000 Oe. Even after 72 hours it had not reached a final, stable value yet. By contrast, $SmCo_{3.5}Cu_{1.35}$ $Fe_{0.4}$ which had been heat treated for optimal coercivity ($_MH_c$ is nearly particle-size independent from 105μm down to the particle size of <37μm used in this test) showed only a rather minor initial drop in H_c from 8, 000 to about 7, 600 Oe where it appeared to remain constant after the first two hours (Curve b). However, the same alloy in the nearly homogenized, metastable state obtained by annealing at 1100°C and water-quenching from there behaves very similar to $SmCo_5$ (Curve c). There is a sharp initial decay which continues at a slow rate even after 72 hours. Curve d refers to results with a (coarser) powder of the alloy $SmCo_{3.5}Cu_{1.5}$ which had received no homogenization anneal but was only heat-treated for 4 hours at 600°C after arc-melting, following approximately the procedure described by Nesbitt et al in their first publication on such alloys. [2] This powder showed a strong initial and a slower continuing decline of H_c, its behavior lying between that of the homogenized and the properly precipitation-treated alloys with an iron addition.

-25-

It is informative to look not only at the coercive force but also at the changes taking place in the hysteresis loop shape during the aging process. Figure 3 shows, superimposed, the loops measured at 0 and 72 hours. It must be noted that only the H-scales are the same for all six curves. Because of the nature of the measurement - on samples of low packing density that contain only approximately the same amount of magnetic powder in a dispersion that may differ from sample to sample - the (B-H)-scales vary slightly. They were left arbitrary, and attention should focus only on loop shape and coercivity.

$SmCo_5$ and the homogenized Sm(Co, Cu, Fe) - alloy initially had loops with a "fat tail" in the first and third quadrants. This indicates the presence of a very high-coercivity fraction of particles whose magnetization reversal begins by domain nucleation on the particle surface. On aging these tails shrink, the magnetization processes near the tips of the loop become reversible, and the loops "square up." One can understand these changes in terms of the model of the magnetization reversal proposed by Becker[8] in the following manner: During aging, surface corrosion of the particles creates low-energy nucleation sites, thus lowering the coercivity especially of the particles that were initially most difficult to reverse, until eventually - after long aging times - $_M H_c$ may drop to the level of the wall-motion coercive force. The latter was determined to be about 1,500 Oe in the Sm(Co, Cu, Fe) by measurements on very coarse powder, but is unknown for our $SmCo_5$ alloy. From the similarity in the behavior between the $SmCo_5$ and the homogenized Sm(Co, Cu, Fe) it is concluded that in the $<37\mu m$ powder of the latter a major portion of the particles reverses by domain nucleation and growth. In the alloy that was heat-treated at 475°C after homogenization, however, the "tail" is much less pronounced. It promptly vanishes on aging, and the moderate loss of

-26-

$_M H_c$ during the first hours is attributable to this. The loop shape in the second quadrant remains essentially unchanged. It seems that only some of the finest particles, which contain little or none of the precipitate, can ever be swept clean of domain walls and forced to renucleate them on the surface. In most of the grains, the precipitate determines the coercivity by providing obstacles to wall motion and internal nucleation or wall-trapping sites. Since these are features of the particle interior, the changes of the particle surface by corrosion cannot influence the coercivity of most of the powder.

d.   Results of Room-Temperature Aging Experiments

        Three of the powders have been air-aged at room temperature up to 100 days (Figure 4). $SmCo_5$ showed again a pronounced initial loss of coercivity, but $_M H_c$ appears to level off after 60 days at a somewhat higher level than before. The test is being continued. $SmCo_{3.5} Cu_{1.35} Fe_{0.4}$ in the precipitated and - somewhat surprisingly - also in the homogenized state, appears rather stable. The fact that there is no initial decline and the considerable scatter of the points may be due to an unfortunate feature of our sample-preparation technique: The temperature of the epoxy binder during curing varied considerably, and it is possible that an appreciable - and unequal - amount of additional particle corrosion took place during the curing. While the tests should therefore be repeated, the results still point out the difference in the sensitivity to aging between $SmCo_5$ and the precipitation-hardened alloy, and they demonstrate how strongly the aging is accelerated at $125^{\circ}C$.

        The different initial values in the $25^{\circ}C$ and the $125^{\circ}C$ aging test are due to the fact that heat-treating, grinding and sifting were done twice. For the powder fraction $<37\mu m$ it is not possible to reproduce the size distribution exactly.

-27-

MAGNETIC AFTEREFFECT

The two-phase alloys containing copper show a very pronounced magnetic aftereffect. The immediate change of the intrinsic induction accompanying a change in the magnetizing field is followed by a further, slow adjustment of (B-H) which takes place over a period of several minutes. This was first pointed out by Becker[10] for the alloy $SmCo_{2.5} Cu_{2.5}$ in the as-cast state.

We have investigated this phenomenon on the same alloys on which the aging studies were made, using as samples magnetically aligned powder compacts of about 60% packing density which were bonded with tin. Figure 5 shows pairs of demagnetization curves, one traced in the usual manner in a few seconds, the other much more slowly with several steps. At each step the field strength was held essentially constant for 3 minutes during which the magnetization continued to drop. Time markers indicate the decreasing rate of the adjustment. It can be seen that in the steep part of the curve the changes can be very large, notably in the properly precipitation heat-treated $SmCo_{3.5} Cu_{1.35} Fe_{0.4}$ where the height of the largest step amounts to 1,960 G, or over 50% of the remanence of the sample. The effect is present, but negligibly small for practical purposes, in $SmCo_5$.

The aftereffect occurs only in those parts of the hysteresis loop where the magnetization processes are irreversible. For the correctly precipitation-hardened alloy it is not observed in the first quadrant or in the straight-line portion of the second from the remanence point to the knee. This indicates that the cause of the phenomenon is a thermally activated creeping of unstable domain walls through the thicket of precipitate particles which act as pinning sites. This type of aftereffect was theoretically described by Néel.[11]

-28-

In practical terms, the existence of the aftereffect means that the equilibrium demagnetization curve - the focus of all steady magnetization states - which is the one of importance for most magnet applications, lies appreciable lower and has a smaller intrinsic coercive force than a quickly-traced curve. This need not adversely affect $_BH_c$ and energy product provided the knee of the demagnetization curve is sufficiently far to the left of the lowest operating point of the magnet. This is, however, not the case for our best sample of $SmCo_{3.5} Cu_{1.35} Fe_{0.4}$ for which the aftereffect begins to become noticeable at approximately 3 kOe.

SUMMARY

The degradation by air-aging and the magnetic aftereffect have been investigated for $SmCo_5$ and Sm-Co based alloys that were magnetically hardened by additions of Cu and Fe and precipitation of a second phase. After the proper heat treatment, $SmCo_{3.5} Cu_{1.35} Fe_{0.4}$ was found to be quite stable on aging, even as a fine powder, in stark contrast to $SmCo_5$. The same alloy, however, shows large changes of the magnetization at constant field for several minutes after a field change occurred. This causes the steady-state magnetization curve to be appreciably different from one measured at the usual traversal speed. The effect is also present in $SmCo_5$ but is insignificant there. Probable physical causes and the practical implications of these phenomena for the application of permanent magnet were discussed.

ACKNOWLEDGMENTS

REFERENCES

1. K. J. Strnat, paper at the 2nd Europ. Conf. on Hardmagnetic Materials. In press: IEEE Trans. Mag. (1970).

2. E. A. Nesbitt, R. H. Willens, R. C. Sherwood, E. Buehler and J. H. Wernick, Appl. Phys. Letters 12 (1968) 361.

3. Y. Tawara and H. Senno, Japan J. Appl. Physics 7 (1968) 966.

4. F. Hofer, paper at the 2nd Europ. Conf. on Hardmagnetic Materials. In press: IEEE Trans. Mag. (1970).

5. E. A. Nesbitt, J. Appl. Physics 40 (1969) 1259.

6. H. Senno and Y. Tawara, Japan J. Appl. Physics 8 (1968) 118.

7. K. Strnat and A. E. Ray, paper at meeting of the Deutsche Ges. f. Metallkunde, Berlin, May 1969. To be published in Z. f . angew. Physik (1970).

8. J. J. Becker, IEEE Trans. Mag., MAG-4 (1968) 239.

9. J. J. Becker, IEEE Trans. Mag., MAG-5 (1969) 211.

10. J. J. Becker and R. E. Cech, Tech. Report AFML-TR-69-46 on Contract No. F33615-68-C-1248 with the USAF Materials Laboratory.

11. L. Neel, Rev. Mod. Physics 25 (1953) 293.

Figure 1: Microstructures of $SmCo_{3.5}$ Cu $Fe_{0.5}$ (250x)
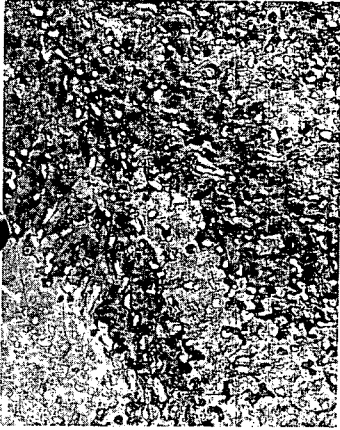
(c) Tempered for 4 hours at 473°C. At this temperature, $_MH_c$ has its optimum value. Note that no precipitate is visible as yet. (not even at 1000x magnification.)
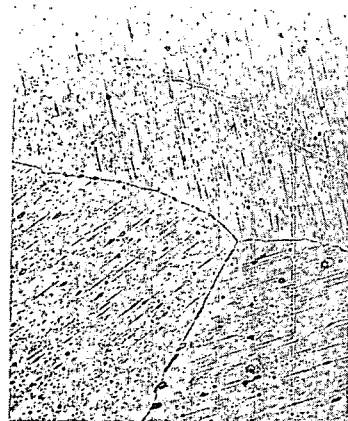
(d) Tempered for 4 hours at 576°C. Precipitate has become visible. $_MH_c$ has dropped appreciably below its optimum.

-31-
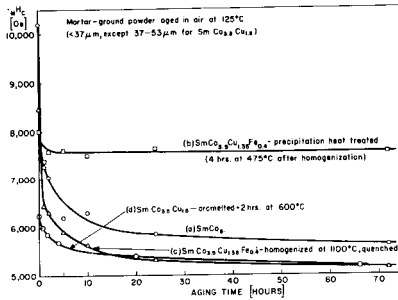
Figure 2: Time dependence of the intrinsic coercive force during air-aging of powders at 125°C.
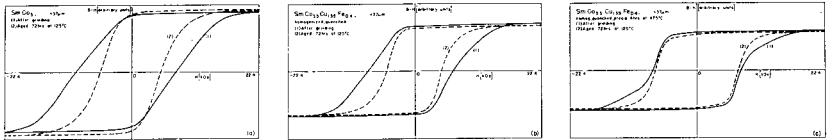
Figure 3: Hysteresis loops of aligned powder samples before (Curves 1) and after (Curves 2) aging in air at 125°C.
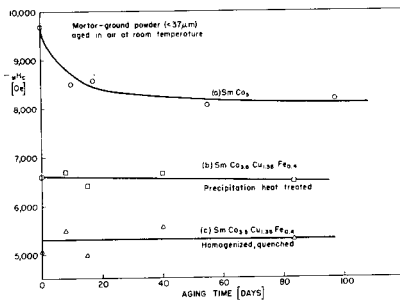
Figure 4: Time dependence of the intrinsic coercive force during air-aging of powders at room temperature.

Figure 5: Magnetic aftereffect:
Comparison of quickly-traversed
demagnetization curves and
curves traced with several 3-
minute stops at constant field.
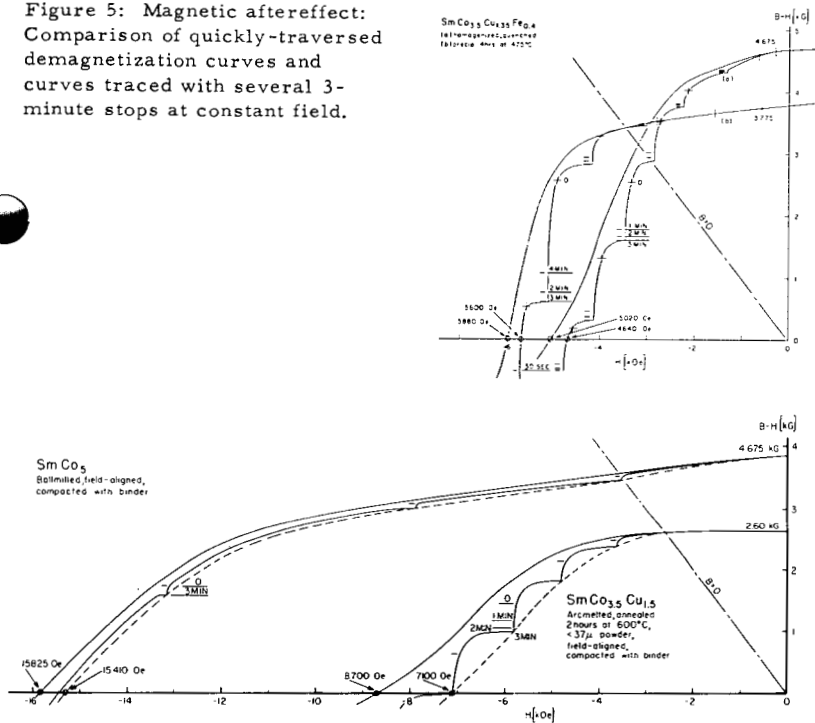
MAGNETIC STRUCTURE OF $HoFe_2$

J-M Moreau, C. Michel, M. Simmons, T. O'Keefe and W. J. James

Departments of Chemistry and Metallurgical Engineering
University of Missouri-Rolla, Rolla, Mo.

Abstract

Neutron diffraction and thermal magnetization analyses were made of $HoFe_2$. The magnetic structure is ferrimagnetic below the Curie temperature with the Ho moments coupled anti-parallel to the Fe moments. The saturation moments at $4.2^{O}K$ are 1.7 ± 0.2 and 9.5 ± 0.2 μ_B for Fe and Ho resp. corresponding to 6.1 μ_B per unit formula. It is concluded that the Ho-Ho interactions decrease rapidly with increasing temperature and that the Ho-Fe interaction must be weak.

Introduction

Magnetic properties of the intermetallic compounds involving transition and the rare earth metals have been extensively studied, particularly the cubic Laves phase compounds ($MgCu_2$ structure). Magnetization measurements which have been made for the RFe_2 series by Wallace and Skrabek[1], Wertheim and Wernick[2], and Crangle and Ross[3] are not in good agreement. No attempts to date have been made to directly determine the individual atomic moments and the magnetic structures of the rare earth-iron alloys. Accordingly neutron diffraction experiments as well as magnetization studies have been carried out on $HoFe_2$ to determine the extent of magnetic interaction and the magnetic moments of Fe and Ho.

Sample Preparation

Ho and Fe in stoichiometric quantities were induction melted under argon in Morganite recrystallized alumina crucibles at 1600°C. The samples were then annealed at 1275°C for 24 hours to yield single phased material as evidenced by both X-ray powder diffraction and metallographic examination. The lattice constant, a, was calculated as 7.303 ± .001 Å in good agreement with the value reported by Wernick and Geller [4]. All samples were retained in an argon ⸺ion and neutron diffraction

⸺surements

was measured on a powdered
⸺xtraction method proposed
⸺he magnetization measure-
⸺0 kOe. At low tempera-
⸺nt for saturation. The
⸺ extrapolated using the
⸺ous magnetization
⸺mu/g was obtained, in
⸺ Wernick [1] but
⸺ and Skrabek [2].
⸺K, is in good
agreement with earlier work   .   ⸺olute saturation
magnetization value, σ = 6.1 μ_B per unit formula, suggested on antiferromagnetic coupling between the Ho and Fe sublattices.

use 5378 500

Neutron Diffraction Analysis

Neutron diffraction analysis was carried out at the Oak Ridge National Laboratory, Oak Ridge, Tennessee. Powder patterns were obtained at 4.2, 77, 298, and $700^{\circ}K$. On one sample, an earlier neutron diffraction analysis taken prior to the magnetization measurements showed small extra peaks present, most of which could be indexed assuming a magnetic cell twice the size of the chemical cell. The presence of such small peaks on low temperature neutron diffraction patterns have been observed for $HoCo_2$ by Moon et al.[6] and by Lemaire[7]. On a later neutron diffraction pattern of another sample of $HoFe_2$, no such peaks were evident suggesting that they were caused by the presence of small amounts of other phases as proposed by Moon et al.[6] for $HoCo_2$.

Below the Curie temperature, the ferrimagnetic behavior of the compound was confirmed. The magnetic structure is similar to that of $HoCo_2$ in that the moments of Fe and Ho are antiparallel; their values at $4.2^{\circ}K$ are 1.7 ± 0.2 and 9.5 ± 0.2 μ_B resp. corresponding to a moment of 6.1 μ_B per unit formula, in good agreement with our magnetization measurements.

Discussion

The saturation moment of 9.5 μ_B is not too far removed from the calculated value of 10 μ_B for the trivalent free ion and thus provides further direct evidence that little or no quenching of the moment of Ho occurs in $HoFe_2$ as reported by Moon et al.[6] for the Laves phase compounds $TbCo_2$, $HoCo_2$, and $ErCo_2$.

The temperature variation of the intensity of two magnetic peaks (222) and (220) provides some knowledge of the magnetization behavior of the two sublattices, Figs. 1 and 2, resp. The (222) peak arises only from Fe contributions and its intensity is constant to just about the Curie temperature at which point it drops sharply. The (220) peak is due only to Ho contributions. After $80^{\circ}K$ the intensity drops sharply. At room temperature moments of 6.0 μ_B and 1.6 μ_B were found for Ho and Fe, resp.

The above observations reveal that the Ho-Ho interaction decreases rapidly with increasing temperature, the Ho-Fe interaction is weak, and the Fe sublattice magnetization persists far beyond room temperature.

Similar studies are in progress on $HoFe_3$ and Ho_2Fe_{17}.
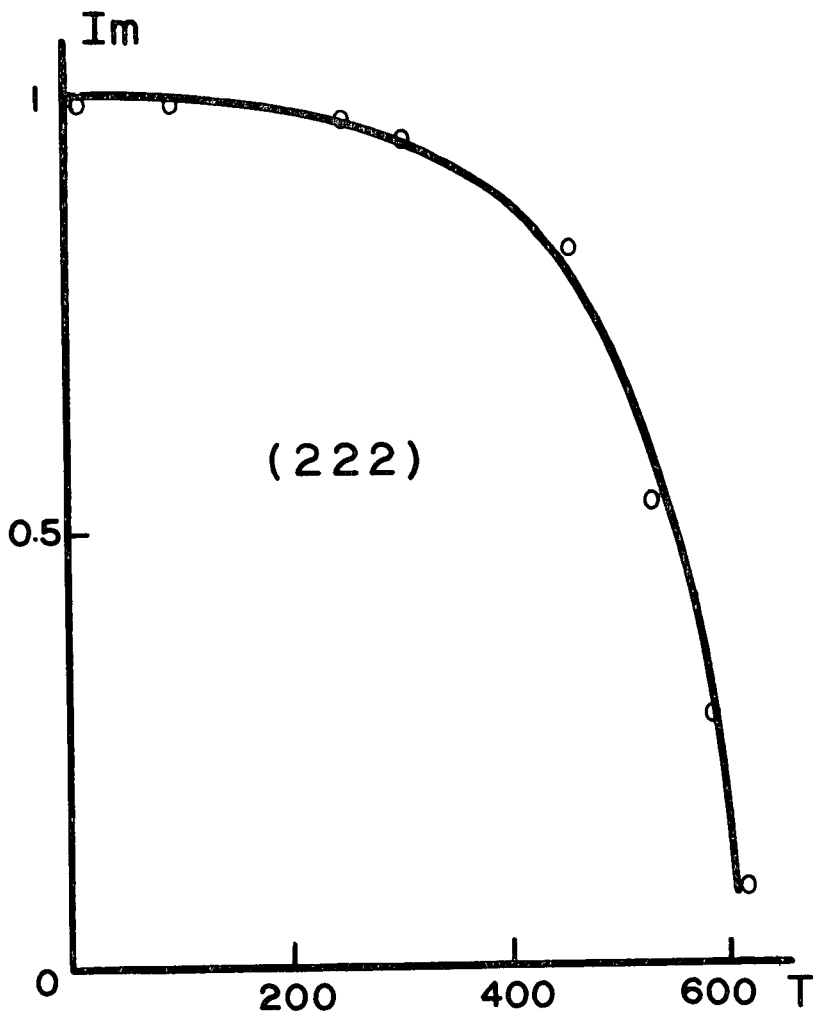
FIG. 1 Variation of neutron diffraction intensity of the (222) peak for HoFe$_2$ with temperature.
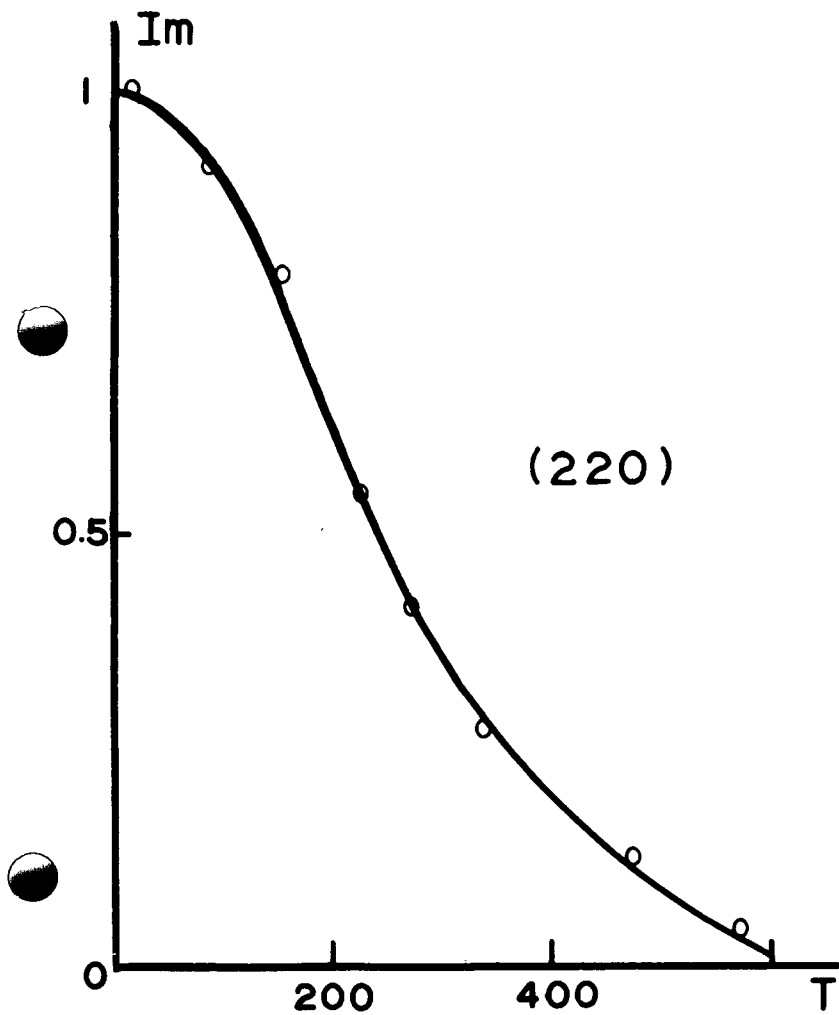
FIG. 2 Variation of neutron diffraction intensity
of the (220) peak for HoFe$_2$ with temperature.

References

(1) W. E. Wallace and E. A. Skrabek, Proc. Third Rare Earth
    Conference, Clearwater, Florida (1963); W. E. Wallace,
    Progr. in Science and Tech. of Rare Earths, Vol. 3, 23
    (1968).

(2) G. K. Wertheim and J. H. Wernick, Phys. Rev., 125, 1937
    (1962).

(3) J. Crangle and J. W. Ross, Proceedings of the
    International Conference on Magnetism, Nottingham, 1964.

(4) J. H. Wernick and S. Geller, Trans. AIME, 218, 866
    (1960).

(5) P. Weiss, J. de Physique, 9, 373 (1910).

(6) R. M. Moon, W. C. Koehler, and John Farrell, J. Appl.
    Phys., 36, 978 (1965).

(7) R. Lemaire, Ph. D. Thesis "Preparation et Proprietes
    Magnetiques des Composes Intermetalliques du Cobalt
    avec les Metaux des Terres Rares ou l'Yttrium,"
    University of Grenoble, Grenoble, France (1966).

MAGNETIC AND STRUCTURAL CHARACTERISTICS OF TERNARY

INTERMETALLIC SYSTEMS CONTAINING LANTHANIDES[*]

Burke Leon and W. E. Wallace

Department of Chemistry
University of Pittsburgh
Pittsburgh, Pa. 15213

670 2000

Pittsburgh Univ., Pa.   Dept. of Chemistry.

Abstract

Structural and magnetic characteristics of two sets of
ternary systems have been studied: (a) $LnNi_{2-x}Al_x$ with Ln = Ce,
Pr, Nd, Gd, Tb, Dy, Ho and Er and (b) $Pr_{1-x}Ln_xCo_2$ where Ln = Dy
and Ho. The temperature range covered was from 2 to 300°K. The
latter ternaries exhibit the C15 structure for all values of x.
In the $LnNi_{2-x}Al_x$ ternaries there is an appreciable range of pri-
mary solubility for phases based on $LnAl_2$. The same is true for
phases based on $LnNi_2$, except for $CeNi_2$; the solubility of $CeAl_2$
in $CeNi_2$ is below the level of detection. An intermediate phase
(C22 structure) based on the composition LnNiAl was observed in all
the Al-containing ternaries. All of the samples except CeNiAl ex-
hibited Curie-Weiss behavior with paramagnetic moments in close
agreement with that expected for free ions. CeNiAl has a very low
susceptibility suggesting the effect of partial crystal field
quenching and/or spin compensation (Kondo effect). Most of the
$LnNi_{2-x}Al_x$ ternaries become ferromagnetic at low temperatures.
The magnetic behavior of $PrNi_{2-x}Al_x$ with x = 1.85 - 1.95 is
anomalous at low temperatures.

The $Pr_{1-x}Ln_xNi_2$ ternaries exhibited normal paramagnetic
behavior. They become ferrimagnetic at low temperatures. There is
a threshhold value of x (~ 0.2) below which Pr has no moment. The
Co-containing systems do not exhibit Curie-Weiss behavior. They
are ferrimagnetic at low temperatures with the Pr and Co moments
aligned parallel and the Pr and Ln moments aligned anti-parallel.

I.   Introduction

Compounds represented by the formulas $LnNi_2$ and $LnAl_2$ (Ln

represents a rare earth or yttrium) are well known and have been

extensively studied.[1-3] The present study was initially concerned

with the replacement of Ni by Al in the $LnNi_2$ phase to ascertain the range of the primary solid solution phase based on $LnNi_2$. These efforts were in time extended to include the entire composition range in the $LnNi_2$-$LnAl_2$ pseudo-binary systems. Eight systems were studied. In addition measurements were made on the four systems $Pr_{1-x}Ln_xNi_2$ and $Pr_{1-x}Ln_xCo_2$ with Ln = Dy and Ho.

The objective in studying the $LnNi_2$-$LnAl_2$ ternaries was to ascertain whether the phase boundaries could be interpreted in terms of Brillouin Zone filling. The motivation for studying the other four ternaries was quite different. $PrNi_2$ becomes a Van Vleck paramagnet at low temperatures indicating[4] that the ground state of the Pr^{+3} ion in this compound is the Γ_1 state. The ion in this state is non-magnetic in the absence of a magnetic field but it acquires a moment when exposed to a field.[5,6] In $Pr_{1-x}Dy_xNi_2$ or $Pr_{1-x}Ho_xNi_2$ Pr^{+3} is acted upon by the field produced by the strongly magnetic Dy or Ho ion. These ternaries were examined to determine the magnetic characteristics of Pr^{+3} under these circumstances. The corresponding cobalt compounds were of interest because they represent a generally similar situation. However, in them the Pr^{+3} moment is generated not only by the field of the Dy or Ho ion but by that of the cobalt constituent as well.

II. Experimental Details

Samples were prepared by levitation melting using the best grade materials available commercially. They were annealed in MgO

crucibles sealed off in Vycor under vacuum. The annealing was carried out under conditions established as optimal by experiment. Annealing temperatures ranged from 550 to 900°C and times varied from about 2 days to 2 weeks. Structures and phases present were determined by a GE XRD-5 diffractometer using Zr-filtered molybdenum radiation.

Magnetic properties were obtained using techniques that are standard in this laboratory.[2,3,7]

III. Results and Discussion

A. $LnNi_2$-$LnAl_2$ Ternaries

In all cases except for Ln = Ce there is a substantial range of primary solubility for the phases based on both $LnNi_2$ and $LnAl_2$. There is in addition an intermediate phase at approximately the composition LnNiAl. The intermediate phase is hexagonal; it has the C22 structure (Fe_2P) recently described by Dwight et al.[8] The solubility of $CeAl_2$ in $CeNi_2$ is below the level of detection in this work (1 mole %). In contrast with this behavior there is substantial solubility of $CeNi_2$ in $CeAl_2$. Similar results were obtained by Wallace et al. in studies of $CeNi_2$-$CeCu_2$ pseudo-binaries.[9]

The phase relationships are summarized in Table I. Diffraction patterns for three samples ($DyNi_{.36}Al_{1.34}$, $HoNi_{1.05}Al_{.95}$ and $ErNi_{1.83}Al_{.17}$) were obtained at 4.2°K. Structures were the same as at room temperature.

-43-

Table I

Ranges Over Which Phases are Stable in $LnNi_2$-$LnAl_2$ Pseudo-

Binaries

(Results are given in mole %-$LnAl_2$)

Ln	C15 phase based[**] on $LnNi_2$	Intermediate phase[**] (C22 structure)	C15 phase based[**] on $LnAl_2$
Ce	*	42.5 - 59	84.5 - 100
Pr	0 - 4	50 - 56	85 - 100
Nd	0 - 5	43 - 50	81 - 100
Gd	0 - 8.5	40 - 51.5	78 - 100
Tb	0 - 8.5	46 - 52.5	79 - 100
Dy	0 - 8.5	44 - 52	81 - 100
Ho	0 - 8.5	44 - 59	77 - 100
Er	0 - 8.5	50 - 60	83 - 100

[*]There is no detectable solubility. The sensitivity of the method
is such that the solubility must be less than 1 mole per cent
$CeAl_2$

[**]Phase boundaries are uncertain by ±0.01 and ±0.02 or 0.03 for the
terminal and intermediate phases, respectively.

-44-

Magnetic characteristics are largely summarized in Tables
II and III. All of the ternaries were paramagnetic at room tempera-
ture as adjudged from the linear variation of magnetization with
field. All samples except CeNiAl exhibited Curie-Weiss behavior
with effective moments in close agreement with those expected for
the free tripositive ion. (See Table II) In most cases the ter-
naries became ferromagnetic upon cooling to $4.2°K$. Three alloys re-
mained paramagnetic down to $4.2°K$. In the majority of cases lowering
the Al/Ni ratio in the sample resulted in a decline of Curie tempera-
ture, Weiss constant and saturation magnetization. Only two systems
were investigated in this respect in detail -- the $TbAl_2$ and $ErAl_2$
primary phases. In the former case there was a linear decline of
T_c, θ and μ_{sat} as Al was replaced with Ni. Data are given in
Table II. The behavior of the Er-containing ternaries is different;
T_c, θ and μ_{sat} pass through a maximum when about 5% of the Al in
$ErAl_2$ is replaced by Ni.

As noted above CeNiAl does not exhibit Curie-Weiss behavior.
Its susceptibility is very low compared to that expected from
Curie's Law, due undoubtedly to crystal field quenching effects
and/or spin compensation by the conduction electrons (Kondo phe-
nomenon). Anderson[10] has shown that if spin compexnation is the
dominant effect in regard to low temperature magnetic behavior, χ^{-1}
varies as $T^{1/2}$ in the low temperature limit. Data for CeNiAl show
that χ^{-1} is linear with T^a where a is very close to 0.5 (actually
0.57) for $T < 60°K$. This lends support to the idea that spin

-45-

Table II

Comparison of Magnetic Behavior of Ternary Systems and Parent

Binary Systems for the Primary Phase Region[*]

Ln	x in $LnNi_{2-x}Al_x$	$T_c(°K)$	$\theta(°K)$	$\mu_{eff}(\mu_B)$	$\mu_{sat}(\mu_B)$
				Ternaries based on $LnNi_2$	
Ce	DNF^a	$--^a$			
Pr	.05	VVP^a	0(4)	3.66(3.57)	
Nd	.04	16(16)	7(10)	3.46(3.74)	1.73(1.84)
Gd	.11	92(85)	79(78)	8.23(7.82)	6.88(7.13)
Tb	.05	53(45)	40(35)	9.91(9.82)	6.59(7.82)
Tb	.09	56(45)	42(35)	9.78(9.82)	6.45(7.82)
Dy	.16	42(30)	26(23)	10.8(10.4)	7.92(9.23)
Ho	.16	30(22)	14(12)	10.6(10.5)	8.02(8.40)
Er	.17	30(21)	8(11)	9.50(9.37)	5.18(6.75)
				Ternaries based on $LnAl_2$	
Ce	1.80	$--^b(3.1)^a$	(-41)		
Pr	1.84	$--^c(37)$	29(30)	3.44(3.46)	$--^c(2.60)$
Nd	1.73	25(76)	19(70)	3.61(3.59)	1.71(2.27)
Gd	1.55	68(182)	58(168)	8.73(7.94)	6.06(7.10)
Tb	1.92	118(121)	102(110)	10.7(9.81)	8.19(8.60)
Tb	1.79	84	72	9.71	7.25
Tb	1.80	59	53	10.1	6.30
Dy	1.80	83(70)	66(64)	10.8(10.7)	8.05(9.62)
Ho	1.55	31(42)	17(30)	10.9(10.7)	8.05(9.16)
Er	1.90	33(24)	16(14)	9.82(9.46)	8.12(9.59)
Er	1.76	27(24)	9(14)	9.87	7.14
Er	1.70	29(24)	6(14)	9.62	6.45

Table II (Continued)

[*]T_c and θ denote the Curie and Weiss temperatures, respectively.
μ_{eff} is the paramagnetic moment; μ_{sat} is the saturation moment
measured at $4.2°K$.

[a]The numbers in parenthesis give the ordering temperature for the
$LnNi_2$ or $LnAl_2$ parent phase. All except $CeAl_2$ order ferromagnetically.
Susceptibility work and heat capacity work show that $CeAl_2$ becomes
antiferromagnetic. DNF signifies that the ternary does not form.
VVP signifies Van Vleck paramagnetism.

[b]$CeNi_{2-x}Al_x$ ternaries remain paramagnetic down to $2.28°K$.

[c]Magnetic nature of these ternaries at low temperatures is in doubt
(vide infra).

-47-

Table III

Magnetic Properties of the C22 $LnNi_{2-x}Al_x$ Alloys

	T_c [a]	θ [a]	μ_{eff} [b]	$g[J(J+1)]^{1/2}$ [b]	μ_{sat} [b]	gJ [b]
$CeNi_{.98}Al_{1.02}$	-- [c]	-- [d]	-- [d]	2.56		2.14
$PrNi_{1.02}Al_{.98}$	-- [c]	-10	3.73	3.62		3.20
$NdNi_{1.20}Al_{.80}$	17	5	3.84	3.62	1.64	3.27
$GdNi_{1.05}Al_{.95}$	61	53	8.90	7.94	6.36	7.00
$TbNi_{1.01}Al_{.99}$	65	52	10.2	9.72	8.01	9.00
$DyNi_{.99}Al_{1.01}$	47	30	11.0	10.6	7.82	10.0
$HoNi_{1.09}Al_{.91}$	27	12	10.6	10.6	7.25	10.0
$ErNi_{0.90}Al_{1.10}$	16	0	9.85	9.59	7.40	9.00

[a] Curie and Weiss temperatures in °K.

[b] Moments in Bohr magnetons.

[c] These ternaries are paramagnetic at 4.2°K.

[d] Does not exhibit Curie-Weiss behavior.

compensation is primarily responsible for the reduction in χ.

Results for $PrNi_{2-x}Al_x$ alloys are also anomalous in the
Al-rich C15 phase. Magnetization versus temperature passes through
a maximum between 15 and 20°K. The reduction in moment below 15°K
is, however, absent at higher fields (> 15 kOe). The decline in
moment below 20°K may indicate the onset of antiferromagnetism,
although this appears unlikely in view of the fact that $PrAl_2$ is
ferromagnetic. It seems more likely that it, i.e. the decline, is
a crystal field effect. Ferromagnetism in $PrAl_2$ grows out of the
$\lceil_1$ (singlet) state by the bootstrap process.[11] It seems likely
that weakened exchange (indicated by the reduced Weiss constant)
results when Al is replaced by nickel and this destabilizes the
ferromagnetic form of the ternary allow. Around 25 or 30°K the
alloy begins to transform into the ferromagnetic form but exchange
is weakened as temperature is lowered, in some way which is as yet
not understood, and the material relaxes into a Van Vleck paramagnet.
The ferromagnetic form can be sustained with the help of an external
field which assists the bootstrap process.

The first and second Brillouin Zone for the C15 structure
are formed by the 111 and 220 planes, respectively. The inscribed
sphere for the first zone holds 0.23 electrons per atom; that for the
second holds 0.99. The full first and second zones hold 0.38 and 1.33
electrons/atom. The phase boundary of the terminal phase based on
$LnNi_2$ occurs at electron concentrations of 1.10 and 1.16 for ternaries

-49-

containing the light and heavy lanthanides, respectively, which is consistent with contact by the Fermi surface at the 220 zone faces. The insolubility of $CeAl_2$ in $CeNi_2$ can be formally understood in terms of a fraction of quadripositive cerium ≥ 0.30, although the situation may be more complex. The band structure in $CeNi_2$ may be substantially different than that in the other $LnNi_2$ compounds so that zone boundary contact occurs at a lower e.c., in which case it is unnecessary to postulate that a portion of Ce^{+3} is ionized into the quadripositive state.

<div align="center">B. $Pr_{1-x}Ln_xNi_2$ and $Pr_{1-x}Ln_xCo_2$ Ternaries</div>

The four $PrNi_2$-$LnNi_2$ and $PrCo_2$-$LnCo_2$ pseudo-binary systems ($Ln = Dy$ and Ho) exhibit continuous solid solubility. Lattice parameters for the nickel systems vary linearly with composition. There seems to be a slight positive deviation from Vegard's Rule for the cobalt systems of about 0.01 A at the composition $Pr_{.5}Ln_{.5}Co_2$.

For simplicity the $Pr_{1-x}Ln_xNi_2$ with $Ln = Dy$ and Ho are designated PDN and PHN, respectively, and the corresponding cobalt compounds PDC and PHC. All the ternaries were found to be paramagnetic at room temperature. Curie-Weiss behavior was observed for PDN and PHN but not for PDC and PHC. The effective moments for PDN and PHN are in close agreement with values expected from the free ion moments.

The magnitude of the saturation magnetization of PDN or PHN for $x > 0.25$ indicated that the Pr and Dy or Ho moments are coupled antiferromagnetically. The saturation magnetization indicates that for $x < 0.2$ Pr carries no moment; for x above this threshhold the Pr

<div align="center">-50-</div>

moment increases with increasing x up to 3.2 μ_B the free ion value

in PDN and PHN.

The saturation magnetizations of PDC and PHC at 4.2°K are given in Table IV. The magnitude of the saturation magnetization and the variation of magnetization with temperature indicate that these ternaries are ferrimagnetic, both the Pr and Co moments being coupled antiferromagnetically to Dy or Ho. The moment of Pr in $PrCo_2$ is 1.2 μ_B; with the insertion of Dy or Ho in place of Pr the Pr moment rises progressively to 3.2 μ_B, the free ion moment. The Pr ion can be regarded as initially in the Γ_1, non-magnetic state. Interaction with Co, and Dy or Ho mixes in the magnetic Γ_i states (i = 3, 4 and 5) increasing the Pr moment to the limiting free ion value, 3.2 μ_B.

Table IV

Saturation Magnetization of $Pr_{1-x}Dy_xCo_2$ and $Pr_{1-x}Ho_xCo_2$ at 4.2°K

	$Pr_{1-x}Dy_xCo_2$		$Pr_{1-x}Ho_xCo_2$
x	μ_{sat} (μ_B/formula unit)	x	μ_{sat} (μ_B/formula unit)
0.10	2.39	0.10	2.80
.34	.19	.20	1.48
.44	.44	.25	.91
.53	1.73	.31	.46
.60	2.58	.46	1.85
.69	3.56	.61	3.29
.81	5.10	.72	4.33
.91	6.67	.85	5.86

References

1. W. E. Wallace, "Electronic Structure of Alloys and Intermetallic Compounds," Progress in Rare Earth Science and Technology, Vol. 3, p. 1 (1968) Pergamon Press, Edited by L. Eyring. This publication contains many references to work on the $LnAl_2$, $LnNi_2$ and $LnCo_2$ compounds.

2. J. Farrell and W. E. Wallace, Inorg. Chem. $\underline{5}$, 105 (1966).

3. W. M. Swift and W. E. Wallace, J. Phys. Chem. Solids, in press.

4. W. E. Wallace and K. H. Mader, Inorg.Chem. $\underline{7}$, 1627 (1968).

5. W. G. Penney and R. Schlapp, Phys. Rev. $\underline{41}$, 194 (1932).

6. D. Schumacher and C. A. Hollingsworth, J. Phys. Chem. Solids $\underline{27}$, 749 (1966).

7. R. A. Butera, R. S. Craig and L. V. Cherry, Rev. Sci. Instr. $\underline{32}$, 708 (1961).

8. A. E. Dwight et al., Trans. Met. Soc. AIME $\underline{242}$, 2075 (1968).

9. W. E. Wallace, T. V. Volkmann and R. S. Craig, in press.

10. P. W. Anderson, Phys. Rev. $\underline{164}$, 352 (1967).

11. K. H. Mader, E. Segal and W. E. Wallace, J. Phys. Chem. Solids, in press.

NMR

MAGNETIC SUSCEPTIBILITY AND NUCLEAR MAGNETIC RESONANCE OF SOME RCu_5

COMPOUNDS

K.H.J. Buschow

Philips Research Laboratories, Eindhoven, The Netherlands

and

A.M. van Diepen[*] and H.W. de Wijn[†]

Natuurkundig Laboratorium der Universiteit van Amsterdam,[‡]
Amsterdam, The Netherlands

057 3300

Amsterdam Univ. (Netherlands). Natuurkundig Laboratorium.

Abstract

Magnetic susceptibilities of the cubic RCu_5 compounds $TbCu_5$, $DyCu_5$, $HoCu_5$, $ErCu_5$, and $TmCu_5$ have been measured between 2.1 and 300 $^{\circ}K$. At the higher temperatures Curie laws are followed. The type of ordering changes with growing atomic number from antiferromagnetic to ferromagnetic, while $DyCu_5$ is metamagnetic at 2.1 $^{\circ}K$. The Knight shifts of the ^{63}Cu NMR in these compounds have been measured between 100 and 300 $^{\circ}K$. The results are discussed in terms of the Ruderman-Kittel-Kasuya-Yosida theory.

Sample Preparation

The samples used in the present investigation were prepared by arc-melting, splat-cooling, and vacuum-annealing techniques. The rare-earth metals were 99.9% and copper was 99.99% pure. For the X-ray, NMR, and susceptibility measurements powdered samples were used. X-ray diffraction showed that after annealing the compounds $TbCu_5$, $DyCu_5$, $HoCu_5$, $ErCu_5$, and $TmCu_5$ had the cubic $AuBe_5$ structure and were free of a second phase. Lattice parameters have earlier been reported.[1] For the other rare-earth elements it was not possible to prepare stable and single-phase cubic RCu_5 compounds.

Magnetic Susceptibility and Magnetization

The susceptibilities were measured between 2.1 and 300 $^{\circ}K$ at the higher temperatures with a Curie balance, while at the lower temperatures a null-coil pendulum magnetometer, employing the Faraday method, was used. From 300 down to at least 20 $^{\circ}K$ the reciprocal susceptibilities are straight lines. Paramagnetic Curie temperatures are small for the Tb and Dy compounds; for the other compounds they are zero within the experimental error. Figs.1-3 show the magnetization versus temperature curves at 6 kOe and the magnetization versus applied field at 2.1 $^{\circ}K$ for $TbCu_5$, $DyCu_5$, and $ErCu_5$. Experimental results for $HoCu_5$ and $TmCu_5$ are similar to those of $ErCu_5$. Table I summarizes the experimental data.

$TbCu_5$ clearly shows antiferromagnetism. There is a peak in the σ-T curve, and at 2.1 $^{\circ}K$, as at other temperatures, the susceptibility

-54-
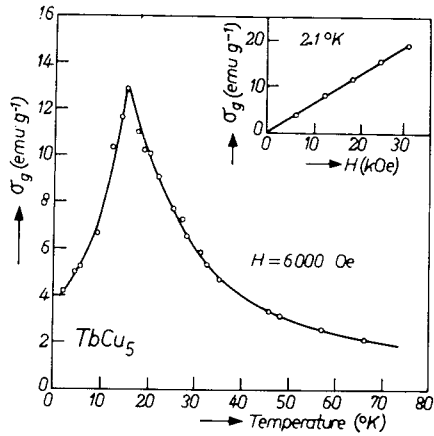
Fig.1. Magnetization versus temperature at 6 kOe for TbCu$_5$. Insert shows the magnetization versus applied field at 2.1 $^\circ$K.
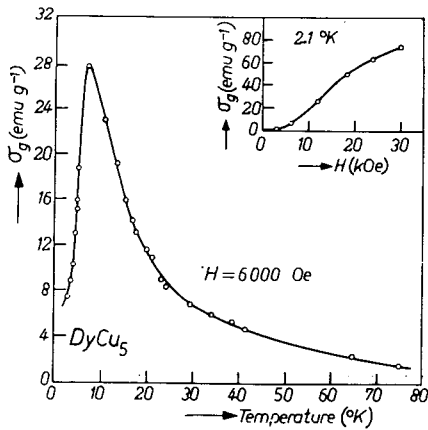
Fig.2. Magnetization versus temperature at 6 kOe for DyCu$_5$. Insert shows the magnetization versus applied field at 2.1 $^\circ$K.
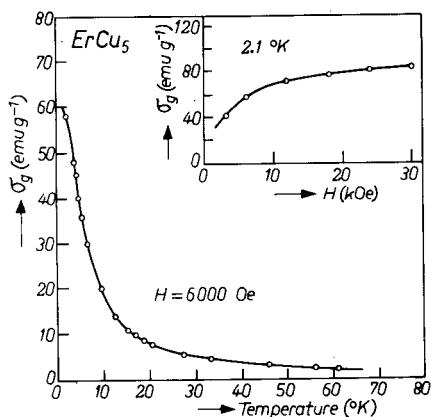
Fig.3. Magnetization versus temperature at 6 kOe for ErCu$_5$. Insert shows the magnetization versus applied field at 2.1 $^{\circ}$K.
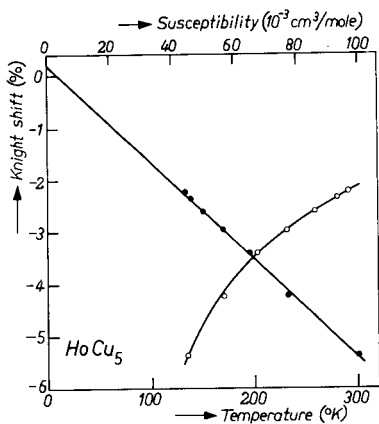
Fig.4. The Knight shift of the ^{63}Cu NMR in HoCu$_5$ as a function of the temperature (open circles), and the Knight shift as a function of the susceptibility (black dots) with the temperature as parameter.

is field independent.

HoCu$_5$, ErCu$_5$, and TmCu$_5$, on the contrary, show a typical ferromagnetic behavior. Towards lower temperatures the magnetization is still increasing, and at 2.1 $^\circ$K the σ-H curve shows field dependence characteristic for a ferromagnet. The magnetic moments at 30 kOe and 2.1 $^\circ$K have been determined (see Table I). The values are considerably lower than the theoretical values for free tripositive rare-earth ions. There are several possibilities for the reduced moments: (1) At 2.1 $^\circ$K the ordering may not yet be complete, since T$_c$ is very low. (2) At 30 kOe saturation may not yet have been achieved. (3) Crystal field effects may be significant.

DyCu$_5$ seems to represent an intermediate case. At low fields it behaves as an antiferromagnet and it shows a peak in the σ-T curve. At higher fields, however, it behaves as a ferromagnet, and no peak is observed. This type of magnetic behavior is commonly referred to as metamagnetism.

Knight Shift Results

The Nuclear Magnetic Resonance (NMR) of the ^{63}Cu nucleus was observed at temperatures ranging from 300 down to 100 $^\circ$K with a crossed-coils induction spectrometer operating at 8 MHz. The Knight shifts were determined relative to the ^{63}Cu NMR in CuCl powder. For all of the compounds they were found to be negative in this temperature region and proportional to the susceptibility. As an example experimental results for HoCu$_5$ are given in Fig.4. For the

-57-

Table I. Effective moments, paramagnetic Curie temperatures, ordering temperatures, magnetic moments at 2.1 °K and 30 kOe, and exchange constants between conduction electrons and 4f spins of RCu_5 compounds.

Compound	μ_{eff} (μ_B)	$g\sqrt{J(J+1)}$	θ_p (°K)	T_N (°K)	Type of ordering	μ_{sat} [a] (μ_B)	gJ	$\jmath_{sf}$ (eV)
$TbCu_5$	9.6	9.72	2	15	antiferro	–	9.0	−0.12
$DyCu_5$	10.9	10.63	2	7	metamagn.	6.5	10.0	−0.12
$HoCu_5$	10.8	10.60	~0		ferromagn.	7.6	10.0	−0.13
$ErCu_5$	9.7	9.60	~0		ferromagn.	7.3	9.0	−0.12
$TmCu_5$	7.4	7.60	~0		ferromagn.	4.9	7.0	−0.13

[a] Determined at 2.1 °K in a magnetic field of 30 kOe.

other compounds they are similar.

The dominant interaction which is responsible for temperature dependent Knight shifts and magnetic ordering in intermetallic compounds as those studied here is generally accepted to be the indirect exchange interaction via the conduction electron spins. The mechanism of this interaction is, up till now, best described by the Ruderman–Kittel–Kasuya–Yosida (RKKY) theory.[2] In the interpretation of Knight shift and magnetic susceptibility the relevant equations are

$$K = K_0 \left[1 + \jmath_{sf}(g_f - 1) \, \chi_f / 2g_f \mu_B^2 \right], \qquad (1)$$

$$\jmath_{sf} = - \, 6\pi z \Gamma \sum_n F(2k_F R_{mn}), \qquad (2)$$

$$\theta_p = -\frac{3\pi z^2 \Gamma^2}{4kE_F} (g_f-1)^2 J(J+1) \sum_{n\neq m} F(2k_F R_{mn}). \qquad (3)$$

The meaning of the symbols is the same as in earlier papers.[3] The
function $F(2k_F R_{mn})$ is the well-known RKKY function

$$F(x) = (x \cos x - \sin x)/x^4. \qquad (4)$$

The parameter γ_{sf} in Eq.(1) can be derived from the slope of the
χ–K curve, provided the Knight shift due to Pauliparamagnetism, K_0,
is known. Since there is no Pauliparamagnetic RCu_5 compound with the
$AuBe_5$ structure, K_0 had to be derived from extrapolation of the χ–K
curves to zero susceptibility. The value derived in this way is
$K_0 = (+0.15 \pm 0.03)\%$.

In these RCu_5 compounds there are two different Cu sites. They
are occupied in the ratio 1:4. The observed resonance is attributed
to the CuII site, the CuI resonance being unobservable due to the
poor signal to noise ratio. In the derivation of γ_{sf} corrections
should be made for the magnetic dipole fields caused by the rare-earth
ions at the copper nuclei. It can easily be derived that the resonan-
ces in powdered samples, in the case of axial symmetry, are shifted
due to magnetic dipole fields over [4]

$$K_{dip} = \frac{1}{2} \chi_f \sum_i (1-3\cos^2 \zeta_i)/r_i^3. \qquad (5)$$

Here r_i is the distance from the Cu nucleus to a rare-earth ion,
ζ_i the angle between the symmetry axis and the direction of r_i, while
the summation extends over all rare-earth ions. The summation has
been carried out for the CuII sites in the RCu_5 compounds over all

-59-

rare-earth sites within a sphere of radius 20 $\overset{o}{A}$ and amounts to
+0.077 × 10^{24} cm^{-3}. This results in a correction on γ_{sf} for TbCu$_5$,
DyCu$_5$, and HoCu$_5$ of −0.01 eV, for ErCu$_5$ and TmCu$_5$ of −0.02 eV. The
numbers given in Table I include these corrections. The axial
symmetry which causes the magnetic dipole shift also should give
rise to electric quadrupole coupling. The measured line widths were
of the order of 30 G and no splitting could be observed. It is not
clear whether quadrupole effects are small or averaged out by
lattice imperfections.

Equations (2) and (3) offer the possibility to determine Γ and
k$_F$. The summations $\sum_{CuI}$, $\sum_{CuII}$, and $\sum_H$ have been calculated for
HoCu$_5$ as a function of the Fermi wave vector k$_F$ (fig.5). With the
observed CuII resonances and θ_p's we can fit the two equations for
Γ = +0.62 eV, k$_F$ = 1.08 $\overset{o}{A}^{-1}$, and also for Γ = −1.86 eV, k$_F$ = 1.48 $\overset{o}{A}^{-1}$.
A decision between these two sets of values can be reached by
considering the magnetic properties of the compound DyCu$_4$Zn. This
compound can be looked upon as DyCu$_5$ in which part of the Cu sites
are occupied by Zn atoms. DyCu$_5$ and DyCu$_4$Zn are isostructural but,
since Zn has one valence electron more than Cu, we expect the value
of k$_F$ to be somewhat higher in the latter than in the former compound.
The paramagnetic Curie temperature θ_p observed for DyCu$_4$Zn is close
to −10 ^{o}K. This means that along with an increase of k$_F$ there goes
a change of sign of θ_p from positive to negative. This condition,
imposed on the value of k$_F$ by experiment, is met only in one of the
two cases discussed above, viz., k$_F$ = 1.08 $\overset{o}{A}^{-1}$ and Γ = +0.62 eV. This
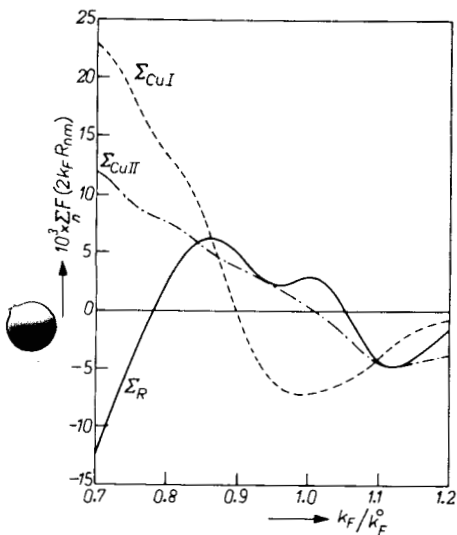
Fig.5. Dependence of the functions Σ_R and Σ_{Cu} on k_F for $HoCu_5$.

is seen in Fig.5, where Σ_R, proportional to $-\theta_p$, changes from negative to positive values when k_F is increased near 1.08 $\overset{o}{A}^{-1}$ $(k_F/k_F^0 = 0.78)$.

Concluding Remarks

It should be noted that the derived Γ is representative for this whole series of RCu_5 compounds. A number of series of intermetallic compounds of rare-earth elements with nonmagnetic other metals have been investigated and analyzed in terms of the RKKY theory as described above.[3,4] The dependence of Γ on k_F is found to be a smooth function, positive for k_F values lower than 1.4 $\overset{o}{A}^{-1}$ and negative for higher

-61-

values. Also the results derived for the RCu_5 compounds lie on this curve. The positive value derived here for Γ again shows that for these smaller k_F values the interband mixing [5] part of the effective exchange integral is small and cannot compensate the pure s-f exchange which is of an electrostatic nature and should always be positive. This result is striking if one thinks of the rough approximations that are inherent to the model and of the fact that the conduction electrons are probably far from behaving as free electrons.

Footnotes and References

* On leave of absence at the Department of Chemistry, University of Pittsburgh, Pennsylvania, where part of this manuscript was written.

† On leave of absence at Bell Telephone Laboratories, Murray Hill, New Jersey.

‡ The part of the work performed in Amsterdam has been supported by the Foundations F.O.M. and Z.W.O.

1. K.H.J. Buschow, A.S. van der Goot, and F. Birkhan, J.Less-Common Met. (1969) in the press.

2. M.A. Ruderman and C. Kittel, Phys.Rev. 96, 99 (1954); T. Kasuya, Progr.Theor.Phys. (Kyoto) 16, 45 (1956); K. Yosida, Phys.Rev. 106, 893 (1957).

3. H.W. de Wijn, K.H.J. Buschow, and A.M. van Diepen, Phys.Stat.Sol. 30, 759 (1968) and references quoted therein.

4. A.M. van Diepen, K.H.J. Buschow, and H.W. de Wijn, J.Chem.Phys. (Dec. 1969) in the press.

5. R.E. Watson, S. Koide, M. Peter, and A.J. Freeman, Phys.Rev. 139, A167 (1965).

$Dy Tl_3$

MAGNETIC PROPERTIES OF ~~DYSPROSIUM THALLIUM THREE~~ *

Clayton E. Olsen, George P. Arnold, Norris G. Nereson

480 8500

Los Alamos Scientific ~~Laboratory~~ *N. Mex.*
~~University of California~~
~~Los Alamos, New Mexico~~ 87544

ABSTRACT

Neutron diffraction and bulk susceptibility measurements have been made on the intermetallic compound dysprosium thallium three. The neutron diffraction investigation confirmed the surmise of Baenziger and Moriarty that this compound had an ordered $AuCu_3$ structure. Below 11K, in addition to the nuclear reflections, a complex set of magnetic reflection appeared which could be indexed at 4.7K on a magnetic cell whose edges were four times the corresponding cube edges of the chemical cell. As yet the magnetic structure has not been derived from the observed powder pattern. A solution of this magnetic structure requires the use of a single crystal.

Bulk susceptibility measurements over the temperature interval 1.4K to 300K show the following: In the temperature interval 10K to 200K the Curie Weiss plot of $1/x$ vs T is linear with an intercept on the temperature axis of -20K confirming the antiferromagnetic nature of the ordered structure observed by neutron diffraction. The paramagnetic moment obtained from the slope of the Curie Weiss plot gave an indicated paramagnetic moment for the dysprosium of 11.3 Bohr magnetons which may indicate substantial crystal field effects and/or conduction electron polarization in this compound. At temperatures above 200K the observed reciprocal susceptibilities become smaller than Curie Weiss extrapolation. Below 11K the bulk susceptibility does not fall in the case of classical antiferromagnets but continues to rise although not as rapidly as would be expected if the compound were ferromagnetic with an inflection at 7.5°K. No remanance was observed in the compound. These results suggest that the antiferromagnetic structure is such that the aligned moments have a ferromagnetic component. The bulk susceptibility measurements below 3.5°K suggest the possibility of a second magnetic structure below 3.5°K.

Introduction

Intermetallic compounds of the rare earth elements having the ordered copper three-gold structure are of interest because of their simple cubic structure. Because of the high magnetic scattering amplitude compounds containing dysprosium are of particular interest for neutron diffraction investigations the only work reported to date on the dysprosium thallium three system is the x-ray work by Baenziger and Moriarty[1] where they report the existence of the compound $DyTl_3$. In their x-ray investigations they were not able to establish whether the compound was ordered because of the relative x-ray scattering factors.

Preparation of Material

The preparation of the $DyTl_3$ sample was accomplished by induction heating stochiometric quantities of the metals (99.9% pure) in an evacuated tantalum container to approximately 1700°C. The container and its contents increased considerably above the latter temperature when the exothermic reaction occurred. The preparation was annealed in the container for 20 hours at 1000°C.

The resulting gray intermetallic compound was crushed and powdered in a dry argon atomsphere. A specimen examined by x-ray powder diffraction showed that the major phase was cubic $DyTl_3$ having a lattice constant of 4.676 Å. This is in good agreement with the lattice constant of 4.6720 Å reported for $DyTl_3$ by Baenziger and Moriarty.[1] Weak lines of α -thallium were also observed in the x-ray pattern; it was estimated that this impurity content was approximately 5%. When this compound was crushed it was observed to be somewhat ductile which is contrary to the brittleness of most rare-earth intermetallic compounds. Deterioration and a change in color of the compound was observed when exposed to air for more than one hour.

Neutron Diffraction Results

The neutron diffraction results from a powder sample of $DyTl_3$, as observed at a temperature of 76°K and a neutron wavelength of 1.14 Å, are shown in the upper portion of Fig. 1. Only lines from the ordered cubic $DyTl_3$ ($AuCu_3$ structure type) were present in the diffraction pattern. The intensities of the various nuclear reflections are reasonably close to that expected as shown in Fig. 2 where $\log F^2 e^{-2W}$ plotted against $\sin^2\theta$ should yield a straight line; here F is the geometric structure factor,

$$2W = (12h^2\sin^2\theta / mk\Theta\lambda^2)[\phi(x)/x + 1/4] \text{ and } \Theta \text{ is the Debye temperature.} \tag{2}$$

The Debye temperature obtained from the slope of the line in Fig. 2 is $100 \pm 15°K$. This is an unusually low Debye temperature for an intermetallic compound and is probably associated with the ductile property of the compound mentioned above.

The neutron data at a temperature of 4.7°K, shown in the lower part of Fig. 1, contains superlattice reflections in addition to the nuclear reflections. The superlattice reflections are evidence for antiferromagnetic ordering of moments in this compound at low temperatures. An attempt was made to measure the intensities of certain magnetic reflections as a function of temperature. Due to the fact that most of the magnetic reflections are small and not well resolved, it was difficult to obtain good data in the vicinity of the Neel point; however, the approximate Neel temperature is $11 \pm 2°K$.

The observed superlattice reflections at T = 4.7°K can all be indexed on a magnetic cell which is four times that of the chemical cell in all directions; the magnetic indices are identified with the letter M in Fig. 1. The calculated angular positions of the magnetic reflections from the quadrupled cell agree well with the centroids of the observed reflections. However, the magnetic reflections (112) and (220) are approximately 25% wider than normal and the

(222) reflection has a width about 10% greater than the standard size. The large reflection widths probably means that additional unresolved reflections are present; these extra reflections could arise from slight distortions of the large cubic magnetic cell. It is also noteworthy that the observed magnetic reflections are quite small compared to those observed in other $AuCu_3$ type compounds. [3] This would indicate that either a low order of magnetic symmetry or an incomplete antiferromagnetic ordering is present; a low dysprosium moment is an unlikely possibility.

There is some evidence that this compound may change structure with increasing temperature. For example, the (112) and (220) magnetic reflections are still resolved and observable as two discreet peaks at T = 6°K; however, at T = 7°K and below, the above reflections are merged into one broad peak. It was not possible to assign a magnetic model or calculate a magnetic moment for this compound on account of the unresolved magnetic reflections and their weak intensities. Further investigation using a single crystal with a better resolution diffractometer is necessary.

Bulk Susceptibility Measurements

The powdered sample in the form of a right cylinder was measured in a helium filled cryostat using a modified Faraday method. The magnet pole faces were stepped producing a uniform gradient of approximate 8% of the mean magnetic field over the sample. The field in gap at the specimen position was mapped using a rotating coil gaussmeter and the sample position determined with respect to the field. The measurements were made using an electrodynamic balance similar to the one described by Butera et al. [4] The capsule correction was determined over the same temperature range as the sample and capsule. This correction was used in the calculations. No demagnetization corrections have been made on the data. The temperature

was measured using thermocouples attached to the wall of the container adjacent to the sample. Where cryogenic fluids were used temperatures were determined using vapor pressure thermometry. Automatic temperature control was used at intermediate temperature points and measurements were made only after the temperature and the magnetic force became stable. At each temperature measurements were made as a function of field.

The results of the measurements are shown in Figures 3 and 4. Measurements of the susceptibility as a function of field were independent of field, with experiment error 4%, from 296K to about 3.5K. Below this temperature the susceptibility showed a slight linear increase with increasing field. No remanance was observed at any temperature.

Discussion of Results

The bulk magnetic measurements are consistent with the neutron measurements. The temperature of the point of inflection corresponds to the temperature at which the (112M) and (220M) magnetic reflections in the neutron diffraction measurements become well separated. The generally complicated magnetic behavior observed in the neutron measurement are reflected in slight bump in the susceptibility data about 3.5K to 7.5K. The bulk measurements below 4K indicate the possibility of a second magnetic structure or a complicated temperature dependent magnetic behavior of a single structure. The bulk measurements indicate that magnetic structure or structures, while they are basically antiferromagnetic, have a ferromagnetic component. The absence of a low temperature remanent moment and the Curie Weiss extrapolation support this conclusion. It appears that the magnetic structure or structures are more complicated than the simpler antiferromagnetic structures found for the ordered $AuCu_3$ compounds $PyPt_3$ and $DyIn_3$.[3]

-67-

The Curie-Weiss plot of $1/X_m$ vs T yields a value of 11.29 Bohr magnetons per dysprosium atom which is considerably higher than the usual free ion moment of 10.5 Bohn magnetons. This indicates a very high conduction electron polarization, most probably. The Curie-Weiss constant for the compound is 17.30 and θ is -20K. Further work on this compound call for the use of single crystals.

Acknowledgements

References

1. N. C. Baenziger and J. L. Moriarty, Jr., Acta Cryst. $\underline{14}$, 948 (1961).

2. For definitions of these customary symbols, see "Neutron Diffraction"
    2nd Ed. by G. E. Bacon, Oxford at the Clarendon Press, London (1962).

3. For $DyPt_3$ and $DyIn_3$, G. P. Arnold and N. Nereson, J. Chem. Phys. $\underline{51}$,
    1495 (1969).

4. R. A. Butera, R. S. Craig and L. V. Cherry, Rev. Sci. Inst. $\underline{32}$, 708 (1961).
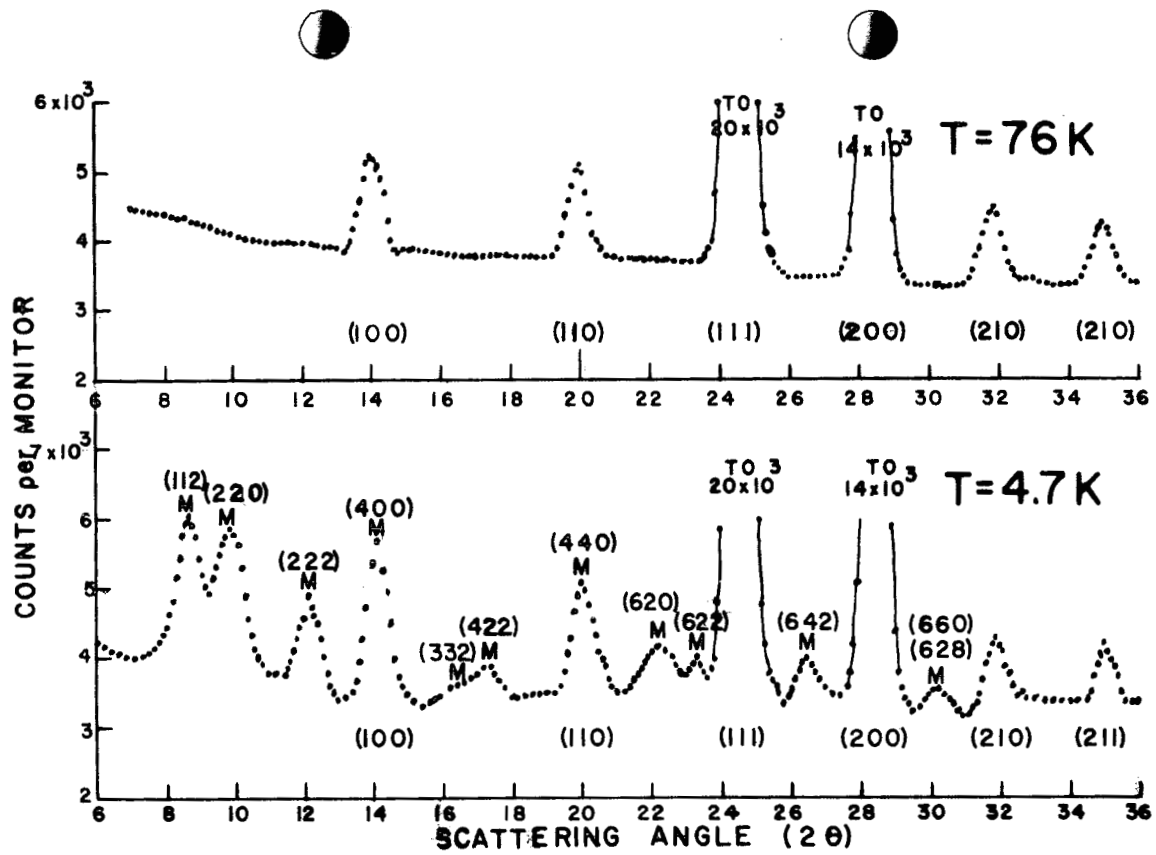
Fig I Neutron diffraction data at 76 K and 4.7 K M are magnetic reflections
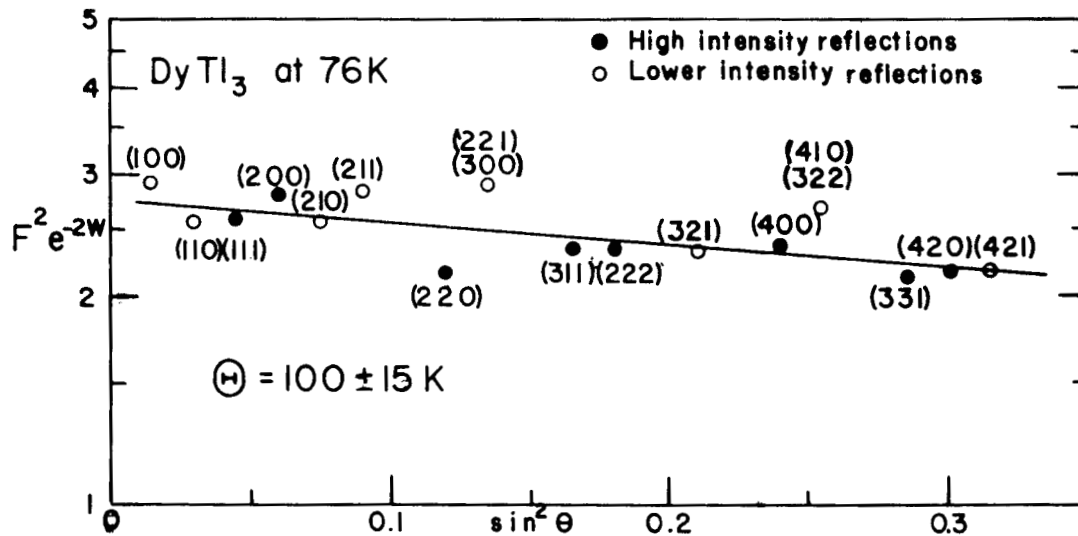
Fig. 2 Debye Temperature Determination

Fig. 3   TEMPERATURE DEGREES ABSOLUTE

Fig. 4 TEMPERATURE DEGREES ABSOLUTE
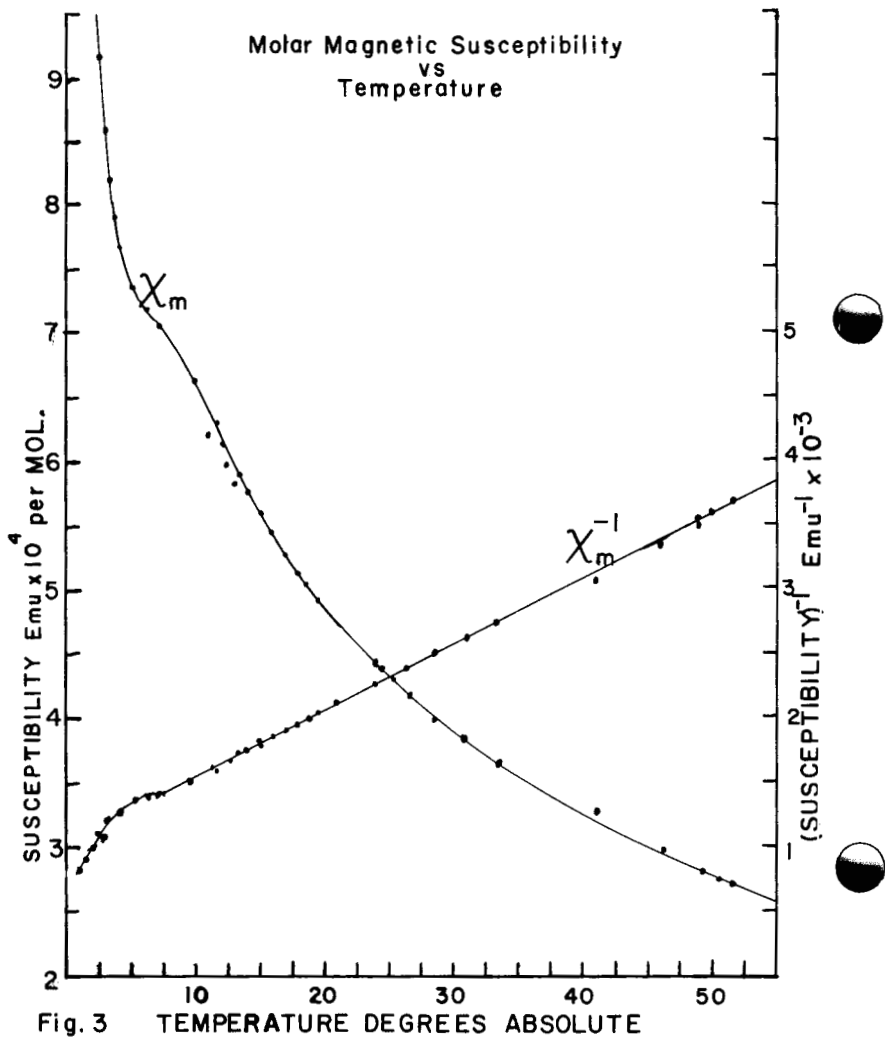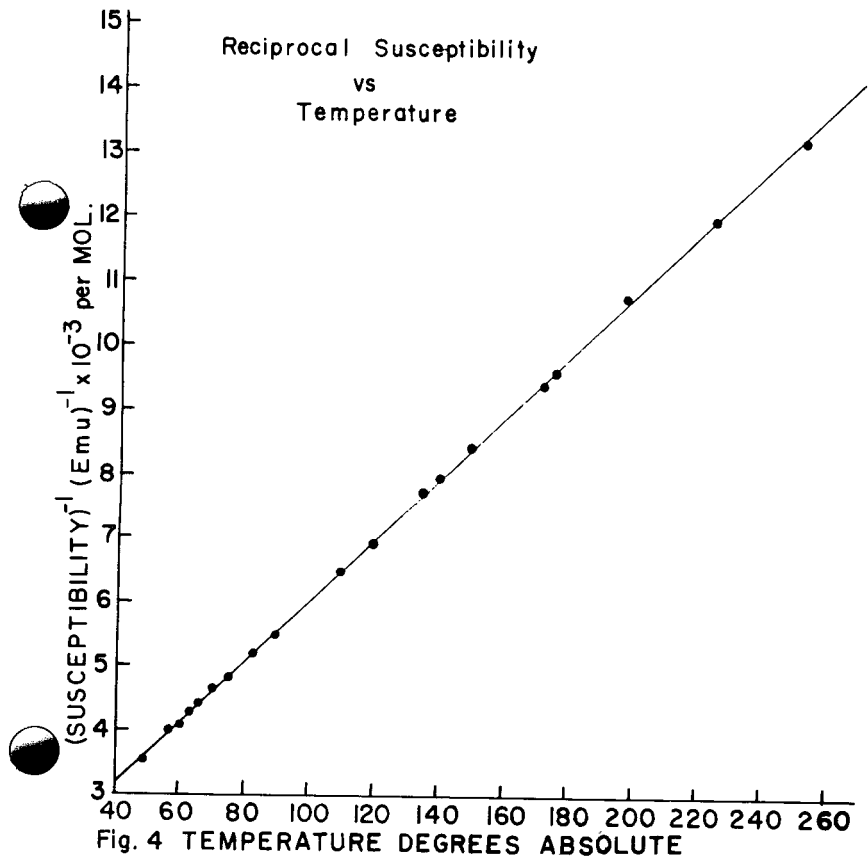
MAGNETIC PROPERTIES AND SPECIFIC HEAT OF

MONOCHALCOGENIDES OF La, Pr AND Tm

by

E. Bucher, A. C. Gossard, K. Andres,
J. P. Maita and A. S. Cooper
Bell Telephone Laboratories, Incorporated
Murray Hill, New Jersey

ABSTRACT

The monosulfides, monoselenides and monotellurides of La, Pr
and Tm have been investigated with respect to specific heat
and their magnetic properties. The La-compounds were found
to be superconductors around 1°K and weak Pauli paramagnets.
All the Pr-compounds show a singlet ground state and do not
order magnetically as demonstrated by susceptibility and
NMR down to 1.4°K. TmS and TmSe are exchange induced anti-
ferromagnets, Tm being trivalent. In contrast, Tm in TmTe
is divalent and orders antiferromagnetically at 0.21°K.

I. INTRODUCTION

The present study of La-, Pr- and Tm- monochalco-
genides was initiated mainly for two reasons: (1) Our
recent discovery of the hyperfine enhanced nuclear magnetic
cooling, first demonstrated in PrBi,[1] suggested the study
of other nonordering Van Vleck paramagnets, being good metals
and having the proper cubic symmetry. (2) Recent theories[2]
extending Trammel's[3] early work predicted interesting effects
around the critical ratio $\mathcal{J}/\Delta$ where $\mathcal{J}$ is the exchange para-
meter and Δ the crystal field splitting. The magnetic
properties of Pr-monochalcogenides have first been studied
by the Russian group of Smolenski, et al.[4] They appeared

-74-

to be an interesting sequence of compounds for our purpose, while on the Tm-monochalcogenides no magnetic data have been published yet. In the nuclear cooling experiments, the crystal field splitting and the exchange interaction strength are two fundamental parameters.[5] In order to determine the crystal field splitting in the Pr-compounds by specific heat, the electronic and lattice part had to be subtracted properly. This was done by measuring all the corresponding La-compounds. The exchange interaction can then be evaluated using Eqs. (2) and (5).

II. EXPERIMENTAL RESULTS

2.1. Preparation of Compounds

Slices of 0.5-1 m/m thickness were cut from solid material and reacted in vapor (weighed in stoichiometric amounts) of S, Se or Te in doubly sealed quartz tubes. After completion of the reaction the temperature was raised to 1050° for 2-3 days; the material crushed, pressed in an agate dye and resintered for 2-3 days. This procedure leads in almost all cases to single phase material. For most of the measurements it is preferable to work with good solid material. Therefore the material was transferred into a Ta-crucible, sealed under vacuum and kept slightly above the melting point for a few minutes. After melting, it was cooled down to room temperature within 30-60 minutes (except TmTe, which was annealed for 9 weeks at 450°C). All chalcogenides of La, Pr and Tm were found to melt congruently

and no attack of the tantalum crucibles was detectable. All samples consisted in large portions of single crystals.

2.2. Magnetic Properties and NMR Results

The magnetic parameters are listed in Table 1 and shown in Figs. 1-4. The magnetization between 1.4 and 300°K was measured with a pendulum magnetometer in fields of up to 15 kOe. The ordering temperatures were determined independently in low fields (10 Oe) by a mutual induction method recording the signal vs. the resistance of a calibrated Ge-thermometer or at higher temperatures vs. the e.m.f. of a calibrated thermocouple. LaS, LaSe, LaTe are good metals and found to be superconducting around 1°K, with an intermediate electronic specific heat and weak Pauli paramagnetism. PrSe and PrTe exhibit a singlet ground state without magnetic ordering, as shown in Fig. 1 and by NMR down to 1.4°K in agreement with Smolenski et al's work.[4] Our results in PrS however disagree considerably with theirs. We found a very weak peak in the low field susceptibility at 7°K, and a very small spontaneous ferromagnetic moment of $\sim 3.1 \cdot 10^{-3}$ μ_B/Pr atom compared to about $5 \cdot 10^{-2}$ μ_B/Pr atom and an antiferromagnetic peak at 16°K given by Smolenski et al.[4] A sample made with a somewhat less pure Pr showed a low field susceptibility peak three times as big and correspondingly a spontaneous ferromagnetic moment about three times as big as in the purest PrS sample. These irreproducible results on PrS soon cast doubts about the true nature of this

	P$_{eff}$	Θ_p(°K)	X (1.42°K) cm^3/mole Pr
□ PrS	3.58	-32	0.023$_2$
○ PrSe	3.58	-26	0.025$_5$
▲ PrTe	3.54	-14	0.037$_4$

H = 14.24 kOe
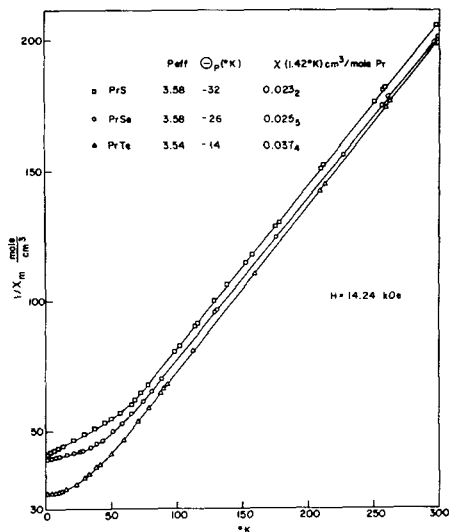
FIG. 1
Inverse molar
susceptibility
vs. temperature
for PrS, PrSe,
PrTe.

material. The fact that we could easily observe a temperature independent NMR signal between 2 and 20.3°K on Pr[141] in PrS proves that our weak anomaly at 7°K as well as the temperature dependent susceptibility displayed in Fig. 1 is an artifact of an impurity phase. Thus, PrS if made with the proper stoichiometry, has to be considered as a new nonordering Van Vleck paramagnet. All the Tm compounds exhibit antiferromagnetic ordering, in contrast to all the neighboring Tm-pnictides,[6] which do not order due to a

-77-
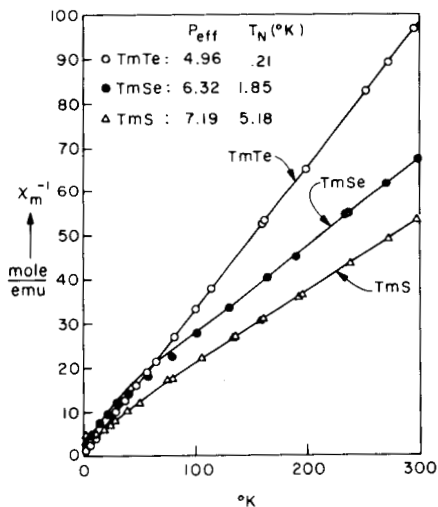
FIG. 2
Inverse molar
susceptibility vs.
temperature for
TmS, TmSe, TmTe.

singlet ground state. The effective moment below room

temperature drops gradually from TmS to TmTe and is

considerably below the value of the free Tm^{3+} ion. The

magnetization curves taken at 1.42°K in TmS and especially

TmSe look quite complex as shown in Fig. 3. In Fig. 4 we

present the magnetization curves at 1.42°K and 4.22°K of

TmTe. Considering the anomalously large lattice constant

of 6.346 Å, the effective moment close to the value of Yb^{3+}

and the light silvery color in contrast to the deep purple
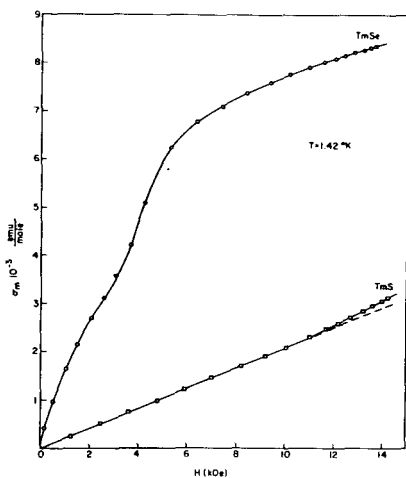
FIG. 3
Molar magnetization
vs. field in TmS
and TmSe at 1.42°K

color of other tellurides, we soon concluded that this
compound presents a relatively rare case where Tm is in
the divalent state. In the course of this work we became
aware that Iandelli and Palenzona[7] were obviously first to
find evidence for the polyvalent behavior of this compound
from their measurements of the anomalously large lattice
constant. It is interesting to note however that annealing
at various temperatures followed by rapid quenching results
in a mixture of Tm^{2+} and Tm^{3+} which is reflected by lattice
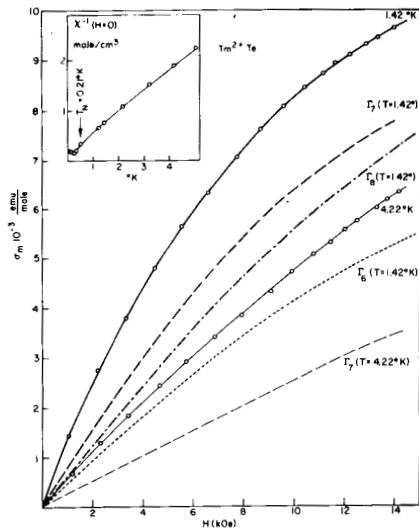
FIG. 4
Molar magnetization
vs. field in Tm^{2+}
Te at 1.42°K and
4.22°K and calcu-
lated magneti-
zation curves for
Γ_6, Γ_7 and Γ_8.

Insert: Inverse
low temperature
molar susceptibility
vs. T in $Tm^{2+}Te$.

parameters ranging from 6.05 to 6.34 Å [a typical value was
a = 6.16 Å from a temperature of 900°C]. The insert in
Fig. 4 shows that $Tm^{2+}Te$ orders at 0.21°K. The deGennes
formula[8] would predict 0.20-0.27°K for the various T_N values
of EuTe reported in the literature.[9-15] The magnetization
at 4.22 and 1.42°K is considerably larger than what one would
expect for any crystal field ground state Γ_6, Γ_7 and Γ_8 in
this structure. Unfortunately our sample is polycrystalline
material and we cannot draw much information from the

magnetization since the off diagonal elements of J_z are all zero but they are different from zero of J_+ and J_-.

2.3. Specific Heat

The low temperature specific heat of TmS, TmSe and TmTe are plotted in Fig. 5.   TmS and TmSe develop a weak anomaly at the Néel temperature.   In TmS e.g. the total entropy [neglecting the nuclear part at low temperature] at °K is only about 3.9 J/°K mole, smaller than R ln 2 = 5.76 J/°K mole which one would expect for a ground state doublet.
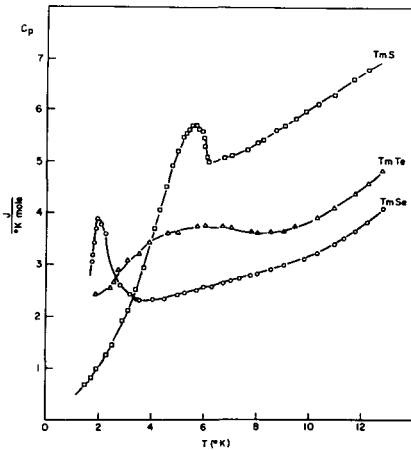
FIG. 5
Specific heat vs. temperature be-
tween 1.5-13°K of
TmS, TmSe and TmTe

If a comparison is made with the Pr-monochalcogenides and the Pr and Tm monopnictides which do not order, the work of Lea Leask and Wolf[16] leads to the conclusion that TmS and TmSe represent new examples where magnetic ordering occurs in spite of the ground state being a singlet. In TmTe the large specific heat is mainly due to crystal field splitting effects.

In Fig. 6, we are trying to deduce some numbers for the crystal field splitting Δ between Γ_1 and Γ_4 in PrSe
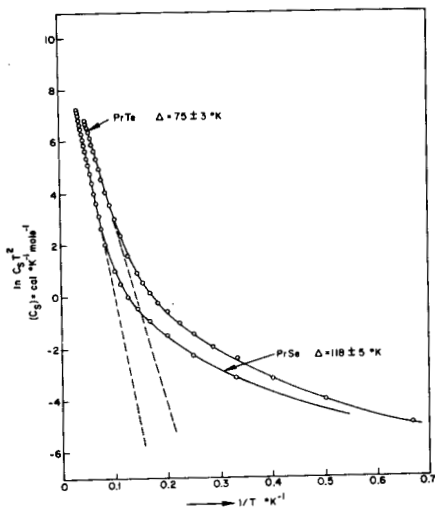
FIG. 6

$\ln \left(C_{PrX} - C_{LaX}\right) \cdot T^2$ vs. $1/T$ for $X = Se$ and Te

and PrTe. We assume the electronic and lattice contribution to the specific heat to be identical in LaS and PrS, LaSe and PrSe as well as in LaTe and PrTe.

At low temperature ($T \ll \Delta$) the Stark specific heat anomaly is given by

$$C_s = \frac{g_4}{g_1} R \left(\frac{\Delta}{T}\right)^2 e^{-\Delta/kT} \tag{1}$$

[g_1 is the degeneracy factor of Γ_1]. We therefore plot ln $[C_{PrX} - C_{LaX}]T^2$ vs. $1/T$, where X stands for Se or Te. The plot is linear only at temperatures above about 10°K. Below, there is a large excess specific heat, the origin of which is currently being explored further. With the linear slopes identified as a crystal field splitting, we get agreement with susceptibility and Knight shift results. In Table 1 we also include the splitting Δ obtained recently from inelastic neutron scattering in PrTe.[17] The agreement between specific heat and the n-experiment is quite good.

III. DISCUSSION

The study of the La-monochalcogenides was mainly undertaken for a better understanding of the low temperature specific heat anomaly found in the corresponding Pr-compounds and especially in order to determine the crystal field splitting and the exchange parameter of the latter. Because of the excess specific heat, our numbers for the crystal field splitting may be somewhat uncertain. The good agreement

-83-

in PrTe with the inelastic n-scattering results[17] however
gives us some faith in these numbers. A further rough
cross test can be made together with the low temperature
Van Vleck susceptibility X_f^{CF} and the Knight shift measure-
ment $K = \Delta H/H$. For Pr^{3+} in octahedral symmetry we have:[18]

$$X_f^{CF} \ (T=0) \ = \ \frac{2Ng_J^2\mu_B^2\langle\Gamma_4|J_z|\Gamma_1\rangle^2}{\Delta} \ = \ \frac{3.19_5}{\Delta[°K]} \tag{2}$$

$$K \ = \ aX_f \tag{3}$$

$$a \ = \ \frac{2F(J,L,S)\langle r^{-3}\rangle}{g_J\cdot N} \ + \ \frac{(g_J-1)H_c}{N\mu_B}$$

$$+ \ \frac{\kappa_o}{X_f}\left[1 \ + \ \frac{\Gamma_{sf}(g_J-1)X_f}{g_Jg_{ce}N\mu_B^2}\right] \tag{4}$$

Generally Eq. (2) does not represent the measured low
temperature susceptibility X_f which can be enhanced (positively
or negatively) over the crystal field susceptibility X_f^{CF} in
the molecular field approximation:

$$X_f \ = \ \frac{X_f^{CF}}{1-\theta X_f^{CF}} \tag{5}$$

Thus, to derive θ, accurate values of Δ and X_f are needed.
X_f on the other hand can be affected by various impurities
and fortunately can be measured in an alternative way by NMR
as shown by (3) and (4). a is the hyperfine constant written
down explicitly in (4) for a given material. The first term

corresponds to the spin dipolar and orbital contribution, the second term is due to the core polarization and the third term due to the conduction electron polarization (assuming it to be uniform). For Pr^{3+} the operator equivalent $F(J,L,S)$ of the spin dipole and orbital operator is 296/225, H_c is an empirical constant (-90 kOe/μ_B). κ_o can be determined from the La resonance in the corresponding a-compound and Γ_{sf} is obtained from the temperature dependent resonance on the nonmagnetic component in the Pr-compound. The second and third term in (4) are usually small corrections of the order of a few percent to the first one and were dropped. For Pr^{3+}, $\langle r^{-3} \rangle = 5.0$ a.u. and $K_{spin\ orbit}$ is given numerically by 184 $X_{f\ [cm^3/mole]}$. The agreement is reasonably good except in PrS where the discrepancy may arise partly from neglecting the conduction electron contribution and partly from difficulties in sample preparation. There is however a small difference between X_{exp} and X_f^{CF} which could be attributed to exchange effects. At least in PrTe, the numbers for Δ should be very reliable from the crosstest by specific heat and inelastic neutron scattering. $\mathcal{J}$ seems to be of antiferromagnetic nature as one would expect from the antiferromagnetic ordering of other monochalcogenides of trivalent lanthanides. The corresponding Tm-chalcogenides could not be explored as thoroughly as the Pr compounds because TmS and TmSe exhibit exchange induced magnetic ordering. The molecular field theory predicts a

-85-

second order phase transition for such materials with a
finite jump in the specific heat anomaly being proportional
to $e^{-2\Delta/kTc}$. Fig. 5 shows however that high temperature
spin correlation and fluctuation effects are considerable
in such materials. If $T_c \ll \Delta$, the magnetic ordering can
no longer be detected by specific heat. In the case of TmS
and TmSe the specific heat maximum in zero magnetic field
coincides perfectly with the maximum of the low field
susceptibility and must be identified as the correct
ordering temperature. It would also be interesting to study
the magnetic properties of $Tm^{3+}Te$. The compound in this
valence state is only stable under pressure[19] or at high
temperature. It is likely that if it orders at all, the
exchange forces must be almost balanced by the crystal field
splitting. In the dilute limit of course (e.g., diluted with
La-, Lu- or Y-sulfide or -selenide) TmS and TmSe are expected
to exhibit Van Vleck paramagnetism. It is clear that Tm
monochalcogenides are unsuitable for nuclear cooling. On
the other hand the Pr monochalcogenides might be very useful
for such an application. Our recent efforts however to use
PrSe and PrTe as nuclear cooling materials failed for reasons
which are not clear yet. Only PrTe showed a small cooling
effect between 50 and 100 m°K but only in small fields. We
have observed similar difficulties in several nonordering Tm-
compounds. It is likely that this failure is linked with the
very large specific heat observed in all these materials

-86-

down to very low temperatures the origin of which has to be explored further.

ACKNOWLEDGEMENTS

We would like to thank Dr. C. W. Chu and L. D. Longinotti for performing the superconductivity measurements and Dr. R. J. Birgeneau for helpful comments on this work.

REFERENCES

1. K. Andres and E. Bucher, Phys. Rev. Letters $\underline{21}$, 1221 (1968).

2. Y. L. Wang and B. R. Cooper, Phys. Rev. $\underline{185}$, 696 (1969). Y. L. Wang and B. R. Cooper, Phys. Rev. $\underline{172}$, 539 (1968). B. R. Cooper, Phys. Rev. $\underline{163}$, 444 (1967).

3. G. T. Trammel, J. Appl. Phys. $\underline{31}$, 362S(1960). G. T. Trammel, Phys. Rev. $\underline{131}$, 932 (1963).

4. G. A. Smolenski, V. P. Zhuze, V. E. Adamyan and G. M. Loginov, Phys. Stat. Sol. $\underline{18}$, 873 (1966). G. A. Smolenski, V. E. Adamyan and G. M. Loginov, Physics Letters $\underline{23}$, 16 (1966).

5. K. Andres and E. Bucher, Phys. Rev. Letters $\underline{22}$, 600 (1969).

6. G. Busch, A. Menth, O. Vogt and F. Hulliger, Phys. Letters $\underline{19}$, 622 (1966). G. Busch, P. Junod, F. Levy, A. Menth and O. Vogt, Phys. Letters $\underline{14}$, 264 (1965). D. P. Schumacher and W. E. Wallace, J. Appl. Phys. $\underline{36}$, 984 (1965).

7. A. Iandelli and A. Palenzona, Propriétés des dérivés
    Semi-métalliques ed CNRS, Paris 1967, 397.

8. P. G. deGennes, Compts. Rendus Ac. des Sciences $\underline{247}$,
    1836 (1958).

9. G. Busch, P. Junod, P. Schwob, O. Vogt and F. Hulliger,
    Physics Letters $\underline{9}$, 7 (1964).

10. U. Enz, J. F. Fast, S. van Houten and J. Smit, Phillips
    Research Repts. $\underline{17}$, 451 (1962).

11. S. Van Houten, Physics Letters $\underline{2}$, 215 (1962).

12. G. Will, S. J. Pickart, H. A. Alperin and R. Nathans,
    J. Phys. Chem. Solids $\underline{24}$, 1679 (1963).

13. G. Busch, J. Appl. Phys. $\underline{38}$, 1386 (1967).

14. G. Busch, P. Junod, R. G. Morris, J. Muheim and W. Stutius,
    Phys. Letters $\underline{11}$, 9 (1964).

15. P. Wachter, Phys. Kond. Materie $\underline{8}$,80 (1968).

16. K. R. Lea, M. J. M. Leask and W. P. Wolf, J. Phys. Chem.
    Solids $\underline{23}$, 1381 (1962).

17. K. C. Turberfield, L. Passell, E. Bucher and R. J.
    Birgeneau (unpublished).

18. E. D. Jones, Phys. Rev. Letters $\underline{19}$, 432 (1967).

19. A. Jayaraman, E. Bucher and D. B. McWhan (this conference).

TABLE 1

	$\gamma^a\left(\dfrac{mJ}{°K^2\,mole}\right)$	$\theta_D^b(°K)$	$T_c(°K)$	$X_{exp}^a(296°K)\dfrac{cm^3}{mole}$	$a(296°K)\overset{\circ}{A}$
LaS	3.28	276	0.84	$34.9\cdot10^{-6}$	5.85_6
LaSe	3.77	231	1.02	$26.2\cdot10^{-6}$	6.06_0
LaTe	4.65	175	1.48	$30.3\cdot10^{-6}$	6.42_1

	$P_{eff}(77\text{-}300°K)$	$\theta_p(°K)$	$T_N(°K)$	$X_f^{exp}\left(\dfrac{cm^3}{mole}\right)$	$X_f^{CF}\left(\dfrac{cm^3}{mole}\right)$	K_{exp}	$K_{spin+orb.}$	$\Delta_{\Gamma_1-\Gamma_4}(°K)$	$a(\overset{\circ}{A})$
PrS	3.58	- 32	-	0.023_2	0.024_6	4.8_4	4.2_7	130 ± 20^c	5.73_5
PrSe	3.58	- 26	-	0.025_5	0.027_1	4.5_2	4.7_0	118 ± 10^c	5.94_2
PrTe	3.54	- 14	-	0.037_4	0.041_5	6.7_8	6.8_9	75 ± 5^c 79 ± 12^d	6.32_0
TmS	7.19	- 25	5.18						5.42
TmSe	6.32	- 33	1.85						5.70
TmTe	4.96	- 0.35	0.21						6.34_6

a Calculated per formula unit

b Calculated per 1/2 formula unit

c Calculated from specific heat 10-30°K

d Calculated from inelastic n-scattering (Ref. 17) the large uncertainty is due to the very broad line.

RARE EARTH IONS IN A HEXAGONAL FIELD I[*]

E. Segal and W. E. Wallace

Department of Chemistry
University of Pittsburgh
Pittsburgh, Pa. 15213

Abstract

Energy levels, eigenfunctions and magnetic moments of rare earth ions in a crystal field of hexagonal symmetry have been obtained using a Hamiltonian of the form $\mathcal{H} = B_4^0 O_4^0 + B_6^0 (O_6^0 + \frac{8}{77} O_6^6)$. Results have been obtained for all J values appearing in the rare earth series and have been tabulated in a form convenient for use in analyzing the influence of the crystal field on the bulk thermal and magnetic properties of compounds containing the rare earths. Since experiment shows that B_6^0/B_6^6 may deviate from $8/77$, a few calculations were made with this ratio deviating by 10 and 20% (from $8/77$). These calculations showed the results to be relatively insensitive to changes in B_6^0/B_6^6.

I.   Introduction

For many years it has been apparent[1-7] that the macroscopic

thermal and magnetic properties of systems containing rare earths

are significantly influenced by the interaction between the rare

earth ion and the ions in its environment. Information has become

available[8] for assessing these effects for crystals having cubic

symmetry but not for hexagonal crystals. The objectives in this

study were (1) to provide for hexagonal crystals information needed

to assess the influence of the crystal field interaction on their

heat capacity and susceptibility behavior and (2) to present the

results of the calculation in a form convenient for use by experi-
mentalists. For simplicity the treatment was limited to hexagonal
crystals having an ideal axial ratio.

II. General Description of the Calculations

A. The Hamiltonian

The most general Hamiltonian for a hexagonal crystal field
contains four independent parameters.

$$\mathcal{H} = B_2^0 O_2^0 + B_4^0 O_4^0 + B_6^0 O_6^0 + B_6^6 O_6^6 \tag{1}$$

To date very few calculations have been made using this complete and
complex Hamiltonian. There are many crystals for which the axial
ratio is ideal (i.e. $c/a = 2\sqrt{2/3}$) or nearly so. For these the term
$B_2^0 O_2^0$ is small and can be neglected. The Hamiltonian can be further
simplified by making use of the result $B_6^0/B_6^6 = \frac{8}{77} = 0.1035$ obtained
if the point charge model applies.

$$\mathcal{H} = B_4^0 O_4^0 + B_6^0 \left(O_6^0 + \frac{77}{8} O_6^6 \right) \cdot \tag{2}$$

Calculations were made using this simplified Hamiltonian. Clearly
these calculations can be regarded as significant only if the simpli-
fied Hamiltonian can be justified. Experiment reveals[9] that the
B_6^0/B_6^6 ratio is relatively insensitive[10] to the particular rare earth
ion and/or the nature of the substance involved. Nevertheless the
possibility exists that this ratio may deviate from 8/77 by 10 to 20%.
Accordingly some calculations were made with variations to this extent;
changes in results obtained were minor.

-91-

B. The Energies, Eigenfunctions and Magnetic Moments

Eigenfunctions of the crystal field states Γ_i are expressed as linear combinations of eigenfunctions for the free ion associated with various values of M, $\left|\Gamma_i\right\rangle = \sum_{M=-J}^{J} a_{iM} \left|M\right\rangle$. The energies and eigenfunctions (i.e. the values of a_{iM}) were evaluated using the Operator Equivalent method of Stevens.[11] The magnetic moments were obtained from the standard expression

$$\mu = \left\langle \Gamma_i \left| (\mu)_{op} \right| \Gamma_i \right\rangle. \tag{3}$$

Further details of the calculations may be found elsewhere.[12,13]

For calculations the Hamiltonian was used in the form

$$\mathcal{H} = W \left[x \, \frac{O_4}{F_4} + (1 - \left| x \right|) \, \frac{O_6}{F_6} \right] \tag{4}$$

where F_4 and F_6 are the common multiplicative factors,[8] the parameter x denotes the relative importance of the 4th and 6th degree terms and W is an energy scaling factor. $O_4 \equiv O_4^0$ and $O_6 \equiv O_6^0 + 77/8 \, O_6^6$. Of course $B_4 F_4 = Wx$ and $B_6 F_6 = W(1 - \left| x \right|)$.

III. Results

Calculations were made for all the J values appearing in the rare earth series. For brevity results are given here only for $J = 15/2$ and 4. Results obtained for other J values are given elsewhere.[12,13] The states into which the 2J+1-fold degenerate multiplets are decomposed by a hexagonal crystal field are given in Table I. Detailed results for $J = 15/2$ and 4 are given in Table II. Results

presented are for cases in which the crystal field interaction is
weak compared to the spin-orbit coupling energy.

Table I

Crystal Field States for Rare Earth Ions in a Hexagonal Field

J	Rare Earth	Crystal Field States[*]
5/2	Ce^{+3}, Sm^{+3}	$\Gamma_7(d) + \Gamma_8(d) + \Gamma_9(d)$
7/2	Yb^{+3}	$\Gamma_7(d) + 2\Gamma_8(d) + \Gamma_9(d)$
4	Pr^{+3}, Pm^{+3}	$\Gamma_1(s) + \Gamma_3(s) + \Gamma_4(s) + 2\Gamma_5(d) + \Gamma_6(d)$
9/2	Nd^{+3}	$\Gamma_7(d) + 2\Gamma_8(d) + 2\Gamma_9(d)$
6	Tb^{+3}, Tm^{+3}	$2\Gamma_1(s) + \Gamma_2(s) + \Gamma_3(s) + \Gamma_4(s)$ $+ 2\Gamma_5(d) + 2\Gamma_6(d)$
15/2	Dy^{+3}, Er^{+3}	$3\Gamma_7(d) + 2\Gamma_8(d) + 3\Gamma_9(d)$
8	Ho^{+3}	$2\Gamma_1(s) + \Gamma_2(s) + \Gamma_3(s) + \Gamma_4(s) +$ $3\Gamma_5(d) + 3\Gamma_6(d)$

[*] s and d in parenthesis indicate a singlet and doublet,
respectively.

-93-

Table II

Energies, Eigenfunctions and Magnetic Moments[*]

$$J = 15/2 \longrightarrow \quad 3\ \Gamma_7(\text{doublet}) + 2\ \Gamma_8(\text{doublet}) + 3\ \Gamma_9(\text{doublet})$$

$$(\text{Dy}^{+3},\ \text{Er}^{+3})$$

$$\left|\Gamma_7'\right\rangle = a_{\frac{13}{2}}\left|\mp\tfrac{13}{2}\right\rangle + a_{\frac{1}{2}}\left|\mp\tfrac{1}{2}\right\rangle + a_{\frac{11}{2}}\left|\pm\tfrac{11}{2}\right\rangle$$

x	E	$\mu_{\|}$	$\mu_{\perp}$	μ	$a_{\frac{1}{2}}$	$a_{\frac{11}{2}}$	$a_{\frac{13}{2}}$
∓1.0	∓189	0.067	0.533	0.538	1.000	0.000	0.000
-0.8	-167	0.066	0.533	0.537	1.000	-0.033	-0.003
-0.6	-145	0.061	0.530	0.534	0.997	-0.083	-0.009
-0.4	-126	0.044	0.520	0.522	0.985	-0.169	-0.021
-0.2	-113	0.015	0.489	0.489	0.943	-0.327	-0.066
0.0	-113	0.099	0.053	0.113	0.676	-0.501	0.540
0.2	2	0.125	0.412	0.431	0.872	0.490	0.201
0.4	38	0.030	0.511	0.512	0.977	0.214	0.013
0.6	85	0.060	0.529	0.533	0.996	0.093	0.007
0.8	137	0.066	0.533	0.537	0.999	0.034	0.003

[*]Explanation of Symbols in Table:

x is a parameter giving the relative importance of the fourth and sixth order terms. E is the energy in units of the parameter W. (For definitions of x and W see text). a_M are the normalized coefficients in the eigenfunction $\left|\Gamma_i\right\rangle = \sum\limits_{m=-J}^{J} a_{iM}\left|M\right\rangle$. $\mu_{\|}$ and $\mu_{\perp}$ are magnetic moments (divided by $gJ\ \mu_B$) along directions parallel and perpendicular to the c axis, respectively. $\mu = \sqrt{\mu_{\|}^{\,2} + \mu_{\perp}^{\,2}}$.

Table II (Continued)

$$\left|\Gamma_9\right\rangle = a_{\frac{9}{2}}\left|\mp\tfrac{9}{2}\right\rangle + a_{\frac{3}{2}}\left|\pm\tfrac{3}{2}\right\rangle + a_{\frac{15}{2}}\left|\pm\tfrac{15}{2}\right\rangle$$

x	E	μ	$a_{\frac{3}{2}}$	$a_{\frac{9}{2}}$	$a_{\frac{15}{2}}$
∓1.0	∓129	0.200	1.000	0.000	0.000
-0.8	-109	0.199	0.998	-0.049	0.037
-0.6	- 90	0.206	0.983	-0.117	0.144
0.4	- 84	0.477	-0.775	0.162	0.610
-0.2	- 69	0.145	0.923	-0.329	-0.198
0.0	- 66	0.025	0.868	-0.483	-0.117
0.2	- 50	0.186	0.714	-0.698	-0.065
0.4	53	0.087	0.916	0.389	-0.102
0.6	72	0.182	0.985	0.163	-0.059
0.8	99	0.198	0.998	0.056	-0.027

$$\left|\Gamma_8'\right\rangle = a_{\frac{7}{2}}\left|\mp\tfrac{7}{2}\right\rangle + a_{\frac{5}{2}}\left|\pm\tfrac{5}{2}\right\rangle$$

x	E	μ	μ	$a_{\frac{5}{2}}$	$a_{\frac{7}{2}}$		
∓1.0	∓23	0.333	0	1.000	0.000	0.467	±101
-0.8	-11	0.319	-0.132	0.991	-0.135	0.452	100
-0.6	- 5	0.268	-0.271	0.958	-0.286	0.402	104
-0.4	- 3	0.190	-0.379	0.906	-0.423	0.323	114
0.2	- 6	0.109	-0.444	0.849	-0.529	0.243	127
0.0	-11	0.042	-0.476	0.797	-0.604	0.175	143
0.2	-15	0.037	-0.493	0.733	-0.681	0.096	105
0.4	70	0.039	0.477	0.795	0.607	0.172	-22
0.6	44	0.211	0.356	0.921	0.391	0.345	-38
0.8	30	0.313	0.154	0.987	0.158	0.447	-66
x			-μ	$a_{\frac{7}{2}}$	$a_{\frac{5}{2}}$	μ	E

$$\Gamma_8' = a_{\frac{7}{2}}\left|\mp\tfrac{7}{2}\right\rangle - a_{\frac{5}{2}}\left|\pm\tfrac{5}{2}\right\rangle$$

Table II (Continued)

$$\left|\Gamma_9\right\rangle = a_{\frac{15}{2}}\left|\mp\frac{15}{2}\right\rangle + a_{\frac{3}{2}}\left|\mp\frac{3}{2}\right\rangle + a_{\frac{9}{2}}\left|\pm\frac{9}{2}\right\rangle$$

x	E	μ	$a_{\frac{3}{2}}$	$a_{\frac{9}{2}}$	$a_{\frac{15}{2}}$
∓1.0	±201	0.600	0.000	1.000	0.000
-0.8	173	0.598	0.049	0.999	0.000
-0.6	148	0.589	0.118	0.993	0.003
-0.4	125	0.563	0.214	0.977	0.012
-0.2	108	0.502	0.344	0.938	0.044
0.0	100	0.305	0.496	0.832	0.247
0.2	60	0.169	0.675	0.709	-0.205
0.4	-63	0.478	-0.389	0.921	0.020
0.6	-102	0.579	-0.163	0.987	0.004
0.8	-150	0.598	-0.056	0.998	0.001

$$\left|\Gamma_7\right\rangle = a_{\frac{11}{2}}\left|\mp\frac{11}{2}\right\rangle + a_{\frac{1}{2}}\left|\pm\frac{1}{2}\right\rangle + a_{\frac{13}{2}}\left|\pm\frac{13}{2}\right\rangle$$

x	E	$\mu_{\parallel}$	$\mu_{\perp}$	μ	$a_{\frac{1}{2}}$	$a_{\frac{11}{2}}$	$a_{\frac{13}{2}}$
∓1.0	±221	0.733	0	0.733	0.000	1.000	0.000
-0.8	170	0.733	0.001	0.733	0.033	1.000	0.000
-0.6	119	0.728	0.004	0.728	0.083	0.997	0.001
-0.4	71	0.710	0.018	0.711	0.169	0.986	0.003
-0.2	28	0.647	0.063	0.650	0.328	0.945	0.008
0.0	1	0.458	0.193	0.497	0.587	0.810	0.016
0.2	-100	0.527	0.060	0.530	-0.485	0.868	-0.107
0.4	-119	0.695	0.048	0.696	-0.215	0.976	0.034
0.6	-150	0.726	0.006	0.726	-0.093	0.996	0.003
0.8	-185	0.732	0.001	0.732	-0.034	0.999	0.000

Table II (Continued)

$$\left|\Gamma_7'\right\rangle = a_{\frac{11}{2}}\left|\mp\frac{11}{2}\right\rangle + a_{\frac{1}{2}}\left|\pm\frac{1}{2}\right\rangle + a_{\frac{13}{2}}\left|\pm\frac{13}{2}\right\rangle$$

x	E	$\mu_{\parallel}$	$\mu_{\perp}$	μ	$a_{\frac{1}{2}}$	$a_{\frac{11}{2}}$	$a_{\frac{13}{2}}$
$\mp$1.0	±91	0.867	0	0.867	0.000	0.000	1.000
-0.8	49	0.867	0.000	0.867	0.003	-0.000	1.000
-0.6	8	0.867	0.001	0.867	0.008	-0.002	1.000
-0.4	-34	0.866	0.005	0.866	0.020	-0.007	1.000
-0.2	-75	0.863	0.019	0.863	0.059	-0.030	0.998
0.0	-119	0.559	0.287	0.628	-0.446	0.306	0.842
0.2	-112	0.852	0.061	0.854	-0.070	0.084	0.994
0.4	-107	0.865	-0.026	0.865	-0.006	-0.036	0.999
0.6	-101	0.867	-0.002	0.867	-0.006	-0.003	1.000
0.8	-96	0.867	-0.000	0.867	-0.002	-0.000	1.000

$$\left|\Gamma_9'\right\rangle = a_{\frac{9}{2}}\left|\mp\frac{9}{2}\right\rangle + a_{\frac{3}{2}}\left|\pm\frac{3}{2}\right\rangle + a_{\frac{15}{2}}\left|\pm\frac{15}{2}\right\rangle$$

x	E	μ	$a_{\frac{3}{2}}$	$a_{\frac{9}{2}}$	$a_{\frac{15}{2}}$
$\mp$1.0	$\mp$273	1.000	0.000	0.000	1.000
-0.8	-206	0.999	-0.037	0.001	0.999
-0.6	-139	0.983	-0.144	0.014	0.990
-0.4	- 62	0.686	0.594	-0.139	0.792
-0.2	0	0.958	0.171	-0.109	0.979
0.0	65	0.881	-0.022	-0.273	0.962
0.2	109	0.955	0.189	0.103	0.977
0.4	149	0.991	0.102	0.022	0.995
0.6	190	0.997	0.059	0.006	0.998
0.8	231	0.999	0.027	0.001	1.000

Table II (Continued)

$J = 4 \longrightarrow$ Γ_1 (singlet) + Γ_3 (singlet) + Γ_4 (singlet) +

2 Γ_5 (doublet) + Γ_6 (doublet)

(Pr^{3+}, Pm^{3+})

$$|\Gamma_1'\rangle \equiv |o\rangle = |0\rangle \qquad\qquad |\Gamma_6'\rangle = |a\rangle = |\pm 1\rangle$$

$\mu = 0$ $\qquad\qquad\qquad\qquad\qquad\qquad\quad$ $\mu = 0.25$

E is a linear function of x $\qquad\qquad$ E is a linear function of x

x	E		x	E
∓1	∓18		∓1	∓9
0	-20		0	1

$$|\Gamma_5'\rangle = a_2 \left|\mp 2\right\rangle + a_4 \left|\pm 4\right\rangle$$

x	E	μ	a_2	a_4		
∓1.0	±11.0	0.500	1.000	0.000	1.000	∓14.0
-0.8	13.6	0.478	0.993	0.121	0.978	-10.8
-0.6	16.8	0.414	0.971	0.239	0.914	- 8.2
-0.4	20.8	0.324	0.940	0.342	0.824	- 6.4
-0.2	25.3	0.230	0.906	0.424	0.730	- 5.1
0.0	30.1	0.145	0.873	0.487	0.645	- 4.1
0.2	23.3	0.031	0.829	0.559	0.531	- 1.9
0.4	17.1	0.216	0.723	0.691	0.284	- 0.3
0.6	-0.9	0.168	0.882	-0.471	0.668	13.1
0.8	-4.9	0.457	0.985	-0.170	0.957	12.5

x		a_4	a_2	μ	E

$$\Gamma_5' = a_4 \left|\mp 4\right\rangle - a_2 \left|\pm 2\right\rangle$$

Table II (Continued)

$$\left|\Gamma_3\right\rangle^* \equiv \left|3^s\right\rangle = \frac{1}{2} \left[\; \left|-3\right\rangle \; + \; \left|3\right\rangle \; \right]; \; \mu = 0 \quad \text{for } x \neq \pm 1$$

x	E	
∓1	±21	Energy is linear with x
0	2.25	

$$\left|\Gamma_4\right\rangle^* \equiv \left|3^a\right\rangle = \frac{1}{2} \left[\; \left|-3\right\rangle \; - \; \left|3\right\rangle \; \right]; \; \mu = 0 \text{ for } x \neq \pm 1$$

x	E	
∓1	±21	Energy is linear with x
0	-36.5	

*When x = ±1, Γ_3 and Γ_4 converge to a doublet whose eigenfunctions are $\left|\pm3\right\rangle$ and the associated moment is 0.75.

References

1. D. H. Parkinson, F. E. Simon and F. H. Spedding, Proc. Roy.
       Soc. A207, 137 (1951).

2. W. G. Penney and R. Schlapp, Phys. Rev. 41, 194 (1932).

3. R. M. Bozorth et al., ibid., 115, 1595 (1959).

4. W. E. Wallace, Progress in Rare Earth Science and Technology,
       Vol. 3, p. 1 (1958) Pergamon Press, Edited by L. Eyring.

5. W. E. Wallace, F. Kissell, E. Segal and R. S. Craig, J. Phys.
       Chem. Solids 30, 13 (1969).

6. K. H. Mader, E. Segal and W. E. Wallace, ibid., 30, 1 (1959).

7. J. A. White et al., Phys. Rev. 131, 1039 (1963).

8. K. R. Lea, M. J. M. Leask and W. P. Wolf, J. Phys. Chem. Solids
       23, 1381 (1962). Our parameters x and W are not identical
       to that of this ref. Here the B_n^m or x and W are expressed
       in a coordinate system in which the z axis is along the cubic
       [100] direction. In the present paper z is along the hexagonal
       c axis corresponding to the cubic [111] direction.

9. G. H. Dieke, "Spectra and Energy Levels of Rare Earth Ions in
       Crystals," Interscience Publishers, New York (1968), p. 148.

10. This ratio is also insensitive to the model used in the calcula-
       tions. The point charge model values are not too different
       from the values computed from the more general ionic model
       which take into account in addition to the point charges
       higher induced moments of the surrounding ions. See ref. 14
       below which shows that the results differ little when dipolar
       and quadrupolar contributions are included.

11. K. W. H. Stevens, Proc. Roy. Soc. (London), A65, 209 (1952).

12. E. Segal in "Thermal, Structural and Magnetic Studies of Metals
       and Intermetallic Compounds" by W. E. Wallace and R. S.
       Craig, Annual Report to the U. S. Atomic Energy Commission,
       NYO-3454-27, May 15, 1969.

-100-

13. E. Segal and W. E. Wallace, J. Solid State Chem., in press.

14. M. T. Hutchings and O. K. Ray, Proc. Phys. Soc. $\underline{81}$, 663 (1963).

MAGNETIC INTERACTIONS AND CRYSTALLINE FIELD IN EQUIATOMIC RARE EARTH - NOBLE METALS COMPOUNDS

Jacques PIERRE

Laboratoire d'Electrostatique et de Physique du Métal,
Cedex 166 - 38-GRENOBLE, France

Abstract

The RCu and RAg compounds with heavy rare earths are antiferromagnets with an ordered structure of ($\pi\pi0$) type. When a divalent metal is substituted for the noble one, the interactions become ferromagnetic. We explain these variations by means of indirect exchange theory.

The crystalline field explains the variations of the susceptibilities in CeAg, PrAg and NdAg at low temperatures and the directions of the rare earth moment in the order range. We observe a direction parallel to <001> axis in TbCu and to <111> axis in HoCu.

1 - Magnetic properties of RCu and RAg compounds

The RCu and RAg compounds with heavy rare earths are antiferromagnets[1,2,3]. The experimental paramagnetic moments μ_{ex} are in agreement with the theoretical values of the trivalent ions. The paramagnetic Curie temperatures Θ_p and Néel température Θ_N vary as De Gennes factor $(g - 1)^2 J(J+ 1)$ (figure 1) ; they are similar for homologous compounds in spite of a 5 % difference in the crystalline parameter.

The magnetic ordered structure has been established by neutron diffraction for TbCu, TbAg[4] and DyAg[5]. We have studied the TbCu and HoCu compounds. We give in figure 2 the patterns observed for HoCu at 4.2 and 77 K. The

propagation vector of the ordered structure is $\vec{\tau} = (\frac{1}{2} \quad \frac{1}{2} \quad 0)$. This (ΠΠ0) structure[6] can be described as ferromagnetic sheets parallel to (110) planes, the moment sign changing from one sheet to the next one.

The magnetic intensities are calibrated with respect to the nuclear ones, taking $b_{Ho} = 0.76 \cdot 10^{-12}$ cm, $b_{Ho} = 0.85 \cdot 10^{-12}$ cm, $b_{Cu} = 0.79 \cdot 10^{-12}$ cm (table I).

TABLE I

Nuclear and magnetic intensities observed at 4.2 K on TbCu and HoCu compounds and corresponding moments

h k l	TbCu			HoCu		
	I_{obs} (barns)	μ.f (μ//001)	μ*(μ$_B$)	I_{obs} (barns)	μ.f (μ//111)	μ**(μ$_B$)
$\frac{1}{2}$ $\frac{1}{2}$ 0	333	8,46	8,66	205	8,10	8,45
$\frac{1}{2}$ $\frac{1}{2}$ 1	191	7,85	9,05	304	6,97	7,93
1 1 0	432	nuclear		542	nuclear	
$\frac{3}{2}$ $\frac{1}{2}$ 0	422	6,73	8,55	290	6,82	8,47
$\frac{3}{2}$ $\frac{1}{2}$ 1	522	6,27	8,71	526	6,40	8,65
2 0 0	251	nuclear		260	nuclear	
$\frac{1}{2}$ $\frac{1}{2}$ 2 } $\frac{3}{2}$ $\frac{3}{2}$ 0 }	197	5,88	8,76	299	5,65	8,20
$\frac{3}{2}$ $\frac{3}{2}$ 1	218	5,35	8,74	166	5,14	8,05
2 1 1	911	nuclear		1022	nuclear	
$\frac{3}{2}$ $\frac{1}{2}$ 2 } $\frac{5}{2}$ $\frac{1}{2}$ 0 }	381	4,81	8,43	512	5,22	9,01

*taking f according to[7] **taking f according to[8]

The moment direction is along the magnetic cell c-axis for TbCu in agreement with Cable et al[4]. Its value is 8.75 $\pm$ 0.3 μ_B at 4.2 K and 7.8 $\pm$ 0.3 μ_B at 77 K. For HoCu, it does an angle $\varphi = 55 \pm 4°$ with the c-axis ($\mu = 8.35 \pm 0.4$ μ_B at 4.2 K) and points thus along the <111> direction.

The SmAg compound presents a Néel temperature at 40.4 K. The variation of the paramagnetic susceptibility can be explained by the Van Vleck - type paramagnetic and antiferromagnetic interactions. From the measurements the L - S coupling constant A = 380 $\pm$ 30 K is deduced[9].

The susceptibilities of CeAg, PrAg, NdAg compounds show at low temperatures deviations from the Curie-Weiss law[2]. The paramagnetic moments rise with temperature and reach towards 200 K the free trivalent ion value (figure 3, table II). The cerium is here trivalent, in agreement with the value of the crystalline parameter. CeAg and PrAg order ferromagnetically at 7 $\pm$ 0.5 K and 14 $\pm$ 1 K; NdAg becomes an antiferromagnet under 20 $\pm$1 K[1,9].

T A B L E   II

Experimental and theoretical values of the paramagnetic moments at low and high temperatures for CeAg, PrAg, NdAg.

	high tempera. ture (T>200 K)		low temperatures			
	μ_{ex} (μ_B)	$\mu_{th}R^{3+}$ (μ_B)	μ'_{ex}	level	μ'_{th} // <100>	μ'_{th} // <111>
CeAg	2,59	2,56	1,96	Γ_8	1,99	1,99
PrAg	3,37	3,58	3,29	Γ_5	isotropic	2,83
NdAg	3,57	3,68	3,31	Γ_8	2,81	3,10

The variation of the moment can be explained by the effect
of the cubic crystalline field, which splits the level
$J = L - S$, as it was observed in $CeAl_2$ [10].

2 - Crystalline field

The crystalline field hamiltonian is written as

$$U_c = A_4 \beta <r^4> O_4 + A_6 \gamma <r^6> O_6,$$

in terms of Stevens operator equivalents O_4 and O_6 and
coefficients β and γ.

In the cas of cerium ($\gamma = 0$), the level is split
in a quadruplet $Q(\Gamma_8)$ and a doublet D (Γ_7) separated by
$\Delta = E_D - E_Q$. The experimental moment at low temperatures
$\mu'_{ex} = 1,96 \mu_B$ is in agreement with the theoretical moment
$\mu'_{th} = 1,99 \mu_B$ of the quadruplet, which is thus the low-
lying level. The susceptibility is expressed without
exchange as :

$$\chi_o = \frac{N\beta^2 g^2}{kT} \frac{1}{4+2 \exp(-\frac{\Delta}{kT})} \left[\sum_{i_Q} M_{ii}^2 + \sum_{j_D} M_{jj}^2 \exp(-\frac{\Delta}{kT}) \right.$$

$$\left. - 2kT \left(\sum_{ij} \frac{M_{ij}^2}{-\Delta} + \sum_{ij} \frac{M_{ji}^2}{\Delta} \exp(-\frac{\Delta}{kT}) \right) \right]$$

The susceptibility with exchange is given by $1/\chi_{ech} = 1/\chi_o - n$
in a molecular field model [11]. By comparison with the
experimental variations we deduce for CeAg

$$\Delta = + 360 \pm 20 \text{ K}$$

$$n \sim 4 \text{ u.e.m.}$$

The geometrical coefficient A_4 is negative and we expect
that it does not vary much in the rare earth series.

In the second group, exchange and magnetocrystal-
line energies are similar. However, we can suppose that the
only effect of the crystal field is to level the directional
degeneracy of the moment. The magnetocrystalline energy is
then written in terms of the direction cosines α, β, γ of
the magnetic moment[12]

$$U_c = K_4(\alpha^4 + \beta^4 + \gamma^4 - \frac{3}{5}) - 4K_6 (\alpha^6 + \beta^6 + \gamma^6 + \frac{15}{4}\Sigma\alpha^2\beta^4 - \frac{15}{14})$$

where $K_4 = 20 \ A_4 \ <r^4> \ <\Sigma P_4(\frac{z}{r})>$

$K_6 = 56 \ A_6 \ <r^6> \ <\Sigma P_6(\frac{z}{r})>$

$<\Sigma P_4(\frac{z}{r})>$ and $<\Sigma P_6(\frac{z}{r})>$ are the 2^4 and 2^6-pole moments of rare
earth ions (table III). The 6-order term is shown by point
charges method to be about one tenth of the 4-order one.
As A_4 is negative, the predicted directions for the moment
are the fourfold axis for compounds with Tb, Er, Tm and the
threefold axis in the case of Dy and Ho. The observed
direction is in agreement with these predictions for TbCu,
TbAg and HoCu, but is not for DyAg[5].

T A B L E   III

Rare Earth	$<\Sigma P_4(\frac{z}{r})>$ [12]	$<\Sigma P_6(\frac{z}{r})>$ [12]	K_4	K_6	expected moment direction
Tb	1/11	- 5/429	-	+	<001>
Dy	- 4/33	25/429	+	-	<111>
Ho	- 1/11	-50/429	+	+	<111>
Er	1/11	50/429	-	-	<001>
Tm	4/33	-25/429	-	+	<001>

However, according to Bleaney[11], the Γ_8 quadru-
plets encountered in ions presenting Kramers degeneracy are
anisotropic ; in this case, the exchange term $(- nM^2)$ is
minimized when the moment points along a fourfold axis.
Moreover the magnetic dipolar energy depends only on the γ
moment direction cosine along the c-axis of the magnetic
cell

$$E_{dip} = 1,34 \ \frac{\mu^2}{a^3} \ (1 - 3\gamma^2)$$

for this type of structure. This term favours the c-axis
direction.

3 - Variation of interactions with number of valency electrons

When substituting a divalent metal for the noble
one, the Curie paramagnetic temperature Θ_p rises (figure 4)
and the ordered state becomes ferromagnetic beyong a certain
number of valency electrons by cell[13, 14, 15].

This behaviour can be explained by the indirect
exchange theory via conduction electrons. In the simple
theory two major assumptions are made :

1 - the s-f interaction takes a contact form,

2 - the Fermi surface is spherical and the conduction band
    parabolic with effective mass m^*:

Within this model, the Curie paramagnetic temperature Θ_p
and the spin-disorder resistivity ρ_m are given by[16] :

$$k_B \ \Theta_p = - \ \frac{3\pi}{4} \ (g - 1)^2 J(J + 1) \ \frac{z^2 \ \Gamma^2}{V^2 \ E_F} \ \sum_{i \neq 0} F(x_i)$$

$$\rho_m = \frac{3\pi}{8} \ (g - 1)^2 J(J + 1) \ \frac{m^*}{e^2 \hbar} \ \frac{\Gamma^2}{V \ E_F}$$

where Γ is the s-f coupling constant, Z the magnetic ion charge, V the cell volume, $F(x_i) = x_i^{-4}(x_i \cos x_i - \sin x_i)$ is the oscillating Rudermann-Kittel function

$$x_i = 2k_F R_{oi}.$$

For an ordered magnetic structure having a propagation vector $\vec{\tau}$, the ordering temperature is given by an expression like θ_p, where $\sum_{i \neq 0} F(x_i)$ is replaced by

$$\sum_{i \neq 0} F(x_i). \exp(2\Pi i \; \vec{\tau}. \vec{R}_{oi}).$$

We have drawn (figure 5) the variations of this quantity versus $k_F a$ for the ferromagnetic configuration (000) and antiferromagnetic ones ($\Pi 00$), ($\Pi \Pi 0$), ($\Pi \Pi \Pi$) corresponding to propagation vectors $(\frac{1}{2} \; 0 \; 0)$, $(\frac{1}{2} \; \frac{1}{2} \; 0)$, $(\frac{1}{2} \; \frac{1}{2} \; \frac{1}{2})$.

Assuming that all valency electrons are free, the ferromagnetic state should be the stable one for rare earth noble metal compounds ($k_{F_o} a \sim 4.9$). Instead, experiment show ($\Pi \Pi 0$). However, it is possible to deduce the correct structures and variations for θ_p and θ_N, taking for the parameter $k_F a$ a smaller value than deduced from free electron model ($k_F a \sim 0.85 \; k_{F_o} a$).

Then, the expression for θ_p gives $\Gamma^2 (eV.\overset{\circ}{A}^3) \sim 2.1 \; E_F(eV)$ and with the free electron value $E_F = 7.3$ eV, we obtain $|\Gamma| \sim 3.9$ eV.$\overset{\circ}{A}^3$ in good agreement with the pure rare earths' results.

We must now explain the reduced value observed for k_F. It can first be an effect of the band structure. We have measured the specific heat of YCu and YAg compounds [3] and found the density of states to be 3 times the free electron value. The high resistivity also shows that the Fermi surface must be distorted.

-108-

Secondly, the exchange integral between two magnetic ions is expressed[17] by

$$J(R_n) \sim \frac{1}{N} \sum_q \Gamma^2_{(q)} X_{(q)} \exp(iq \cdot R_n).$$

If the s-f interaction Fourier transform $\Gamma_{(q)}$ is taken as constant (Rudermann-Kittel), the cut off of the suscepti-bility function $X_{(q)}$ at $q = 2k_F$ gives for $J(R_n)$ an oscilla-tory behaviour like $\cos 2k_F r$. Freeman-Watson[18] have shown that $\Gamma_{(q)}$ actually decreases and changes sign for $q_o < 2k_F$. Thus the exchange integral should oscillate as $\cos q_r$ where $q < 2k_F$.

Conclusion

It is possible to explain the ordered structures observed in TCu and TAg compounds, and their changes with the number of valency electrons in terms of indirect exchange theory. Use of elaborated models need more detailled knowledge of the band structure.

The moment directions in ordered state can be predicted with help of the crystalline field and magnetic dipolar energy.

References

1 - WALLINE R.E., WALLACE W.E.
J. Chem. Phys., 41, (1964), 3285 and 42, (1965), 604.

2 - PIERRE J., PAUTHENET R.
C. R. Acad. Sc. Paris, 260, (1965), 2739.

3 - PIERRE J.
Colloque Intern. du C.N.R.S. sur les Eléments des
terres rares (Paris-Grenoble, 1969), to be published.

4 - CABLE J.W., KOEHLER W.C., WOLLAN E.O.
Phys. Rev., 136, (1964), A240.

5 - ARNOLD G., NERESON N., OLSEN C.
J. Chem. Phys., 46, (1967), 4041.

6 - GERSCH H.A., KOEHLER W.C.
J. Phys. Chem. Solids, 5, (1958), 180.

7 - BLUME M., FREEMAN A.J., WATSON R.E.
J. Chem. Phys., 37, (1962), 1245.

8 - KOEHLER W.C., WOLLAN E.O., WILKINSON M.K.
Phys. Rev., 110, (1966), 37.

9 - PIERRE J.
Thesis, Grenoble University, (1969).

10 - WHITE J.A., WILLIAMS H.J., WERNICK J.H., SHERWOOD R.C.
Phys. Rev., 131, (1963), 1039.

11 - BLEANEY B.
Proc. Roy. Soc., A276, (1963), 19.

12 - TRAMMEL G.T.
Phys. Rev., 131, (1963), 932.

13 - SEKIZAWA K., YASUKOCHI K.
J. Phys. Soc. Japan, 46, (1966), 684.

14 - PIERRE J.
C. R. Acad. Sc. Paris, 265, (1967), B1169.

15 - ALFIERI G.T., BANKS E., KANEMATSU K.
J. Appl. Phys., 37, (1966), 1254.

16 - ROCHER Y.A.
Phil. Mag Suppl., 11, (1962), 233.

17 - YOSIDA K., WATABE A.
Progr. Theor. Phys., 28, (1962), 361.

18 - WATSON R.E., FREEMAN A.J.
Phys. Rev., 152, (1966), 566.

Figure 2

Ho Cu
T = 4,2 °K
λ = 1,10 Å

Neutron diffraction patterns of HoCu at
4. 2 K and 77 K.

Figure 1 :

Paramagnetic Curie temperatures θ_p and
Neel temperatures θ_N of TCu and TAg
compounds.

Neutron diffraction patterns of HoCu at
4. 2 K and 77 K.

Paramagnetic Curie temperatures θ_p and
Neel temperatures θ_N of TCu and TAg
compounds.

Figure 4
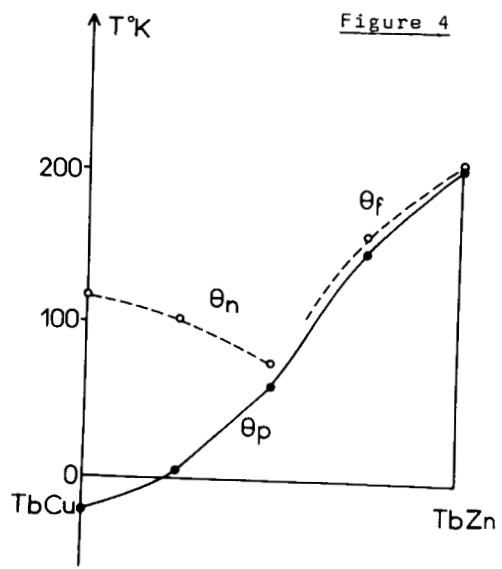
Paramagnetic Curie temperatures θ_p and ordering temperatures of $TbCu_{1-x}Zn_x$ compounds.

Figure 3

Reciprocal susceptibilities of CeAg, PrAg, NdAg compounds.

Figure 5
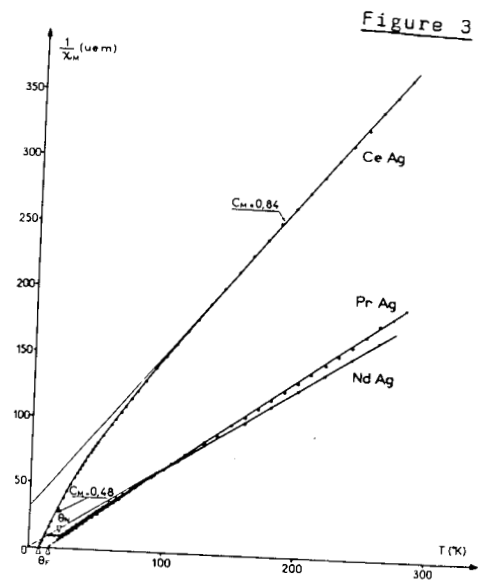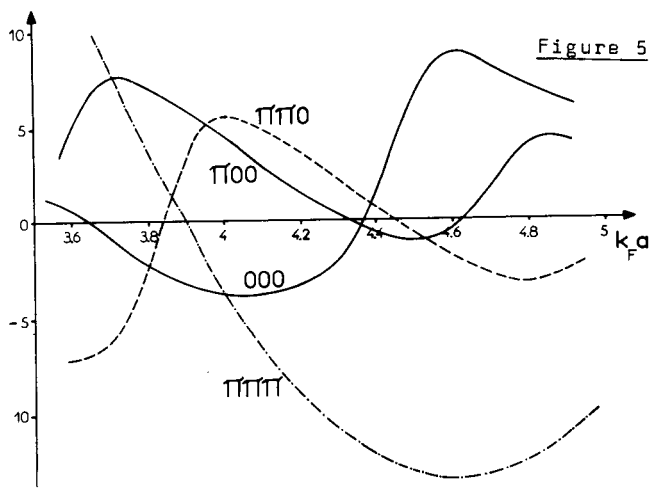
Reduced ordering temperatures (arbitrary unit).

MIXED CRYSTAL PHASES IN THE SYSTEM $ThO_2 - PrO_x$

G. Brauer and B. Willaredt

Chemical Laboratory of the University of Freiburg
Freiburg im Breisgau, Fed. Rep. Germany

ABSTRACT

Praseodymia and thoria form homogeneous crystalline phases
when mixed and heated to 1300°C. The oxygen content of these phases
depends on the pressure of molecular oxygen maintained during the
cooling of the samples from 500°C down to room temperature. It is
surprising that the admixing of thoria does not favor the uptake of
oxygen to form more Pr(IV) compared with the case of pure praseo-
dymia. The lattice constants of the mixed crystal series $(Pr, Th)O_2$
and $(Pr, Th)O_{2-x}$ show appreciable deviations from Vegard's law. It
is suggested to explain this by the ionic size effect.

INTRODUCTION

The higher oxides of praseodymium and terbium are interest-

ing examples of nonstoichiometric compounds. They have been very

successfully investigated in the composition range from $LnO_{1.5}$ to

$LnO_{1.83}$ by balancing oxide samples with molecular oxygen of different

pressures and at temperatures ranging from 300 to 1000°C, using

mainly thermogravimetric methods. Toward low values the tempera-

ture of the experiments is generally limited, as the rate of reaction

of the oxides with the gas atmosphere and the rate of ion diffusion in

the crystal lattices become very slow. The oxygen pressures

involved in those experiments varied from very low values up to 760 torr. The results of many isobaric, isothermal, and X-ray investigations are represented in the well-known (p, T, x) phase diagrams for PrO_x and TbO_x by L. Eyring, B. G. Hyde, and D. J. M. Bevan.[1]

Compared to these thoroughly investigated regions $LnO_{1.5}$ to $LnO_{1.83}$, the oxygen richest part of the phase diagrams; i.e., $LnO_{1.83}$ to $LnO_{2.00}$, is less known because it is hardly accessible by usual experimental techniques. As the limiting factor of the reaction rate at low temperatures cannot be eliminated, all experiments have to be done at an adequate temperature under an accordingly high oxygen pressure. Simon and Eyring in 1954[2], Sieglaff and Eyring in 1957[3], and MacChesney et al. in 1964[4] and 1966[5] have published the results of such high pressure investigations on PrO_x and TbO_x. However, these authors, though obtaining many valuable data, could not advance to final statements on the phase relationships and on the precise equilibrium pressures in the range from $LnO_{1.83}$ to $LnO_{2.00}$.

We took up the problem and extended it to the question whether or not an oxide admixture to the praseodymium or terbium oxide could lower the dissociation pressures and hence favor the oxidation to tetravalency at any given pressure; e.g., one atmosphere. At the Fifth Rare Earth Research Conference in Ames, Iowa, I referred to experiments with mixtures of praseodymia and several trivalent

-116-

R. E. oxides. Our results were unexpected and could not be under-
stood insofar as the influence of some of the admixed oxides turned
out to be either positive or negative depending only on the mixing ratio.

We decided then to carry on with a simpler system consisting
of praseodymia and thoria. Besides, we noticed that the phase
relationships of the system PrO_2 - ThO_2 seem to have never been
investigated before, in contrast to other similar dioxide systems with
the elements Th-Ce, Th-Zr, Th-U, Ce-U, Ce-Pr.

RESULTS

We prepared a sequence of mixed oxides of praseodymium and
thorium with different molar ratios extending from 0% to 100% and
ignited the mixtures several hours at about 1300°C to ensure the
random distribution of the two kinds of cations. The samples were
then subjected to two different treatments. In a first series, the
samples were cooled down from 500°C very slowly to 20°C in the
open air, corresponding to 0.2 atm of oxygen pressure. In the second
series of runs, the same careful cooling was done under 150 atm of
oxygen pressure. This high pressure was chosen as we soon
recognized that the usual pressure of about 10 atm was not sufficient
to oxidize all the praseodymium to the tetravalent state. Both series
of samples were analyzed chemically for the oxidation state of the
praseodymium, and by X-ray diffraction for the phases present.

The two series of samples, differing by the pressure during the preparation, turned out to represent two pseudobinary sections: PrO_2-ThO_2 and $PrO_{1.85}$-ThO_2, both with the f. c. c. fluorite-like structure. Table 1 gives the main data as observed. Figure 1 represents the curves obtained from plotting the cubic lattice constants vs. mixing ratios of the cations. Main features of the two series are:

I.   The plots of lattice constants vs. cation ratio are not Vegard straight lines. The lines are more or less curved, indicating a deviation of the mixed crystals from the behavior as ideal solutions or even indicating a slight tendency of the one phase to split into two.

II.   The oxidation of praseodymium to the tetravalent state is by no means favored in the presence of the tetravalent thorium in the joint oxide lattice. The oxidation stops at $PrO_{1.85}$ without regard to the thoria content when the oxygen pressure is 0.2 atm.

DISCUSSION

To discuss these results, one may compare our findings with the measurements of Hoch and Yoon[6] on the ThO_2-CeO_2-$CeO_{1.5}$ system or those of McCullough[7] on the CeO_2-PrO_2-$PrO_{1.5}$ system. In these latter two cases, no such high degree of miscibility has been observed as in the system referred to here. In Fig. 3, the phase diagram given by Hoch and Yoon for ThO_2-CeO_2-$CeO_{1.5}$ is compared

-118-
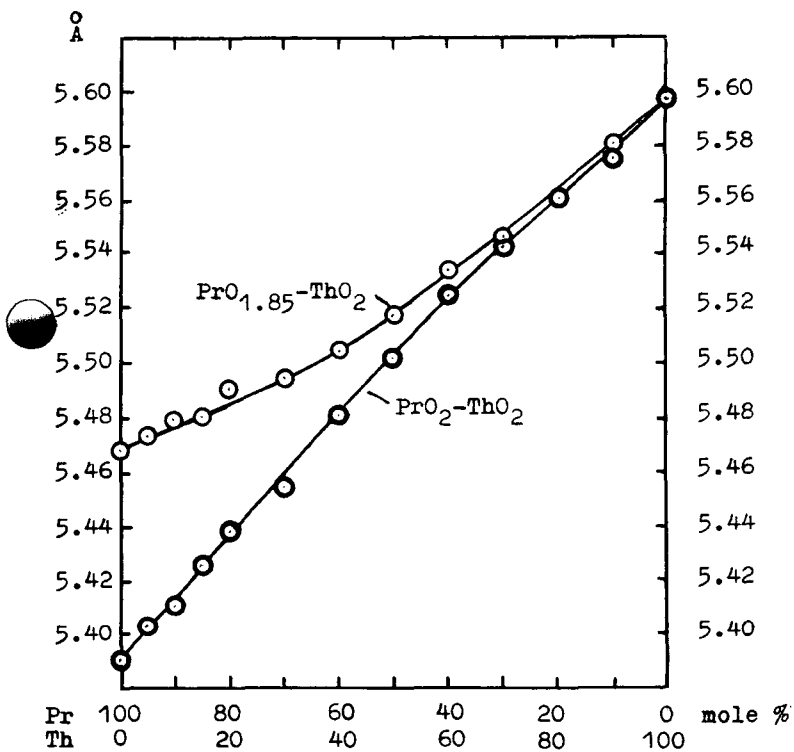
Fig.1   Lattice constants of mixed crystal
series PrO_2-ThO_2 and $PrO_{1.85}$-ThO_2
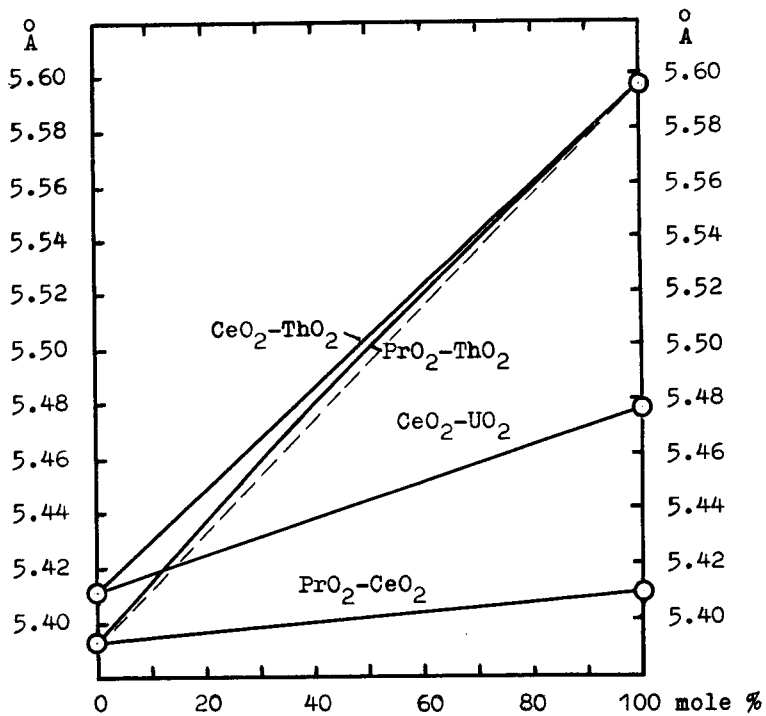
Fig.2 Lattice constants of mixed crystal
series of different dioxides (f.c.c.)

with a tentative diagram for ThO_2-PrO_2-$PrO_{1.5}$ derived from our observations. We postulate a broad homogeneity range of the cubic $(Pr, Th)O_x$ phase. However, the miscibility gap of the pure praseodymium system - ranging from $PrO_{1.83}$ to PrO_2 - must extend also into the ternary phase field. In Fig. 3, the border line of this miscibility gap has been drawn rather speculatively.

Thus, curiously enough, the thoria-praseodymia system does not resemble the thoria-ceria system in spite of the close chemical relationship. However, in reading and comparing the two diagrams, one has to consider that the observation temperatures (or preparation temperatures) are rather different (about 400°C in the case of $(Pr, Th)O_x$ and about 1200°C in the case of $(Ce, Th)O_x$) and that the oxygen pressure (a very important variable) is neither constant nor exactly defined in both investigations compared.

The experiments of McCullough[7] on the CeO_2-PrO_x system do not give enough information to construct a ternary phase diagram. However, there is no doubt that a continuous series of mixed crystals extends between CeO_2 and PrO_2 with a straight linear function of the lattice constants.

The deviation of the lattice constants from Vegard's law observed with the PrO_2-ThO_2 series is not excessive. However, it is unique among similar dioxide systems as shown in Fig. 2 .
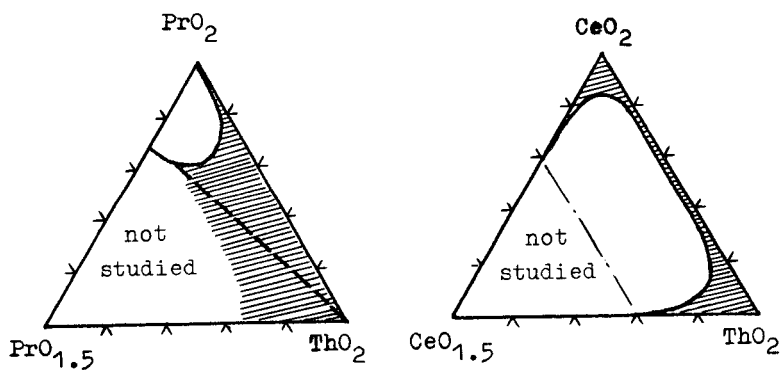
Fig.3 Phase diagrams of ThO_2-PrO_2-$PrO_{1.5}$ (tentative) and ThO_2-CeO_2-$CeO_{1.5}$ (after Hoch and Yoon)

The curve of the lattice constants of the $PrO_{1.85}$ - ThO_2 series is appreciably bent in the middle region (see Fig. 1) whereas the two terminal branches may be approximated by straight lines which have different directions. Patterns taken in a high resolution focusing camera did not show any deviation from the f.c.c. symmetry.

Finally, we want to understand the failure of thoria admixtures to favor the oxidation of praseodymia. It seems that there are two effects with opposite sign involved. On the one hand, a dilution of praseodymium oxide by thoria in solid solution should reduce the oxygen activity, according to the equations:

$$PrO_2 \rightleftharpoons PrO_{2-\Delta} + \frac{\Delta}{2}O_2 \text{; dissoc. pressure } \overset{o}{p}O_2$$

$$(Pr_{1-y}Th_y)O_2 \rightleftharpoons (Pr_{1-y}Th_y)O_{2-\Delta} + \frac{\Delta}{2}O_2 \text{; dissoc.}$$
$$\text{pressure } \overset{y}{p}O_2$$

$$\overset{y}{p}O_2 = const \cdot y \cdot \overset{o}{p}O_2 \quad (y \ll 1), \quad \text{Raoult's law}$$
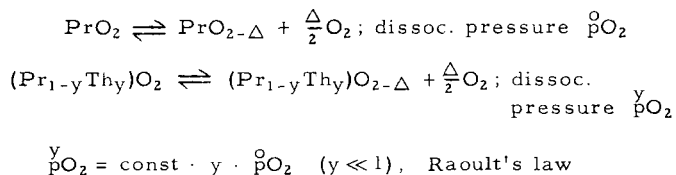
On the other hand, a solid solution of thoria in praseodymia extends the crystal lattice; i.e., a spatial condition is produced which favors the larger trivalent over the smaller tetravalent praseodymium ions. In the case investigated here, the second effect must preponderate. As a consequence of this interpretation, praseodymium should be more easily oxidized to tetravalency if a dioxide with smaller lattice constant is present. Work is under way to check this assumption.

ANALYTICAL

A main experimental difficulty was to determine the oxidation state of praseodymium in the mixed oxides. The only satisfactory procedure was to reduce the samples with hydrogen at 700°C, taking for granted that the final products were ThO_2 and $PrO_{1.5}$ when constant weight was achieved. The weight loss gives the quantity of oxygen corresponding to the part of praseodymium with a valency higher than three. Attempts to evaluate the oxidation state by a more sensitive titration method failed as no appropriate solvent for the high temperature ignited thoria-mixtures could be found. The accuracy of the weight controlled reduction procedure is quite sufficient at high praseodymia contents but decreases appreciably with raised thoria contents. Thus, deviations of the oxygen coefficient x (in PrO_x) from 2.00 toward slightly higher values, as seen in some cases in Table 1, have no real significance.

REFERENCES

[1] B. G. Hyde, D. J. M. Bevan, and L. Eyring, Phil. Trans. Roy. Soc., London, Ser. A, 259, 583 (1966)

B. G. Hyde and L. Eyring, Rare Earth Research III, New York 1965, p. 623

[2] W. Simon and L. Eyring, J. Am. chem. Soc. 76, 5872 (1954)

[3] C. L. Sieglaff and L. Eyring, J. Am. chem. Soc. 79, 3024 (1957)

[4] J. B. MacChesney, H. J. Williams, R. C. Sherwood, and
J. F. Porter, J. Chem. Phys. $\underline{41}$, 3177 (1964)

[5] J. B. MacChesney, H. J. Williams, R. C. Sherwood, and
J. F. Porter, J. Chem. Phys. 44, 596 (1966)

[6] M. Hoch and H. S. Yoon, Rare Earth Research III, New York
1965, p. 665

[7] J. D. McCullough, J. Am. chem. Soc. $\underline{72}$, 1386 (1950)

TABLE 1.

Oxidation states and f.c.c.lattice constants of mixed phases ThO_2-PrO_x (x = oxidation coefficient of praseodymium).

Sample Mole % Pr:Th	Anneal. temper. °C	Cooled from 500°C under 0.2 atm O_2		Cooled from 500°C under 150 atm O_2	
		Ox.coeff. x	Lattice const.Å	Ox.coeff. x	Lattice const.Å
100: 0	–	1.835	(5.469)	2.00	5.392
90:10	1300		5.480	1.99	5.412
80:20	1450	1.86	5.491	2.00	5.439
70:30	1300	1.87	5.495	1.99	5.455
60:40	1310	1.85	5.505	2.00	5.481
50:50	1300		5.518	2.00	5.502
40:60	1300		5.535	1.99	5.525
30:70	1300		5.547	2.05	5.543
20:80	1300	1.85	5.561	2.02	5.561
10:90	1300		5.581	2.1	5.576
0:100	1000	–	5.597	–	5.597

FLUOROSULFIDES, SULFOBROMIDES AND SULFOIODIDES
OF THE RARE EARTH ELEMENTS

by C. DAGRON, J. ETIENNE, J. FLAHAUT, M. JULIEN-
POUZOL, P. LARUELLE, N. RYSANEK, N. SAVIGNY,
G. SFEZ and F. THEVET.

Laboratoire de Chimie Minerale - Equipe associee au C. N. R. S.
et Laboratoire de Physique de la FACULTE DE PHARMACIE
4, Avenue de l'Observatoire - PARIS 6° (75) - FRANCE.

ABSTRACT

Preparation and crystallographic study of the LSX compounds of
the rare earth elements, with X = F, Br and I. Nine crystal
structures are observed among these compounds. Only one of them
is already known: the PbFCl-type of the LSF compounds (L = La to Er).
Description of two new crystal structures: the orthorhombic CeSI-type
and the rhombohedral SmSI-type. In all these structures, the rare
earth atoms form $[L_4X]$ tetrahedra containing the smallest non-metal
atoms.

Except three fluorosulfides (La, Ce, Eu), obtained by HAHN and

SCHMID (1) in 1965, all the compounds of this paper are prepared for

the first time. We shall especially study here the crystallographic

point of view. That is the reason why the chlorosulfides will not be

studied: the chlorine atoms cannot be distinguished from the sulphur

atoms by the usual X-ray crystallographic process. Moreover, many

new crystal types are present in these compounds, and we are studying

all these structures with single crystals.

Preparations. Fluorosulfides are obtained by direct union of L_2S_3

sulfides and LF_3 fluorides. We use graphite crucibles, located inside

sealed and evacuated silica tubes. At 1000-1200° C, the reaction
quickly occurs. These compounds are not altered by atomospheric
moisture.

Sulfobromides and sulfoiodides are obtained by successive action
of halogen and sulphur on the metal, in definite proportions corresponding
to the LSX composition. But, usually, we use a deficit of sulphur, in
order to have an excess of rare earth halide, in which the LSX compound
gives small single crystals. The three elements are, at the beginning
of the reaction, in three different regions of a long sealed pyrex tube.
The non-metals are in small silica ampullas which are broken inside the
silica tube at the convenient times. The temperatures of the three elements
must be strictly fixed for each step of the reaction. First the halogen
(at room temperature for Br, or at about 110° for I) reacts with the
metal heated at about 400° C. Then the sulphur is heated at about 250° C,
and its vapor reacts with the mixture of free metal and halide previously
prepared. When excess of halide is used, crystallization occurs during
heating at 500-800° C for a week, the temperature depending on the
compounds. The excess of halide is eliminated by fast washing with
alcohol.

Fluorosulfides. Only two crystal types are observed in this family.
From La to Er: tetragonal PbFCl-type space group P/4nmm. From Ho
to Lu: hexagonal new crystal structure; space group $P6_322$. YSF, HoSF
and ErSF are dimorphous, and their hexagonal form, stable at high
temperature, is obtained by quenching from 1200° C.

The structure of the tetragonal compounds was established using a least-squares refinement involving the intensities of the diffraction lines determined from a powder diffractogram. For YSF, we have, in the positions of the P4/nmm space group: (centrosymmetric)

F (2a) : 3/4 , 1/4 , 0 ; 1/4 , 3/4 , 0

Y (2c) : 1/4 , 1/4 , $\bar{z}$; 3/4 , 3/4 , z   z = 0,226

S (2c) : 1/4 , 1/4 , $\bar{z}'$; 3/4 , 3/4 , z'   z' = 0,643

The reliability factor is 0. 07 (2).

Each fluorine atom is at the center of an elongated tetrahedron of yttrium atoms. The structure can be seen as formed by flat sheets of Y_4F tetrahedra, in which each Y atom belongs to four neighbouring tetrahedra. These sheets alternate with double layers of sulphur atoms.

The crystal structure of the hexagonal compounds is not yet completely achieved.

Iodosulfides. Three crystal types are observed.

1) - An orthorhombic structure exists with La and Ce. It was studied with a single crystal of CeSI (3). The cell contains 8 formulas and the atoms have the following positions of the Pcab space group:

$$\pm \ (x, y, z) \pm (\frac{1}{2} +x, \ \frac{1}{2} -y, \bar{z}) \ \pm \ (x, \frac{1}{2}-y, \ \frac{1}{2} + z)$$
$$\pm \ (\frac{1}{2} +x, \ y , \ \frac{1}{2} -z)$$

with:

Ce : x □ 0, 0293   y = 0,0841   z = 0, 2426

S : x = 0, 2584   y = 0. 4759   z = 0. 4994

I : x = 0, 4061   y = 0. 1991   z = 0. 3159.

-129-

Anisotropic least-squares refinement gives a final R of 0.08. In this structure, sheets of $(CeS)_n$ alternate with double layers of iodine atoms. The sheets of $(CeS)_n$ can be considered as formed by strongly distorted tetrahedra of Ce atoms, each of them containing a sulphur atom. These tetrahedra have roughly tetragonal arrangement, each Ce atom belonging to four neighbouring tetrahedra. From this point of view, this structure has some similarity with the PbFCl-type of the fluorosulfides. But, because of the distrotion, $a \approx c \approx a'\sqrt{2}$ and $b \approx 2c'$ (the prime referring to the PbFCl-type cell).

2) - A rhombohedral structure is observed from Ce to Sm. It was studied with a single crystal of SmSI (4). The space group is R $\bar{3}$m. The elongated cell contains 2 formulas. In the corresponding hexagonal pseudo-cell, which has the parameters a_h = 4.54 Å and c_h = 32.69 Å, the atoms have the special positions 6c:

$$0\ 0\ z \text{ and } 0\ 0\ \bar{z} \text{ with } + (0\ 0\ 0\ , \ \frac{2}{3}\frac{1}{3}\frac{1}{3}\ , \ \frac{1}{3}\frac{2}{3}\frac{2}{3}\ ).$$

The parameters are: Sm : z = 0.388

I : z = 0.116

S : z = 0.302 with R = 0.08.

Initially, an alternate cell was used, monoclinic B2/m, containing 4 formulas, and related to the pseudo-hexagonal cell by

$$a_m = a_h\ \sqrt{3} \qquad b_m = \sqrt{\left(\frac{c_h}{3}\right)^2 + \left(\frac{a_h\ \sqrt{3}}{3}\right)^2} \qquad c_m \approx a_h$$

$$tg\ \gamma = \frac{c_h}{a_h\ \sqrt{3}}\ .$$

This pseudo-cell has the advantage of being more compact.

The SmSI structure can be considered from two different points of view. First, it can be regarded as an array of hexagonal layers of atoms which have the three fundamental relative positions A, B, and C. The 18 layers of the hexagonal pseudo-cell have the following positions:

I   Sm S S Sm   I I   Sm S S Sm   I I   Sm S S Sm   I

C | A BAB | C A | B CBC | A B | C ACA | B

The second way of considering this structure involves hexagonal sheets of general composition $[SmS]_n$ (surrounded in the preceding description) which alternate with double layers of iodine atoms. These sheets are formed by regular tetrahedra of Sm, which contain in their center the sulphur atoms. Each Sm atom belongs to four neighbouring tetrahedra, in such a way that it has a trigonal symmetry.

3) - A hexagonal structure is observed for the last rare earth elements (from Ho to Lu) and for Y. The flat cell contains 4 formulas. It is a new structure, characteristic of this kind of compounds, as the two preceding ones. But it is not possible, at the present time, to obtain good single crystals convenient for a structural study.

Bromosulfides. This family is the richest in the crystal types:

1) - The orthorhombic type of CeSI, observed only with the three first elements (La, Ce, and Pr), also exists with the first chlorosulfides; so this crystal structure is characteristic of the halogenosulfides of the 2 or 3 first rare earth elements. For PrSBr, which is trimorphous, this variety is obtained at the lowest temperatures, below 500° C.

-131-

2) - A monoclinic structure exists from Pr to Tb. It is studied with a

single crystal of NdSBr. Its space group is $P2_1/b$. The large cell

contains 12 formulas (5). In the case of PrSBr, it is the high temperature

γ variety, obtained by quenching from 800° C.

3) - A monoclinic structure, only observed with the third β variety of

PrSBr, is obtained at about 700° C in presence of an excess of $PrBr_3$

flux. Its space group is $P2_1/b$, and the cell contains 4 formulas (6).

4) - An orthorhombic structure is obtained for the last rare earth

elements (from Dy to Lu) and for Y. Its space group is Pmmn and the

cell contains 2 formulas. The same crystal type is equally observed

with the chlorosulfides of the last rare earth elements, and the structure

is now studied with a single crystal of ErSCl. Its identity with the

FeOCl orthorhombic structure seems quite possible.

5) - An unknown structure exists for second varieties of DySBr, HoSBr,

and YSBr which are stable at low temperature (the high temperature

varieties obtained at about 900° C have the preceding orthorhombic -

type).

The 2) and 3) monoclinic structures are not yet completely known

But they are closely related to the orthorhombic CeSI structure, as it

results from the comparison of the parameters of the 3 varieties

of PrSBr:

PrSBr α	PrSBr β	PrSBr γ
Orthorhombic	Monoclinic	Monoclinic
CeSI-type		NdSBr-type
$a = 7.08 \text{ Å}$	$c = 7.11 \text{ Å}$	$c = 7.09 \text{ Å}$
$c = 6.90 \text{ Å}$	$a = 6.91 \text{ Å}$	$b = 6.93 \text{ Å}$
$b = 13.73 \text{ Å}$	$b = 6.88 \text{ Å}$	$a = 20.94 \text{ Å}$
	$\beta = 98°48'$	$\beta = 99°18'$
$z = 8$	$z = 4$	$z = 12$

We see that the two first parameters are quite identical, and that the third parameters are exactly like the number 2, 1 and 3. So, these structures must contain nearly the same basic arrangement which is repeated 2, 1 or 3 times with only some very slight distortion. At the present time, this conception is supported by the first structure, which contains two superposed nearly identical basic arrangements. Moreover, the present state of the study of the NdSBr structure shows that superposition of three nearly identical basic arrangements, which seem closely related to the preceding one.

So, it appears that these 3 structures must contain sheets of $(LS)_n$ composition which alternate with double layers of bromine atoms; these sheets are formed by distorted tetrahedra L_4 which contain the sulphur atoms, and every L atom of the apex of the tetrahedra is shared between 4 neighbouring tetrahedra.

Conclusions. All the LSX compounds seem to have sheet-structures.

In all the known structures, the sheets are formed by tetrahedra of rare earth atoms, and have a tetragonal flat arrangement in the PbFCl-type, or distorted tetragonal arrangements in the CeSI, PrSBr β and

NdSBr types, or an exactly ternary flat arrangement in the SmSI-type. Inside these tetrahedra are the smallest non-metal atoms: fluorine in the fluoro-sulfides, sulphur in the bromo and iodosulfides. Between the sheets of $(LF)_n$ or $(LS)_n$ tetrahedra are double layers of the second non-metal [a single layer would give the $(LX)_2Y$ composition and the structures observed in the hexagonal oxysulfides $(LO)_2S$ or in the tetragonal oxytellurides $(LO)_2Te$]. With all the first rare earth elements, the second non-metal atoms have not a tetrahedral environment of metal atoms: in these cases the two non-metal atoms X and Y have very different structural behaviours. At the end of the rare earth family, although the crystal structures are not yet completely known, it seems that the two non-metals do not have such a different behaviour and can occupy nearly similar positions with tetrahedral environment of metal atoms (like in the FeOCl structure). Moreover, a more elaborate study shows that the hexagonal structure of the SmSI-type occurs in an intermediate step, between the PbFCl-like structures in which the two non-metals have highly different positions, and the more symmetrical structures in which the two non-metals have similar positions.

This evolution is especially characteristic of the fluorosulfide, bromosulfide and iodosulfide series. In the chlorosulfides, the two non-metal atoms have quite analogous sizes and electronegativities and must have similar environments of metal atoms. We shall study this last series in the near future.

- References -

1 - H. HAHN and R. SCHMID - Naturwiss. <u>16</u>, 1965, p. 475.

2 - F. THEVET - Thesis - Faculté des Sciences - PARIS 1970.

3 - J. ETIENNE - Bull. Soc. fr. Mineral. Cristallogr. <u>92</u>, 1969, p. 134.

4 - N. SAVIGNY and P. LARUELLE - Comptes Rendus - 1970.

5 - N. SAVIGNY and P. LARUELLE - to be published.

6 - M. JULIEN-POUZOL and P. LARUELLE - to be published.

7 - C. DAGRON - Comptes Rendus <u>260</u>, 1965, p. 1422.

8 - C. DAGRON - Comptes Rendus <u>262 C</u>, 1966, p. 1575.

9 - C. DAGRON and F. THEVET - Comptes Rendus <u>268</u>, 1969, p. 1867.

- Table I -

Crystal structures of the LSX compounds

| (1) | LaSI, CeSI (α) | LaSBr, CeSBr, PrSBr (α) | LaSF, CeSF, PrSF, NdSF, SmSF, GdSF, TbSF, * YSF (α), DySF, HoSF (α), ErSF (α) |

(1)
LaSI
CeSI (α)

LaSBr
CeSBr
PrSBr (α)

LaSF
CeSF
PrSF
NdSF
SmSF

(2)
CeSI (β)
PrSI
NdSI
SmSI

(4)
PrSBr (β)

GdSF
TbSF
* YSF (α)
DySF
HoSF (α)
ErSF (α)

(7)

(5)
PrSBr (γ)
NdSBr
SmSBr
GdSBr
TbSBr

(3)
GdSI
TbSI
* YSI
DySI
ErSI
YbSI
LuSI

(6)
* YSBr (β)
DySBr (β)
HoSBr (β)
ErSBr
YbSBr
LuSBr

(8)
* YSF (β)
HoSF (β)
ErSF (β)
YbSF
LuSF

		Crystal type	Spatial group
(1)	ORTHORHOMBIC	CeSI (×)	P cab
(2)	RHOMBOHEDRAL	SmSI (×)	R $\overline{3}$m
(3)	HEXAGONAL	? (×××)	?
(4)	MONOCLINIC	PrSBr (×)	P 2_1/b
(5)	MONOCLINIC	NdSBr (×)	P 2_1/b
(6)	ORTHORHOMBIC	? (×××)	P mnm ou P mn2_1
(7)	TETRAGONAL	PbFCl (××)	
(8)	HEXAGONAL	? (×××)	P $6_3$22

(×) studied on single crystal data
(××) studied on powder diffractogram
(×××) in course of work.

-136-

- Table II -

LSF compounds

	a($\overset{\circ}{A}$)	c($\overset{\circ}{A}$)	$d_{calc.}$ (g/cm^3)
TETRAGONAL	Spatial group		
PbFCl type	P 4/mmn		Z = 2
LaSF	4.04	6.97	5.54
CeSF	4.01	6.95	5.67
PrSF	3.96	6.92	5.90
NdSF	3.93	6.91	6.06
SmSF	3.87	6.88	6.49
GdSF	3.83	6.85	6.85
TbSF	3.81	6.84	7.04
YSF (α)	3.77	6.80	4.79
DySF	3.78	6.82	7.31
HoSF (α)	3.76	6.79	7.46
ErSF	3.74	6.78	7.63
HEXAGONAL	Spatial group		
	P $6_3$22		Z = 4
HoSF (β)	4.04	16.50	6.16
ErSF (β)	4.03	16.45	6.28
YbSF	3.99	16.39	6.58
LuSF	3.97	16.37	6.73
YSF (β)	4.05	16.51	3.97

- Table III -

LSBr compounds

	a($\overset{\circ}{A}$)	b($\overset{\circ}{A}$)	c($\overset{\circ}{A}$)		$d_{calc.}$ (g/cm^3)
ORTHORHOMBIC CeSI-type	Spatial group P cab				Z = 8
LaSBr	7.19	13.99	7.02		4.74
CeSBr	7.12	13.82	6.94		
PrSBr (α)	7.08	13.73	6.90		5.01
MONOCLINIC	Spatial group P $2_{1/b}$			γ	Z = 4
PrSBr (β)	6.92	6.88	7.11	98°48'	5.10
MONOCLINIC	Spatial group P $2_{1/b}$			γ	Z = 12
PrSBr (γ)	20.94	6.93	7.09	99°18'	4.96
NdSBr	20.82	6.91	7.05	99°16'	5.10
SmSBr	20.58	6.86	7.01	99°19'	5.35
GdSBr	20.39	6.81	6.96	99°14'	5.62
TbSBr	20.25	6.77	6.89	99°20'	5.79
ORTHORHOMBIC	Spatial group P mnm (ou P mn2$_1$)				Z = 2
DySBr	5.35	8.08	4.02		5.24
HoSBr	5.34	8.09	4.03		5.28
ErSBr	5.32	8.08	4.01		5.39
YbSBr	5.27	8.07	3.97		5.60
LuSBr	5.27	8.07	3.95		5.67
YSBr	5.35	8.09	6.06		3.79

- Table IV -

LSI compounds

	a(A)	b(A)	c(A)		$d_{calc.}$ (g/cm^3)
ORTHORHOMBIC CeSI-type	Spatial group P cab				Z = 8
LaSI	7.38	14.57	7.10		5.18
CeSI (α)	7.33	14.35	7.05		5.36
RHOMBOHEDRAL SmSI-type	Spatial group R $\overline{3}$m			α	Z = 2
CeSI (β)	11.26			23°53'	4.80
PrSI	11.24			23°46	4.88
NdSI	11.22			23°40'	5.01
SmSI	11.20			23°23'	5.27
HEXAGONAL	Spatial group ?				Z = 4
GdSI	10.73		4.24		4.98
TbSI	10.66		4.20		5.11
DySI	10.64		4.16		5.23
ErSI	10.61		4.13		5.39
YbSI	10.55		4.09		5.60
LuSI	10.53		4.05		5.70
YSI	10.64		4.16		4.03

ELECTRON-DIFFRACTION STUDIES ON THIN FILMS of Sm_2O_3

C. Boulesteix,* P. E. Caro,** M. Gasgnier,**
C. Henry La Blanchetais,** and B. Pardo*

* Institut d'Optique, Orsay - France

** Laboratoire des Terres-Rares du C.N.R.S., Bellevue-

0920 France

Centre National de la Recherche Scientifique Bellevue (France). Laboratoire des Terres Rares

190

ABSTRACT

Samarium metal thin films were oxidized to $C-Sm_2O_3$. By heating, $C-Sm_2O_3$ recrystallizes into large crystals of $B-Sm_2O_3$. The crystals are all almost perpendicular to the $[10\bar{1}]$ direction of the monoclinic B-type unit cell. The plane of the film is $(20\bar{1})$. The crystals exhibit twins with respect to the planes $\{111\}$ and $\{313\}$. The $(20\bar{1})$ plane is the basal plane for the $(LnO)_n^{n+}$ packing of OLn_4 tetrahedra in B-type Ln_2O_3 which is a slight deformation of A-type Ln_2O_3. Twinning is easily explained on the basis of the close connection to $A-Ln_2O_3$.

Large thin single crystals (between 500 $\overset{o}{A}$ and 1,500 $\overset{o}{A}$ thick) of samarium sesquioxide Sm_2O_3 were grown by oxidation of thin films of vacuum-deposited samarium metal. Oxidation of samarium metal and the formation of the large crystals were detected when attempts were made to observe thin films of samarium metal in the electron microscope (1), (2).

The samarium is oxidized by heating under dynamic vacuum (10^{-5} mm Hg). C-type oxide is made first. Formation of C-type Ln_2O_3 has been observed on thin films of erbium, holmium, and dysprosium metals (3), (4). In the case of samarium, by heating above 800° C, germs of the monoclinic well known B-type, stable at high temperature, are created, and large crystals develop quickly from the small C-type crystals. Formation of large crystals on a phase transition in a thin film is a general phenomenon for polymorphic

materials (it does occur for instance for ytterbium metal (5). **The**
B-type crystals keep their structure by returning to room temperature.
Their size is several dozens of microns; i.e., more than one hundred
times their thickness. This is attributed to the initial small number
of seeds.

I - STRUCTURE AND ORIENTATION OF THE CRYSTALS

It is ordinarily difficult to know the structure and the orientation of
the crystals because they have numerous plane defects. However,
we observed a crystal (plate 1) with an exceptionally small amount

Plate 1.

of defects. By tilting the plane of the thin film a few degrees, the electronic beam was brought along a main crystallographic direction as shown by the appearance of the extinction. The points of the diffraction diagram (plate 2) were indexed (fig. 1). The corresponding
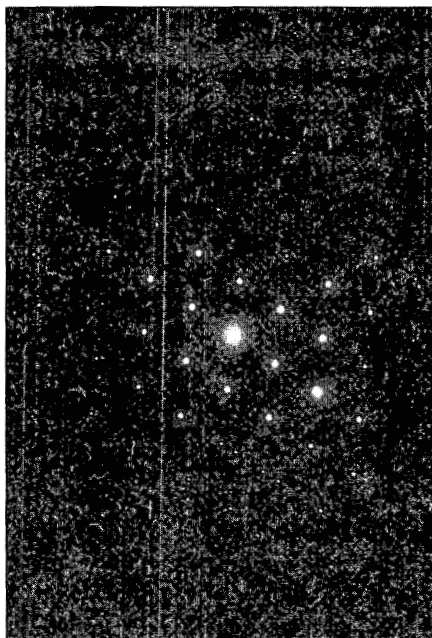
Plate 2.

crystallographic planes all have the $[10\bar{1}]$ direction in common, which is the direction of the electron beam. A simple geometric drawing (fig. 2) shows that the angle between the normal to the plane $(20\bar{1})$ and the direction $[10\bar{1}]$ is close to $3°$; this being the tilting angle to bring the electronic beam along $[10\bar{1}]$. The plane of the thin film is accordingly the plane $(20\bar{1})$. That orientation being systematic, the plane must be a special one in the $B\text{-}Sm_2O_3$ structure.

-142-

This is in accordance with a previous theoretical work by one of us (6). The B-Ln_2O_3 structure is derived from the A-Ln_2O_3 structure. The A-type structure is characterized by a complex cation $(LnO)_n^{n+}$, corresponding to a packing of OLn_4 tetrahedra sharing edges, which is a bi-dimensional entity perpendicular to the c-axis in the hexagonal A-type.

A very small displacement of the $(LnO)_n^{n+}$ units with respect to one another destroys the hexagonal symmetry and yields the monoclinic B-Form as shown (fig. 3). The plane of the $(LnO)_n^{n+}$ group is then the $(20\bar{1})$ plane of the B-monoclinic structure. The former c-axis in the A-Form is now the monoclinic $[10\bar{1}]$ direction. We see that the thin films crystals develop parallel to the $(LnO)_n^{n+}$ group basal planes. We consider this to be a proof of the importance of that entity in rare earth oxide crystal structures.

II - TWINNING

The crystals are twinned along planes almost perpendicular to the surface of the film. By tilting the crystal one finds that twin planes always contain the $[10\bar{1}]$ direction.

By doing a microdiffraction on both crystals on each side of the twin plane, the symmetry which describes the twin can be found. We were able to determine two types of twins. One is characterized on the diffraction pattern by a symmetry with respect to the directions [111] or $[1\bar{1}1]$ in reciprocal space, which means a symmetry in real space with respect to the planes (111) or $(1\bar{1}1)$. The diagram on plate no. 4
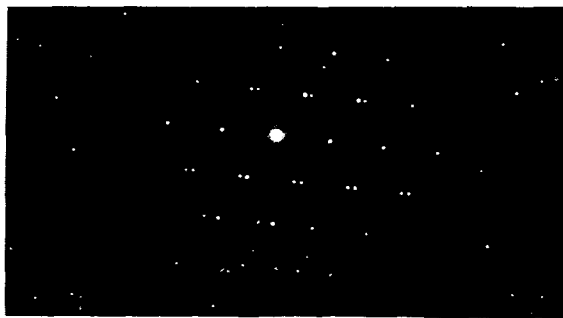
Plate 4.

is associated with the microdiffraction of the zone on plate no. 3.
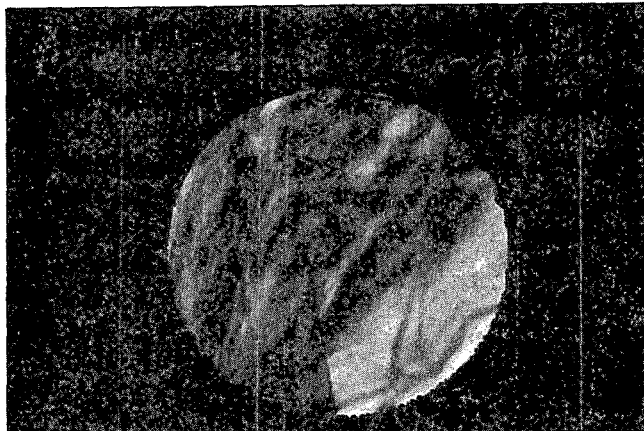
Plate 3.

The measure of the rotation of the image in the microscope under the magnitude used shows that the contact plane is (111) itself. That first type of twinning is extremely frequent in our crystals.

But a second type is also common. In the same conditions as above, the diffraction pattern is characterized by a symmetry with respect to the directions $[313]$ or $[3\bar{1}3]$ in reciprocal space (symmetry with respect to planes (313) or $(3\bar{1}3)$ in real space). Plate no. 5 is for a crystal having $(1\bar{1}1)$, (313) and $(3\bar{1}3)$ as planes of twinning. Diffraction pattern on plate no. 6 represents the micro diffraction on each side of the plane of twinning, $(3\bar{1}3)$. Plate no. 7 represents twinning with respect to $(3\bar{1}3)$.

We consequently observe two systems of twinning along planes $\{111\}$ and $\{313\}$ which all have the direction $[10\bar{1}]$ in common.

-144-
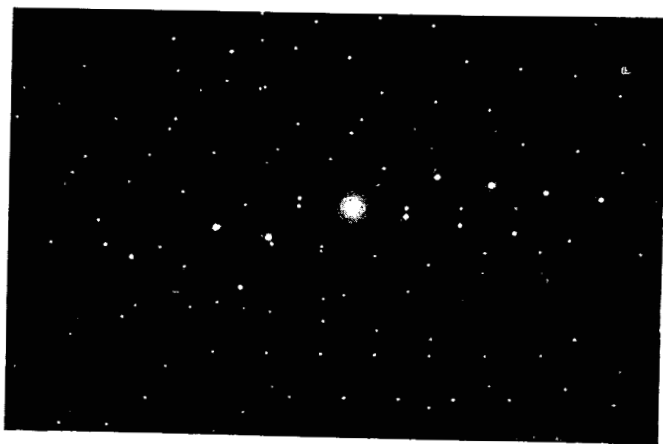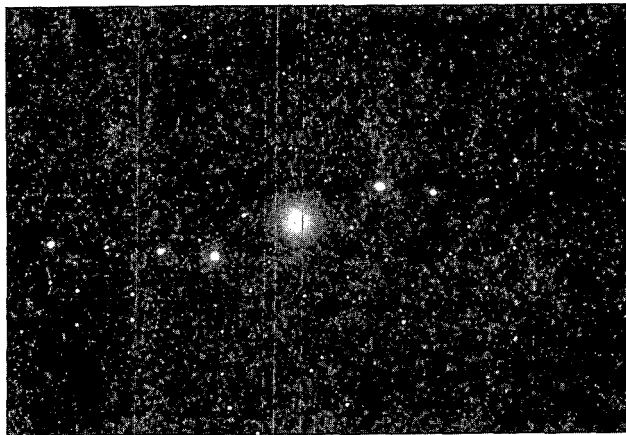
Plate 5.

Plate 6.

Plate 7.

The twinnings observed can be easily explained in terms of the close relationship between the $A-Ln_2O_3$ type and the $B-Ln_2O_3$ type as exhibited on fig. 3. The B-structure derives from the A-structure by a glide of the $(LnO)_n^{n+}$ groups, along a $[01\bar{1}0]$ direction of the hexa-gonal. But there are three equivalent such directions, the other ones being $[10\bar{1}0]$ and $[1\bar{1}00]$. If we look at the B-structure as a super-position of hexagonal nets slightly displaced with respect to one another along one of those directions as in fig. 4, it is immediately obvious that the connection of crystalline blocks corresponding to different glide directions will generate twin planes $\{313\}$ and $\{111\}$

Twinning is, consequently, in accordance with the $(LnO)_2O$ type of structure proposed for B-type Ln_2O_3.

Sustained electronic beam impact can produce holes in the thin films. These holes have regular geometric shapes with contours parallel to the (202), (111), and (1$\bar{1}$1) planes of the monoclinic structure. The contours are then parallel to the sides of the basal plane of the OLn_4 tetrahedron in the $(LnO)_n^{n+}$ group. The electron beam produces heating (because of the insulating character of the material) and it is suggested that the holes express the departure of the gaseous molecule LnO from the $(LnO)_n^{n+}$ groups.

-146-

A feature visible on plate 7 was not interpreted. In the direction
[202], supplementary points are observed which correspond to an
interplanar distance triple of the normal one. This may correspond
to a superstructure or some kind of regular disorder phenomenon.
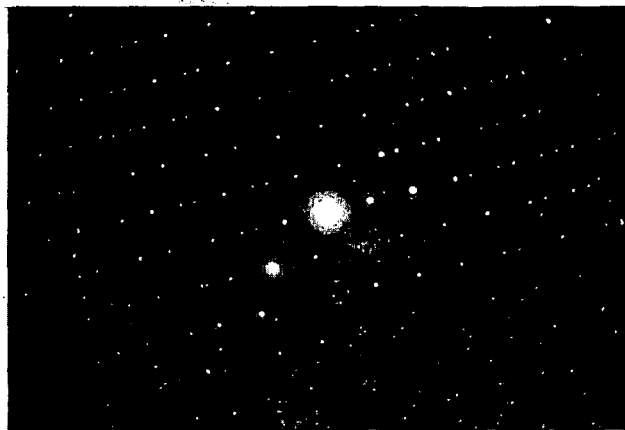
Plate 8.

REFERENCES

(1) C. BOULESTEIX, M. GASGNIER, C. HENRY LA BLANCHETAIS
   and L. VALIERGUE Colloque International du C. N. R. S. sur
   les Elements des Terres Rares Paris, Mai 1969 (to be published).

(2) C. BOULESTEIX, M. GASGNIER, C. HENRY LA BLANCHETAIS
   and L. VALIERGUE (to be published).

(3) L. E. MURR, Phys. Stat. Sol. , 24, 135, (1967).

(4) H. P. SINGH and O. N. SRIVASTAVA, Phil. Mag. , 19, (161),
   1079, (1969).

(5) C. BOULESTEIX, M. GASGNIER, C. HENRY LA BLANCHETAIS
   and L. VALIERGUE Thin Solid Films No. 1, (1970).

(6) P. E. CARO, J. Less Common Metals, 16, 367, (1968).

-147-
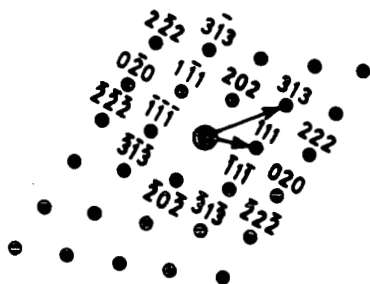
Figure I

Electron diffraction diagram of a thin crystal of monoclinic $B-Sm_2O_3$ when the electronic beam is along the direction $[10\bar{1}]$. If the crystal is twinned with twin planes (111) or (313), the pattern in the twinned zone is deduced from the one above by a symmetry with respect to the corresponding directions.
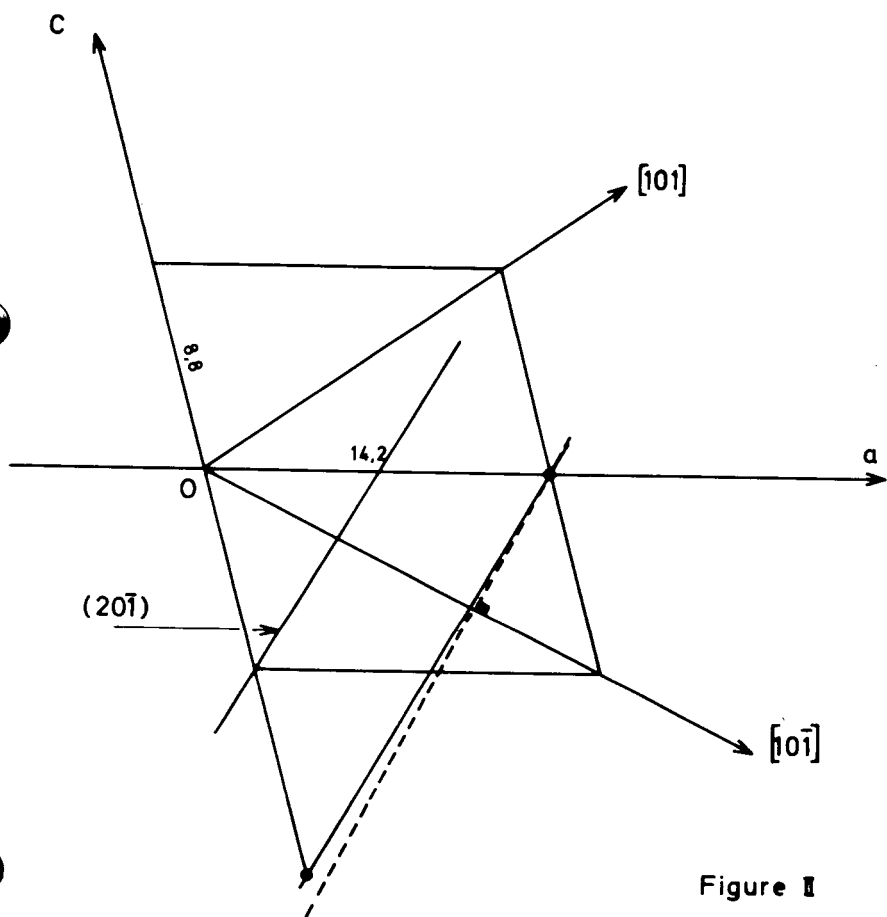
Figure II

Position of the directions [101] and [10$\bar{1}$] in the real unit cell of monoclinic Sm_2O_3. Plane of paper contains axis a and c. The trace of the plane (20$\bar{1}$) is shown and as a dashed line the trace perpendicular to [10$\bar{1}$].

[1̄100]

C AXIS HEXAGONAL

$(MO)_n^{n+}$

$(MO)_n^{n+}$

$(MO)_n^{n+}$

O IN PLANES 0-1

M IN PLANES 0-1

O IN PLANE 1/2
+
O IN PLANE 1/2
WITHIN $(MO)_n^{n+}$
SHEETS

M IN PLANE 1/2

(A)

1Å

$\underline{a}$

$(MO)_n^{n+}$

Plane parallel

to $(20\bar{1})$

$(MO)_n^{n+}$

-150-

$(MO)_n^{n+}$

(B)

1Å

$\underline{c}$
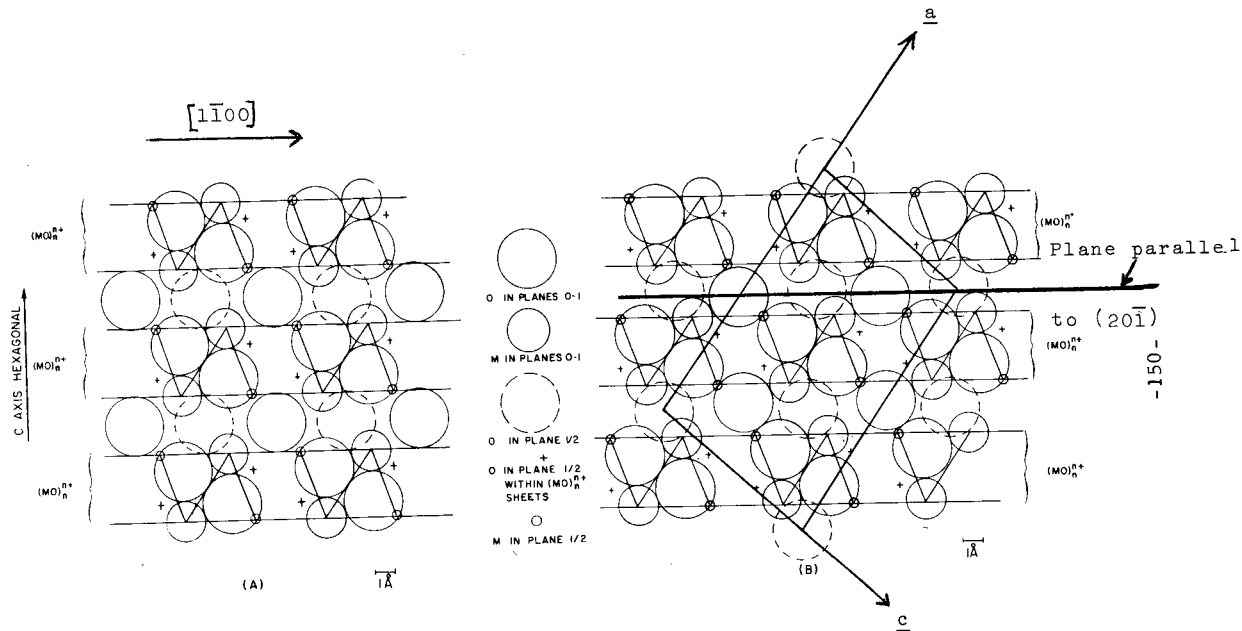
Fig. 3. a) Hexagonal A-M_2O_3 structure; plane of paper is parallel to (110). b) Monoclinic B-M_2O_3 structure; plane of paper is perpendicular to the $\underline{b}$ monoclinic axis. Projection of the unit cell is outlined.

(A)
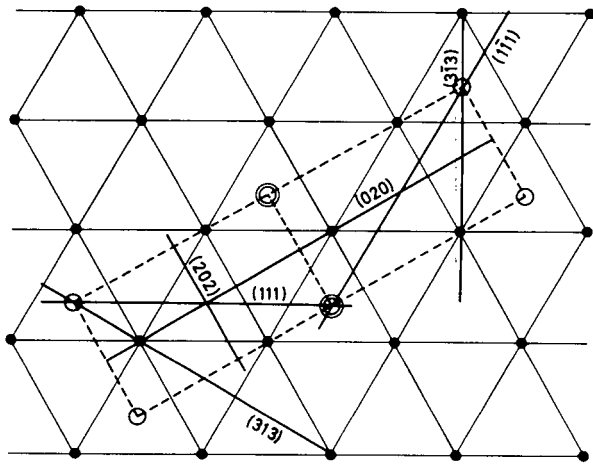
Fig. 4 - A : Projection of an ideal monoclinic B-Ln$_2$O$_3$
unit cell in the hexagonal lattice of
A-Ln$_2$O$_3$. Plane of paper is parallel to
(20$\bar{1}$)(monoclinic). Traces of perpendicular
planes of interest are indicated (mono-
clinic indices).

B : Displaced hexagonal lattices showing two
types of twinning in B-Ln$_2$O$_3$. O is above
the plane of paper ● in the plane ⊙ under,
(displacement is greatly exaggerated).

(B)

-151-
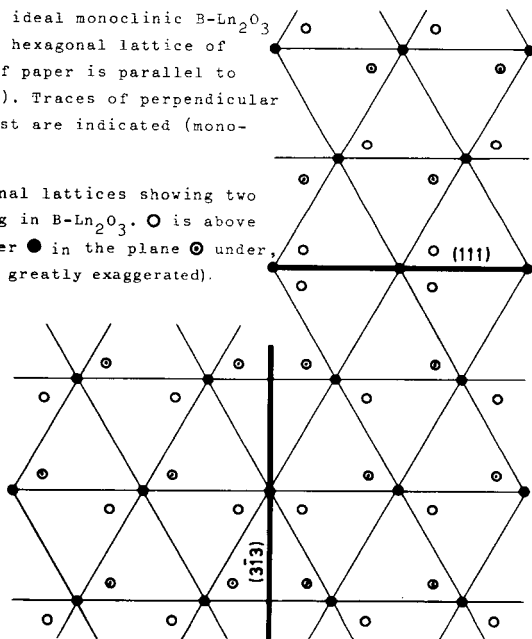
REACTIONS OF THE SESQUIOXIDES OF Pm, Nd, AND Sm WITH WATER

Harold T. Fullam and Frank P. Roberts

Battelle-Northwest, Richland, Wash~~ington~~. *Pacific Northwest Lab.*

115 800

Abstract

The reactions of Pm_2O_3, Nd_2O_3, and Sm_2O_3 with water were investigated. Thermograms were obtained for the reaction products, as well as for the hydroxides of Pm, Nd, and Sm prepared by precipitation techniques. The solubility and dissolution rates of Pm_2O_3 in distilled water and synthetic sea water were determined.

Introduction

A program has been underway at the Pacific Northwest Laboratory (PNL)* for a number of years to develop the technology of promethium. One major phase of the program has involved the preparation of high purity promethium sesquioxide (Pm_2O_3), determination of its chemical and physical properties, and development of possible applications for the oxide.

One potential use of Pm_2O_3 is as fuel in radioisotope heat sources If Pm_2O_3 is used in this application, safety considerations dictate the assurance of adequate containment of the oxide under all foreseeable conditions. One possible environment which the source may encounter is exposure to water. Under such a circumstance, adequate containment of the fuel must be assured by either the integrity of the oxide cladding or by the low solubility or slow dissolution rate of the oxide in the water environment. This requirement led to a study of the solubility and dissolution rate of Pm_2O_3 in fresh and synthetic sea water, and to an attempt to define the mechanism by which the oxide reacts with water. The study was expanded to include the reactions of Sm_2O_3 and Nd_2O_3 with water as well. (It should be noted at this point that all Pm_2O_3 sources contain varying amounts of Sm_2O_3 due to radiolytic decay.) This paper summarizes the results of the study.

Dissolution Rates of Promethium Oxide

Several experiments were performed to observe the dissolution of Pm_2O_3 in water. The objective was to ascertain if any reliance could be placed on low dissolution rates to minimize the spread of radioactivity in the event the integrity of the cladding material was lost when the source was immersed in water. As will be seen in the following discussion, dissolution rates of compact Pm_2O_3 are reasonably low but after relatively short times the compacts disintegrate resulting in rapid dissolution limited only by the solubility.

Compact Sources of Pm_2O_3: Tests were carried out to measure the dissolution of compacted Pm_2O_3 pellets in distilled water and in synthetic sea water. Both low density and high density pellets were tested.

Pellets prepared by cold pressing Pm_2O_3 and sintering at 1400°C resulted in compacts of 84% of theoretical density while hot pressing at 1700°C gave compacts of > 95% of theoretical density. The Pm_2O_3 used contained $\sim$ 2.5% Sm_2O_3 as the result of the decay of ^{147}Pm.

The test procedure was to place the Pm_2O_3 pellet of known surface area in a small glass vessel fitted with a glass frit at the exit and to flow either distilled water or synthetic sea water[1] through the vessel at a uniform rate. The effluent was collected in a graduated cylinder and the time required to collect a measured volume was noted. The amount of ^{147}Pm collected was determined by beta counting. The rate of dissolution per cm^2 of pellet surface area could then be calculated.

The duration of each test was at least 8 hours with measurements taken at 1-hour intervals. At the conclusion of the tests the flow of water was terminated and the pellets were left immersed in the water, and their behavior was observed.

The results obtained are presented in Tables I and II.

Table I: Dissolution Rates of Pm_2O_3 Pellets in Distilled Water

Time, hrs	Dissolution Rate, µg/cm²/hr	
	Low Density Pellets	High Density Pellets
1	4.0	12.1
2	3.7	12.1
3	3.5	12.6
4	4.0	11.7
5	3.8	11.8
6	3.5	11.9
7	3.0	12.1
8	4.5	11.8

Table II: Dissolution Rates of Pm_2O_3 Pellets in Sea Water

Time, hrs	Dissolution Rate $\mu g/cm^2/hr$	
	Low Density Pellets	High Density Pellets
1	0.06	0.51
2	0.05	0.57
3	0.05	0.60
4	0.04	0.58
5	0.04	0.58
6	0.05	0.53
7	0.05	0.57
8	0.03	0.57

The high density pellets developed cracks after approximately 48 hours immersion and during the following 3 days completely disintegrated. The low density pellets showed no indication of disintegration until the fifth day. At that time cracks formed and the pellets began to fall apart. In both cases the disintegration resulted in the formation of very fine crystalline particles.

Powdered Pm_2O_3: Experiments to measure the dissolution rate of powdered Pm_2O_3 were limted to batch equilibrations in which a small amount of Pm_2O_3 was placed in water, stirred, and sampled periodically. Three samples of Pm_2O_3 prepared by calcining promethium oxalate at 700°, 850°, and 1000°C were placed on glass filters and washed with CO_2 free water. About 25 mg of each was placed in 150 ml of CO_2^- free water in a closed glass vessel thermostated at 25 ± 0.1°C. The mixture was agitated by means of a magnetic stirrer and sampled periodically. The samples were centrifuged to remove the solids, and the [147]Pm content was determined by beta counting.

The results given in Table III show the promethium in the supernate quickly reaches a limiting value. The values are much higher than would be predicted from the solubility of Pm_2O_3 (discussed in the next section) and may be attributed to the formation of a colloid which is not removed by centrifuging.

Table III: Dissolution of Pm_2O_3 Powder

Time, hrs	Pm_2O_3 calcined at 700°C	Pm_2O_3 calcined at 850°C	Pm_2O_3 calcined at 1000°C
	Pm Concentration in Solution mg/l		
0.5	19	28	28
1.0	18	28	29
5.5	20	30	31
55	20	30	30
80	25	31	30
104	21	32	31

Solubility of Pm_2O_3 in Water

Hydrous Promethium Hydroxide: It has long been recognized that the basicities of the rare earths decrease with increasing atomic numbers.[2] The solubility of Pm(III) would therefore be expected to lie between Nd(III) and Sm(III). To verify this assumption the solubility product of Pm(III) in water was measured using the titrimetric method described by Moeller.[3]

In this technique a solution containing a known amount of the rare earth is titrated with a standard base using a pH meter to observe the pH after each increment of base added. If the reaction

$$Pm^{+3} + 3OH^- = Pm(OH)_3 \text{ (solid)}$$
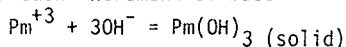
is assumed, the Pm(III) in solution can be estimated from the titration curve, and the hydroxyl ion concentration is given by the pH.

An apparent solubility product is given by:

$$K = [Pm^{+3}] [OH]^3.$$

For our measurements a 0.100M solution of Pm(III) was prepared by dissolving a weighed amount of Pm_2O_4 in a slight excess of perchloric acid and diluting to a measured volume. Aliquots of this were titrated with standardized 0.1M sodium hydroxide in a thermostated vessel held to within ± 0.2°C of the desired temperature. After each increment of base added the mixture was stirred 10 minutes with a magnetic stirrer and the pH measured with a glass electrode. Titrations were carried out at 10, 20, 30, and 40°C. In addition to the measurements with Pm(III), titrations were made with Nd(III) and Sm(III) under identical conditions.

Figure 1 shows the data obtained. As expected, the values for Pm(111) are between those for Nd(111) and Sm(111). Increasing the temperature gives lower apparent solubility products which agrees with the observations made by Meloche.[4]

.Solubilities based on these apparent solubility products calculated from the equation

$$S = \sqrt[4]{K/27}$$

are given in Table IV.

Table IV: Solubilities of Rare Earth Hydroxides

Temperature °C	Solubility, M X 10^6		
	Nd	Pm	Sm
10	5.7	3.5	2.7
20	3.9	2.8	2.0
30	2.8	1.8	1.5
40	2.0	1.4	1.1

The data obtained by this titrimetric method only give, at best, a measure of the relative solubility of the freshly precipitated solid formed on reaction with hydroxyl ions. Further experiments were carried out to get solubilities for the reaction product of anhydrous promethium oxide and water. These were done by equilibrating Pm_2O_3 with water for extended time periods and measuring the ^{147}Pm in solution. The equilibration was done in a closed thermostated vessel to prevent absorption of carbon dioxide from the atmosphere. The Pm_2O_3, prepared by ignition of promethium oxalate at 900°C, was washed exhaustively with carbon dioxide - free water. About 0.5 g was placed in the vessel with 400 ml water and mixed continuously with a magnetic stirrer. The temperature was held at 20 ± 0.2°C. Periodically samples were removed and filtered. The ^{147}Pm content was determined by beta counting aliquots of the filtrate.

Samples taken during the first 48 hours contained a colloidal dispersion which passed through the filter and gave high values. After 7 days agglomeration had occurred and fairly reproducible results were obtained. A value for the solubility, based on ten measurements, of 5.3 X $10^{-7}\underline{M}$ ± 30% was obtained.

Hydrolysis of Rare Earth Oxides

As stated previously, when a compacted shape of Pm_2O_3 is contacted with water the shape cracks and disintegrates in a relatively short time even though the dissolution rate is very slow. Given sufficient time the oxide ends up as finely divided particles dispersed throughout the system. Compacted shapes of Nd_2O_3 and Sm_2O_3 exhibit the same type of reaction with water. In fact, Nd_2O_3 and Sm_2O_3 shapes exposed to atmospheric moisture will, given sufficient time, disintegrate in the same way. Pm_2O_3 shapes, however, do not appear to react with atmospheric moisture at any appreciable rate, perhaps because of the heat of radioactive decay.

The disintegration of the compacted shape by reaction with water results in a large increase in volume. If oxide enclosed in a container is contacted with water, the resultant swelling of the oxide can result in the destruction of the container. Figure 2-A shows a Haynes 25 capsule which originally contained Sm_2O_3 at 90% of theoretical density. A small hole was drilled in one end of the capsule, and the capsule placed in water. After several days, swelling of the oxide was sufficient to rupture the capsule at the end opposite to where the hole had been drilled. Figure 2-B shows a stainless steel capsule which originally contained Pm_2O_3 at 50% of theoretical density. Pressure generated when the oxide was contacted with water was sufficient to swell the capsule but not rupture it. If the initial oxide density had been higher, the capsule would undoubtedly have ruptured.

These data show that containment of the promethium oxide must be assured through the integrity of the heat source cladding, even though the dissolution rate in water is very slow.

In general, it can be stated that Nd_2O_3 will react with water at the fastest rate, Sm_2O_3 at the slowest rate, while Pm_2O_3 reacts at an intermediate rate. Qualitative data on the rates at which compacted shapes of the three oxides react with water are shown in Table V. The data were obtained by placing oxide pellets in water and watching for the first visible evidence of cracking. Reproducibility of results was quite poor, and the data are presented only to show the trend of lowered rate of reactivity with water from Nd_2O_3 to Sm_2O_3.

A number of factors affect the rate at which the oxides react with water or water vapor. They include:

- the oxide species under consideration,
- the oxide crystal structure,
- the temperature at which the oxide is calcined prior to exposure to water, and
- the water temperature.

Table V: Disintegration of Oxide Pellets in Water

Oxide	Method of Preparing Pellets	Initial Pellet Density,% of theoretical	Time to Initial Evidence of Disintegration
Nd_2O_3	Sintered at 1500°C	94-95%	4-12 hours
Nd_2O_3	Hot Pressed at 1700°C	95-96%	4-12 hours
Pm_2O_3	Sintered at 1400°C	84%	5 days
Pm_2O_3	Hot Pressed at 1700°C	95%	48 hours
Sm_2O_3	Sintered at 1500°C	95-96%	10-20 days
Sm_2O_3	Hot Pressed at 1700°C	96-97%	8-20 days

Space limitations do not permit a detailed discussion of all of these factors, but Figures 3, 4, and 5 demonstrate typical effects one can expect. Figure 3 shows the rate at which samples of Nd_2O_3 and Sm_2O_3 react with atmospheric moisture. Under similar conditions Pm_2O_3 does not react appreciably, perhaps because of the heat of radioactive decay. Figure 4 shows data for the rates of reaction of Pm_2O_3, calcined at various temperatures, with water. The data were obtained by exposing the oxide to water for varying periods of time, drying at 100°C, and then determining the water content by thermogravimetric analysis. As one would expect, oxide calcined at the highest temperature exhibits the slowest rate of reaction. When Nd_2O_3 calcined at various temperatures was exposed to atmospheric moisture, the rates of reaction shown in Figure 5 were obtained. In this case it is interesting to note that the reaction rate increased with increased calcining temperatures. The difference in temperature effect between Pm_2O_3 and Nd_2O_3 probably results from the different structures of the two oxides, the Pm_2O_3 being monoclinic and the Nd_2O_3 hexagonal.

Several experiments were carried out to try to determine the products formed when the three oxides react with water. Thermogravimetric analyses was carried out on the various reaction products using a Cahn electrobalance and a Moseley X-Y recorder. Figure 6 shows typical thermograms for Nd_2O_3 and Sm_2O_3 which had been equilibrated with atmospheric moisture. In each case the reaction product appears to be a compound with the empirical formula $R_2O_3 \cdot 3H_2O$. The water in excess of three moles per mole of oxide is apparently adsorbed water and is not part of the compound structure. X-ray diffraction analysis indicates the two products are not hydroxides--$R(OH)_3$[5,6]--but rather hydrated oxides of some type. The hydrated Nd_2O_3 exhibits a slightly greater temperature stability than the Sm_2O_3 product, as well as a more complex dehydration curve.

Figure 7 shows typical thermograms for the oxides of Nd, Pm, and Sm after equilibration with water. For Nd, the thermogram indicates

a more complex structure (empirical formula $Nd_2O_3 \cdot 5H_2O$) than was obtained with Nd_2O_3 exposed to atmospheric moisture. The thermogram for Pm is less well defined than those obtained with Sm and Nd. However, the equilibrium product appears to have the empirical formula $Pm_2O_3 \cdot 3H_2O$. Again, X-ray diffraction analysis shows the products do not have the typical hydroxide structure, but rather are probably hydrated oxides.

When Nd, Pm, and Sm were precipitated from nitric acid solutions with sodium hydroxide, the products obtained, after washing and drying, gave much more complex thermograms than those obtained by reacting the corresponding oxides with water (see Figure 8). The empirical formulas for the three products are $Nd_2O_3 \cdot 9H_2O$, $Sm_2O_3 \cdot 7H_2O$, and $Pm_2O_3 \cdot 5H_2O$. Again, Pm gives a less well defined thermogram than either Sm or Nd. X-ray diffraction analysis of each product indicates the basic structures corresponds to the hydroxide $R(OH)_3$ with a number of extraneous lines which could be identified. Unfortunately, time and budget limitations did not permit a more detailed study to determine the exact structures of the various reaction products or the intermediate compounds formed during dehydration.

In comparing the thermograms for the three neodymium reaction products under consideration (see Figure 9) it is interesting to note that the products appear distinctly different. In addition, intermediate compounds formed during dehydration of the various products show little, if any, similarity. Similar differences were noted for the three samarium products and the two promethium products.

One general similarity was noted for the various products formed between Nd, Sm, and Pd and water. In each case a temperature of approximately 800°C was required to convert the material to the anhydrous oxide.

One other factor concerning the reaction of the oxides with water should be mentioned. Limited data obtained with Nd_2O_3 indicate that when the oxide reacts with atmospheric moisture, intermediate compounds are not formed. Instead, each molecule of oxide reacts to form the equilibrium product $Nd_2O_3 \cdot 3H_2O$. This can be seen from the data presented in Figure 10, in which it is readily apparent that the thermograms for oxide, not at equilibrium with atmospheric moisture, show the same structural detail as oxide at equilibrium.

References

1. May, T. P. and A. T. Alexander, Proc. A.S.T.M. 50, 1131-41 (1950).
2. Moeller, T. and H. E. Kremers. Chem. Rev. 37, 97-159 (1945).
3. Moeller, T. and H. E. Kremers. J. Phys. Chem. 48, 395-405 (1944).
4. Meloche, C. E. and F. Vratny. Anal. Chim. Acta 20, 415-19 (1959).
5. Fricke, R. and Seitz, A. Z Anorg. Chem. 254 (9), 107-115 (1947).
6. Roy, R. and McKinstry, H. A. Acta Cryst. 6 (4), 365-66 (1953).
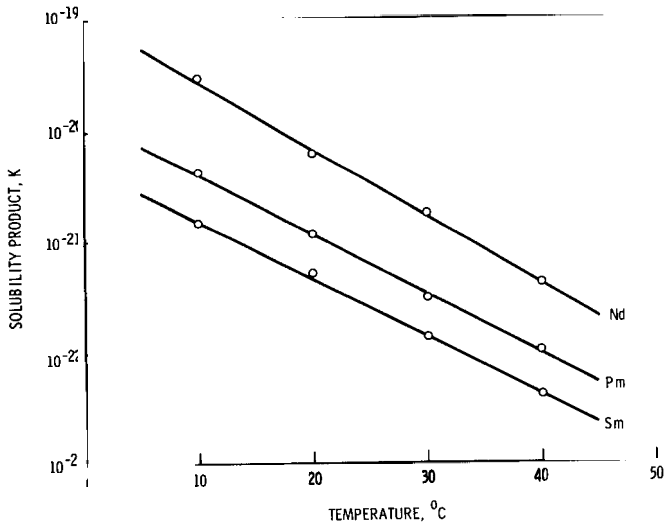
FIGURE 1. SOLUBILITY OF RARE EARTH HYDROXIDES
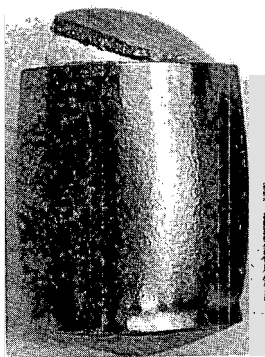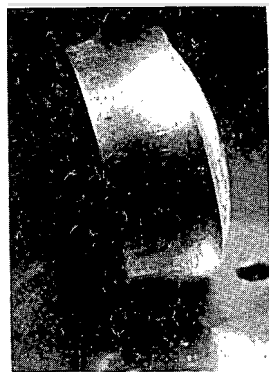
(A) Sm_2O_3 CAPSULE (B) Pm_2O_3 CAPSULE

FIGURE 2. CAPSULES CONTAINING RARE EARTH OXIDES AFTER EXPOSURE TO WATER
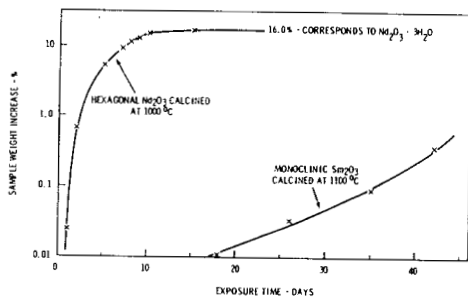
FIGURE 3. REACTION RATES OF RARE EARTH OXIDES WITH ATMOSPHERIC MOISTURE
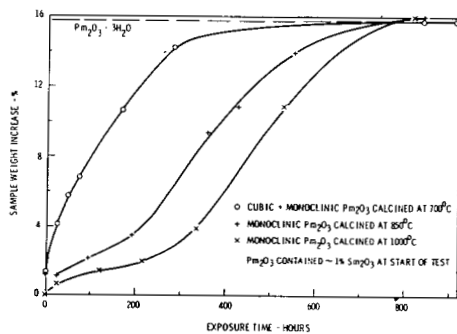
FIGURE 4. REACTION OF Pm_2O_3 WITH WATER AT 25 °C
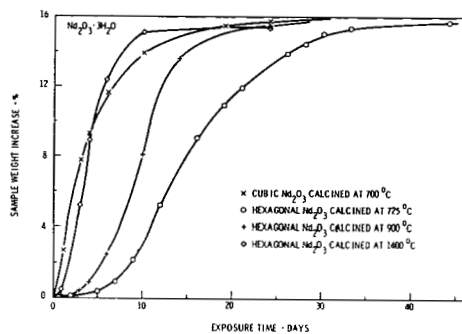
FIGURE 5. EFFECT OF CALCINING TEMPERATURE ON THE RATE OF REACTION OF Nd_2O_3 WITH ATMOSPHERIC MOISTURE

-161-
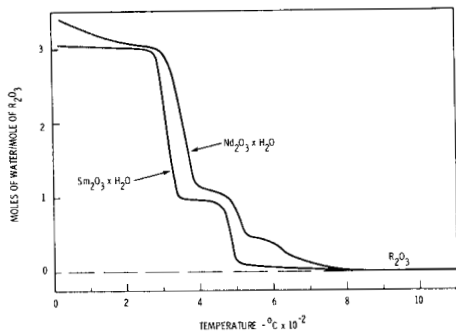
FIGURE 6. THERMOGRAMS FOR Nd_2O_3 AND Sm_2O_3 EQUILIBRATED WITH ATMOSPHERIC MOISTURE
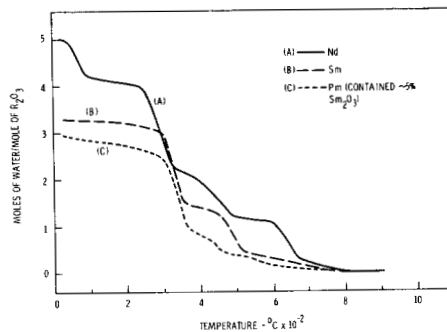
FIGURE 7. THERMOGRAMS FOR THE OXIDES OF Nd, Pm AND Sm EQUILIBRATED WITH WATER
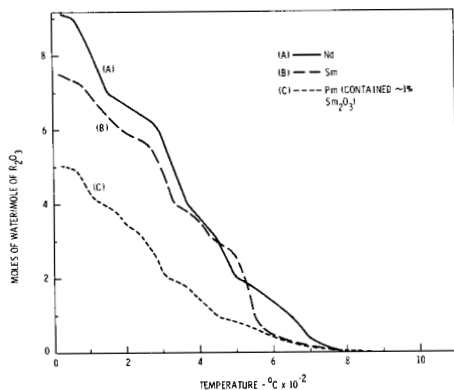
FIGURE 8. THERMOGRAMS FOR Nd, Pm AND Sm PRECIPITATED FROM SOLUTION WITH NaOH
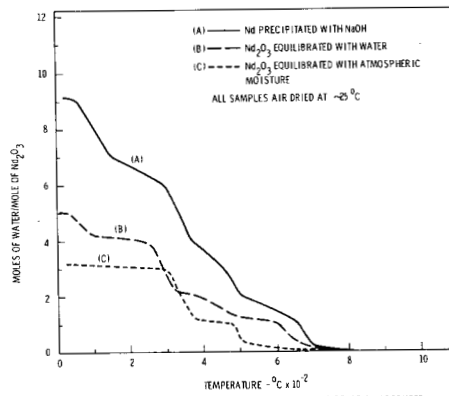
FIGURE 9. COMPARISON OF THERMOGRAMS FOR $Nd_2O_3 \cdot H_2O$ REACTION PRODUCTS
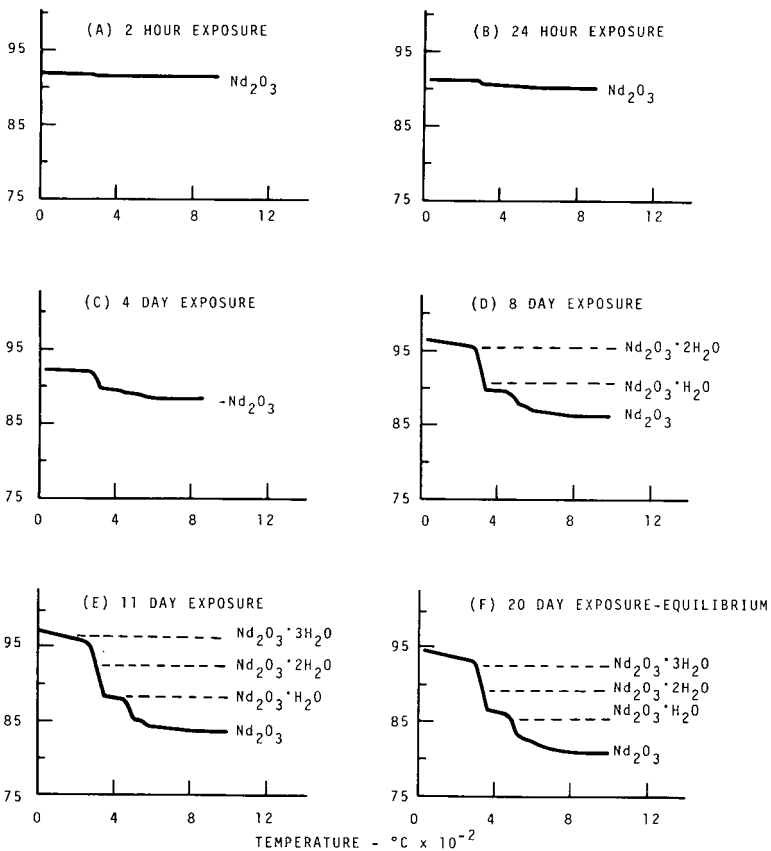
FIGURE 10. THERMOGRAMS FOR Nd_2O_3 EXPOSED TO ATMOSPHERIC MOISTURE FOR VARYING PERIODS OF TIME

-163-

COMPLEXES OF THE RARE EARTH SESQUIOXIDES WITH
DIVALENT EUROPIUM OXIDE*

Edward Catalano and Bettie L. Shroyer

University of California, Lawrence Radiation Laboratory

Livermore, California

William O. J. Boo

Department of Chemistry, University of Mississippi

University, Mississippi

"Abstract"

Eu_3O_4, $EuGd_2O_4$, and $EuDy_2O_4$ are known orthorhombic complexes
having interesting cooperative magnetic transitions. [1-3] We have
surveyed the lanthanon sesquioxide-divalent europium oxide complexes
to see if a homologous series of orthorhombic stable complexes form.
Such a homologous series of complexes would provide valuable
magnetic data and also data relating to the stability of the divalent
states of lanthanon ions. Results on the preparations and structures
of the various complexes are presented.

Introduction

Eu_3O_4, $EuGd_2O_4$, and $EuDy_2O_4$ are complexes which have
cooperative magnetic transitions at low temperatures. [1-3] These
transitions are presumably due to the presence of divalent europium
ions in the complex. The magnetic properties of Eu_3O_4 have been more
extensively studied than have those of $EuGd_2O_4$ and $EuDy_2O_4$. The
Eu_3O_4 appears to be a metamagnetic material. $EuGd_2O_4$ and $EuDy_2O_4$
have not as yet been investigated carefully enough to unequivocally
determine the details regarding the kind of magnetic cooperative

-164- 8

transitions that occur. Detailed magnetic structural data is not available for any of these complexes. X-ray structural information[1] has shown that these three complexes are isostructural. The structure of Eu_3O_4 has been extensively studied and shown to be orthorhombic.[4,5] Another structural analog to Eu_3O_4 is Eu_2SrO_4, whose lottice parameters are virtually identical to Eu_3O_4. In the latter complex Sr^{++} apparently substitutes for the Eu^{++} in the former complex. Eu_2SrO_4 provides an interesting diamagnetic analog as an aid in the interpretation of the magnetic information obtained in the complexes containing Eu^{++}.

We have surveyed the lanthanon sesquioxide-divalent europium complexes to see if a complete homologous series of orthorhombic $EuO \cdot Ln_2O_3$ complexes form. Such a series would provide candidates from which to obtain valuable magnetic data. In addition to magnetic information, it is possible that one might be able to observe charge transfer processes in such complexes and derives some information relating to the stability of the Ln^{++} states.

Experimental

Two different preparative approaches were used in this study.

(1) The reduction of Eu_2O_3 by the Ln metals. These reductions were carried out using Ln metals of nominal 99. 0% purity with Eu_2O_3 of nominal 99. 9% purity which had previously been dehydrated and heated in air to ~ 1000°C. The weighed reactants were sealed in Mo capsules by electron beam welding techniques (EBW). Two series of reductions were made both at ~ 1700°C by heating the capsules in an RF vacuum induction furnace. The samples were cooled relatively slowly. Weight checks made at various stages of these preparations were used to monitor possibilities of leaky capsules. The products were examined by optical microscopic and X-ray powder pattern techniques.

(2) Metalhetical Synthesis using equimolar amounts of EuO and Ln_2O_3
were attampted at $1500^\circ C$ and at $2100^\circ C$. EuO prepared by the
reduction of Eu_2O_3 by Eu followed by melting the resulted EuO in Mo
containers was one of the reactants. The other reactants were the
Ln_2O_3. In general these were dehydrated and heated in air at $\sim 1000^\circ C$.
For Ce, Pr, and Tb, the reactant sesquioxides were prepared by heat-
ing the commercially available oxides in H_2. All oxides were nominal
99.9% purity. The Eu metal was of nominal 99.0% purity. The
reactants were weighed and sealed into Mo capsules by EBW techniques.
The capsules were heated in an RF induction furnace as in (1) above.
Again, the products were examined by optical microscopic and X-ray
powder pattern techniques.

Results and Discussion

If the one-to-one complexes $EuO \cdot Ln_2O_3$ form and are stable under
the conditions of the reduction preparations, the expected reactions is

$$2Ln + 3 Eu_2O_3 = EuO \cdot Ln_2O_3 + 5EuO$$
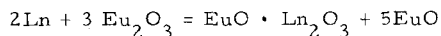
The presence of EuO is easily detected in the reaction products by
optical microscopy. EuO is opaque even in extremely thin sections the
Ln_2O_3 are generally colorless and transparent in thin section. The
one-to-one complexes are probably deep red and transparent in analogy
to Eu_3O_4. Thus optical evidence in conjunction with X-ray powder
pattern analysis can help to identify the products of these reactions.

No EuO was found by either optical or X-ray analysis for La, Ce,
Pr, Nd, Gd, Tb, Dy, or Yb. EuO was found for Sm, Ho, Tm, and Lu.
(The reduction was not attempted with Er). When an excess of Ln
metal (for the reaction as written above) was used, EuO was found for
Gd and Dy at $2100^\circ C$. Also, for Sm and Ho used in excess for the
reaction as written above, at $2100^\circ C$, new F.C.C. materials with a

-166-

lattice parameters of 5.121 A and 5.131 respectively were found. In no case was unreacted Ln metal detected in the products. In no case was EuO found in such a quantity as to correspond to the reaction as written. The following is a summary of the X-ray powder pattern results on the complex oxides obtained by the reduction.

Monoclinic Structures:	La, Ce, Pr, Nd, Gd
Orthorhombic Structures:	Sm, Tb, Dy, Tm, Yb, Lu
Body Centered Cubic Structures:	La, Ce, Pr, Ho
Face Centered Cubic Strictures:	Sm, Ho

It is clear from the results obtained from the reductions of Eu_2O_3 by Ln metals that the reactions as written above are not the reactions that generally occur. It is also clear that for any Ln there is more than one complex oxide formed with perhaps the exception of Tm.

The observations on the products from the metathetical preparations confirm that there are a large variety of complexes that can form. In general, optical observations on the products indicated multiphase products and/or solid solution formation. In many cases multiple phases which could be easily seen optically could not be detected by X-ray analysis. The X-ray results are:

(2100°C)

Monoclinic Structures:	Sm, Gd
Orthorhombic Structures:	Tb, Dy, Tm, Yb
Hexagonal Structures:	La, Nd
Body Centered Cubic Structures:	Pr, Ho, Er, Lu

(1500°C)

Monoclinic Structures:	Tb
Orthorhombic Structures:	Sm, Gd, Tb, Dy, Ho, Tm, Yb
Hexagonal Structures:	La, Ce, Nd
Body Centered Cubic Structures:	Pr, Ho, Er, Lu

-167-

While a number of orthorhombic complexes of Eu^{++} with Ln^{+++} oxides have formed, in the above preparative methods, in general these oxide systems are complicated as this survey has shown. The possible exception is for Tm. The new F.C.C. phases obtained in the Ln reduction of Eu_2O_3 for Sm and Ho are opaque and have reddish black color. Charge transfer may occur in these phases. The $EuO - Ln_2O_3$ systems may turn out to be as or even more complex than the analogous $SrO - Ln_2O_3$ systems that have been investigated by Barry and Roy.[6]

Acknowledgements

We wish to thank V. Silviera for performing the X-ray analyses.

References

1. A. A. Samokhvalov, V. G. Bamburov, N. V. Volkenstein, T. D. Zotov, Yu N. Morozov, and M. I. Simonova, Soviet Physics - Solid State 9, 428 (1967).

2. H. H. Wickman and E. Catalano. J. App. Physics 39, 1248 (1968).

3. L. Holmes and M. Schieber, Phys. Rev. 167, 449 (1968).

4. H. Barnighausen and G. Brauer, Acta Cryrt 15, 1059 (1962).

5. R. C. Rau, Acta Cryrt 20, 716 (1966).

6. T. L. Barry and R. Roy, J. Inorg. Nucl. Chem. 29, 1243 (1967).

THERMAL ANALYSIS OF LANTHANIDE HYDROXIDE PREPARATIONS*

R. G. Haire

Oak Ridge National Laboratory, Oak Ridge, Tennessee

Abstract

Hydroxide preparations of the lanthanides and yttrium were obtained by precipitating the metal ions from nitrate solutions with ammonium hydroxide. The initial precipitates gave amorphous-like diffraction patterns. Colloidal solutions of the amorphous material were obtained by extensively washing the precipitates until peptization occurred. After a sufficient period of aging, the colloidal material became crystalline. Previous studies[1] showed that the lanthanides could be divided into two groups based on crystallization time and the crystalline microstructures obtained for each element. This paper is concerned with the thermal stability of the amorphous and crystalline forms of the hydroxide preparations, as studied by thermogravimetry, differential thermal analysis and x-ray diffraction. The investigation showed that the amorphous and crystalline forms exhibited different patterns of solid-state decomposition. With the amorphous materials, the decompositions were characterized by a continuous weight loss and broad DTA peaks. When the crystalline forms were studied, sharper DTA peaks and more distinct weight changes were obtained. The TG and DTA curves for each form were similar for all the lanthanides, although there was a gradual shift in the decomposition temperatures in moving across the series. In the absence of carbonate impurities, the decomposition of both amorphous and crystalline material was complete by 600°C, and yielded the stable oxide. The results from the study are compared to the trends previously obtained from the electron microscopy and diffraction studies.[1]

Introduction

The hydroxides and hydrous oxides of the lanthanides have been discussed in the literature for several decades. Weiser[2] has reported on the colloidal nature of these materials and discussed preparative methods presented by workers prior to 1935. Many researchers have studied the hydroxides by x-ray diffraction. Duval

reported thermogravimetric analysis of some of the lanthanide hydroxides up to terbium.[3] Other workers have done isobaric studies on some of the lighter lanthanides.[4,5] Milligan and Dwight[6] used electron microscopy and diffraction to study the crystallization of neodymium hydroxide and found the amorphous precipitate crystallized into rod-like structures after aging in water. Hardy et al.,[7,8] subsequently investigated praseodymium, neodymium and europium hydroxides and found a similar crystallization behavior for these elements. The hydroxides of the entire lanthanide series and yttrium were studied by Haire and Willmarth.[1]

The work described here is concerned with the thermal stability of lanthanide and yttrium hydroxide preparations. The materials were studied by thermogravimetry, differential thermal analysis, x-ray and electron diffraction and electron microscopy. The present study was mainly concerned with two aspects of the lanthanide hydroxides: (1) a comparison of the thermal decomposition of the amorphous and the crystalline forms; and (2) to determine if any differences in the thermal decomposition pattern could be observed for the different elements. A comparison of the elements before and after the dysprosium-holmium region was of special interest, since a noticeable change in the crystallization behavior was observed at this point in the series.[1]

Experimental

Preparation - The hydroxide preparations were obtained by adding metal nitrate solutions to an excess of 8 M NH_4OH; the procedure has been previously described.[1,7,8] All of the precipitates obtained in this manner were extensively washed (10 to 15 times with triple-distilled water) and then divided into two fractions: one fraction being retained for the amorphous material while the second was used for preparing the crystalline form. The crystalline preparations were obtained by aging the amorphous material in water.[1] Solid forms of the preparations were obtained by several methods (air evaporation, extraction of water by alcohols, etc.) but the preferred procedure employed vacuum-freeze drying of the colloidal solutions.

Methods of Analysis - Thermogravimetry studies were made with an Ainsworth semi-micro recording balance and a Cahn RG Electrobalance, at linear heating rates of 1 to 5 degrees/minute. Differential thermal analysis was done in a special unit equipped with stone-ring type thermocouples and sample cups. Heating rates of 10 to 15 degrees/minute were used. Samples for both types of analysis ranged from 3 to 100 mg. The decompositions were carried out in flowing air, argon and helium atmospheres.

The preparation and analysis of samples by electron microscopy and electron and x-ray diffraction have been described.[1]

Results and Discussion

The hydroxide preparations were found to be amorphous-like immediately after precipitation but after a sufficient period of aging in an aqueous media, the material became crystalline. Previous studies have shown that during conversion to the crystalline state, the microstructure changes from amorphous, 20-50 Å symmetrical particles to larger crystalline rods or platelets.[1] The size, shape and conversion time varied for the different elements, and could be used to divide the series into two groups, with the second group beginning with holmium. Electron micrographs and diffraction patterns for the two stages of gadolinium are shown in figure 1, and serve to illustrate the conversion.

Although the thermal decomposition patterns for several of the lighter lanthanides have been reported, there has been no distinction made between amorphous and crystalline products and often the level of contaminants have been neglected. Duval[3] reported ammonia and carbonate impurities were present in several of his preparations. The amount of the original anion retained by the precipitates is important in understanding the decomposition curves. The products prepared for this work contained up to 0.3 NO_3^-/M mole ratio (the ratio was generally 0.05 to 0.20), even though an excess of base was used and the precipitates washed extensively. In the case of nitrate anion, a NO_3^-/M ratio of 0.15 is equivalent to a ratio of 0.5 H_2O/M, with regard to the weight loss observed during heating.

The dynamic methods of TG and DTA were used for the present study of the lanthanides and yttrium. These methods are relatively rapid and provide a continuous record from small, undisturbed samples. However, they do not allow a state of equilibrium to be reached, as obtained by an isobaric measurement, and the results must be interpreted with this in mind.

A comparison of the TG and DTA curves for amorphous and crystalline hydroxide preparations showed that there was a distinct difference between the thermal decomposition of the two forms. In figures 2 and 3 are shown the TG and DTA curves for the amorphous and crystalline hydroxide preparations of gadolinium and for $Gd(NO_3)_3 \cdot 4H_2O$. The latter material was included for comparison with the hydroxides. The results in figures 2 and 3 were for decompositions carried out in a flowing-air atmosphere but identical results were obtained in helium or argon atmospheres. The TG curve for the amorphous preparation is characterized by an

Fig. 1. Electron Micrographs and Diffraction Patterns for Gadolinium Preparations.
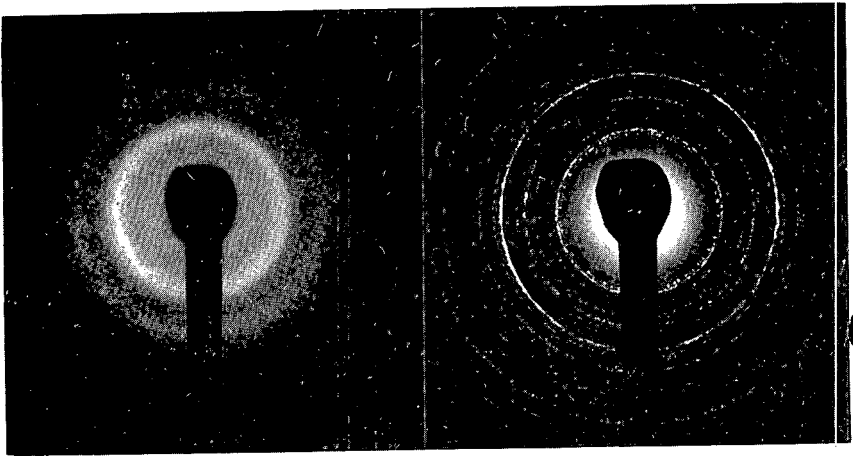
AMORPHOUS GD   -172-   CRYSTALLINE GD
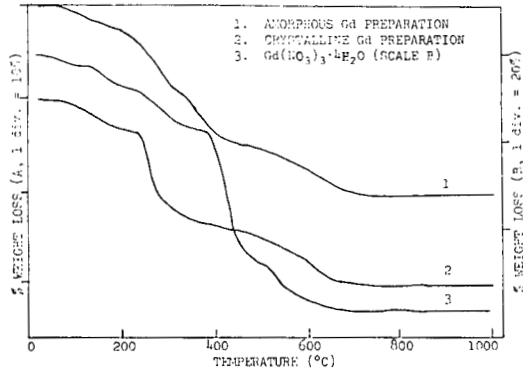
Fig. 2. THERMAL DECOMPOSITION OF Gd PREPARATIONS.
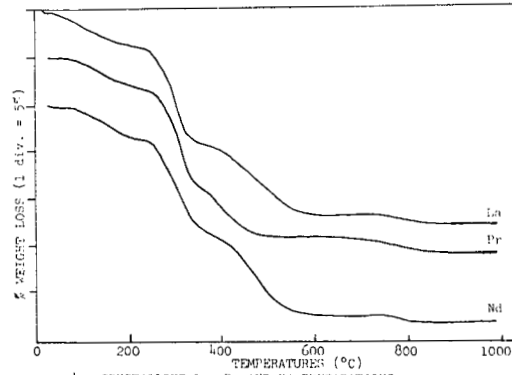
Fig. 4. CRYSTALLINE La, Pr AND Nd PREPARATIONS.
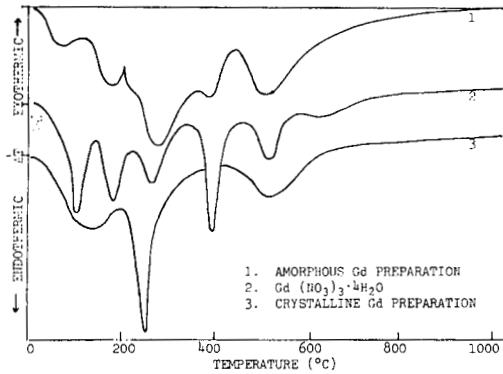
Fig. 3. DIFFERENTIAL THERMAL ANALYSIS OF Gd PREPARATIONS.
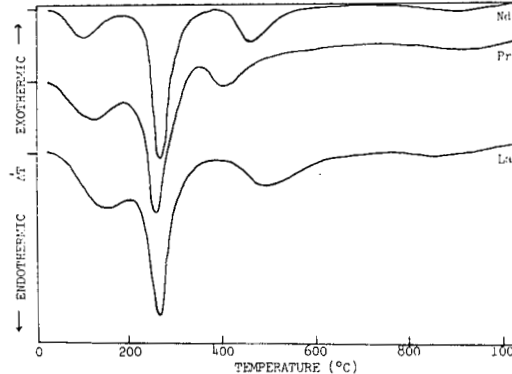
Fig. 5. CRYSTALLINE La, Pr, AND Nd PREPARATIONS.

essentially continuous weight loss, with only small inflections to indicate successive reactions. The curve for the crystalline preparation shows more distinctive weight changes, with a sharp transition at 250°C. Although the different weight losses were not isolated by distinct plateaus, the data can be extrapolated to give reasonable estimates for the magnitude of the changes. The TG curve for $Gd(NO_3)_3 \cdot 4H_2O$ shown in figure 2 is essentially identical to that reported by Wendlandt and Bear.[9] The loss up to 400°C was attributed to the loss of water. The curve shows small inflections that indicate overlapping transitions. The rapid weight loss at 400 to 450°C has been reported to be due to $Gd(NO_3)_3$ going to $GdONO_3$, with the latter converting to the sesquioxide at a slightly higher temperature. The decomposition of the nitrate present in the gadolinium hydroxide preparations was also found to occur in this 400 to 600°C region, although the apparent change is more gradual, due in part to the smaller quantity of nitrate present. Differences were also observed in the DTA curves (figure 3) for the amorphous and crystalline products. The curve for the amorphous form contains more peaks and the curve remains endothermic up to 700°C, which is expected from the continuous weight loss observed in the TG curve. The curve for the crystalline form has three peaks, with a large endothermic peak that corresponds to the weight loss at 250°C. The curves for the crystalline form indicate more distinctive transitions than found for the amorphous material. The DTA curve shown in figure 3 for $Gd(NO_3)_3 \cdot 4H_2O$ agrees with that reported by other workers.[9] The two endothermic peaks at 400 and 500°C are attributed to the two-step decomposition of nitrate. The nitrate present in the hydroxide preparations decomposed over a temperature region very similar to that reported for the decomposition of $GdONO_3$, which is formed from heating the hydrated nitrate salt. Although the hydroxide preparations have NO_3^-/M mole ratios much lower than 1, it appears the nitrate that was present just prior to the decomposition temperature existed as an oxynitrate. The TG and DTA curves shown for the gadolinium preparations are in, general, typical for the respective preparations of the other lanthanides. However, some of the preparations contained small amounts of carbonate, and in these cases the TG and DTA curves reflect the loss of the carbonate impurity at higher temperatures.

In preparing the hydroxides of the lighter lanthanides (La-Nd), the rapid conversion of the amorphous precipitate to the crystalline state[1] did not permit the preparation of a well-washed, amorphous hydroxide. Amorphous preparations of yttrium and the lanthanides beyond neodymium were readily obtained, as the conversion times were much longer. Most of the attempts to prepare the amorphous form of the lighter lanthanides resulted in a partially crystalline material, which produced TG and DTA curves that had characteristics of both forms. By using methanol or propanol to complete the washing

and remove excess water from the precipitates, amorphous products could be obtained. However, as a result of the high-surface area of the materials, some alcohol was sorbed which could not be readily removed. Although the contribution of the residual alcohol to the weight loss was almost negligible, small exothermic peaks due to the decomposition of the alcohol were observed when the material was heated in air. Preparations made in this manner did show that the TG and DTA curves for the amorphous forms of lanthanum through neodymium hydroxides were very similar to that shown for gadolinium. The TG and DTA curves for crystalline forms of lanthanum through neodymium were also nearly identical to those for crystalline gadolinium preparation. In figures 4 and 5 are shown the curves for lanthanum, praseodymium and neodymium crystalline hydroxides run in air. The decomposition in argon, helium and air was the same for lanthanum and neodymium. The final products were the sesqui-oxides, except for cerium and praseodymium. With praseodymium, the so-called Pr_6O_{11} oxide was obtained in air but oxidation was incomplete in argon or helium; partial oxidation probably resulted from the decomposition products of nitrate which were generated. With cerium, the dioxide was always obtained. With both cerium and praseodymium, the loss of nitrate was complete at slightly lower temperatures than observed for the other lanthanides. With lantha-num, the nitrate decomposed at a higher temperature, reflecting the greater basicity of this ion.

In figures 6, 7, 8 and 9 are shown the TG and DTA curves for the amorphous preparations of samarium, dysprosium, erbium, ytterbium, lutetium and yttrium in air. The decomposition was identical in air, argon or helium atmospheres. The curves for europium, terbium, holmium and thulium were essentially identical to the above elements. The sesquioxide were the final products obtained except for the terbium preparation; in air Tb_4O_7 was obtained while oxidation was not complete when an inert atmosphere was used. The interpretations made for the gadolinium amorphous preparations can also be applied to the decomposition of these materials. In progressing to the heavier lanthanides, it was apparent that the DTA curves for the amorphous preparations contained more peaks and appeared to be more complex. This trend was also observed in the DTA curves obtained for the hydrated nitrate salts, probably reflecting the smaller ionic radius and greater complexing ability of the heavier lanthanides. The decomposition of the crystalline preparations in air for the corres-ponding lanthanides are shown in figures 10, 11, 12 and 13. The decomposition of the europium, terbium, holmium and thulium prepara-tions were essentially the same. The final products obtained for the
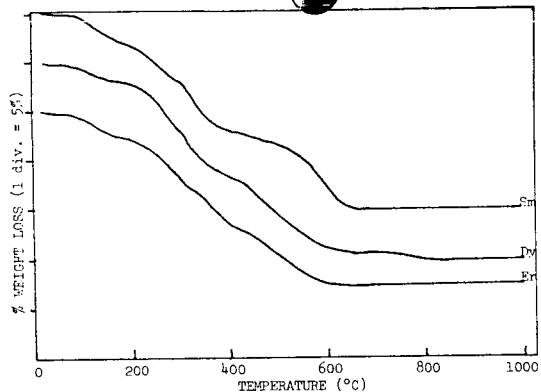
Fig. 6. AMORPHOUS Sm, Dy AND Er PREPARATIONS.
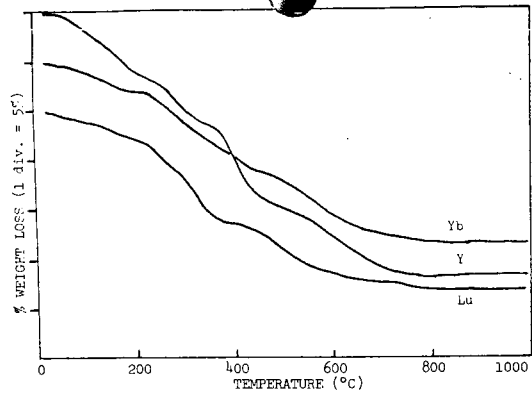
Fig. 8. AMORPHOUS Yb, Lu, AND Y PREPARATIONS.
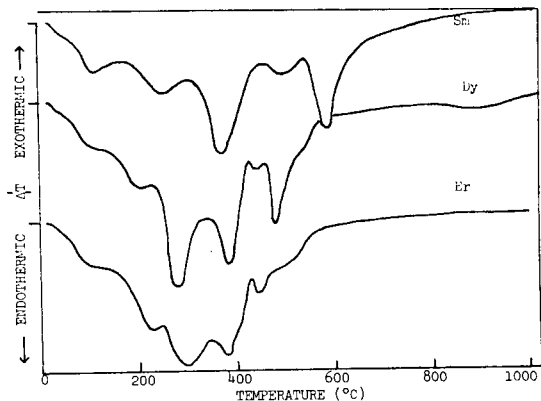
Fig. 7. AMORPHOUS Sm, Dy, AND Er PREPARATIONS.
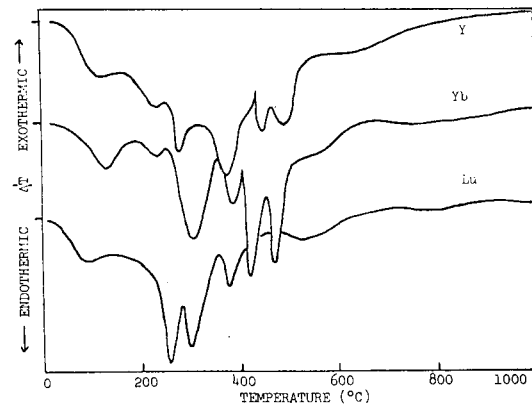
Fig. 9. AMORPHOUS Yb, Lu, AND Y PREPARATIONS.
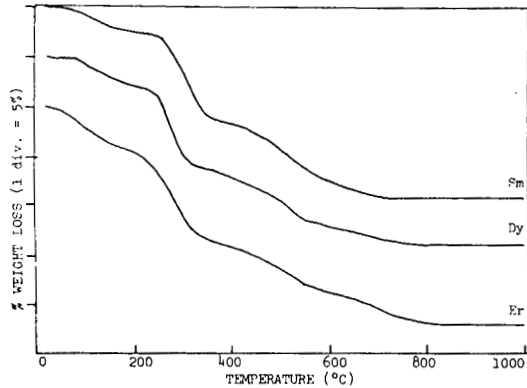
Fig. 10. CRYSTALLINE Sm, Dy AND Er PREPARATION.
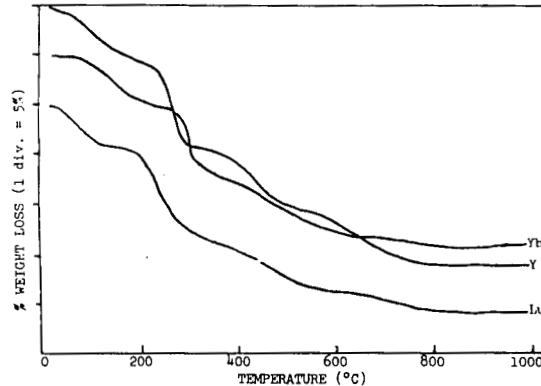
FIG. 12. CRYSTALLINE Yb, Lu, and Y PREPARATIONS.
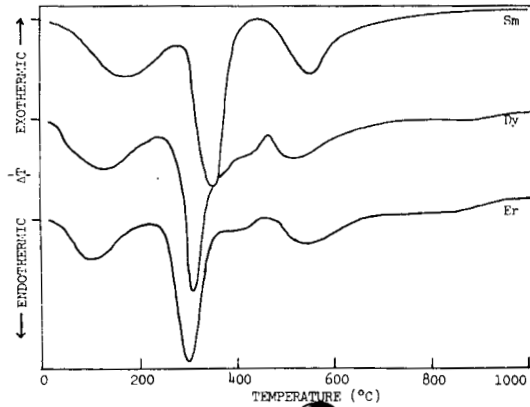
Fig. 11. CRYSTALLINE Sm, Dy, AND Er PREPARATIONS.
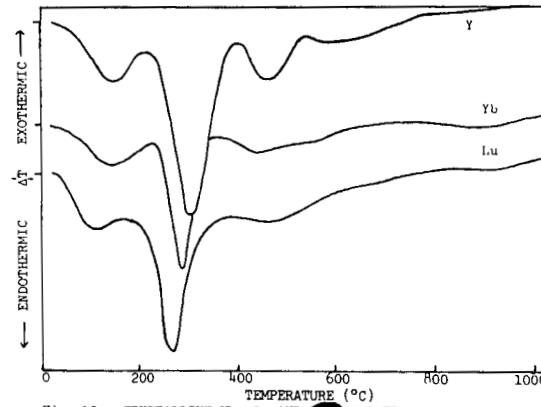
Fig. 13. CRYSTALLINE Yb, Lu AND Y PREPARATIONS.

amorphous preparations, were also obtained for the crystalline forms, and, except for terbium, decomposition in helium or argon was the same as in air. The number of DTA peaks observed for the crystalline forms did not increase in going to the heavier lanthanides. This indicates a greater similarity in the crystalline products than for the amorphous products. The crystalline yttrium product used to obtain the results in figures 12 and 13 contained a sufficient quantity of carbonate to show a distinctive weight change and a broad endothermic peak in the region of 700°C.

Examination of the TG and DTA curves showed that the decomposition for each class of preparation is comparable for all the lanthanides and yttrium. The fact that the curves are different for the amorphous and crystalline forms can aid in the interpretation of some hydroxide decompositions reported previously.[3] A knowledge of the amount of original anion remaining in the preparations is essential in understanding the TG and DTA curves. The presence of some carbonate is less objectionable since the decomposition occurs at higher temperatures and is more readily recognized as due to carbonate. The removal of excess water from the hydroxide preparations presents a special problem, especially in view of the high surface area of the products and their ability to tightly sorb materials. It was assumed here that vacuum-freeze drying did not alter the preparations; the similarity of the decomposition curves to those of hydroxides dried in other manners supports this assumption. One can conclude that the analysis of "wet" hydroxides or precipitates containing ammonium impurities would be difficult to resolve. All of the materials prepared here had an ammonium content below detectible limits when analyzed by a micro-Kjeldkhl method.

By extrapolation of the more prominent inflections of the TG curves, the weight changes could be used to calculate the H_2O/M, NO_3^-/M and $CO_3^=/M$ mole ratios for the products. The ratios calculated in this manner agreed quite well with analytical data. Analytical values are listed in Table I for the elements shown in the figures. The values for the other lanthanides were very similar. A weight loss that corresponds to 1.5 H_2O/M is expected for decomposition of the trihydroxide. However, the presence of nitrate and/or carbonate complicates the estimation for the water loss. If the nitrate ion replaced the hydroxide ion, the weight loss due to water would yield a lower H_2O/M ratio. If the nitrate was present in some other capacity (as believed to exist for the colloidal particles in solution) a decrease in the H_2O/M ratio may not be observed. The presence of some sorbed water is believed to account for H_2O/M ratios greater

-178-

than 1.5. For the majority of the amorphous preparations, the inflections in the TG curves were too gradual to permit extrapolation of the successive dehydration steps. In a few cases, estimates of the changes indicated three successive steps, each corresponding to 0.5 H_2O/M. In the dehydration of the crystalline forms, the losses indicated changes of 0.5 and 1.0 H_2O/M. For both the amorphous and crystalline forms, the loss of water was of the magnitude expected for the trihydroxides, and it appears that all of the products were hydroxides. Further work is necessary to fully characterize the lanthanide hydroxide system. The intent of this work was to survey the entire lanthanide series, to ascertain if significant differences existed between the different products. It was concluded that the thermal decomposition of the amorphous and crystalline hydroxide preparations was different but that the decomposition of each form was similar for all the lanthanides.

Table I. Analyses of the Lanthanide Hydroxide Preparations

Element	Amorphous			Crystalline		
	H_2O/M*	NO_3^-/M	$CO_3^=/M$	H_2O/M*	NO_3^-/M	$CO_3^=/M$
La	--	--	--	1.73	.30	.14
Pr	--	--	--	1.62	.17	.10
Nd	--	--	--	1.67	.25	.15
Sm	1.75	.22	.055	1.65	.24	.099
Gd	1.87	.20	.042	1.59	.25	.081
Dy	1.76	.15	.036	1.80	.15	.054
Er	1.71	.15	.056	1.85	.15	.22
Yb	1.69	.18	.080	1.85	.25	.12
Lu	1.73	.20	0.38	1.75	.23	.16
Y	1.66	.16	.024	1.62	.16	.16

*Based on water evolved.

Acknowledgement

References

1. R. G. Haire and T. E. Willmarth, Paper to Seventh Rare Earth Conference, Coronodo, California, Oct. 28-30, 1968: ORNL-TM-2387.

2. H. B. Weiser, *Inorganic Colloid Chemistry*, Vol. 11, Wiley, New York, 1935.

3. C. Duval, *Inorganic Thermogravimetric Analysis*, Elsevier, New York, 1963.

4. H. B. Weiser and W. O. Milligan, J. Phys. Chem. 42, 673 (1938).

5. R. Fricke and A. Seitz, Z. Naturforsch, 1, 321 (1946); Z. Anorg. Allgem. Chem. 107, 116 (1947).

6. W. O. Milligan and D. W. Dwight, J. Electron Microscopy 14, 264 (1965).

7. C. J. Hardy, S. R. Buxton, M. H. Lloyd, *Preparation of Lanthanide Oxide Microspheres by Sol-Gel Methods*, ORNL-4000 (Aug. 1967).

8. C. J. Hardy, S. R. Buxton and T. E. Willmarth, *Proc. 6th Rare Earth Research Conf.*, May 3-5, 1967, Gatlinburg, Tennessee.

9. W. W. Wendlandt and J. L. Bear, J. Inorg. and Nuclear Chem. 12, 276 (1960).

PSEUDOPHASE BEHAVIOR IN THE EPSILON AND IOTA REGIONS OF THE PRASEODYMIUM OXIDE-OXYGEN SYSTEM

R. P. Turcotte,
M. S. Jenkins
and
L. Eyring

Arizona State University, Dept. of Chemistry, Tempe, Arizona

064 5200

ABSTRACT

Besides line and nonstoichiometric phases complex oxide systems exhibit reproducible bivariant behavior, termed pseudophases, in the two-phase regions which leads to hysteresis. Two of these pseudophases in the praseodymium oxide-oxygen system are examined in detail by tensimetric and high temperature X-ray studies.

The tensimetric measurements show marked and progressive shifting of the curves away from stoichiometry with increasing pressure. In addition unusual reversals are seen to occur both in oxidation and reduction. X-Ray diffraction patterns at temperature are seen to show systematic changes in line positions and line widths. These are analyzed and their implications discussed in terms of suggested structural changes. Similarities and relevance to other systems are discussed.

INTRODUCTION

A phenomonological description of a system in the solid state which pretends to be exhaustive must distinguish a wide variety of behavior. For example there are line phases at stoichiometric composition with only very slight variation in composition with temperature such as $ThO_{2-\delta}$ (1,2) or line phases with more complicated stoichiometry such as the homologous series Ti_nO_{2n-1} (3). In addition there are line phases which have an appreciable range of composition and/or exhibit polymorphism as in the system Pr_nO_{2n-2} (4).

One must add to these, nonstoichiometric phases having reversible bivariant character over a wide range of composition. The most studied of these include UO_x ($2.0 \leq x \leq 2.25$), FeO_x ($1.05 \leq x \leq 1.19$), TiO_x ($0.7 \leq x \leq 1.25$) and PrO_x ($1.50 \leq x \leq 1.69$ and $1.72 \leq x \leq 2.00$). Various observers have described these as microheterogeneous, having microdomains, microphasic, coherently intergrown,

hybrid crystals, etc., which implies that thermodynamically and/or structurally they possess texture above the atomic or unit cell level. In recent months subtle discontinuities in thermodynamic and structural behavior have suggested that these wide regions must be divided into areas having more coherent properties. For example, the FeO_x ($1.05 \leq x \leq 1.25$) phase has been seen to have at least three distinct regions (5,7) and PrO_x ($1.71 \leq x \leq 2.00$) at least four (6).

Of course in any system having many phases there must be two-phase regions separating them. These transitional regions are themselves being seen to be extremely complex showing marked premonitory behavior (8), hysteresis (4,9), and pseudophase formation (4).

Pseudophases in the present usage are reproducible and bivariant in p, T, x studies as a system transforms from one phase to another in one direction. The degree of pseudophase formation varies as between the directions one is going in composition and is more pronounced in going from less to more ordered regions among phases which may intergrow coherently. They may, however, be observed on both compositional sides of a stoichiometric phase. Hysteresis results from this asymmetric behavior.

In this paper we shall focus on a particular type of pseudophase behavior on the oxygen-rich side of the ι and ϵ phases of the praseodymium oxide-oxygen system. The phase diagram including the regions of our interest is shown in Figure 1 (4). The tensimetric studies illustrated by the isobaric curves of Figure 2 (10) include the behavior we wish to examine more closely. The isobaric development for each phase in the homologous series is seen to result in increasing displacement of vertical curves to significantly higher compositions than expected if the intermediate phases are highly ordered. As the curves shift they are observed to become less steep and show a mysterious crossing in the hysteresis loop in that region.

EXPERIMENTAL PART

All experiments were carried out using 99.999% PrO_x supplied by the Lindsay Division of the American Potash and Chemical Corporation. The tensimetric studies were made using an Ainsworth balance possessing automatic temperature and pressure control with an eight gram sample suspended in an alumina bucket by a platinum wire (6). X-Ray studies were accomplished by means of a Philips high temperature diffractometer (11) and a high temperature Nonius

Guinier-Lenné camera (12). Temperatures were measured in all cases with Pt-Pt/10%Rh thermocouples calibrated as required. Thoria was used as an internal standard in the X-ray patterns and all data were reduced by computer methods ($\lambda(K_{\alpha 1}) = 1.54051$).

RESULTS AND DISCUSSION

Thermogravimetric Analysis

Isobaric thermogravimetric experiments as displayed in Figure 3, performed at a rate of temperature increase of 0.5° per minute, portray graphically the transformation of $PrO_{1.833}$ (β phase) to $PrO_{1.800}$ (ε) to PrO_x (α) and return. The δ phase ($PrO_{1.818}$) will be seen to be complicating the reaction to some degree. It is important to realize that the observed behavior is reproducible in all the regions discussed. A shift to higher composition with increasing pressure is marked as is the narrowing of the temperature range of the reaction.

Similar isobaric runs in the $PrO_{1.714}$ (ι) region have been done with great care and behavior similar to that shown in the two highest pressure curves in Figure 2 are confirmed. Even upon holding conditions for one month there was actually no tendency for conversion to stoichiometric ι. In fact the unique ι line phase is not attained until the pressure is reduced to about 10 Torr.

In order to observe the transit from the oxygen excess ι pseudophase to stoichiometric composition isotherms of the following type were performed. At 843° and 676 Torr the specimen is in the low temperature region of the pseudophase ($\alpha\iota$) with a composition of $PrO_{1.753}$. When the pressure was reduced to 6.80 Torr at constant temperature the oxide reduced to $PrO_{1.714}$. When the pressure was restored to 676 Torr the composition increased only to $PrO_{1.721}$ indicating at this pressure a narrow compositional variation of ι phase at 843°, the irreversible nature of the change, and the metastability of the pseudophase.

In related experiments at 32.79 Torr and 569°, the ζ phase has a composition of $PrO_{1.789}$ based on the assumption that at a pressure of 6.46 Torr the composition was $PrO_{1.778}$. When the pressure was restored the composition increased only to $PrO_{1.780}$ giving a phase variation for ζ of 0.002 in oxygen to praseodymium ratio compared to 0.007 for ι phase and similar experiments in the ε region gave a composition increase of 0.004 at 138 Torr.

X-Ray Analysis

The Epsilon Pseudophase Region.--Diffraction patterns obtained at temperature for the β, δ, ε, ζ and ι phases shown in Figure 4 confirmed those observed earlier on samples quenched after long anneals (13) except for the ζ phase which appears to be polymorphic.

The diffraction patterns of samples traversing the isobars shown in Figure 3 at 5°/hr are shown in Figures 5, 6, and 7. The symbol α is used when general reference to the nonstoichiometric phase is intended. The symbol α* is used to indicate probable short range order characterized by regularly increasing line widths as the Bragg angle increases and α** indicates the nonstoichiometric phase which gives a slight distortion from cubic symmetry as evidenced by a diffraction pattern having $\beta_{111} > \beta_{200} < \beta_{220}$ (β_{111} = line width of the (111) reflection, etc.). Transitions between α, α*, and α** are continuous in passing from high to low temperature.

In Figure 5 the oxidation reduction cycle is shown for a 41 Torr isobar. In cooling, the transformations
$$\alpha \xrightarrow{475°} \epsilon \xrightarrow{410°} \beta$$
are observed while in heating the sequence is
$$\beta \xrightarrow{440°} \delta \xrightarrow{475°} \epsilon \xrightarrow{520°} \alpha$$
in substantial agreement with the tensimetric isobars with increasing temperature. Figures 6 and 7 give further indication of the diffraction behavior during isobaric transit comparable to those in Figure 3. It is clear that X-ray diffraction does give information concerning the structural changes occurring in this pseudophase region. The detailed discussion of these results will be given in the presentation although restricted space will not permit it here.
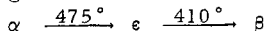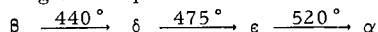
Figure 8 shows the diffraction behavior for certain preparations as explicitly given. It may be seen, for example, that at 41 Torr in cooling the pseudophase diffraction appears to be a superposition of α and ε.

Figure 9 shows the variation of lattice parameter with temperature. The variation is due both to compositional and elastic factors. At 102 mm O_2 one may observe the contraction of the lattice as the temperature is decreased from 540°. At 500° (see Fig. 3) the sample is reduced from $PrO_{1.817}$ to about $PrO_{1.808}$ at 470° as a result of the curve reversal. The composition reversal is reflected here as a decrease in the rate of lattice parameter increase

with temperature. The transition to β at 460° gives an even greater value of $\Delta a/\Delta t$ than observed at $t > 510°$ as would be expected because of the narrow composition range of β. Analogous behavior is seen at lower pressures as shown.

The Iota Pseudophase Region.--The tensimetric isobaric studies (4,10) demonstrate a well developed pseudophase behavior in the $\alpha\iota$ region at pressures in excess of 150 Torr. High temperature diffractometer measurements were made at several pressures in this region. The profile for the 220 reflection at 635 Torr are shown as representative of these in Figure 10. The 220 peak which is single for α but is split equally for ι was analyzed on a curve resolver. A single phase α peak is shown at 779°. At 881° conversion to ι is about 50% complete. As the temperature is increased the α peak is seen to move to lower 2θ values in the constellation of ι as it weakens and disappears. This movement results from the rapid decrease in composition and increase in lattice parameter as the temperature increases while the ι phase remains virtually unchanged. Sigma phase exists alone at 1133°C.

At 1087°, in cooling, the peak was split evenly with a separation of 0.10° in 2θ. It is believed that the low angle peak is α while the other is the $(\bar{2}20)$ reflection of ι. The $\sigma \rightarrow \alpha$ conversion presumed to have occurred between 1135 and 1087° was not seen, probably because the peak separation for the narrow miscibility gap is so small (0.001Å expected). As the temperature was further reduced the reverse movement of the α peak in the ι constellation was observed. At 920° there appeared to be only ι phase with unequal peak height suggesting a distortion resulting from a composition in excess of $PrO_{1.721}$.

Superficially the X-ray results agree with the interpretations of the tensimetric work but there are some anomalies in apparent relative phase intensities as between the X-ray and gravimetric work and in other details when the results are examined in detail.

CONCLUSIONS

It is apparent from these observations that there exist many superficial similarities in behavior in the $\alpha\iota$ and $\alpha\epsilon$ pseudophase regions when seen in both tensimetric and X-ray work, however, there are marked differences in detail and these differences depend to some extent on temperature and pressure.

A point which has not been discussed so far is the appearance
of the very weak superstructure lines characteristic of the ϵ phase
in the α^{**} phase. The slight broadening of certain of the main lines
of this phase plus the weak superstructure indicate a very slight
deviation from cubic symmetry (a rhombohedral distortion of as
little as 0.03° in a). Previous work (6) has indicated at least four
regions of the α phase. It is suggested that short range ordering
in α yields α^* having lines which increase in breadth in a regular way
with increasing Bragg angle indicating lattice strain rather than
particle size broadening. At lower temperature longer range ordering
produces α^{**} with its uneven broadening of lines plus very weak
superstructure lines.

The following model of pseudophase formation in the ϵ region
is suggested. Order → order transformations become progressively
less complete with increasing temperature. Microdomains of the
starting and product material intergrow to give a metastable phase
capable of developing long range order. In the cooling cycle there
is an increasing order as α^* → α^{**} → ϵ pseudophase.
Having long range order in a broadly nonstoichiometric α phase
is mirrored in the σ phase ($1.5 \le x \le 1.69$) which has good super-
structure lines characteristic of C-type $PrO_{1.5}$ even when the com-
position is $PrO_{1.69}$.

Willis (14) has shown by neutron diffraction that there are
defect clusters in UO_{2+x} at high temperatures which produce the
U_4O_9 phase when they are fully ordered. Belbeoch et al., (15)
have shown that U_4O_9 exists in varying degrees of order.

Structural studies of Roth (16), Manenc (17) and Koch and
Cohen (18) on the Wüstite phase have led to a description of the
$Fe_{1-x}O$ as composed of defect clusters of more or less order at
high temperatures. The domains grow with cooling and are period-
ically spaced at room temperature.

These are but the early chapters in understanding materials
having extended defects.

-186-

1. R. J. Ackermann, E. G. Rauh, R. J. Thorn and M. C. Cannon, J. Phys. Chem., 67, 762 (1963).

2. J. S. Anderson in "High Temperature Technology," Proceedings of a conference Butterworths, Washington, 1964, p. 285.

3. S. Andersson, B. Collén, U. Kuylenstierna and A. Magnéli, Acta Chem. Scand., 11, 1641 (1957).

4. B. G. Hyde, D. J. M. Bevan, and L. Eyring, Proc. Roy. Soc., 259, 583 (1966).

5. P. Vallet and P. Raccah, C.R. Acad. Sci. Paris, 258, 3679 (1964).

6. M. S. Jenkins, R. P. Turcotte and L. Eyring, "Chemistry of Extended Defects in Non-Metallic Solids," (L. Eyring and M. O'Keeffe, eds.) North Holland Publishing Co., Amsterdam, 1970.

7. B. E. F. Fender and F. D. Riley, J. Phys. Chem. Solids, 30, 793 (1969).

8. A. R. Ubbelohde, J. Chim. Phys., 33 (1966).

9. P. A. Faeth and A. F. Clifford, J. Phys. Chem., 67, 1453 (1963).

10. J. Kordis and L. Eyring, J. Phys. Chem., 72, 2044 (1968).

11. A. D. Burnham and L. Eyring, J. Phys. Chem., 72, 4415 (1968).

12. R. P. Turcotte and L. Eyring, to be published.

13. J. O. Sawyer, B. G. Hyde and L. Eyring, Bull. Soc. Chim. France, 1190 (1965).

14. B. T. M. Willis, Nature, 197, 755 (1963).

15. B. Belbeoch, J. C. Boivineau and P. Perio, J. Phys. Chem. Solids, 28, 1267 (1967).

16.   W. L. Roth, Acta Cryst., 13, 140 (1960).

17.   J. Manenc, J. Bougeot and J. Benard, C.R. Acad. Sci. Paris, 256, 931 (1963).

18.   F. Koch, and J. B. Cohen, Acta Cryst., B25, 275 (1969).
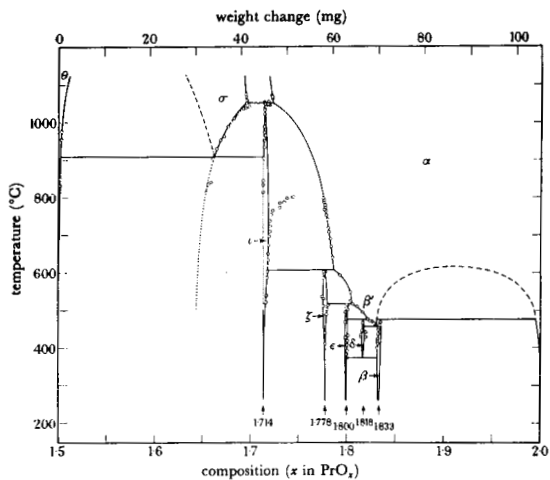
Figure 1.   Phase Relations in the
Praseodymium Oxide System.
(Hyde et al.)
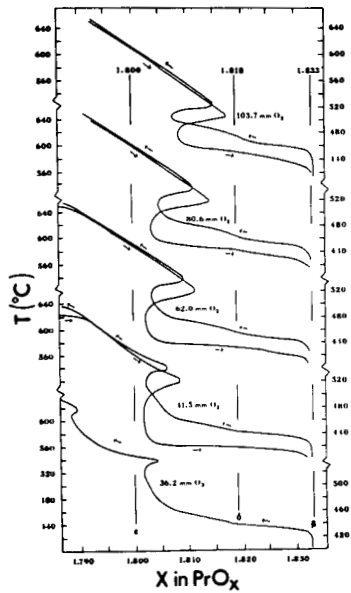
Figure 3. Isobars in the
Epsilon Alpha Region.
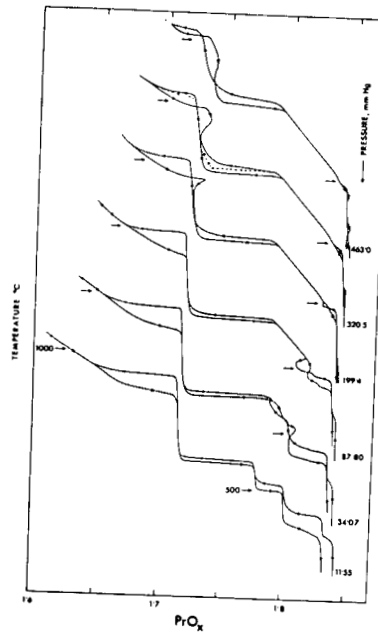
Figure 2. Representative Isobars
in Praseodymium Oxide System.
(Kordis and Eyring)
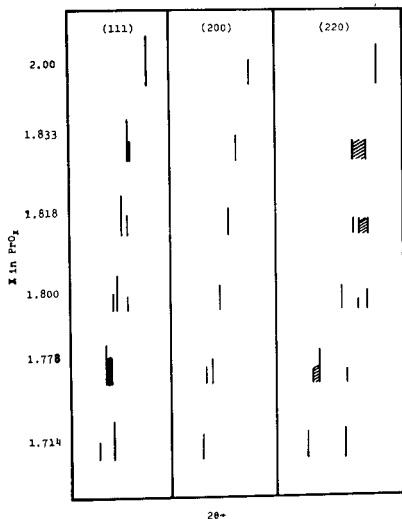
Figure 4. Main Reflections
of Ordered Phases in the
PrO_x-O_2 System.

Figure 8. Diffraction Patterns
in the Epsilon-Alpha
Pseudophase Region
at 463°.
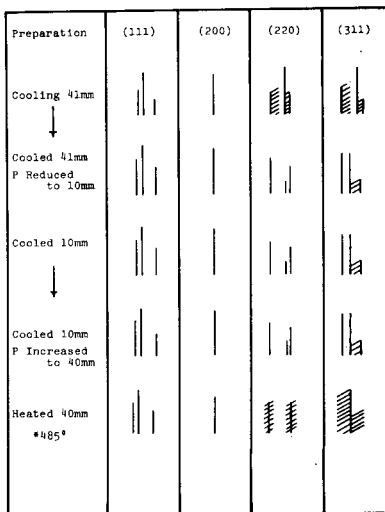
Continuous High Temperature Diffraction Patterns
in the Epsilon Alpha Region
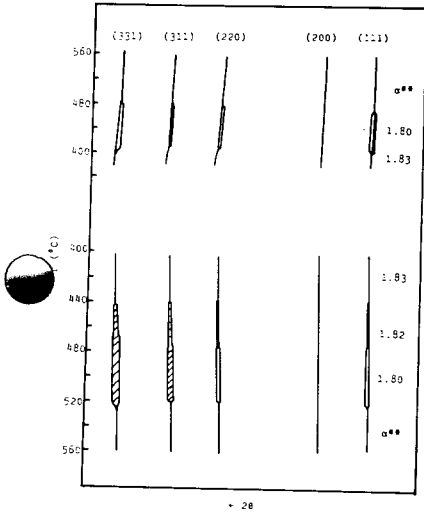
Figure 5.
41 mm O$_2$ with
Decreasing t
(top) and
Increasing
t (bottom).
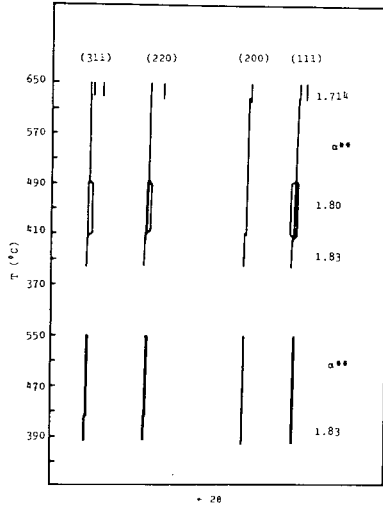
Figure 6.
30 mm O$_2$ (top)
and 80 mm O$_2$
(bottom).
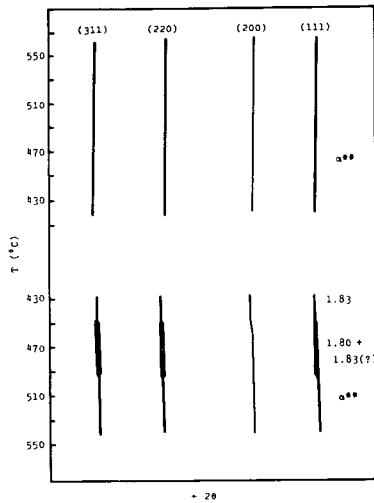
Figure 7. 100 mm
O$_2$ for Decreasing
t (top) and Increasing
t (bottom).

-191-
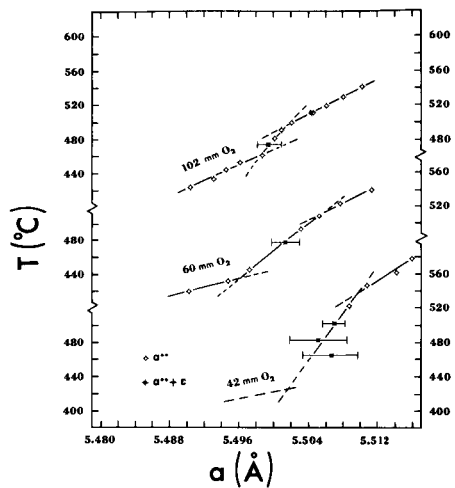
Figure 9. Lattice Parameter Variation
with Temperature at Different Pressures.
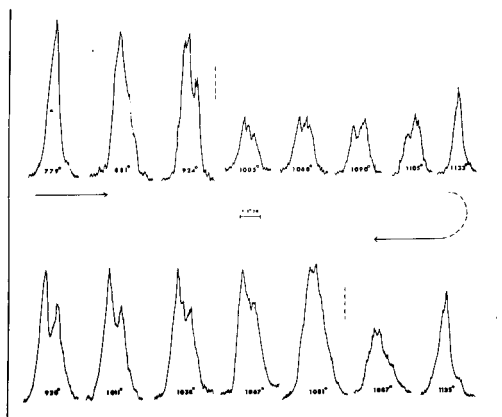
Figure 10. (220) Reflections in the Iota Pseudo-
phase Region at 635 mm O_2.

THULIUM OXIDE MICROSPHERE PREPARATION
AND CHARACTERIZATION

C. J. Ambrose

Donald W. Douglas Laboratories
McDonnell Douglas Astronautics Company - Western Division
2955 George Washington Way
Richland, Washington 99352

Abstract

Thulium-170 is a potential candidate for a short duration radioisotope fuel for a heat source. An experimental program was initiated to prepare microspheres of thulia, coat the microspheres with tungsten, and irradiate the non-radioactive thulia-169 to form radioactive thulium-170.

Modifications in the sol-gel process were necessary to produce thulia microspheres. The thulia microspheres were fragile and necessitated a careful handling technique. Dense microspheres of $^{169}Tm_2O_3$ were achieved by calcining the microspheres at 1400° to 1500°C in air. Shrinkage measurements on the spheres after removal from the alcohol showed an overall reduction of 43% at the elevated temperatures. The load required to crush the microspheres was about 1500 grams for microspheres fired at 1000° or 1100°C. X-ray analysis of microspheres fired at various temperatures yielded the following results: 500°C in vacuum-amorphous, 1000°C in air-cubic, and 1500°C in air-cubic phases. High-temperature-fired microspheres were used for the testing program.

Coating experiments were conducted using a chemical vapor deposition technique to apply a uniform dense tungsten deposit. Hydrogen and tungsten hexafluoride were thermally decomposed in the fluidized bed of thulia microspheres to form the tungsten coating. Approximately a 20 volume-percent coating was applied on the spheres.

Introduction

$^{170}Tm_2O_3$ is being considered as a potential radioisotope fuel for heat sources. It has the advantage that the fuel form can be prepared in a non-radioactive laboratory because thulium-169 is not radioactive. After the thulium has been formed into the desired fuel form, it is irradiated in a reactor, and neutrons convert the Tm^{169} to Tm^{170}.

-193-200

Upon removal from the reactor, the fuel is encapsulated and used as a radioisotope heat source. Thulia-170 is advantageous for short-duration missions because it has a 0.35 yr half-life. The heat emitted by ^{170}Tm$_2$O$_3$ is 1.2 watts/gram.

The sol-gel process was used to form microspheres of thulium oxide. These microspheres were coated with tungsten using a chemical vapor deposition technique. Irradiation tests were performed to measure the radiation decay of the tungsten on the microspheres, and this was compared to uncoated microspheres. A radioisotope heat source was fabricated using ^{170}Tm$_2$O$_3$ microspheres.

Experimental

Formation of microspheres is best accomplished by the sol-gel process. Figure 1 shows the basic steps used in the production of sol-gel microspheres for thulium. Thulium sol is prepared by dissolving the Tm(NO$_3$)$_3$ solution, then precipitating with NH$_4$OH (50% excess of 8 $\underline{M}$) solution with rapid stirring. The precipitate is then washed with distilled water until the pH of the filtrate is 9.5 or lower. Acceleration of crystal growth in the solution was achieved by heating at 80°C for one hour (Reference 1). Excess water was removed by vacuum evaporation of the sol. A 0.5-molar sol was produced after concentration, and this was used in microsphere formation. The technique for microsphere formation was described in a previous paper.[2]

Calcining the microspheres caused major problems in this process development. After the microspheres were removed from the drying alcohol and subjected to a routine[2] methanol wash to remove excess alcohol, they consistently split into two halves. This problem was solved by air-drying the microspheres. While the microspheres were vacuum outgassed up to 500°C, the most critical region of the heating cycle was up to 400°C. Too fast a heating ramp resulted in broken microspheres. Above 400°C, microspheres showed no detrimental effects from thermal shock or transients. Figure 2 shows thulium oxide microspheres formed by the sol-gel process.

These calcined microspheres were coated with tungsten using a chemical vapor deposition technique. Figure 3 is a schematic of the CVD system. Microspheres are loaded in the top of the chamber, and the furnace is heated to 500°C. An upward flow of reactant gases suspends the microspheres in a fluidized bed for coating. Decomposition occurs according to the chemical equation:

$$WF_6 + H_2(\text{excess}) \xrightarrow{500°C} W_{(s)} + HF_{(g)} + H_{2(g)}$$
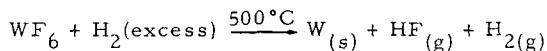
The HF gas is trapped in NaF pellets and excess hydrogen is burned. Microspheres are removed from the reaction chamber by stopping the flow of gas; the coated microspheres then fall into the receiver at the bottom of the chamber.

Discussion

Analysis of the amount of shrinkage the microspheres experienced as functions of heat treatment were conducted. Figure 4 shows the results of these experiments. It is obvious from this test that there is quite a change in microsphere size. Ten microspheres were used for these tests throughout the entire experiment, and up to 1000°C, the spheres were isolated in a fixed position in the boat. Average values are reported for the microspheres because the average deviation is less than one percent. Above 1000°C, the microspheres were fired in a platinum crucible. Diametral changes were measured with a calibrated micrometer eyepiece on a microscope. After these tests were completed, the microspheres were used for crush strength measurements.

Mechanical integrity of microspheres is determined by crush strength. [3] Briefly, this measurement is performed by placing a microsphere between two flat surfaces and measuring the load required to break or crush the sphere. Figure 5 shows the crush strength values of the microspheres fired at various temperatures. Essentially, the shape of the curve is identical to previous experiments

with other materials.[3] The low-fired material is amorphous, while the high-fired spheres are crystalline. Maximum crush strength values are around 1500 grams at 1000° to 1100°C. Above this temperature the crush strength decreases to about 500 grams. With high-temperature firing (1400°C and higher), the microspheres approach theoretical density.

Some high-density microspheres were coated with tungsten prior to irradiation. Using the chemical vapor deposition process, a 20 volume-percent uniform tungsten deposit was achieved. The tungsten encircles the $^{170}Tm_2O_3$ microspheres with an impermeable metal coating, which can be considered as the primary container for the radioactive fuel.

The crystal structure of the microspheres was determined by x-ray analysis. Microspheres which had been vacuum outgassed at 500°C showed an amorphous structure. Microspheres air-calcined at 1000° and 1500°C were analyzed; these showed a cubic phase at both temperatures. Warshaw and Ray[5] analysis of the rare-earth sesquioxide showed a continuous cubic phase for thulium oxide.

Conclusions

The sol-gel process was successfully adapted to the production of Tm_2O_3 microspheres. Thulia microspheres were significantly more fragile than samaria, promethia, neodymia, erbia, or plutonia-239 microspheres produced by the sol-gel process. Problems were encountered in the vacuum outgassing of the microspheres up to 500°C. A very slow controlled heat rate up to 400°C eliminated the cracking problem of the microspheres, and thermal shocks after this treatment did not affect the microspheres.

Characterization of the thulia microspheres was performed. A maximum crush strength of about 1500 grams was observed for spheres calcined at 1000° and 1100°C. X-ray analysis of the microspheres shows an amorphous phase up to 500°C and a cubic phase existing at

1000°C and higher. A very rapid shrinkage of about 20% was observed between 200° and 400°C, and an overall shrinkage of about 43% was determined for high-temperature-calcined microspheres.

References

1. C. J. Hardy, S. R. Buxton, and T. E. Willmarth. Chemical Electron Optical Studies on Sols, Gels, and Oxide Microspheres Prepared from Rare-Earth Oxides. Proceedings of the Sixth Rare-Earth Research Conference, Gatlinburg, Tenn., 175, 1967.

2. C. J. Ambrose and R. L. Andelin. Preparation of Rare-Earth Oxide Microspheres by the Sol-Gel Process. Trans Am. Nucl. Soc., 10, 429, 1967, MDAC Paper No. 5002.

3. C. J. Ambrose. Characterization of Samaria and Neodymia Microspheres Prepared by the Sol-Gel Process. Proceedings of the Seventh Rare Earth Conference, Coronado, Calif., 687, 1968, MDAC Paper No. 5134.

4. R. D. Allen and W. M. Lysher. Nuclear Insulating Powders Evaluated with Radioisotope Sources. Presented to Am. Ceramic Soc., Seattle, Washington, 1969, MDAC Paper No. 10,201.

5. I. Warshaw and R. Ray. Polymorphism of the Rare-Earth Sesquioxides. J. Phy. Chem. 65 (11), 2048, 1961.

```
┌─────────────────────┐      ┌─────────────────────┐      ┌─────────────────────┐
│ DISSOLVE Tm(NO3)3   │─────▶│ PRECIPITATE WITH    │─────▶│ WASH PRECIPITATE AND│
│ IN WATER            │      │ 8 MOLAR NH4OH (50%  │      │ AGE SOL AT 80°C FOR │
│                     │      │ EXCESS)             │      │ 1 HR                │
└─────────────────────┘      └─────────────────────┘      └─────────────────────┘

┌─────────────────────┐      ┌─────────────────────┐      ┌─────────────────────┐
│ FORM MICROSPHERES   │◀─────│ HEAT IN VACUUM AT   │◀─────│ CALCINE IN AIR AT   │
│ AND DRY IN ALCOHOL  │      │ RATE OF 100°C/HR TO │      │ 1300°C OR HIGHER    │
│ FOR 0.5 HR          │      │ 500°C               │      │                     │
└─────────────────────┘      └─────────────────────┘      └─────────────────────┘
```
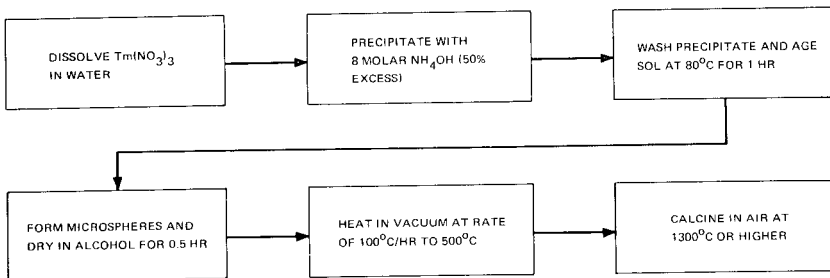
Figure 1. Sol–Gel Preparation of Tm_2O_3 Microspheres
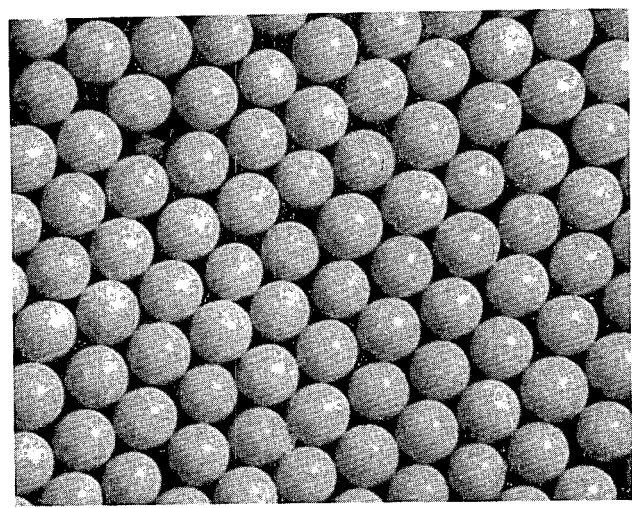
Figure 2. Sol-Gel Tm_2O_3 Microspheres (~180 Microns)
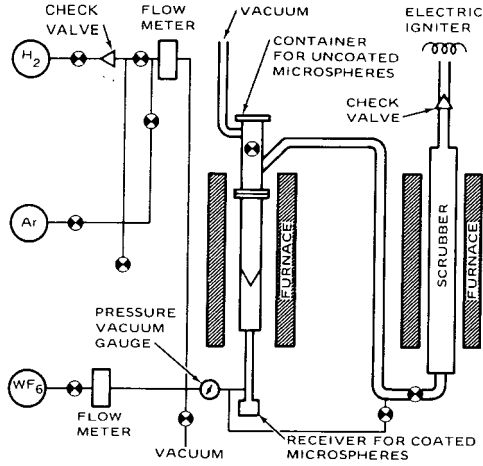
Figure 3. Chemical Vapor Deposition Apparatus
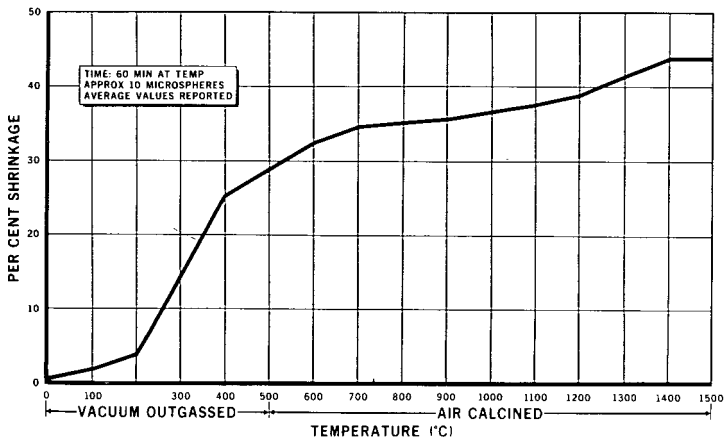
Figure 4. Shrinkage of Microspheres as a Function of Temperature
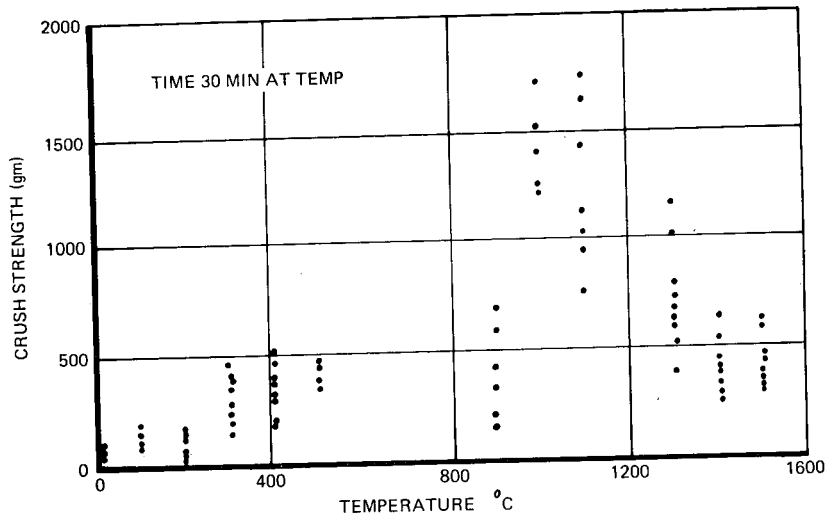
Figure 5. Crush Strength of Tm_2O_3 Sol-Gel Microspheres

PROPERTIES OF THULIUM OXIDE MICROSPHERES PREPARED BY SOL-GEL METHODS*

S. R. Buxton, M. H. Lloyd, and T. E. Willmarth

Oak Ridge National Laboratory
Oak Ridge, Tennessee 37830

617 1000

ABSTRACT

The sintering behavior of thulium oxide microspheres prepared by sol-gel techniques has been investigated. In these studies, the micelles of the hydrosols used to prepare the microspheres varied from highly distinctive crystalline forms to very small amorphous particles.

A procedure for preparing lanthanide oxide microspheres of controlled particle size by sol-gel techniques has been previously described. This procedure utilizes highly crystalline sols; however, with suitable modifications, it can also be used to prepare microspheres from sols composed of small amorphous particles.

Several properties relative to sintering behavior were found to be functions of the sol crystalline habit. The results suggest that the characteristics of lanthanide oxide microspheres can be tailored to provide the desired variations in crushing strength, density, porosity, and densification temperature.

INTRODUCTION

Calcined microspheres of lanthanide oxides, prepared by sol-gel techniques have characteristics that are desirable in certain types of scientific investigations. The potential usefulness of these materials has stimulated interest in their production.

A process for preparing lanthanide hydroxide sols composed of crystalline micelles and for converting these sols into lanthanide oxide microspheres of controlled size has been described previously.[1] An essential part of the original procedures consisted of digesting freshly precipitated lanthanide hydroxide to convert the amorphous solids into small crystallites which spontaneously changed the

gelatinous solids into a very fluid sol. It has been found that fluid sols can be formed from the amorphous solids and that microspheres formed from these "amorphous sols" have noted differences in sintering behavior as compared with microspheres formed from "crystalline sols". The capability of producing "amorphous sols" not only makes it possible to prepare microspheres with a variety of properties, but it also extends the versatility of these techniques to the heavy lanthanide elements which have long crystallization conversion times.[2] The investigations reported in this paper were made with thulium hydroxide, which remains amorphous for greater than five months at room temperature but most of which converts to rectangular crystalline platelets when digested at 80°C for 24 hr.

Microspheres formed from "amorphous sols" and calcined at 1000°C were relatively dense ($\sim$ 85% of the theoretical crystal density) and exhibited unusually high crushing strengths. Microspheres formed from "crystalline sols" and calcined at 1000°C were very weak and porous with essentially all the voids connected to the sphere surface through pores of uniform diameter; calcination at 1450°C was required to sinter these microspheres to high density and good strength. Microspheres prepared from mixed "amorphous and crystalline sols" had somewhat intermediate properties but were more nearly like those produced from "crystalline sols".

EXPERIMENTAL

The rare earth sol process used in these experiments has been described previously.[1] Briefly, this procedure involves precipitation of the metal hydroxide by adding a dilute solution of the metal nitrate to a large excess of 8 $\underline{M}$ NH_4OH, washing the precipitate until the final wash water pH is 9.0 - 9.5, and digesting the gelatinous precipitate to convert it to a fluid sol which can be concentrated and formed into microspheres. All of the lanthanide hydroxides originally form as small, amorphous particles 20 to 50 $\overset{\circ}{A}$ in diameter which are converted to small crystallites during the digestion step. It is this conversion to crystalline micelles that produces the sol. The time required for the conversion process increases with

increasing atomic number and varies from a few minutes for the lightest lanthanides to days, and even months for the heaviest lanthanides.[2]

It was found that crystallization was not necessary but that fluid sols can also be made by vigorous agitation of the washed, gelatinous precipitates. These sols composed of amorphous materials are referred to as "amorphous sols". With the exception of lanthanum, cerium, praseodymium, and neodymium hydroxides which convert to crystalline material in 1 to 4 hr, most of the lanthanide hydroxide sols prepared in this manner retain their amorphous characteristics for long periods of time.

Amorphous thulium hydroxide sols prepared for these studies did not crystallize within 5 months at 25°C. Since most sols were formed into microspheres within 24 hr, thulium hydroxide was completely amorphous. The 20 to 50 Å particles comprising a typical thulium hydroxide sol of this type are shown in Fig. 1. Electron diffraction patterns of this material show only broad, diffuse lines, which are characteristic of amorphous material.

Thulium hydroxide sols composed primarily of crystalline particles and referred to in this paper as "crystalline sols" were prepared by digesting the washed hydroxide precipitate for 24 hr at 80°C. An electron micrograph (Fig. 1) illustrates the extremely thin rectangular platelet forms, varying from about 2000 to 4000 Å on a side, that are present. Some small, unconverted amorphous-appearing particles can also be seen; however, it has been found that further aging does not completely eliminate amorphous material and frequently results in the formation of unstable colloids.

Since the "crystalline sols" were very fluid they were concentrated to ∼0.8 $\underline{M}$ by evaporation at 80°C. The "amorphous sols" were not quite so fluid and ∼0.4 $\underline{M}$ sols were used to form microspheres. Microsphere forming techniques have been described previously[1,3] and will not be discussed here. The drying solvent used to convert the sols to gel spheres was composed of 80–20 vol % mixture of 2-ethyl-1-hexanol and 2-octanol containing 0.1 vol % Span 80 (Atlas Powder Co.) and 0.2 vol %
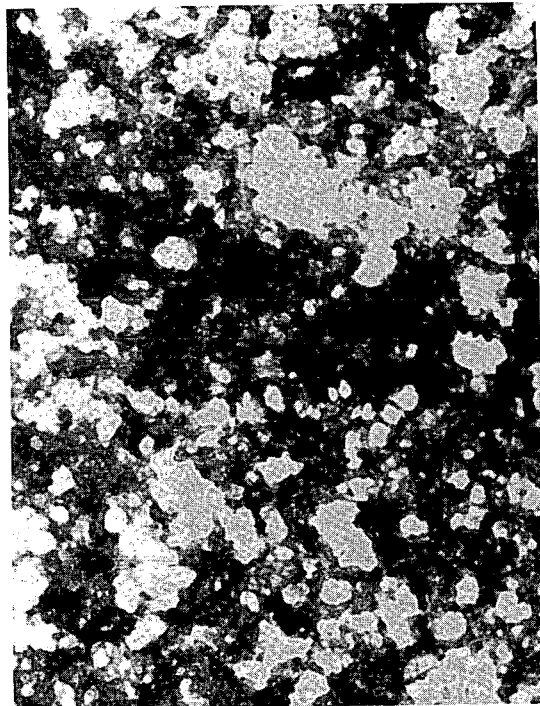
AMORPHOUS ⊢——⊣ CRYSTALLINE ⊢——⊣
1850 Å 1850 Å

Figure 1. Electron Micrographs of Thulium Hydroxide

Amine-O (Geigy Chemical Co.). The gel microspheres were air dried at 100°C to remove residual solvent prior to calcination. Typical products calcined at 1450°C are shown in Fig. 2.

The major objective in this study was to evaluate microspheres that were prepared from "amorphous," "crystalline," and mixed "amorphous-crystalline" sols and that were calcined at 1000, 1200, and 1450°C. The calcined products were evaluated by optical microscopy, X-ray diffraction, and transmission and scanning electron microscopy. Density, pore volume, and pore size distribution were determined by mercury porosimetry. Crushing strengths were determined for spheres 260 μ in diameter.

RESULTS AND DISCUSSION

Products with relatively high densities, low porosities, and excellent crushing strengths are obtained when spheres prepared from "amorphous sols" are fired at temperatures as low as 1000°C. On the other hand, spheres prepared from "crystalline sols" exhibit very low density, low crushing strength, and high porosity on being fired at 1000°C. This difference appears to result, primarily, from differences in the geometric arrangement of the crystallites in the gel sphere since after firing there is no significant difference in crystallite size, as determined by X-ray line broadening and since the oxide form was determined to be greater than 90% cubic Tm_2O_3 (A_0 = 10.488) in all cases.

Several other variations in microsphere properties are indicated by the data given in Table 1. The density of spheres prepared from "amorphous sols" increases only slightly (i.e., from 86% of theoretical* to 90% of theoretical) when the firing temperature is increased from 1000°C to 1450°C. On the other hand, products obtained from "crystalline sols" have a very low density on firing at 1000°C (i.e., 33.5% of theoretical) but exhibit almost theoretical density (99.5%) on firing at 1450°C.

---

*Theoretical crystal density.

Table 1. Properties of Tm_2O_3 Microspheres Prepared from Thulium Hydroxide Sols

	Calcination Temperature (°C)		
	1000	1200	1450

Microspheres Prepared from "Amorphous Sols"

Density	7.63	8.12	7.96
% theoretical crystal density*	85.9	91.4	89.6
Surface-connected porosity, %	9.5	3.0	2.7
Crushing strength, g	1860	1800	624
Crystallite size, Å	300–360	730–850	1350–1440

Microspheres Prepared from "Crystalline Sols"

Density	2.98	3.82	8.84
% theoretical crystal density	33.5	43.0	99.5
Surface-connected porosity, %	64.6	58.5	0.64
Crushing strength, g	< 170	< 180	745
Crystallite size, Å	350–575	725–1035	1100–1580

Microspheres Prepared from Mixed "Amorphous-Crystalline Sols"

Density	4.14	4.08	8.53
% theoretical crystal density	46.6	45.8	96.1
Surface-connected porosity, %	55.7	56.1	0.5
Crushing strength, g	< 180	185	584
Crystallite size, Å	530–850	830–1330	1370–1625

*Density of Tm_2O_3 is considered to be 8.884 g/cm^3 at 25°C.[4]
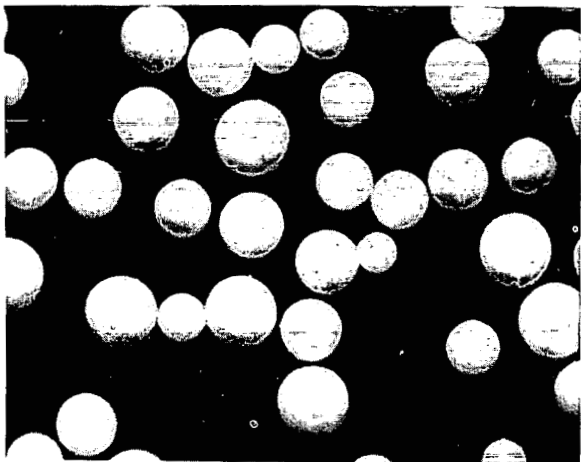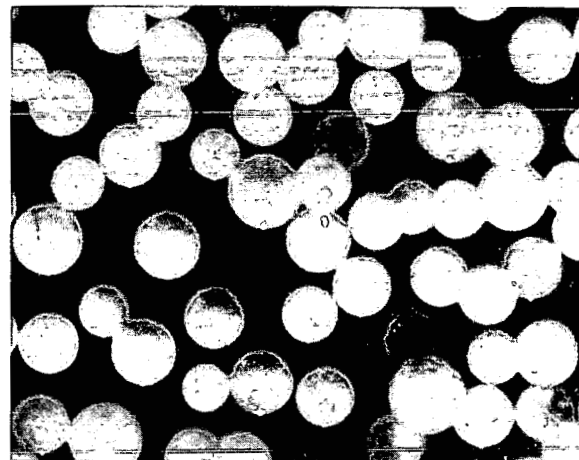
PREPARED FROM AMORPHOUS SOL   PREPARED FROM CRYSTALLINE SOL

150 μ

Figure 2. Photomicrograph of Thulium Oxide Microspheres Fired at 1450°C.

Microspheres prepared from "amorphous sols" exhibit a high loss in crushing strength from 1860 g for 260-μ-diam spheres calcined at 1000°C to only ~600 g for spheres calcined at 1450°C; however, this agrees favorably with the strength of 1450°C microspheres prepared from "crystalline sols" and calcined at 1450°C.

Microspheres formed from "amorphous sols" exhibit a decrease in surface connected porosity from 9.5% at a calcination temperature of 1000°C to 2.7% at 1450°C with very little increase in particle density. This suggests a tendency for surface connected pores to seal at 1200°C or less. This behavior would interfere with normal pore shrinkage and prevent migration of internal voids to the surface which occurs in "crystalline sol" material.

Scanning electron micrographs and electron micrographs of replicas of external sphere surfaces demonstrate a substantial difference in the surface appearances of the two types of products (Fig. 3). Spheres prepared from "amorphous sols" exhibit an extremely rough platelet type of surface, whereas spheres prepared from "crystalline sols" are characterized by a relatively smooth surface. Electron micrographs of replicas of fractured surfaces of microspheres calcined at 1000°C and at 1450°C are shown in Fig. 4. Fractographs of both types of spheres calcined at 1000°C present the same general appearance and indicate approximately the same crystallite size. The fractograph of 1450°C-fired spheres prepared from "amorphous sols" shows several spherical voids. The largest void has an apparent diameter of about 6000 Å. In these and other fractographs, voids of this size are prevalent in products prepared from amorphous material, but are nearly absent in products made from crystalline material. Fractured surfaces of microspheres prepared from "amorphous sols" indicate a highly stressed internal structure and possibly numerous stacking faults and dislocations. These surfaces look very much like those seen in broken fragments of untempered glass. There is also an indication of greater grain growth for these spheres than for those prepared from "crystalline sols".
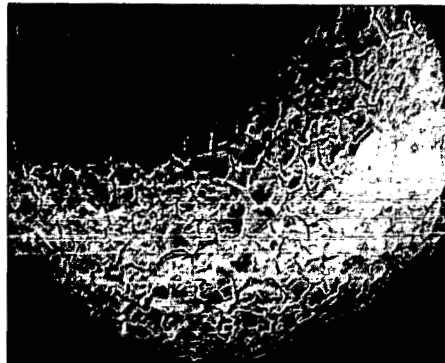
(A) Scanning electron micrograph of Amorphous Sol Product. 500 X.

(B) Scanning electron micrograph of Crystalline Sol Product. 500 X.

(C) Replica of Amorphous Sol Product, 12000 X.

(D) Replica of Crystalline Sol Product, 54000 X.

Figure 3. External Surface of Thulium Oxide Microspheres Fired at 1000° C.

(A) 1000°C AMORPHOUS ⊢——⊣ 1850 Å
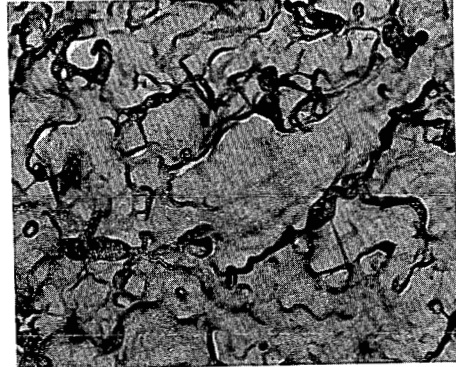
(B) 1000°C CRYSTALLINE ⊢——⊣ 1850 Å
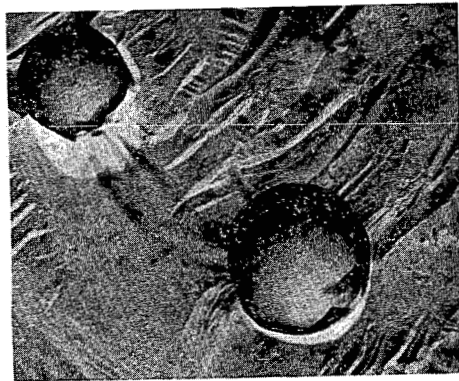
(C) 1450°C PREPARED FROM AMORPHOUS SOLS

(D) 1450°C PREPARED FROM CRYSTALLINE SOLS

Figure 4. Electron Micrographs of Replicas of Fractured Surfaces of Fired Tm_2O_3 Microspheres.

Pore size analysis indicates another difference in the two products. Spheres prepared from amorphous material exhibit pore diameters that vary from 0.01 to nearly 20 microns; size distribution appears to be random within this range. In contrast, pore diameters of spheres prepared from "crystalline sols" are quite uniform and usually are within $\pm$ 0.1 μ although the pore size does vary from sol to sol within the range of 0.1 to 0.5 μ.

Spheres formed from "amorphous sols" tend to crack during calcination. This undesirable property is dependent on particle size. For example, crack-free spheres with diameters of about 300 μ can be produced; however, most of the spheres with larger diameters will be cracked. Spheres prepared from crystalline material do not exhibit this phenomenon.

Spheres prepared from mixed "amorphous-crystalline" sols were very much like those prepared from "crystalline sols" in most respects. However, the densities of products calcined at 1000°C and at 1200°C were higher (see Table 1), and most of the spheres with diameters as large as 450 μ did not crack during calcination. Crushing strength was not improved to a practical extent, and a firing temperature of 1450°C was required for high density. Pore size distribution was similar to that observed for spheres prepared from "crystalline sols".

REFERENCES

1. C. J. Hardy, S. R. Buxton, and M. H. Lloyd, Preparation of Lanthanide Oxide Microspheres by Sol-Gel Methods, ORNL-4000 (August 1967).

2. R. G. Haire and T. E. Willmarth, Trends and Differences in the Crystallization Behavior of Lanthanide Hydroxide Preparations, ORNL-TM-2387 (October 1968).

3. R. G. Wymer and D. A. Douglas, Status and Progress Report for Thorium Fuel Cycle Development for Period Ending December 31, 1964, ORNL-3831, pp. 35-81 (May 1966).

4. E. H. Swanson, I. M. Cook, T. Isaacs, and E. H. Evans, Standard X-Ray Diffraction Powder Patterns, National Bureau of Standards Circular 539, Vol. 9, pp. 58-59, 1960.

STUDIES OF THE EUROPIUM-OXYGEN-FLUORINE
AND SAMARIUM-OXYGEN-FLUORINE SYSTEMS[*]

R. G. Bedford and E. Catalano

Lawrence Radiation Laboratory, University of California

Livermore, California 94550

ABSTRACT

A portion of the ternary system $Eu-Eu_2O_3-EuF_3$ has been investigated by equilibrating $EuO-EuF_3$ and $EuO-EuF_2$ mixtures at 1500°C and examining the products with a polarizing microscope and by x-ray diffraction. The composition of the liquid-solid boundary was not measured directly, but has been estimated. A phase diagram is presented for that part of the system studied. No ternary compounds are formed with Eu in an oxidation state lower than +3 in samples cooled from 1500°C.

Several compositions of the $Eu_2O_3-EuF_3$ and $Sm_2O_3-SmF_3$ binary systems were examined using differential thermal analysis and x-ray powder diffraction. In these systems, at least one intermediate phase (and probably two or more) in addition to LnOF is stable. These additional phases all lie on the fluoride side of LnOF. At temperatures above 600°C, solid solutions extend approximately from $LnO_{0.8}F_{1.4}$ to $LnO_{0.6}F_{1.8}$.

INTRODUCTION

A few years ago we observed anomalous magnetic behavior in EuF_2 which was associated with trace impurities in the single crystals.[1] The magnetic and optical properties of the inclusions in the EuF_2 crystals did not appear to correspond to any known Eu compound. This prompted us to investigate the $Eu-EuF_3-Eu_2O_3$ system to attempt to identify the impurity since oxygen seemed to be the most probable contaminant. The EuF_2-EuF_3 and the $EuO-Eu_2O_3$ binary systems have been described in detail elsewhere.[2-5]

Bevan et al.[6] have discussed the lanthanon oxyfluorides and reviewed the literature on these systems. Oxyfluorides have been reported for all of the Ln elements and Yb and the structures for the stoichiometric MOF compounds at room temperature for all but Ce, Tm, Yb, and Lu seem to be established as the rhombohedral LaOF-type

---

-213-

described by Zachariasen[7] for LaOF and YOF.[6-15] For La and Y, Zachariasen[7] found tetragonal solid solutions $MO_{1-x}F_{1+2x}$ (0.0 < x < 0.3) in addition to the stoichiometric rhombohedral LaOF and YOF. Bevan et al.[6] have shown that for the Y, Sm, Gd, and Er oxy-fluorides, the composition region between the stoichiometric MOF and the trifluoride is much more complicated than had been previously as-sumed. A report of the continuing investigation of the intermediate composition region and the transition of stoichiometric MOF from rhombohedral to cubic (fluorite) for La, Nd, Sm, and Gd has been given by Brauer and Roether.[14] Recently, Shinn and Eick[15] have published a paper on the rhombohedral-to-cubic transition for MOF compounds (M = La, Nd, Sm, Eu, Gd, Tb, Dy, Ho, Er, and Y).

Detailed investigation of the phase relationships in the extremely complex oxyfluoride systems was not attempted here since we were primarily interested in the possible existence of a compound containing Eu in the divalent state. However, differential thermal analysis and Debye-Scherrer x-ray powder diffraction studies were made for several compositions in the $EuF_3-Eu_2O_3$ system, and the results provide evi-dence for previously unknown oxyfluoride phases of Eu^{III}, supporting the findings of Bevan, Brauer and co-workers[6,14] that the region between stoichiometric MOF and the trifluorides for Ln elements is occupied by a number of discrete phases which undergo transitions or dispropor-tionation reactions on heating. Similar studies were attempted with the analogous Sm system, but useful quantitative information was ob-tained only for stoichiometric SmOF.

Our present study shows no ternary compounds in the $Eu-EuF_3-Eu_2O_3$ system with Eu in an oxidation state lower than +3, and that the only phase in this system which resembles in any respect the impurities in the EuF_2 crystals of Ref. 1 is Eu_3O_4. The color and structure of Eu_3O_4 are consistent, but the magnetic properties do not correspond to those of the impurity material. Recently, Shafer and Kuptsis[16] have published convincing evidence that the impurity in EuF_2 which was responsible for the anomalous magnetic behavior observed in Ref. 1 and other work was a sulfide of Eu.

THE EuF_2-EuO SYSTEM

EuF_2 was prepared by hydrogen reduction of EuF_3 in a Mo container. EuO was made by reduction of Eu_2O_3 by Eu in a sealed Mo capsule. These materials are described in more detail in Refs. 2 and 5.

Mixtures of EuO and EuF_2[*] were encapsulated in Mo by electron bombardment welding (EBW). The samples were heated to 1500°C in a vacuum induction furnace, held at that temperature for at least 2 hr and cooled quickly by turning off the power and introducing argon or helium. About 2 min were required for the temperature to fall below 750°C. The resulting products were examined by x-ray powder diffraction and optical microscopy.

The EuF_2-EuO mixtures had all completely melted. Microscopic examination of the products showed the composition 0.4 EuF_2—0.6 EuO to be very near the eutectic. Samples with larger proportions of EuF_2 showed the eutectic structure in a matrix of EuF_2. X-ray analysis showed the products of all of these runs to be EuO (cubic), a = 5.14_4 and EuF_2 (fcc), a = 5.84_3.

THE EuF_3-Eu_2O_3 AND SmF_3-Sm_2O_3 SYSTEMS

Mixtures of EuF_3 and Eu_2O_3 or SmF_3 and Sm_2O_3 were sealed in Pt-10%Rh capsules by EBW and heated to 1500°C in an induction furnace. The products were crushed and resealed in Pt-10Rh capsules, again heated to 1500°C for 2 hr and rapidly cooled by turning off the furnace power. Starting materials were nominal 99.9% oxides and trifluorides which had been heated in air or under HF to reduce contamination and stored in desiccators.[2,5]

Samples from the above preparations were examined by x-ray powder diffraction, optical microscopy, and DTA. A description of the DTA apparatus and procedures is given in Ref. 3. Samples for DTA were encapsulated in Pt-10Rh containers by EBW in a vacuum of ~10^{-5} torr. Measurements were made at heating rates of 10°C min^{-1} from 200° to 1500°C.

Our observations on EuF_3-Eu_2O_3 and SmF_3-Sm_2O_3 are insufficient to provide a complete understanding of these systems. Seven compositions in each system were studied. Optical examination did not provide useful information because of the similarity of the appearance of all phases under either unpolarized or polarized light. Refractive

---

[*] The compositions are plotted in Fig. 2.

index measurements would be required to distinguish between the various phases. Since DTA measurements were limited to temperatures below 1500°C, melting was observed only for compositions rich in trifluorides. However, we did observe a number of effects which may help to provide a better understanding of these systems. A summary of our observations and interpretations is given in Table I, and a tentative phase diagram for the Eu_2O_3-EuF_3 system is presented in Fig. 1. Other possible phase diagrams are consistent with the observations. The drawing is presented primarily to describe the general behavior of the binary system and to define assumptions used in interpreting the Eu-EuF_3-Eu_2O_3 ternary system.

Reversible thermal effects were observed beginning at 501°C for SmOF and at 503°C for EuOF (Table I). The temperatures for these effects are in good agreement with those reported by Brauer for the rhombohedral-cubic transitions in oxyfluorides of La, Nd, Sm, and Gd.[14] Brauer found these transitions in the range from 450 to 550°C with the value for Sm close to 500°C. The thermal effect beginning at 481°C in the sample with composition $EuO_{0.9}F_{1.2}$ is probably due to the same transition, lowered in temperature by solution of fluoride.

X-ray analyses indicated that except for the sample of stoichiometric SmOF, the Sm oxyfluoride mixtures did not reach equilibrium. Mixtures of composition $SmO_{0.9}F_{1.2}$, $SmO_{0.8}F_{1.4}$ and $SmO_{0.7}F_{1.6}$ appeared to be mixtures of SmOF (rhombohedral) + Sm_2O_3 (bcc) after heating at 1500°C as described above. We observed thermal effects in these samples which were similar to those seen in the Eu samples, but with lower intensities.

The Eu_2O_3-EuF_3 system was apparently better behaved than the corresponding Sm system, although it is possible that the effects observed in both systems correspond to metastable equilibria. Observation of the thermal effect at 720°C for $EuO_{0.9}F_{1.2}$ and $EuO_{0.8}F_{1.4}$ and the absence of the rhombohedral-cubic transition in $EuO_{0.8}F_{1.4}$ implies the existence of an intermediate compound such as that reported by Brauer[14] for the Sm system. The thermal effect at 1293°C for $EuO_{0.3}F_{2.4}$ was due to melting, confirmed by visual inspection of the

samples which had been heated to 1500°C in sealed Pt-10Rh containers before being loaded into the DTA capsules. The $SmO_{0.3}F_{2.4}$ sample also was completely melted at 1500°C and none of the other samples showed any evidence even of partial melting after being heated to 1500°C. The small temperature range of the thermal effect indicates that the eutectic composition lies very close to $EuO_{0.3}F_{2.4}$.

The disappearance of the thermal effect corresponding to the rhombohedral-to-cubic transitions of the stoichiometric oxyfluorides in samples of higher fluoride concentration is at variance with the x-ray results which indicates the presence of LnOF (rhombohedral) at room temperature for all compositions down to $LnO_{0.6}F_{1.8}$ in both the Sm and Eu systems. A possible explanation for this discrepancy is that phases identified as SmOF (rhombohedral) and EuOF (rhombohedral) in the fluoride-rich samples were actually compounds with closely related structures in the composition range $LnO_{0.9}F_{1.2}$ to $LnO_{0.6}F_{1.8}$. The structures of all of these phases reported by Brauer are closely related to the fluorite structure.[14] Our specimens could also be composed of phases quenched in from solid solution regions at higher temperatures.

Attempts to prepare an oxyfluoride Eu_3O_4F ($EuO_{1.33}F_{0.33}$) analogous to the phase Eu_3O_4Br reported by Bärnighausen[4] were unsuccessful. Mixtures on the oxide side of EuOF yielded EuOF (rhombohedral) plus Eu_2O_3 (monoclinic) in all cases when annealed at 1500°C and quickly cooled.

The similarity between the oxyfluoride systems and the reduced fluoride systems is worthy of some attention. In the oxyfluoride systems, Bevan, Brauer and co-workers[6,14] and Zachariasen[7] have reported solid solutions and other phases at high temperatures with structures based on an fcc fluorite lattice. In the cubic oxyfluoride phases, the O^{-2} and F^- must be distributed randomly on the anion sites. The predominant lattice defects in a number of non-stoichiometric oxides, fluorides, and oxyfluorides based on the fluorite structures are interstitial anions or anion vacancies.[17] Interstitial anions have been shown to be the primary lattice defect in several such solid solutions involving

a lanthanon trifluoride in a difluoride or an oxyfluoride.[2,17-20] The cation sublattice in these systems is essentially ideal.

Because of the energy involved in anion-cation separation, it is unlikely that configurations which do not satisfy local charge compensation will be significant in these systems. In LnOF (fluorite) the oxide and fluoride ions are randomly distributed on the anion lattice sites, satisfying the condition that unit cells with excess oxide ions contain corresponding anion vacancies and cells with excess fluoride ions contain corresponding interstitial ions. For solid solutions containing excess LnF_3 which have either the fluorite or a closely related structure, the extra fluoride ions are introduced as pairs, one substituting for an oxide ion and the other as an associated interstitial ion. Changes in structure involving ordering of these "defects" require interdiffusion of the anions. As pointed out by Brauer,[14] dimorphic transitions become more difficult in these systems as the interstitial sites are filled.

In the reduced fluoride systems with compositions LnF_{2+x}, the excess F^- ions are introduced as associated pairs of interstitial F^- ions and trivalent cations. Phase changes in these systems should occur more readily because they require only local rearrangements of anions and electron transfers. In fact, the manifestation of this behavior is observed in the difference between DTA thermograms for the difluoride-trifluoride,[3] and the oxide-fluoride systems. The hysteresis for non-stoichiometric samples is much more pronounced for the oxyfluoride material.

<div style="text-align:center">

THE TERNARY SYSTEM IN THE REGION BOUNDED

BY THE COMPOSITION EuF_2-EuF_3-Eu_3O_3-EuO

</div>

Compositions within the ternary field were prepared by equilibrating mixtures of EuF_3 and EuO. The mixtures were encapsulated in either Mo or Pt-10Rh crucibles. Starting materials were the EuF_3 and EuO already described. Molybdenum crucibles were used for mixtures for which the EuO/EuF_3 mole ratio-exceeded 0.43 and Pt-10Rh crucibles for mixtures with $EuO/EuF_3 \leq 0.82$. Several intermediate compostions were heated in both kinds of containers. The samples were held at 1500°C in an induction furnace for at least 2 hr before being cooled rapidly.

The products of the equilibrated mixtures of EuF_3 and EuO were examined by x-ray powder diffraction and optical microscopic techniques.

Optical identification of EuO and Eu_3O_4 is unambiguous because no other phases in this system appear similar to either of these materials. Fluorides on the divalent side of $EuF_{2.1}$ are transparent, nearly colorless, and non-birefringent. Fluorides from $EuF_{2.1}$ to $EuF_{2.3}$ are transparent, light brownish-yellow and weakly birefringent. Compositions from $EuF_{2.3}$ to EuF_3 are transparent, nearly colorless and brightly birefringent.[2] It is difficult to detect small concentrations of EuO in Eu_3O_4 or of EuF_{2+x} in one of the other transparent colorless phases. It is not possible to distinguish between EuF_3, EuOF, and Eu_2O_3 without using more sophisticated techniques than those applied in this study. However, very small amounts of EuO can be detected in phases other than Eu_3O_4. It is also easy to detect very small amounts of one of the trivalent species or of Eu_3O_4 in any of the other phases.

The compositions of the fluorides found in the products were obtained from x-ray lattice parameters using data reported in Ref. 2. In a number of runs, microscopic examination indicated the presence of more than one fluoride composition. For these cases, x-ray powder diffraction patterns were taken for several samples. The x-ray data confirmed that two different fluoride compositions were present in some of the products, and three fluoride compositions were found in one sample. The composition of crystalline products in rapidly cooled samples depends upon the phase boundary surfaces in the system and the crystallization paths. Since our samples were cooled rapidly, equilibrium was not necessarily maintained and more than three phases were found in some of the products.

The interpretation which is most consistent with the ternary equilibration data and the available information about the three binary systems is illustrated in Fig. 2.

CONCLUSIONS

The ternary equilibria in the Eu-O-F systems are well established at 1500°C, with the following exceptions: The structures and exact

composition of the oxyfluoride phases in the range $\sim EuO_{0.6}F_{1.8}$ to $EuO_{0.8}F_{1.2}$ are unknown. In fact, even the number of phases in this range is uncertain. The phase diagram (Fig. 2) is drawn on the assumption that the EuF_3-Eu_2O_3 system is binary and is correctly represented in Fig. 1. The liquidus points on the EuF_3-Eu_2O_3 and EuF_2-EuO joins can be estimated with fair reliability, but the liquid-solid phase boundaries in the intermediate region is pure speculation. The products of the EuF_3-EuO reactions all appeared to have been completely melted, but since the samples were not crushed and reheated nor analyzed by DTA, the possibility that some of these compositions could have been only partially liquid at 1500°C cannot be excluded. The diagram is drawn as if there is only one liquid phase, but there is no direct evidence for this. There may be a miscibility gap between anion-rich and metal-rich liquids such as the miscibility gaps found in other lanthanon—lanthanon-halide systems.[21-27] The region of the system on the metal-rich side of EuO-EuF_2 has not been investigated.

There is clearly no evidence for a ternary compound in this system other than those between EuF_3 and Eu_2O_3. It is possible that one or more other ternary compounds may exist, but we think that this is unlikely as their was no sign of such a phase in any of the preparations, neither those that were cooled rapidly nor those cooled slowly.

The optical and x-ray properties of the three oxide phases prepared in the presence of fluorides are identical to those observed for samples in which no fluoride was present. Also, the properties of the fluorides formed in the presence of oxides or oxyfluorides are identical to those of fluorides for which analysis indicated negligible oxygen content. Therefore, we believe that the solubility of fluorides in any of the oxide phases or of oxide in the fluorides is very small in the crystalline state. Since there were no color changes in the oxyfluoride samples equilibrated with reduced fluorides similar to the color changes observed when lanthanon sesquioxides are partially reduced,[5,28] partially reduced or anion-deficient lanthanon oxyfluorides may not be stable. One would have expected to observe solid solutions based on the fluorite structure with anion vacancies, particularly in the Eu system.

ACKNOWLEDGMENTS

REFERENCES

1. K. Lee, H. Muir and E. Catalano, J. Phys. Chem. Solids 26, 523 (1965); M. W. Shafer and J. D. Kuptsis, IBM Research, RC 2400 (No. 11650), 1969.
2. E. Catalano, R. G. Bedford, V. G. Silveira and H. H. Wickman, J. Phys. Chem. Solids 30, 1613 (1969).
3. R. G. Bedford and E. Catalano, "Phase Diagrams of the SmF_2-SmF_3, EuF_2-EuF_3 and YbF_3 Systems," to be published.
4. H. Bärnighausen, J. Prakt. Chem. 34, 1 (1966).
5. R. G. Bedford and E. Catalano, "The Eu-Eu_2O_3 System and Related Studies," to be published.
6. P. J. M. Bevan, R. S. Cameron, A. W. Mann, G. Brauer, and A. Roether, Inorg. Nucl. Chem. Letters 4, 241 (1968).
7. W. H. Zachariasen, Acta. Cryst. 4, 231 (1951).
8. N. C. Baenziger, J. R. Holden, G. E. Knudsen, and A. I. Popov, J. Am. Chem. Soc. 76, 4734 (1954).
9. D. H. Templeton and C. H. Dauben, J. Am. Chem. Soc. 76, 5237 (1954).
10. K. S. Vorres and R. Riviello, in Proc. Fourth Rare Earth Research Conf., April 1964, p. 521.
11. L. R. Batsonova and G. N. Kustova, Russ. J. Inorg. Chem. 9, 181 (1964).
12. N. N. Podberegskaya, L. R. Batsonova, and L. S. Egorova, J. Struct. Chem. (USSR) 6, 815 (1965).
13. W. Finkelnburg and A. Stein, J. Chem. Phys 18, 1296 (1950).
14. G. Brauer and U. Roether, Proc. Seventh Rare Earth Research Conf., Coronado, California, 1968, p. 253 (availability restricted to attendees).
15. D. B. Shinn and H. A. Eick, J. Inorg. Chem. 8, 232 (1969).
16. M. W. Shafer and J. D. Kuptsis, J. Phys. Chem. Solids 30, 2325 (1969).
17. L. E. J. Roberts, Non-stoichiometric Compounds, R. F. Gould, ed., Am. Chem. Soc., Washington, D. C., 1963, pp. 66-73.
18. E. Zintl and A. Udgard, Z. Anorg. Allgm. Chem. 240, 150 (1934).
19. W. Klemm and H. A. Klein, Z. Anorg. Chem. 248, 167 (1941).
20. J. Short and R. Roy, J. Phys. Chem. 67, 1860 (1963).
21. J. F. Druding and J. D. Corbett, J. Am. Chem. Soc. 83, 2462 (1961).
22. R. A. Salbach and J. D. Corbett, Inorg. Chem. 2, 451 (1963).
23. L. F. Druding, J. D. Corbett and B. H. Ransey, Inorg. Chem. 2, 869 (1963).

24. J. E. Mee and J. D. Corbett, Inorg. Chem. 4, 88 (1965).
25. J. D. Corbett and B. C. McCollum, Inorg. Chem. 5, 938 (1966).
26. G. I. Novikov and O. G. Polyachenok, Russ. J. Inorg. Chem. 8, 545 (1963).
27. O. G. Polyachenok and G. I. Novikov, Russ. J. Inorg. Chem. 8, 1478 (1963).
28. A. E. Miller and A. H. Daane, J. Inorg. Nucl. Chem. 27, 1955 (1965).

Table I. X-ray and DTA results for the Eu_2O_3-EuF_3 system.

Composition	X-ray powder diffraction analysis of products	DTA results	
		Temperature range	Peak height[*]
EuOF	EuOF (rhomb)	503- 505°C	5.3
$EuO_{0.9}F_{1.2}$	EuOF (rhomb) + wk lines	481- 498 718- 734	1.8 1.5
$EuO_{0.8}F_{1.4}$	EuOF (rhomb) + wk lines	721- 734	4.1
$EuO_{0.7}F_{1.6}$	EuOF (rhomb) + EuF_3 (orth)	505- 522	1.0
$EuO_{0.6}F_{1.8}$	EuOF (rhomb) + EuF_3 (orth) + wk lines	553- 578	0.7
$EuO_{0.3}F_{2.4}$	EuF_3 (orth) + wk lines	568- 588 1293-1315	0.5[**] 8.8
EuF_3	EuF_3 (orth)	776- 806 1180-1258	~3 21.9
SmOF	SmOF (rhomb)	501- 508	7.7

[*]Peak heights normalized to average sample size of 0.4 g, assuming peak height directly proportional to mass of sample.

[**]Peak detectable only on cooling.
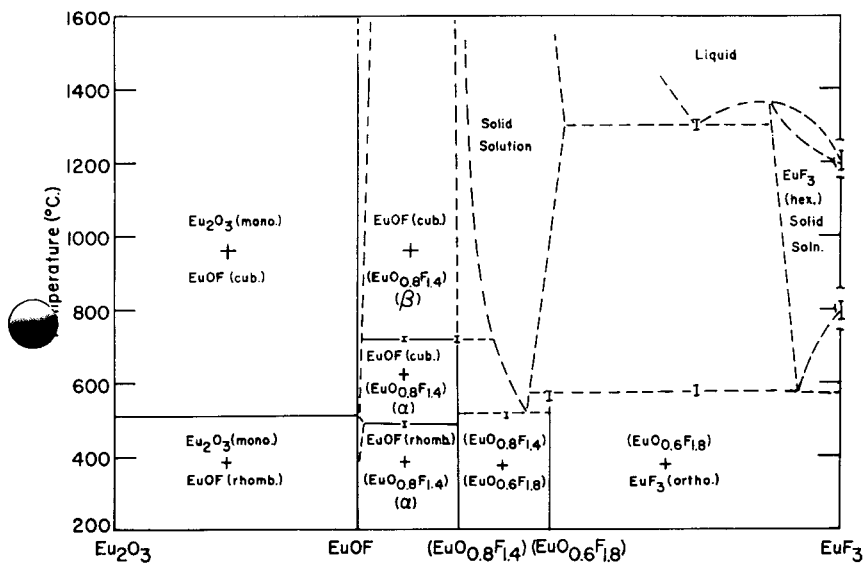
Fig. 1. The binary system Eu_2O_3-EuF_3.
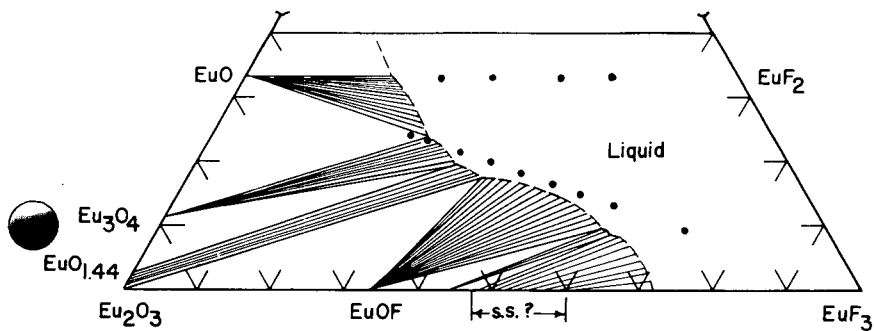
Fig. 2. A section of the ternary system Eu-Eu_2O_3-EuF_3 at 1500°C.

The Relative Stabilities of the B and C Forms

of Sm_2O_3, Eu_2O_3, and Gd_2O_3[*]

$H80~8500$

by

George C. Fitzgibbon, Daniel Pavone, and Charles E. Holley, Jr.

~~University of California,~~ Los Alamos Scientific Lab~~oratory~~,
~~Los Alamos, New Mexico~~ 87544 $N,~mex.$

Abstract

The enthalpies of solution of the B (monoclinic) and C
(cubic) types of Sm_2O_3, Eu_2O_3, and Gd_2O_3 have been measured in
hydrochloric acid, and of Eu_2O_3 in nitric acid. It appears
that for Eu_2O_3 and Gd_2O_3 the C form is the stable form at 298 K
and for Sm_2O_3 there remains considerable uncertainty.

Introduction

The sesquioxides of the rare-earth elements are known to exist at
room temperature in one or more crystalline modifications of hexagonal,
monoclinic, or cubic structure generally designated as type A, B, and C
respectively (1). Foex and coworkers (2) have shown that there are also
high temperature modifications of these oxides. The relative stabili-
ties of the low temperature forms of the oxides have been rather well
established except for Sm_2O_3, Eu_2O_3, and Gd_2O_3. These three oxides may
be obtained in both the B and C forms depending upon the temperature of
preparation. Thermal decomposition of the hydroxide, oxalate, etc., at
relatively low temperatures, depending upon the particular rare earth
element, results in the formation of the cubic or C-form oxide. At
higher decomposition temperatures the monoclinic or B-form is obtained.
Subsequent heating of the C-form to higher temperatures results in
transformation to the B-form which is retained at room temperature.
The question then is whether or not the C → B transformation is revers-
ible and which crystalline modification is thermodynamically stable at

---

[*] Work supported by the U. S. Atomic Energy Commission.

room temperature.

Experimental observations reported in the literature lead to conflicting answers to these questions. Thus, the C-form is obtained by thermal decomposition of salts at relatively low temperatures, and the B → C transition for Eu_2O_3 and Gd_2O_3 at 950°C has been observed (3), indicating the C-form to be the stable modification. Contrariwise, Brauer has obtained the B-form of these oxides at 400°C by precipitation from molten anhydrous alkali nitrate salt baths (4). Also, most investigators have not been able to observe the B → C transition on cooling from high temperatures. In addition, the temperature of the C → B transition appears to vary with the rate of heating, the salt from which the oxide was prepared, its prior treatment, and the enclosing atmosphere. Such variation of the transition temperature implies that it is not a true equilibrium temperature, but rather represents a transition from a meta-stable C-form to a stable B-form. Further, applying the relationship between the volume change and heat of formation (5), we note the density of the B-form is greater than that of the C-form of these oxides and therefore expect a more negative heat of formation for the B-form compared to that of the C-form.

A precise thermodynamic answer is not yet possible because the necessary data are not available. Except for one measurement of the enthalpy of transition for Sm_2O_3 (6), neither the entropies nor the enthalpies of transition have been measured. Gvelesiani and Yashvili report an enthalpy of transition of Sm_2O_3 (6) which differs considerably from that reported here. Our previously reported value for the enthalpy difference of the two forms of Eu_2O_3 (7) is not correct, as evident from the results below, presumably because the oxide samples had not been prepared free of H_2O and CO_2. The absolute entropies of Sm_2O_3-B and Gd_2O_3-C (8) have been measured, and the entropy change for the C → B reaction has been estimated by Hoekstra from high pressure work to be 1.5 entropy units (3). Heat capacity measurements from room temperature to rather high temperatures have also been completed (9).

In this paper measurements of the enthalpies of solution of the B and C forms of Sm_2O_3, Eu_2O_3 and Gd_2O_3 in aqueous hydrochloric acid and

of Eu_2O_3 in aqueous nitric acid are reported. These data and the high temperature heat capacity measurements referred to above are then combined to estimate the enthalpies and entropies of transition as a function of temperature.

Experimental

Equipment and Procedure

The equipment and procedure have been described (10).

Materials

Commercially available, 99.9% pure, oxides obtained from Research Chemical Co. were used to prepare samples of both forms of the three oxides. As received, the oxides were in the cubic modification and contained varying amounts of water and carbon dioxide.

Samples of the B-form of the oxides were prepared by igniting the "as received" oxide, contained in an alundum crucible, in vacuum at a temperature sufficiently high to insure conversion to the monoclinic structure and removal of water and carbon dioxide. The temperatures were Sm_2O_3, 1175°C; Eu_2O_3, 1500°C, and Gd_2O_3, 1500°C.

The C-form samples of Eu_2O_3 and Gd_2O_3 were prepared free of H_2O and CO_2 by ignition, in a platinum boat, in an oxygen atmosphere at 1030°C. The C-form of Sm_2O_3 could not be obtained free of H_2O and CO_2 by simple ignition. The temperature of ignition must be below 900°C to avoid conversion to the B-form, and at this temperature some H_2O and CO_2 is retained by the Sm_2O_3. Therefore, four preparations of salts of samarium made from a solution of the "as received" material decomposed at appropriate temperatures to yield a series of samples of variable composition with respect to H_2O and CO_2. The course of the decomposition was followed with a thermobalance and the product analyzed by ignition in oxygen with absorption of H_2O on $Mg(ClO_4)_2$ and CO_2 on ascarite in a standard combustion apparatus. The results from the solution experiments on the series of samples were then extrapolated to yield a value for the pure material. Table I lists the preparations and their analyses.

Table I
Preparation of Sm_2O_3-C

Salt:	$Sm(OH)_3$	$Sm(OH)_3$	$Sm_2(C_2O_4)_3$	$Sm(C_2H_3O_2)_3$[*]
Decomp. Temp.	590°C	700°C	790°C	870°C
% H_2O	1.02 ± 0.05	0.60 ± 0.14	0.23 ± 0.07	0.24 ± 0.09
% CO_2	0.45 ± 0.01	0.36 ± 0.16	0.23 ± 0.01	0.11 ± 0.04
Total	1.45 ± 0.05	0.96 ± 0.23	0.46 ± 0.07	0.35 ± 0.10

[*] This preparation contained an estimated 2-5% of the B-type.

The C-type structure of each oxide sample prepared was confirmed by x-ray diffraction analysis with the exception noted.

The HCl and HNO_3 solutions were prepared from analytical grade acids and standardized against mercuric oxide using phenolphthalein as the indicator.

Results

In order to observe the variation of the enthalpies of solution with change of acid concentration, measurements were made in 2 M, 4 M, and 6 M HCl. In addition to yielding improved statistical data, this procedure helps to reveal any systematic errors. Enthalpies of solution of the two crystal modifications of Eu_2O_3 in 6 M HNO_3 were also obtained for comparison with previous work (7).

Tables II, III, and IV summarize the results, converted to a molar basis using the 1961 atomic weights.

Table II. Enthalpies of Solution of Sm_2O_3

Oxide	Solvent	ΔH_{soln} kcal/mole	ΔH_{tr} (C→B) kcal/mole
Sm_2O_3-C	2 M HCl	-98.3 ± 1.4(extrap. value)	
Sm_2O_3-B	2 M HCl	-99.24 ± 0.31	0.9 ± 1.4
Literature - Gvelesiani and Yashvili (7):			
Sm_2O_3-C	1 M HCl	-94.8 ± 0.3	
Sm_2O_3-B	1 M HCl	-93.4 ± 0.5	-1.4 ± 0.6

Table III. Enthalpies of Solution of Eu_2O_3

Oxide	Solvent	ΔH_{soln} kcal/mole	ΔH_{tr} (C→B) kcal/mole
Eu_2O_3-C	2 M HCl	-95.19 ± 0.11	
Eu_2O_3-B	2 M HCl	-97.62 ± 0.53	
			2.43 ± 0.40
Eu_2O_3-C	4 M HCl	-95.69 ± 0.32	
Eu_2O_3-B	4 M HCl	-98.78 ± 0.51	
			3.09 ± 0.60
Eu_2O_3-C	6 M HCl	-96.39 ± 0.32	
Eu_2O_3-B	6 M HCl	-99.00 ± 0.77	
			2.61 ± 0.81
Eu_2O_3-C	6 M HNO_3	-98.40 ± 0.37	
Eu_2O_3-B	6 M HNO_3	-100.80 ± 0.35	
			2.40 ± 0.51
		Weighted Mean	2.61 ± 0.28

Literature - Stuve (8):

Oxide	Solvent	ΔH_{soln} kcal/mole	
Eu_2O_3-C	4 M HCl	-96.92 ± 0.22	

Table IV. Enthalpies of Solution of Gd_2O_3

Oxide	Solvent	ΔH_{soln} kcal/mole	ΔH_{tr} (C→B) kcal/mole
Gd_2O_3-C	2 M HCl	-94.69 ± 0.25	
Gd_2O_3-B	2 M HCl	-98.60 ± 0.15	
			3.93 ± 0.29
Gd_2O_3-C	4 M HCl	-96.17 ± 0.58	
Gd_2O_3-B	4 M HCl		
Gd_2O_3-C	6 M HCl	-96.64 ± 0.44	
Gd_2O_3-B	6 M HCl	-99.87 ± 0.54	
			3.23 ± 0.70

-228-

The generally smaller uncertainties listed for the enthalpies of solution of the C-oxides as compared to those of the corresponding B-oxides is a consequence of the relative rates of solution. The C-oxides haveing been prepared at lower temperatures, are more readily dissolved, thus permitting a more accurate determination of the corrected tempera-ture rise. In the case of Sm_2O_3-C, however, there is a rather large uncertainty because of the extrapolation required.

Discussion

The enthalpy of solution of Sm_2O_3 results may be compared to those of Gvelesiani and Yashvili (6), see Table II. The difference in the results of the two measurements is greater than that which can be accounted for by the difference in the concentration of the acid solvent. These authors report, in the same paper, values for the enthalpy of solution of La and La_2O_3 which agree, within the range of the uncertain-ties involved, with values we have obtained (11) with the same apparatus used for this investigation. This seems to indicate, then, that the difference in the results is due to differences in the samples of Sm_2O_3. They prepared the sample of Sm_2O_3-C by decomposing the oxalate at 750-800°C. In our experience, this temperature is not sufficiently high to completely remove all of the H_2O and CO_2. However, the Sm_2O_3-B was prepared at 1200°C, which should yield a satisfactory product. Their value for ΔH_{tr} almost agrees with the one reported here within the relatively large uncertainties involved.

Stuve (12), see Table III, has reported a value for the enthalpy of solution of Eu_2O_3-C in 4 M HCl that is 1.24 ± 0.46 kcal/mole more nega-tive than that reported here. The difference is significantly greater than the combined estimated uncertainties. His sample was prepared from the nitrate at 750°C and he reported less than 0.05% weight loss on ignition in vacuum for one hour at 980°C. Thus, there is no readily apparent explanation for the difference in the results.

Although the absolute entropies are not known for these oxides, except as noted earlier, heat capacity measurements from room tempera-

-229-

ture to rather high temperatures are available. These results have been
critically reviewed (13) and the tables given in that reference are used
for the calculations reported here. For the cubic to monoclinic transi-
tion (C → B) an expression for the enthalpy of transition at any temper-
ture may be derived as follows.

$$(H_T^\circ - H_{298}^\circ)_B - (H_T^\circ - H_{298}^\circ)_C = (H_T^\circ)_B - (H_T^\circ)_C - (H_{298}^\circ)_B + (H_{298}^\circ)_C$$

$$(H_T^\circ)_B - (H_T^\circ)_C = \Delta H^\circ(tr, \ T^\circ K)$$

and $\qquad -(H_{298}^\circ)_B + (H_{298}^\circ)_C = -\Delta H^\circ(tr, \ 298^\circ K)$

$$\therefore \ \Delta H^\circ(tr, \ T^\circ K) = [(H_T^\circ - H_{298}^\circ)_B - (H_T^\circ - H_{298}^\circ)_C] + \Delta H^\circ(tr, \ 298^\circ K) \qquad (1)$$

The quantity inside the square brackets is obtained from tables in ref-
erence 13 and $\Delta H^\circ(tr, \ 298^\circ K)$ from the experimental data given in Tables
II, III, and IV. In a similar manner the entropy of transition at any
temperature is given by

$$\Delta S^\circ(tr, \ T^\circ K) = [(S_T^\circ - S_{298}^\circ)_B - (S_T^\circ - S_{298}^\circ)_C] + \Delta S^\circ(tr, \ 298^\circ K) \qquad (2)$$

Thus, for gadolinium oxide, which has a reported transition of $1550^\circ K$
(9), assuming this is indeed an equilibrium temperature, $\Delta H^\circ(tr, \ 1550^\circ K)$
= 3290 ± 400 calories/mole and $\Delta S^\circ(tr, \ 1550^\circ K) = (3290 \pm 400)/1550 = 2.1$
± 0.3 e.u. These values may be compared with the corresponding values of
2000 calories/mole and 1.5 e.u. estimated by Hoekstra (3) for the C → B
transition in the higher atomic number members of the rare earth
elements. Substituting this value of the entropy of transition in equa-
tion (2) along with data from reference (13), the entropy of transition
at 298°K is determined as $\Delta S^\circ(tr, \ 298^\circ K) = 3.0 \pm 0.4$ e.u. If the lower
limit of the enthalpy of transition at 1550°K is used the corresponding
values of the entropy of transition are 1.9 e.u. at 1550°K and 2.7 e.u.
at 298°K. Figure 1 shows a plot of $\Delta H^\circ(tr, \ T^\circ K)$ vs. temperature along
with curves of T∆S based upon values of $\Delta S^\circ(tr, \ 1550^\circ K)$ of 2.1 and 1.9
e.u.

For the europium oxides an estimated transition temperature is
1350°K (9). Treatment of the data in like manner to that given above
for gadolinium oxides, gives, for the C → B transition in Eu_2O_3,
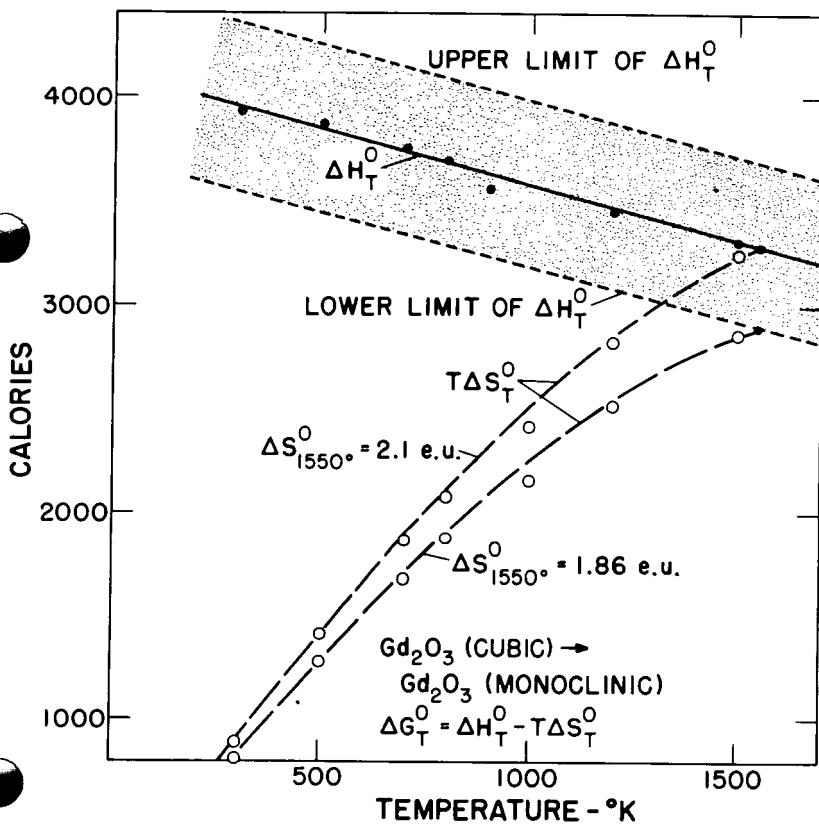
Fig. 1 - Plot of ΔH_{tr} and $T\Delta S$ vs. Absolute Temperature
for Gd_2O_3 Polymorphs

$\Delta H°$(tr, 1350°K) = 2100 ± 400 cal/mole and $\Delta S°$(tr, 1350°K) = 1.6 ± 0.3 e.u.

In the case of samarium oxide, the estimated transition temperature is low and the data are not very precise. We must proceed in a different manner. If we assume that the entropy of transition is 1.5 e.u. at the equilibrium temperature then, using $\Delta H°$(tr, 298°K) = 700 cal/mole, we find $T_{tr} = \sim 450°K$. The extremes of $\Delta H°$(tr, 298°K) lead on the one hand to $T_{tr} > 1200°K$, which is higher than the observed transformation temperature, and on the other hand, to the conclusion that the B-form is stable even at low temperatures. More precise measurements are needed to narrow the limits.

Heat capacity measurements from low temperatures to 300°K for Sm_2O_3-C, Eu_2O_3-B, Eu_2O_3-C and Gd_2O_3-B would allow determination of the absolute entropies of these phases and either confirm or contradict the above estimates.

Finally, let us consider Brauer's experiments in which the B-form of the three oxides was prepared at 400°C ≡ 673°K. Table V gives our estimate for the free energy change for the C → B transition at 700°K. For Sm_2O_3 the results are consistent with Brauer's experiments, and for the others the free energy change is so small that it seems entirely possible that impurities could change its sign.

Table V

The Differences in the Gibbs Energies of Formation

of the B and C forms of Sm_2O_3, Eu_2O_3 and Gd_2O_3 at 700°K

Oxide	ΔH (C → B) cal/mole	ΔS (C → B) e.u./mole	ΔG (C → B) cal/mole
Sm_2O_3	700 ± 1400	1.5 (assumed)	-350 ± 1400
Eu_2O_3	2300 ± 300	1.8 ± 0.5	1040 ± 500
Gd_2O_3	3800 ± 400	2.6 ± 0.5	1980 ± 560

References

(1) G. Brauer, *Progress in the Science and Technology of the Rare Earths*, L. Eyring, Editor, Pergamon Press, New York, Volume 1, 1964, p. 152; Volume 2, 1966, p. 312.

(2) M. Foex, Z. anorg. allgem. Chem. $\underline{337}$, 313 (1965); M. Foex and J. P. Traverse, Bull. Soc. France Mineral Cust. $\underline{89}$, 184 (1966); Compt. rend. Ser. C. $\underline{262}$, 743 (1966).

(3) H. R. Hoekstra, Inorg. Chem. $\underline{5}$, 754 (1966).

(4) G. Brauer, Proc. 6th Rare Earth Research Conference, Gatlinburg, Tennessee, 1967, p. 385.

(5) O. Kubaschewski, E. L. Evans and C. B. Alcock, Metallurgical Thermochemistry, Pergamon Press, Oxford, 4th Edition 1967, pp 220-237.

(6) G. G. Gvelesiani and T. S. Yashvili, Zh. Neorg. Khim. $\underline{1967}$, 3233.

(7) E. J. Huber, Jr., G. C. Fitzgibbon, and C. E. Holley, Jr., J. Phys. Chem. $\underline{68}$, 2720 (1964).

(8) B. H. Justice and E. F. Westrum, Jr., J. Phys. Chem. $\underline{67}$, 345 (1963).

(9) L. B. Pankratz, E. G. King, and K. K. Kelley, U. S. Bur. Mines Rept. Invest. No. 6033 (1962).

(10) G. C. Fitzgibbon, D. Pavone, E. J. Huber, Jr., and C. E. Holley, Jr., "A New Solution Calorimeter", Los Alamos Scientific Laboratory Report LA-3031, 1964.

(11) G. C. Fitzgibbon, C. E. Holley, Jr., and I. Wadsö, J. Phys. Chem. $\underline{69}$, 2464 (1965).

(12) J. M. Stuve, U. S. Bur. Mines Rept. Invest. No. 6640 (1965).

(13) C. E. Holley, Jr., E. J. Huber, Jr., and F. B. Baker, *Progress in the Science and Technology of the Rare Earths*, L. Eyring, Editor, Pergamon Press, N. Y., Volume 3, 1968, p. 343.

The Systems $Bi_2O_3 - R_2O_3(R=Y,Gd)$

R. K. DATTA and J. P. MEEHAN
Lighting Research Laboratory, General Electric Company
Nela Park, Cleveland, Ohio 44112

Subsolidus regions of the systems $Bi_2O_3-R_2O_3(R=Y,Gd)$ were investigated. Oxide mixtures or coprecipitated oxalates contained in platinum or silica crucibles were equilibrated in air atmosphere in the temperature range 600-1150°C. The phase transitions and reaction products were characterized by differential thermal and X-ray diffraction analyses, respectively.

In the systems studied, extensive solid solution of Bi_2O_3 in the cubic Y_2O_3 lattice has been observed. In addition, a new compound with the approximate composition, $2Bi_2O_3 \cdot R_2O_3(R=Y,Gd)$ is isolated. This has a face-centered cubic structure and exists over a wide range of temperature and composition. At high Bi_2O_3 contents and low temperatures, the cubic phase undergoes a reversible tetragonal distortion.

The crystal chemical aspects of the systems will be discussed.

<u>PHASE TRANSITIONS IN COMPLEX PEROVSKITES OF THE</u>
<u>TYPE Ba_2LnMoO_6 *</u>

C. D. Brandle and H. Steinfink
Materials Science Laboratories
Department of Chemical Engineering
The University of Texas At Austin
Austin, Texas 78712

Abstract

    Materials with the composition Ba_2LnMoO_6 (Ln = rare
earth) have been prepared. A transition between the cubic
and tetragonal phases has been directly observed in six of
the materials (Ba_2PrMoO_6 thru Ba_2TbMoO_6) and a transition
between the orthorhombic and tetragonal phase has been
indirectly observed in one material (Ba_2CeMoO_6). A linear
relationship between the phase transition temperature and
the rare earth radius has been found to exist for the
tetragonal to cubic transition. DTA results on Ba_2PrMoO_6
and Ba_2NdMoO_6 indicated that no heat of transition is
associated with the change from tetragonal to cubic
symmetry while x-ray data indicated no discontinuity in the
unit cell volume. These results indicate that the transition
is probably second order or higher and of the displacive
type.

Introduction

    Over the past several years, about 500 compounds having
the perovskite structure have been reported in the litera-
ture[1,2,3]. Approximately one-half of these materials have
the general formula $A_2BB'O_6$. Both tetragonal and orthorhombic
distortions of the ideal face-centered cubic structure have
been reported for this type of compound[4]. The compounds
selected for a detailed study have the general formula
Ba_2LnMoO_6 (Ln = rare earth). This group of materials
provided an excellent means to determine the effect of ionic

size on the type of distortion produced in the perovskite
structure and the relationship between ionic size and the
transition temperature could be determined.

Material Preparation

The equipment used to react the components was a rf
heated furnace capable of temperatures in excess of 2000°C.
The furnace liner was calcia stabilized ZrO_2 tubing.
Additional insulation was obtained by using crushed ZrO_2 as
a filler between the ZrO_2 and Vycor tubing. The susceptor
was an iridium crucible fitted with a lid. All reactions
were carried out within the iridium crucible. The entire
furnace was then placed within a bell jar which could be
evacuated to 15 microns and filled with either nitrogen,
argon or hydrogen.

Stoichiometric amounts of Ln_2O_3 (rare-earth oxide),
MoO_3 and $BaCO_3$ were weighed and thoroughly mixed. The
conditions which gave the best results were an initial gas
pressure of 600 mm with hydrogen content of about 12 per
cent by volume with the remaining gas being nitrogen. The
heating schedule was as follows:

Temperature	Duration
700°C	15 min
900°C	15 min
1100°C	15 min
1300°C	15 min
1400°C	15 min
1150°C	10 min
Cool down to R.T.	20 min

This heating schedule and reaction conditions gave
single phase perovskite material in all cases except two.

When the compounds Ba_2CeMoO_6 and Ba_2PrMoO_6 were formed a
more strongly reducing atmosphere was necessary, i.e. the
hydrogen content was increased from 12 percent to 20 per-
cent by volume to obtain a single phase product. This
increase was necessary due to the presence of Ce^{4+} and Pr^{4+}
in the initial reactants.

The stoichiometry of the final product was checked by
observing the weight loss due to formation of CO_2 and
oxygen which occurred in the sample during reaction. The
served weight loss was usually within 1.0 percent of the
calculated weight loss.

Oxidation State of Sample

All compounds, Ba_2LnMoO_6, as prepared by this procedure
are black, have a metallic luster and are quite crystalline.
X-ray powder patterns showed the diffraction lines of the
basic perovskite subcell in addition to the weak (111),
(311) and (331) superstructure lines due to the ordering
of the rare earth and molybdenum ions. However, it is
believed that the as prepared materials are oxygen deficient
and contain both oxygen vacancies and molybdenum ions in
other oxidation states as shown by Equation (1).

$$4BaCO_3 + 2MoO_3 + Ln_2O_3 \xleftrightarrow[\text{conditions}]{\text{reducing}} 2Ba_2LnMo_x^{3+}Mo_{1-x}^{5+}O_{6-x}$$

$$+ \frac{1+x}{2} O_2 + 4CO_2 \tag{1}$$
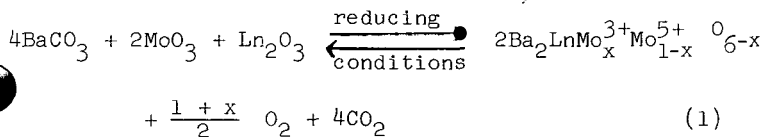
To determine the degree of reduction of the molybdenum,
samples of known weight were oxidized and the weight gain
measured using a Cahn Electrobalance with a sensitivity of
$\pm$ 0.02 mg. Sample weights were about 22 mg. i.e. weight
changes of greater than 0.1 percent could be detected. The

procedure used consisted of first weighing the sample
container, filling the container with the reduced material,
heating the material and container in air at $600°C$ for
15 minutes and then re-weighing the sample. Heating of the
sample was repeated until a constant weight gain ($\pm$ 0.02 mg)
was obtained. From the weight gain the oxygen deficiency was
calculated assuming the following reaction occurred during
oxidation:

$$Ba_2LnMo_x^{3+}Mo_{1-x}^{5+}O_{6-x} + \frac{x}{2} O_2 \xrightarrow[\text{Air}]{600°C} Ba_2LnMo^{5+}O_6 \qquad (2)$$
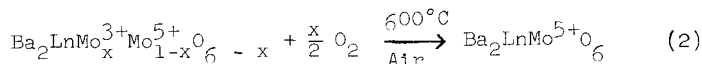
A summary of the results obtained when various samples were
oxidized is given below:

Compound	Weight Gain (%)	x($\pm$ 0.03)	Color after oxidation
Ba_2GdMoO_6	2.43	0.95	Yellow
Ba_2TbMoO_6	0.32	0.13	Red-Brown
Ba_2TmMoO_6	0.65	0.26	Green-Blue
Ba_2EuMoO_6	0.81	0.31	Yellow
Ba_2NdMoO_6	0.20	0.08	Light Blue
Ba_2LuMoO_6	0.56	0.22	Green-Blue

From the above table, it can be seen that the degree of
reduction of the molybdenum ion varies from almost none,
Ba_2NdMoO_6, to almost complete reduction to form the material
Ba_2GdMoO_5 with the average x value being about 0.25. It is
interesting to note that in the case of Ba_2GdMoO_6, the
compound retains the perovskite structure even though there
are on the average approximately four oxygen vacancies per
unit cell.

X-ray Powder Work

Two distortions of the ideal cubic perovskite structure
were observed at room temperature. For the La and Ce

compounds, the powder pattern showed splitting of the basic
perovskite lines into triplets which could be indexed using
an orthorhombic cell with a, b and c approximately equal to
8.6 Å. The Pr, Nd and Sm compounds gave powder patterns
which showed the basic perovskite lines being split into
either a doublet or triplet. All lines in the pattern
could be indexed using a tetragonal cell with a and c
approximately 8.5 Å. The remaining compounds, Ge thru Lu
and including Y gave the basic cubic perovskite pattern
with no observable line splitting. The Sc compounds, however,
did not have the perovskite structure but rather the powder
pattern was typical of the hexagonal $BaTiO_3$ structure. The
lattice parameters for the entire series are given in
Table I. These parameters were determined from Debye-
Scherrer films using a least squares refinement of all
diffraction lines with 2θ angles greater than $90°$. The
standard deviation of the parameters are given in parentheses.

Both high and low temperature x-ray powder diffraction
techniques were used to detect phase changes in these
materials. The patterns were obtained using a Philips
vertical diffractometer. Diffraction lines between $34°$ 2θ
and $90°$ 2θ were used in a least squares refinement to
obtain the lattice parameters. Knowing the lattice parameters,
the c/a ratio could then be determined. The resolution of
the instrument placed a lower limit on the observed c/a
ratio of about 1.002. Because of this limitation, powder
patterns were run at several different temperatures below
the transition temperature. From these patterns, the c/a
ratio was obtained for each material. A linear least squares
fit of the c/a ratio as a function of temperature,
Figure 1, was then performed. This curve was then extrap-
olated to 1.0000 to obtain the transition temperatures which
are also listed in Table I. It is estimated that the
transition temperatures given in Table I are accurate to

withinin $\pm$ 10°C of the actual value. This estimate is based
on the error of the observed c/a ratio.

As can be seen from Figure 1, the slope of each of the
lines is approximately the same. This fact was used to
determine the transition temperature for Ba_2TbMoO_6. For
this compound, line splitting (indicating a phase change)
was seen only at the lowest possible temperature which could
be obtained, i.e. -175°C. Using the average of the slopes
of the previously determined compounds, a transition
temperature of -117°C was calculated from the one datum
point.

Examination of the x-ray powder patterns indicated
that the change from cubic to tetragonal symmetry occurred
with no abrupt change in the lattice parameters, but rather
the parameters were a smooth, continuous function of
temperature. Figure 2 gives the lattice constants for
Ba_2NdMoO_6 as a function of temperature. This Figure is
representative of the entire series.

Knowing the lattice constants for the compounds as a
function of temperature, the volume of the unit cell can be
determined. Figure 3 shows the volume versus temperature
curves for each of the compounds in which phase changes were
detected. Examination of these curves shows that within
experimental error the curves are linear for each phase;
however, the slope of the curve is different for the
tetragonal and cubic phases. Except for the compound
Ba_2PrMoO_6, the slopes of the curves for the various materials
are the same in both the cubic and tetragonal regions.

The results as described above indicate that the phase
transition is higher than first order. To further support
this hypothesis, DTA runs were made using samples of Ba_2PrMoO_6
and Ba_2NdMoO_6. In both cases, no evidence of the phase
change appeared in the DTA charts again indicating that

the phase transition is higher than first order. In a recent paper by Geller[5], similar results concerning the nature of the phase transition in $LaAlO_3$ were reported. Thus, it was concluded that (1) the phase change observed in these materials is of the displacive type which results in a gradual displacement of the ions from the high symmetry position (cubic) and (2) the phase change is higher than first order, i.e. it has no discontinuities in volume, etc. associated with it; however, it does not imply the transition is second order.

Figure 4 shows the observed transition temperature as a function of the rare earth ionic radius. Within experimental error this curve is linear over the range of materials covered. The expression for the transition temperature as a function of the ionic rare earth radius was obtained by a linear least squares fit of the data and is given by:

$$T = 2843r_{Ln} - 2769 \tag{3}$$

where T = transition temperature (°C)

r_{Ln} = rare-earth ionic radius (Ahren's).

This curve was then extrapolated to predict transition temperatures for other cubic members of the series. These values are also shown in Table I.

Table I

Lattice Parameters, Symmetry and Transition Temperatures
for Ba_2LnMoO_6 Compounds

Material	Symmetry[+]	Lattice Constants[+]	Transition
Ba_2LaMoO_6	Orthorhombic		
Ba_2CeMoO_6‡	Orthorhombic	a = 8.52 b = 8.74 c = 9.07	>1000°C and <1550°C
Ba_2PrMoO_6	Tetragonal	a = 8.495(3) c = 8.597(2)	252°C Tetragonal→Cubic
Ba_2NdMoO_6	Tetragonal	a = 8.491(4) c = 8.556(4)	176°C Tetragonal→Cubic
Ba_2SmMoO_6	Tetragonal	a = 8.472(3) c = 8.500(3)	87°C Tetragonal→Cubic
Ba_2EuMoO_6	Cubic	a = 8.466(2)	10°C Cubic→Tetragonal
Ba_2GdMoO_6	Cubic	a = 8.454(1)	-16°C Cubic→Tetragonal
Ba_2TbMoO_6	Cubic	a = 8.425(2)	-117°C Cubic→Tetragonal
Ba_2DyMoO_6	Cubic	a = 8.409(1)	-153°C*
Ba_2YMoO_6	Cubic	a = 8.391(1)	
Ba_2HoMoO_6	Cubic	a = 8.387(1)	-192°C*
Ba_2ErMoO_6	Cubic	a = 8.369(2)	
Ba_2TmMoO_6	Cubic	a = 8.356(2)	
Ba_2YbMoO_6	Cubic	a = 8.331(2)	
Ba_2LuMoO_6	Cubic	a = 8.321(1)	
Ba_2ScMoO_6‡	Hexagonal	a = 5.90 c = 14.32	

+ Room temperature.

‡ Lattice constants obtained from precession films.

* These values obtained from Equation (3).

References

1. Sleight, A. W., Longo, J., and Ward, R., Inorg. Chem. 1, 245 (1962).

2. Katz, L. and Ward, R., Inorg. Chem., 3, 205 (1964).

3. Goodenough, J. B. and Longo, J. M., (private communication).

4. Sleight, A. W., Ph.D. Thesis, The University of Connecticut (1963).

5. Geller. S., (private communication).
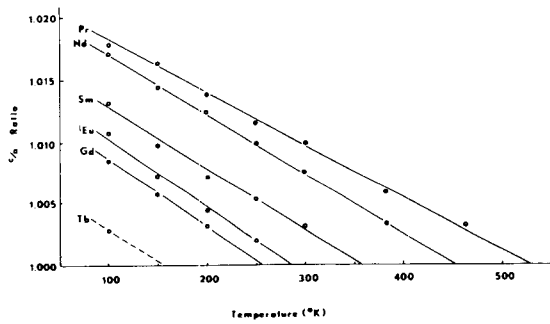
Fig. 1.   c/a Ratio Versus Temperature for
Tetragonal Compounds
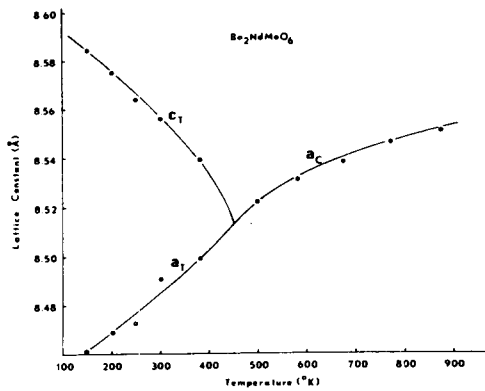
Fig. 2.   Lattice Constants for Ba₂NdMoO₆
Versus Temperature
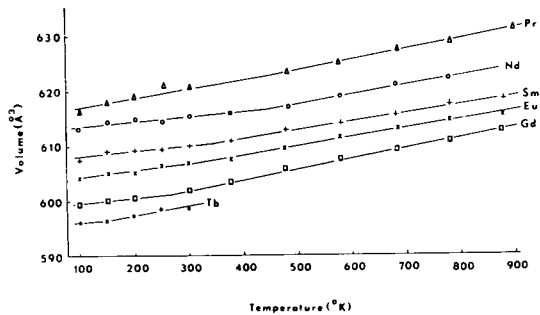
Fig. 3. Unit Cell Volume Versus Temperature
for Tetragonal Compounds
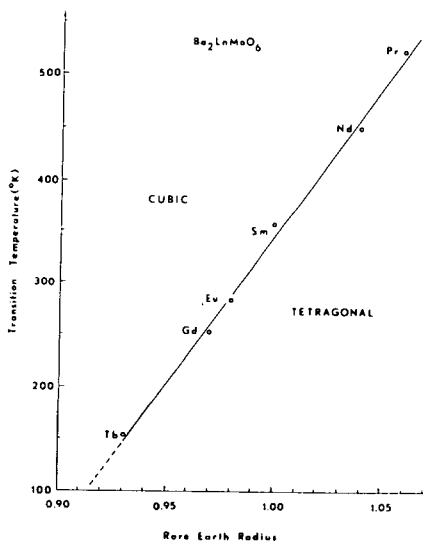
Fig. 4. Transition Temperature Versus
Rare-Earth Radiun

COMPARISON OF ELUTING AGENTS FOR

ION-EXCHANGE PURIFICATION OF PROMETHIUM[1]

E. J. Wheelwright

Battelle Memorial Institute, Pacific Northwest Laboratory
Richland, Washington 99352

Battelle - Northwest, Richland, Wash. Pacific Northwest Lab.

ABSTRACT

Laboratory experiments have shown that NTA (nitrilotriacetic acid) is markedly superior to EDTA (etnylenediaminetetraacetic acid) or DTPA (diethylenetriaminepentaacetic acid), the complexing agents previously used, for kilogram-scale ion-exchange purification of promethium. With NTA elution at 60°C, the position of yttrium is changed from the critical Sm-Pm-Nd zone (with DTPA the sequence is Sm-Y-Pm) to a place ahead of gadolinium; yielding an elution order: Y, Gd, Eu, Sm, Pm, Nd, Pr. As a result of faster kinetics in the NTA system, a 100% increase in the rate of band advance, compared to the rate obtained in the previously used DTPA process, can be achieved with equal or superior separation efficiency. The time required for a 300,000 Ci purification run has been reduced from 21 days with EDTA or 6 days with DTPA to less than 3 days with NTA.

INTRODUCTION

J. E. Powell[2] has reviewed the rather large number of eluting agents that have been proposed for the separation of the lanthanide elements from each other by both cation and anion exchange processes. Of these, EDTA (ethylenediaminetetraacetic acid), HEDTA (N-hydroxyethylethylenediaminetriacetic acid), and DTPA (diethylenetriaminepentaacetic acid) have been used most successfully for the purification of the individual "light" lanthanides on a macro scale.

EDTA was used with an Y^{+3} restraining ion by Wheelwright and Roberts[3] in 1961 to upgrade 26,000 Ci ^{147}Pm. Pure Pm was not obtained because the quantity then available was too small compared to the diameter (2 inch) of the installed columns. In a subsequent purification, performed 14 months later in properly sized columns, 13,000 Ci of high purity (> 99 wt. %) ^{147}Pm were obtained.[3] P. B. Orr[4] successfully used DTPA with a H^+ restraining ion for

-246-

similar macro-scale separation of Pm in 1962. A thermodynamic
treatment of this type of system and the requirements of the
"barrier" or "restraining" ion are reviewed elsewhere.[2,3,5]

During 1965, a pilot plant, consisting of seven 9-foot-high
water-thermostated ion-exchange columns, ranging from 8 to 1 inch
I.D., plus associated tanks, pumps, and instrumentation was in-
stalled in one of the hot cells at the Pacific Northwest Laboratory.[6]
Since that time, in excess of 5 x 10^6 Ci ^{147}Pm have been purified
at this facility. Because of the 2.2% per month decay to stable
Sm, removal of all of the fission product samarium is pointless,
and the absorbed Pm band is usually collected in a manner to yield
99% chemical purity. However, the center of the band contains Pm
exceeding 99.9% chemical purity. The only radiochemical impurity
detected, ^{154}Eu, is present in the product at concentrations
$< 10^{-9}$ Ci ^{154}Eu/Ci ^{147}Pm. The subsequent addition of 14 and 11-inch
I.D. columns of the same height has permitted an increase in the
amount of ^{147}Pm processed per run from 65,000 Ci to 300,000 Ci.

In developing a process for separating Pm from the adjacent
lanthanides, it is essential to minimize exposure of the resin and
eluting agent to radiolysis by choosing process parameters which
yield an optimum degree of purification in a minimum of exposure
time. Both kinetic and thermodynamic effects must be considered.

EDTA was used with a Zn^{+2} barrier for the first pilot plant
production run. As a result of a careful laboratory evaluation of
the eluting agents EDTA, HEDTA, and DTPA, the optimum elution
conditions for each were determined.[7] DTPA was shown to be
superior and a switch to DTPA (with a Zn^{+2} barrier) reduced the
time required to complete a Pm purification run from 21 days to
6 days.[6] In subsequent evaluations of other complexing agents,
NTA (nitrilotriacetic acid) was found to be superior to DTPA for
the purification of Pm and its use in pilot plant production re-
duced the time required for a purification run to less than 3 days.
The experimental results which lead to these conditions are des-
cribed herein.

EXPERIMENTAL

Elution Sequence

A series of ion-exchange separations experiments were performed
to determine the elution sequence of various ions contained in the
Pm feed. In these experiments, small beds of Dowex 50W, X-8 (50-
100 mesh) resin were loaded to saturation with simulated feed solu-
tions containing both macro and radiochemical tracer quantities of
the ions in question. In each experiment, the absorbed band was

then eluted two band lengths down a second bed of the same resin, in the Zn^{+2} cycle, and the effluent solution collected in fractions as the absorbed band was eluted from the second resin bed. Each eluting solution was prepared at optimum pH and concentrations. pH adjustment was made with NH_4OH. The columns were jacketed and the temperature maintained at 60°C. Sufficient analytical work was done to locate the relative positions of the maximum concentration of each ion. Identification and concentration measurements were made on macro rare earth constituents by use of a Cary Model 14 spectrophotometer. Because of potential problems of identification of the radiotracers, separate experiments were performed for those which did not have a distinct, identifiable, noninterfering gamma spectrum. The elution sequences obtained are given in Table 1. Er, Ho, and Dy would not be expected to be present in any Pm feed, but were included in the DTPA and NTA experiments to provide reference points for the other ions.

TABLE 1

Elution Sequence

0.012M EDTA at pH 8.5

Zn^{+2}, Al^{+3}, Y^{+3}, Gd^{+3}, Eu^{+3}, Sm^{+3}, Pm^{+3}, Nd^{+3}, Pr^{+3}, Ce^{+3}, La^{+3}

0.030M HEDTA at pH 5.0

Zn^{+2}, Pb^{+2}, Al^{+3}, Gd^{+3}, Eu^{+3}, Sm^{+3}, Y^{+3}, Pm^{+3}, Nd^{+3}, Pr^{+3}, Ce^{+3}, La^{+3}

0.050M DTPA at pH 6.5

Zn^{+2}, Pb^{+2}, $(Er^{+3}-Ho^{+3}-Dy^{+3})$ (Cm^{+3}, Am^{+3}) Gd^{+3}, Eu^{+3}, Sm^{+3}, Y^{+3}, Pm^{+3}, Nd^{+3}, Pr^{+3}, Ce^{+3}, La^{+3}

0.105M NTA at pH 6.4

Zn^{+3}, $(Cm^{+3}-Y^{+3})$, Gd^{+3}, $(Eu^{+3}-Am^{+3})$, Sm^{+3}, Pm^{+3}, Nd^{+3}, Pr^{+3}, Ce^{+3}, La^{+3}

From the point of view of promethium separation efficiency, the significant information in Table 1 is the elution sequence of yttrium (a fission product present in most promethium feed solutions). In the DTPA (or HEDTA) elution sequence, yttrium elutes between samarium and promethium. The resultant Y-Pm separation coefficient is significantly smaller than the Sm-Pm or Pm-Nd separation coefficients. As a result, the Y-Pm binary mixture zone contains a larger fraction

-248-

of the total promethium than does the Pm-Nd binary zone. This results in an increase in the percentage of promethium that must be recycled from each run. The product elution curve from a DTPA promethium production run, shown in Figure 1, illustrates this problem. With NTA (or EDTA), yttrium elutes in an innocuous position ahead of gadolinium and production experience has shown that the front and back edges of the promethium band contain equal amounts of promethium for recycle.

Experimental Evaluation of Elution Parameters

In a previous publication[6], a standardized ion-exchange elution procedure is described in which a 100 ml bed of resin is completely saturated with equivalent amounts of Sm^{+3}, Nd^{+3}, and Pr^{+3}, then eluted down a second column of the same resin under carefully controlled conditions. Neodymium serves as a convenient stand-in for promethium in these laboratory experiments. The amount of resin in the second column (the elution column) can be altered to examine the effect of various elution distances. When the absorption column contains 100 ml of resin and the elution column 200 ml of resin, the elution distance is defined as being two band lengths. Fractionation of the effluent solution and analysis of the fractions provide data from which a descriptive elution curve can be constructed such as the one shown in Figure 2. Graphical integration of the various areas of the elution curves thus obtained, permits an accurate comparison of the relative effectiveness of eluting agents under a variety of eluting conditions.

One parameter previously used to compare the effectiveness of various separations is the ratio of the amount of neodymium obtained 100% pure divided by the total amount of neodymium present in the experiment.[6,7] This criterion provides a valid basis for estimating the effectiveness of eluting agents for promethium separation if the Sm-Nd separation is similar to the Nd-Pr separation. Such is true with EDTA, HEDTA, and DTPA when an allowance is made for the fact that neodymium and praseodymium are adjacent elements whereas samarium and neodymium are separated by two atomic numbers. However, the results obtained with NTA show that the Sm-Nd separation is dramatically superior to the Nd-Pr separation. Since the separation achievable in the Sm-Nd region should be more representative of promethium purification (promethium lies between samarium and neodymium in the elution order), the ratio of the quantity of neodymium contained in the Sm-Nd intermediate zone of binary mixing, divided by the total quantity of neodymium present in the experiment, should provide a more valid basis for comparison of eluting agents and operating conditions for promethium purification. Such a ratio is conveniently expressed as:

PROMETHIUM DTPA ELUTION CURVE
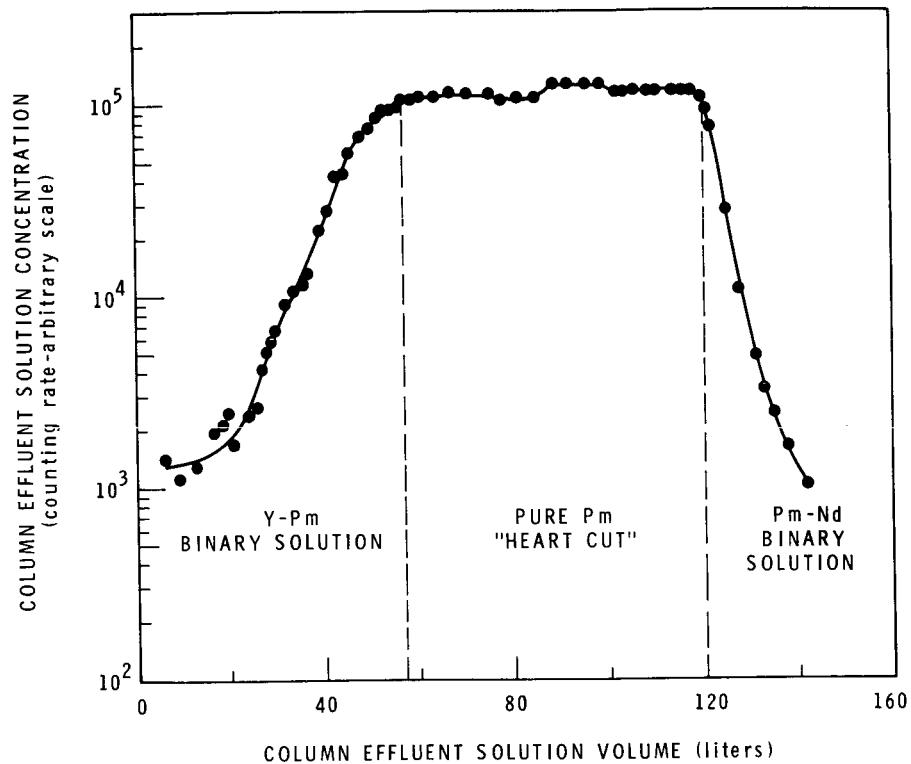
FIGURE 1

IDEALIZED ELUTION CURVE

Samarium   Neodymium   Praseodymium

Effluent Solution Rare Earth Concentration

Column Effluent Volume

E B   A   B E

D C   C D

FIGURE 2

-251-
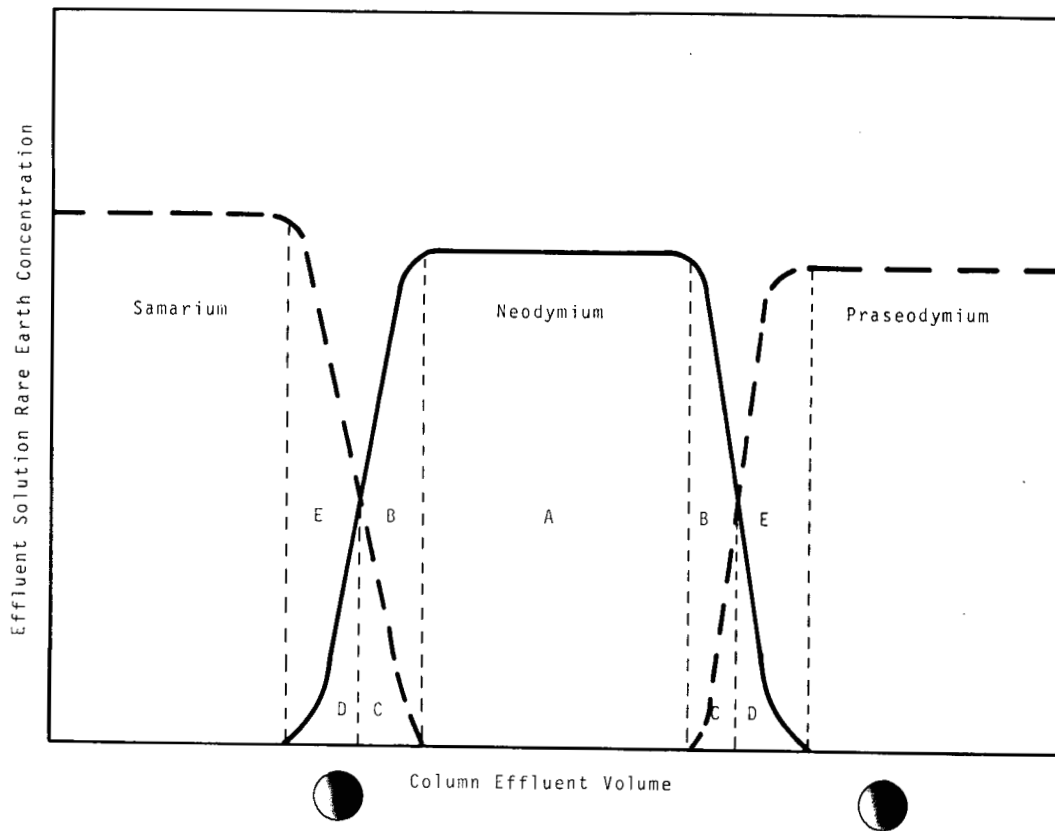
$$F = 100(1-R)$$

where

$$R = \frac{Nd_{Binary\ Zone}}{Nd_{Total}} = \frac{D + C + B}{D + C + B + A + B' + C' + D'}$$

The area ratio R is obtained from graphical integration of the elution curves from each experiment (letters A through D refer to the lettered areas of the sample elution curve shown in Figure 2). The value of $\underline{F}$ is proportional to the separation achieved, i.e., a value of 100 would imply no binary mixing or perfect separation.

The effect of eluting solution pH changes upon the Sm:Nd separation efficiency is shown in Figure 3. With both NTA and DTPA, the permissible pH range is fairly broad, but the optimum pH is close to 6.0. Eluant pH values less than 5.0 were not considered because of the resultant decrease in the rate of advance of the absorbed band. EDTA is very pH-sensitive; below pH 8.0 the metal ion complexes precipitate, and above 8.8 the lanthanides pass through the Zn^{+2} barrier.

The striking superiority of NTA is shown in Figure 4. The DTPA process flowsheet specified a mass flow rate of 0.36 milliequivalents/min-cm^2. With NTA, essentially no change is observed in the separation efficiency at twice that rate. Indeed, in the pilot plant, promethium purification runs with NTA have been made at flow rates corresponding to 1.1 milliequivalents/min-cm^2 with no detectable loss in separation efficiency.

CONCLUSIONS

It will be obvious to the reader that sufficient work to uniquely determine the optimum operating conditions for NTA elutions has not been done. In particular, the minimum elution distance necessary to bring about separation and the maximum elution rate consistent with an acceptable degree of separation, have not been fully determined. In previous work with EDTA, HEDTA, and DTPA, optimum operating conditions were determined and the data, shown in Figure 4 for those three complexing agents, were obtained at optimum concentration and pH. Specifically, the elution distance was shown to be sufficient to yield a maximum separation consistant with other operating conditions.

-252-

EFFECT OF CHANGES IN ELUTING SOLUTION pH UPON SEPARATION EFFICIENCY

▼ 0.012M EDTA; pH 8.7

▽ 0.030M HEDTA; pH 5.5

● 0.025M DTPA; pH 6.5

○ 0.050M DTPA; pH 6.5

□ 0.105M NTA; pH 6.4

RESIN: DOWEX 50W, X-8 (50-100 MESH)

TEMPERATURE: 60°C

ELUTION DISTANCE: 2 BAND LENGTHS
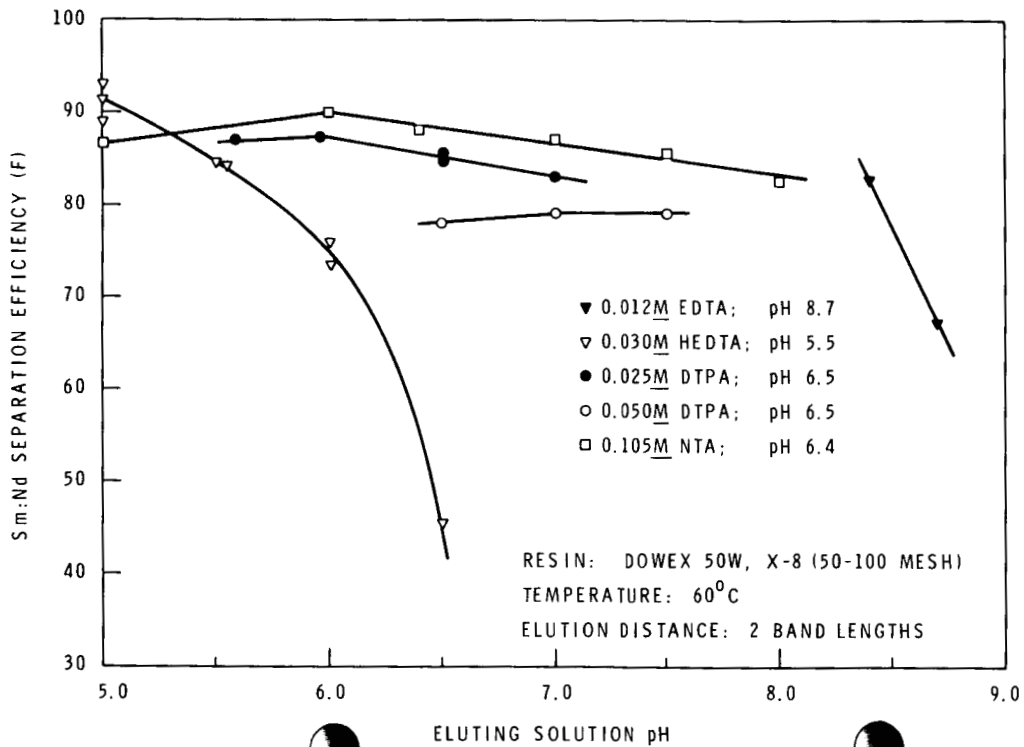
FIGURE 3

-253-

COMPARISON OF EDTA, HEDTA, DTPA AND NTA SEPARATION EFFICIENCY AS A FUNCTION OF MASS FLOW RATE

Legend:
- ▼ 0.012M EDTA; pH 8.7
- ▽ 0.030M HEDTA; pH 5.5
- △ 0.012M DTPA; pH 6.5
- ▲ 0.036M DTPA; pH 6.5
- ○ 0.050M DTPA; pH 6.5
- ● 0.062M DTPA; pH 6.5
- ☐ 0.105M NTA; pH 6.4
- ■ 0.105M NTA; pH 7.0

RESIN: DOWEX 50W, X-8 (50-100 MESH)
TEMPERATURE: 60^{0}C
ELUTION DISTANCE: 2 BAND LENGTHS

Y-axis: Sm:Nd SEPARATION EFFICIENCY (F)

X-axis: MASS FLOW RATE (MILLIEQUIVALENTS/MIN-cm^2)
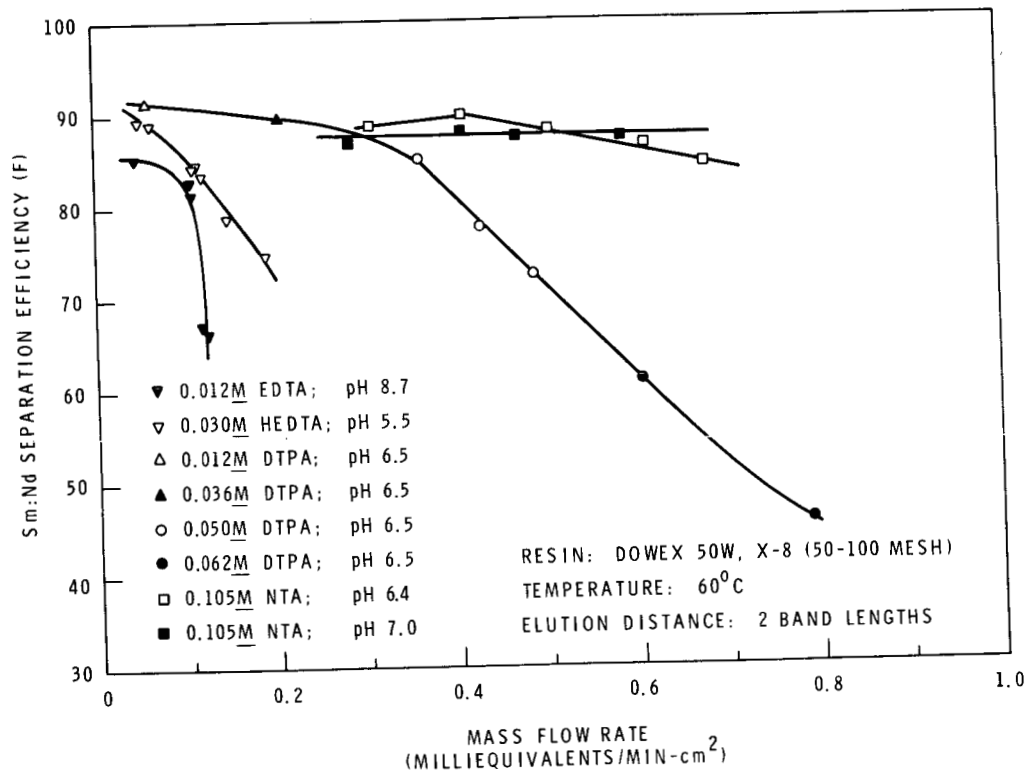
FIGURE 4

-254-

It has shown[2,5] that the separation coefficient for any two rare earths, R_1 and R_2, can be approximated as a ratio of the stability constants of the complexes formed between the cations and the complexing agents.

$$K_{sep} \approx \frac{K_{R_2Ch}}{K_{R_1Ch}},$$

where the symbol Ch represents the anion.

With NTA, both 1:1 and 1:2 complexes can be formed with the rare earths and the equation takes the form[8]

$$K_{sep} = \frac{K_{R_2Ch} \, K_{R_2(Ch)_2}}{K_{R_1Ch} \, K_{R_1(Ch)_2}}.$$

The stability constants between the "light" lanthanides and the four complexing agents have been measured.[8,9,10,11] The promethium stability constants have not been determined so values midpoint between samarium and neodymium were assumed in calculating the approximate coefficients shown in Table II.

TABLE II

Approximate Separation Coefficients

	K_{sep}			
Lanthanide Pair	EDTA	HEDTA	DTPA	NTA
Pm-La	38.9	51.3	380.0	56.2
Pm-Ce	8.3	7.1	34.7	19.1
Pm-Pr	3.6	3.5	4.9	5.0
Pm-Nd	1.8	1.7	2.0	2.3
Pm-Sm	1.8	1.7	2.0	2.3
Pm-Eu	2.4	1.9	2.3	4.7
Pm-Gd	2.5	1.5	3.0	4.1
Pm-Y	11.8	2.8	1.4	3.2

An examination of Table II suggests that the superiority of NTA for this separation results from much faster kinetics rather than thermodynamic effects.

REFERENCES

2. J. E. Powell, Separation of Rare Earths by Ion Exchange, In THE RARE EARTHS (Edited by F. H. Spedding and A. H. Daane). Wiley, New York (1961).

3. E. J. Wheelwright and F. P. Roberts, UNITED STATES ATOMIC ENERGY COMMISSION UNCLASSIFIED REP. HW-73651, REV (1963).

4. P. B. Orr, UNITED STATES ATOMIC ENERGY COMMISSION, UNCLASSIFIED REP. ORNL-3271 (1962).

5. J. E. Powell and F. H. Spedding, CHEM. ENGNG PROG. SYMP. SER $\underline{55}$, 24, 101 (1959).

6. E. J. Wheelwright, et. al., UNITED STATES ATOMIC ENERGY COMMISSION UNCLASSIFIED REP. BNWL-318 (1966).

7. E. J. Wheelwright and T. R. Myers, UNITED STATES ATOMIC ENERGY COMMISSION UNCLASSIFIED REP. BNWL-69 (1965).

8. S. C. Levy and J. E. Powell, UNITED STATES ATOMIC ENERGY COMMISSION UNCLASSIFIED REP. IS-421 (1962).

9. F. H. Spedding, J. E. Powell, and E. J. Wheelwright, J. AM. CHEM. SOC. $\underline{78}$, 34 (1956).

10. E. J. Wheelwright, F. H. Spedding, and G. Schwarzenback, J. AM. CHEM. SOC. $\underline{75}$, 4196 (1953).

11. R. Harder and S. Chaberek, J. INORG. NUCL. CHEM. $\underline{11}$, 197 (1959).

INFRARED AND RAMAN SPECTRA OF TRIVALENT LANTHANIDE -
DI-(2-ETHYLHEXYL) PHOSPHORIC ACID SOLVENT EXTRACTION
ORGANIC EQUILIBRIUM PHASES

Robert C. Lloyd* and Harry Bostian

Department of Chemical Engineering
University of Mississippi
University, Mississippi 38677

Infrared analyses and Raman polarization studies have been made on
organic phases of the systems: Di-(2-ethylhexyl) phosphoric acid - $Re(NO_3)_3$ - H_2O,
where Re represents a trivalent lanthanide, either lanthanum or neodymium.
These studies substantiated extraction stoichiometries suggested by semimicro
material balance data and aided in determining the structure of the extracted
complexes. The principal stoichiometries suggested were:

$$Re^{3+}_{aq} + 3\left[(HDEHP)_2 \cdot H_2O\right]_{org} \longrightarrow Re\left[H(DEHP)_2\right]_{3\,org} + 3H_2O_{aq} + 3H^+_{aq} \text{ , and}$$

$$Re(NO_3)^{a+}_{b\,aq} + a\left[(HDEHP)_2 \cdot H_2O\right]_{org} \longrightarrow Re(NO_3)_b\left[H(DEHP)_2\right]_{a\,org} + aH_2O_{aq} + aH^+_{aq} \text{ ,}$$
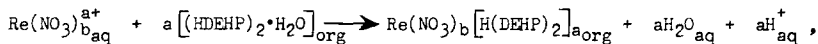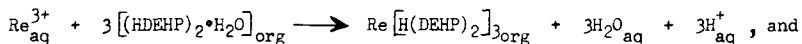
where HDEHP represents Di-(2-ethylhexyl) phosphoric acid, DEHP is the acid
monomer less a hydrogen ion, aq refers to aqueous, org to organic, a is the charge
on the rare earth nitrate complex and b represents the number of nitrate anions.
The first stoichiometry was found to hold at low aqueous phase concentrations.
The second stoichiometry with a=2 and b=1 was found to be the principal mechanism
of extraction in the mid concentration range and the reaction with a=1 and
b=2 the principal extraction stoichiometry near saturation. In addition to
confirming the above stoichiometries, the infrared spectra indicated nature of
bonding. The Raman polarization data showed that the nitrate groups were bound
in a bidentate fashion to the rare earth.

---

* To present the paper, presently with E. I. DuPont de Nemours and Co.,
Nylon Technical Section, Chattanooga, Tennessee.

Pm, Cm, Bk, and Cf

TRICYCLOPENTADIENYL COMPLEXES OF PROMETHIUM, CURIUM,

BERKELIUM AND CALIFORNIUM: THEIR PREPARATION

AND IDENTIFICATION BY MICROTECHNIQUES[*]

P. G. Laubereau[†] and J. H. Burns

~~Transuranium Research Laboratory, Chemistry Division~~
Oak Ridge National Lab~~oratory~~
~~Oak Ridge,~~ Tenn~~essee~~ 37830

6/7 1000

Abstract. - The compounds $Pm(C_5H_5)_3$, $Cm(C_5H_5)_3$, $Bk(C_5H_5)_3$ and $Cf(C_5H_5)_3$ have been synthesized in microgram amounts with techniques specially adapted to the minuteness of the samples. In addition evidence was obtained for the possible formation of a complex $(C_5H_5)_2BkCl$. The existence of the compounds was established by comparison of their X-ray powder patterns with those of the known compounds $Pr(C_5H_5)_3$, $Sm(C_5H_5)_3$, $Eu(C_5H_5)_3$, $Gd(C_5H_5)_3$ and $Tb(C_5H_5)_3$. In case of the tricyclopentadienyls of Pm, Cm, Bk and Cf further proof of their identity was obtained from single-crystal data. It was also possible to record electronic spectra which will be reported together with other properties of the compounds.

Schematically the method of synthesis of microgram quantities of tricyclopentadienyls was as follows:

M^{3+} in 0.05 N HCl

↓

M^{3+} on ion-exchange bead

↓   oxidize in air at $1200^{\circ}C$

M_2O_3 (probably MO_2 in case of Bk)

↓

-258-

↓   HCl gas at 500°C

MCl$_3$

↓   Be(C$_5$H$_5$)$_2$ melt

M(C$_5$H$_5$)$_3$,
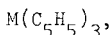
where the last reaction step corresponds to the equation:

$$2MCl_3 + 3Be(C_5H_5)_2 \text{ (melt at 70°C)} \rightarrow 2M(C_5H_5)_3 + 3BeCl_2$$
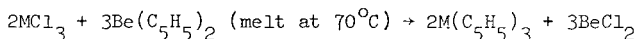
and M = ^{248}Cm, ^{249}Bk, ^{249}Cf, ^{147}Pm, Sm or Tb. The pure actinide and lanthanide complexes were crystallized by fractional sublimation in high vacuum at temperatures from 135-220°C. The reactions were carried out with the apparatus shown in Fig. 1. The reaction vessel was a quartz capillary tube, shown in Fig. 2, in which "A" marks the reaction zone, "B" is the zone where the pure product is deposited, and "C" is the zone for temporary storage of Be(C$_5$H$_5$)$_2$.

For comparison Pr(C$_5$H$_5$)$_3$, Sm(C$_5$H$_5$)$_3$ and Gd(C$_5$H$_5$)$_3$ were synthesized on the gram scale with modified established methods and Eu(C$_5$H$_5$)$_3$ in a new way by reaction of EuCl$_3$ with Be(C$_5$H$_5$)$_2$ followed by isolation of the pure compound by extraction with pentane.

Cm(C$_5$H$_5$)$_3$, Bk(C$_5$H$_5$)$_3$ and Cf(C$_5$H$_5$)$_3$, prepared for the first time in the course of this work, and Pm(C$_5$H$_5$)$_3$, prepared for the first time in a weighable quantity (see ref. 1,2), showed essentially the expected properties of tricyclopentadienyls of lanthanides[1,2,3,4] and actinides.[5,6] Because of this identification was possible by comparison of X-ray powder diagrams and other properties.

Table I shows the powder diagrams of the tricyclopentadienyls of Pm, Cm, Bk and Cf together with those of the tricyclopentadienyls
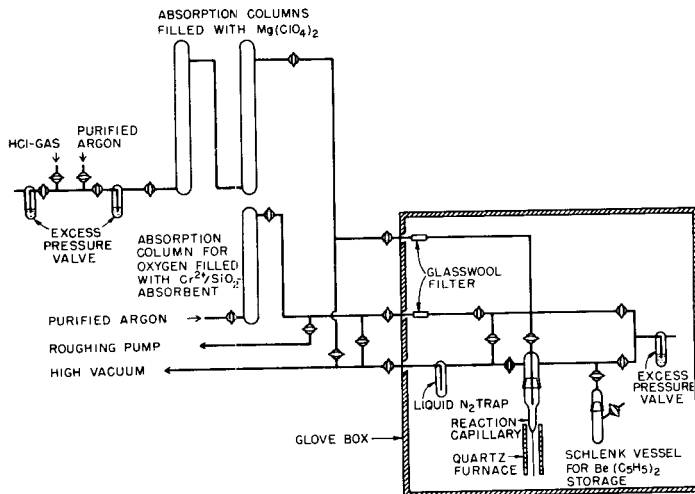
SCHEMATIC DRAWING OF THE APPARATUS FOR THE SYNTHESIS
OF THE TRICHLORIDES AND THE TRICYCLOPENTADIENYLS

Fig. 1
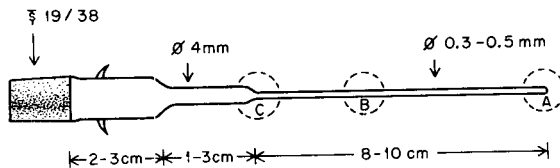
REACTION CAPILLARY

Fig. 2

-260-

Indexed Powder Patterns

Table I

hkl	I_{obs}[a]	d_{obs}, Å	d_{calc}, Å	d_{calc}[b], Å	d_{obs}[c], Å	Pr(C₅H₅)₃ d_{obs}, Å	Pm(C₅H₅)₃ d_{obs}, Å	Eu(C₅H₅)₃ d_{obs}, Å	Gd(C₅H₅)₃ d_{obs}, Å	Tb(C₅H₅)₃ d_{obs}, Å	Cm(C₅H₅)₃ d_{obs}, Å	Bk(C₅H₅)₃ d_{obs}, Å	Cf(C₅H₅)₃ d_{obs}, Å
			Sm(C₅H₅)₃										
120	m	7.47	7.44	7.42	7.46	7.56	7.50	7.47	7.45	7.36	7.48	7.49	7.39
200	s,br	7.04	7.06	7.11	7.02	7.11	7.04	7.04	7.04	6.98	7.07	7.07	7.00
021	vw	6.63	6.52	6.49				6.58	6.45	6.68	6.68		
121	vs	5.93	5.92	5.90	5.88	5.94	5.92	5.90	5.88	5.89	5.92	5.91	5.89
002	s	4.85	4.88	4.86	4.86	4.87	4.87	4.87	4.82	4.82	4.80	4.81	4.83
102 310	vw	4.65	4.61 / 4.55	4.60 / 4.58				4.68	4.63	4.64			4.63
040	w	4.40	4.38	4.35				4.37	4.39	4.38	4.44	4.42	4.40
320 122	w	4.16	4.15 / 4.08	4.16 / 4.07		4.15		4.13	4.19 / 4.11	4.10	4.18	4.15	4.12
202 041	s	3.982	4.015 / 3.994	4.016 / 3.971		4.022		4.002	3.982	3.965	3.97	3.974	3.960
321	vw	3.806	3.817	3.829		3.818		3.809	3.809		3.83	3.809	3.834
222	vw	3.611	3.650	3.646		3.655		3.648	3.500		3.73		
400 241	w,br	3.490	3.532 / 3.477	3.557 / 3.468		3.485	3.487	3.476	3.450	3.473	3.57 / 3.49	3.472	3.471
042	m	3.341	3.259	3.243		3.270	3.283	3.255	3.240	3.240		3.236	3.237
322 250	vw	3.153	3.160 / 3.138	3.164 / 3.126		3.167		3.153	3.140	3.148		3.089	
123 242	s	2.975	2.981 / 2.959	2.972 / 2.951	2.97	3.051 / 2.981	2.969	2.975	2.950	2.950	2.950	2.946	2.950
402 160	m	2.855	2.861 / 2.858	2.872 / 2.842	2.84	2.871	2.865	2.860	2.876 / 2.838	2.844	2.873	2.856	2.860
440 161	vw		2.749 / 2.743	2.754 / 2.728		2.757		2.736			2.771	2.747	
520	vw		2.689	2.705		2.694							
441	w	2.661	2.646	2.650		2.655	2.656	{2.639	2.657	2.647	2.659	2.666	2.659
043 521 143 530	m	2.603	2.611 / 2.593 / 2.568 / 2.543	2.600 / 2.606 / 2.558 / 2.555		2.599	2.595	2.639	2.622 / 2.594 / 2.571	2.585	2.592	2.593	
323	m	2.549	2.559	2.559		2.562		2.558	2.537	2.523	2.527	2.531	2.520
062	vw	2.501	2.505	2.491					2.500				
360 162 170 531 243	s,br	2.470	2.481 / 2.466 / 2.463 / 2.461 / 2.449	2.474 / 2.454 / 2.449 / 2.471 / 2.442	2.45	2.486 / 2.457	2.468	2.460	2.465	2.457	2.471	2.460	2.461

[a] Visually estimated intensities: vs = very strong, s = strong, m = medium, w = weak, vw = very weak, br = broad

[b] Based on data of C. Wong, T. Lee and Y. Lee, Proc. Tenth Int. Conf. Coord. Chem., Tokyo and Nikko, Japan, p. 95 (1967).

[c] G. W. Watt and E. W. Gillow, J. Am. Chem. Soc., 91, 775 (1969).

of Pr, Sm, Eu, Gd and Tb obtained by us and indexed by use of the

single-crystal data of Table II. Additionally, in the case of Sm,

Table II

Unit-cell Dimensions[a] of Tricyclopentadienyls

Metal, M	Radius(M^{3+})	$a, \text{Å}$	$b, \text{Å}$	$c, \text{Å}$	Vol., Å^3	$d_{calc.}$[b], $g \cdot cm^{-3}$
Pr	1.013	14.20	17.62	9.79	2449	1.82
Pm	0.979	14.12	17.60	9.76	2425	1.88
Cm	0.979	14.16	17.66	9.69	2423	2.43
Sm	0.964	14.15	17.52	9.77	2422	1.90
Bk	0.954	14.11	17.55	9.63	2385	2.47
Eu	0.950	14.10	17.57	9.79	2425	1.90
Cf	0.944	14.10	17.50	9.69	2391	2.47
Gd	0.938	14.09	17.52	9.65	2382	1.97
Tb	0.923	14.20	17.28	9.65	2368	1.99

[a]Accurate to about 0.5%.

[b]Density is calculated assuming 8 formula weights per unit cell.

---

the d-values found by Watt and Gillow[7] and d-values calculated

from the data of Wong, et al.[8] are also given. The good agree-

ment among all the data is offered as proof of the existence of

$Pm(C_5H_5)_3$, $Cm(C_5H_5)_3$, $Bk(C_5H_5)_3$ and $Cf(C_5H_5)_3$.

Results obtained from single-crystal studies are shown in

Table II together with the lanthanide radii of Templeton and

Dauben[9] and the actinide radii of Peterson and Cunningham.[10] All

the cyclopentadienyl compounds reported here crystallize with orthorhombic symmetry. Systematic absences of the type $0k\ell$ for $k = 2n + 1$ and $h0\ell$ for $\ell = 2n + 1$ were observed. These are characteristic for the space groups Pbcm and Pbc2_1; the first of these was chosen by Wong, et al.[8] as the correct one. Evidence for a possible second, but closely related, structure for some of these compounds was observed by us. Moreover, we have some data showing that a structure different from these is obtained when the radius of the central ion becomes very small, as in the case of $Tm(C_5H_5)_3$ (0.869Å).

Although the described synthesis proved to be a reliable way to obtain tricyclopentadienyls, under certain conditions it was possible to synthesize $(C_5H_5)_2BkCl$ (light amber in color). Its higher sublimation temperature and the agreement of its powder pattern with that of a compound which we believe to be $(C_5H_5)_2SmCl$ suggested the formula.

The following colors of the freshly sublimed compounds were observed: $Cm(C_5H_5)_3$, nearly colorless; $Bk(C_5H_5)_3$, amber (with a max. of 1% [249]Cf impurity); $Cf(C_5H_5)_3$, ruby red; $Pm(C_5H_5)_3$, dark orange (with a max. of 8.3% [147]Sm impurity). Determination of the colors was limited by the minuteness of the samples, by possible effects of radiolysis, and in some cases, by rapid formation of daughter elements from nuclear decay. The survey of the f-f spectra in the region 400-700 nm (350-1000 nm for $Bk(C_5H_5)_3$) gave no indication for the presence of impurities.

With special microtechniques the following visible absorption spectra were obtained:[11]

$Cf(C_5H_5)_3$ - broad absorptions beginning at 600 nm and extending into the blue (can be attributed to "electron transfer processes").

$Bk(C_5H_5)_3$ - absorptions at 435-450 (broad), 462,477 (shoulder), 483,494 (shoulder), 514,540 (broad), 615-640 (broad), 650-660 (shoulder) and 730 (broad) nm (can be attributed to f-f transitions).

$Cm(C_5H_5)_3$ - several sharp absorptions near 640 nm; bright red fluorescence by excitation with UV light of 360 nm.

$Pm(C_5H_5)_3$ - sharp absorptions at 497, 505, 510, 550, 552, 554, 558, 562, 564, 568, 570, 577, 579, 582, 584, 587, 590, 592, 595, 599, 601, 608 and 620 nm (can be attributed to f-f trans.; no $Sm(C_5H_5)_3$ f-f trans. detected, however, interference by much stronger and broad $Sm(C_5H_5)_3$ electron-transfer band in the region < 540 nm was evident).

The cyclopentadienyl complexes of ^{248}Cm, ^{249}Bk, ^{249}Cf, and ^{147}Pm were comparatively stable against autoradiolytic decay. Resublimation with high yields was possible after eight days of storage in each case. In an attempted synthesis with the short-lived α-emitting ^{244}Cm, however, a rapid radiolytic decomposition of the $CmCl_3-Be(C_5H_5)_2$ reaction mixture occurred and no $Cm(C_5H_5)_3$ was obtained.

The overall similar properties of the new tricyclopentadienyls as compared with the properties of the known tricyclopentadienyls of the lighter lanthanides and actinides suggest a very similar character of the metal-ligand bonds.

<div align="center">References</div>

1) F. Baumgartner, E. O. Fischer, and P. G. Laubereau, Radiochimica Acta, $\underline{7}$, 188 (1967).

2) R. Kopunee, F. Macasek, V. Mikulaj, and P. Drienovsky, <u>Radiochem.</u>
   <u>Radioanal. Letters</u>, <u>1</u>, 117 (1969).

3) J. M. Birmingham and G. T. Wilkinson, <u>J</u>. <u>Am</u>. <u>Chem</u>. <u>Soc</u>., <u>78</u>, 42
   (1956).

4) E. O. Fischer and H. Fischer, <u>J</u>. <u>Organometal</u>. <u>Chem</u>., <u>3</u>, 181 (1965).

5) F. Baumgärtner, E. O. Fischer, B. Kanellakopulos, and P. Laubereau,
   <u>Angew. Chem.</u>, <u>77</u>, 866 (1965); <u>Angew</u>. <u>Chem</u>. <u>Int</u>. <u>Ed</u>., <u>4</u>, 878 (1965);
) F. Baumgärtner, E. O. Fischer, B. Kanellakopulos, and P. Laubereau,
   <u>Angew</u>. <u>Chem</u>., <u>78</u>, 112 (1966); Angew. Chem. Int. Ed., <u>5</u>, 134 (1966).

7) G. W. Watt and E. W. Gillow, <u>J</u>. <u>Am</u>. <u>Chem</u>. <u>Soc</u>., <u>91</u>, 775 (1969).

8) C. Wong, T. Lee, and Y. Lee, <u>Proc</u>. <u>Tenth Int</u>. <u>Conf</u>. <u>Coord</u>. <u>Chem</u>.,
   Tokyo and Nikko, Japan, p. 95 (1967).

9) D. H. Templeton and C. H. Dauben, <u>J</u>. <u>Am</u>. <u>Chem</u>. <u>Soc</u>., <u>76</u>, 5237
   (1954).

10) J. R. Peterson and B. B. Cunningham, <u>Inorg</u>. <u>Nucl</u>. <u>Chem</u>. <u>Letters</u>, <u>3</u>,
    327 (1967).

11) L. J. Nugent, P. G. Laubereau, G. K. Werner, and K. L. Vander Sluis,
    <u>Proc</u>. <u>Eighth Rare Earth Conf</u>., Reno, Nevada (1970).

FORMATION CONSTANTS OF THE RARE-EARTH COMPLEX SPECIES

Yasuo Suzuki and Mariko Mikado

Radioisotope School

Japan Atomic Energy Research Institute

2-28-49 Honkomagome, Bunkyo-ku, Tokyo

Japan

Abstract

The formation constants of the rare-earth α-hydroxyisobutyrate complex species have been determined potentiometrically at 25.0° and 40.0°C and at an ionic strength of 0.10 with sodium perchlorate as a supporting electrolyte. A double-junction calomel reference electrode was used throughout the work in order to minimize the errors due to the formation of slightly soluble potassium perchlorate, resulting in more accurate constants than ever. Both an IBM 7044 and a FACOM 230-60 computers were employed for the calculations. The constants versus atomic number curve obtained is smoother than the ones previously reported, although two minor breaks are apparently observed at gadolinium and also at neodymium. The constant for yttrium falls between those for dysprosium and holmium, as predicted from their ionic radii.

Introduction

Since Choppin, Harvey, and Thompson[1] first reported the use of

α-hydroxyisobutyric acid as a new eluant for the cation-exchange separation

of the actinide elements, this reagent has been used extensively for

separating tracer amounts of the rare-earth elements[2-5]. The formation

constants of the rare-earth α-hydroxyisobutyrates have been determined by

several authors as will be discussed later.

Although chelate formation constants furnish much information about the

ion-exchange separation of the metals involved, the actual ion-exchange

behavior is often far from that expected from formation constants. For example, the cation-exchange separation of europium and gadolinium has been carried out efficiently by using α-hydroxyisobutyrate as an eluant[3-5], while the formation constants of the corresponding complex species obtained by the previous authors are too close to each other to account for the ion-exchange phenomena. Such discrepancy should necessarily be interpreted to obtain maximum applicability of formation constants to ion-exchange separations.

The formation constant versus atomic number curves for the rare-earth α-hydroxyisobutyrate complexes based on the previous works are all quite winding, and the trend is not consistent among those curves, except the gadolinium break. In the present work, it was intended to redetermine the formation constants and to correlate ion-exchange behavior with the constants obtained. The gadolinium break and the position of yttrium are also the problems to be investigated.

The potentiometric method of determining stability constants, which was developed by Bjerrum[6,7], Leden[8,9], and Fronaeus[10], has been reviewed in detail by Sonesson[11]. The pH measurements involved in this method were improved by incorporation of a double-junction calomel reference electrode, to remove the error due to formation of potassium perchlorate. The electrode behaved quite satisfactorily, resulting in more reliable constants than previously reported.

Experimental

Rare-earth perchlorate solutions. --- The rare-earth oxides were

-267-

supplied by the Department of Nuclear Engineering, Tohoku University, and by

Shin-etsu Chemical Industries, Co., Ltd., and all were of 99.9 % or greater

purity. Rare-earth perchlorate solutions were prepared from these oxides,

and adjusted to the equivalent pH values.

α-Hydroxyisobutyric acid. --- This reagent, which was purified by

sublimation at Wako Pure Chemicals Industries, Ltd., and had a melting point

of 78.8 – 81.0°C, was used without further purification.

pH meter and electrodes. --- A Beckman model 1019 Research pH meter was

used with the Beckman 41263 and 39000 glass electrodes. Since it is impos-

sible to use the regular calomel reference electrode with good accuracy and

reproducibility in the perchlorate solutions, a sodium chloride electrode,

which was simply prepared by the replacement of a saturated potassium

chloride solution in the regular calomel electrode by a saturated sodium

chloride solution,[12] was used. Due to the appreciable difference

between the ionic mobilities of potassium and sodium ions, errors as

much as 0.3 in pH unit were observed in various electrolyte solutions at an

ionic strength of 0.1, with poor reproducibility. This electrode tends to

to accumulate the errors in pH as much as ± 0.2 per 1 pH unit difference

from a standard buffer solution. A salt bridge[13] has been used in per-

chlorate solutions at an ionic strength of 2, to avoid the difficulty. In

this work, a double-junction calomel reference electrode of Denki Kagaku

Keiki, Co., Ltd., filled with an ammonium chloride solution, was employed

in combination with the glass electrode. The concentration of ammonium

chloride chosen was 4.16 $\underline{M}$ (the concentration of the saturated potassium

chloride solution at 25°C). This electrode was tested over a wide pH range

and compared with a regular calomel reference electrode in solutions

-268-

containing various salts. The results revealed that the double-junction electrode could safely be used in the pH region from 2 to 5, where most of the pH readings in the stability constant work should fall, within the accuracy of the pH meter used. Quite stable pH readings were obtained even at the highest sensitivity.

The apparent activity coefficients of hydrogen ion were determined by titrating a known amount of perchloric acid at an ionic strength of 0.10 with a standard sodium hydroxide solution, and were found to be 0.9089 and 0.9158 at 25.0 and 40.0°C, respectively. These coefficients were used to calculate the hydrogen-ion concentrations from the pH readings. A buffer solution of pH 4.008 at 25.0°C was carefully prepared, and used as a standard throughout the measurements[14].

Other experimental details are the same as described in the authors' previous report[15].

The dissociation constant of α-hydroxyisobutyric acid at an ionic strength of 0.10 and at 25.0°C was determined potentiometrically with sodium perchlorate as the supporting electrolyte. The constant obtained was $(1.617 \pm 0.002) \times 10^{-4}$. This value compares quite favorably with values reported by the previous authors as shown in Table I. At 40.0°C, the dissociation constant varied somewhat with increasing buffer concentrations, but the value 1.515×10^{-4}, obtained by extrapolation, was used for subsequent computations.

As shown by the previous authors[18], α-hydroxyisobutyric acid combines with metal ions as monobasic bidentate ligands, and the rare-earth cations form at least 1:1, 1:2, and 1:3 species with α-hydroxyisobutyrate anion.

-269-

TABLE I

Dissociation Constants of α-Hydroxyisobutyric Acid

Authors	Temp., $^{\circ}$C	Ionic strength	Dissociation constant	Ref.
Ostwald	25	0	1.06×10^{-4}	16
Stagg and Powell	25	0.5	1.76×10^{-4}	12
Deelstra and Verbeek	25	0.2	1.614×10^{-4}	17
Suzuki and Mikado	25	0.1	1.617×10^{-4}	this work

For the heavy rare earths, however, all the following equilibria were con-

sidered to obtain greater accuracy.

$$R^{3+} + A^- \rightleftharpoons RA^{2+} \; ; \quad K_1 = [RA^{2+}]/[R^{3+}][A^-],$$

$$RA^{2+} + A^- \rightleftharpoons RA_2^+ \; ; \quad K_2 = [RA_2^+]/[RA^{2+}][A^-],$$

$$RA_2^+ + A^- \rightleftharpoons RA_3 \; ; \quad K_3 = [RA_3]/[RA_2^+][A^-],$$

$$RA_3 + A^- \rightleftharpoons RA_4^- \; ; \quad K_4 = [RA_4^-]/[RA_3][A^-].$$
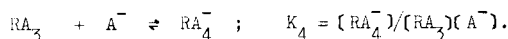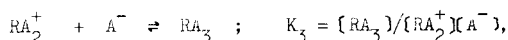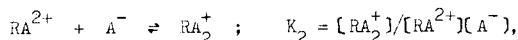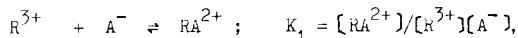
Calculation of the individual constants was performed by the computa-

tional programs, originally prepared for the IBM 7074 computer at the Iowa

State University Computation Center, Ames, Iowa, and adapted to the IBM 7044

and the FACOM 230-60 computers at the Japan Atomic Energy Research Institute,

Tokai, Ibaraki, Japan.

The results obtained are shown in Tables II and III and in Figure 1.

Discussion

The stability constants obtained by Choppin and Chopoorian[13], Stagg

and Powell[12], and Deelstra and Verbeek[19], determined at higher ionic

strengths, are similar and appreciably lower than those reported by Powell,

-270-

TABLE II

Stepwise Stability Constants[a] of the Rare-Earth α-Hydroxyiso-
butyrate Species at 25.0°C and μ = 0.10 ($NaClO_4$).

Element	K_1	K_2	K_3	K_4	log K_1	K_1/K_2	K_2/K_3
La	324.7	44.0	21	-	2.511	7.38	2.1
Ce	-	-	-	-	-	-	-
Pr	529.3	108.	14	-	2.724	4.91	7.6
Nd	591.9	102.	12	-	2.772	5.80	8.5
Sm	844.3	172.	27	13	2.926	4.92	6.4
Eu	921.5	187.	32	5	2.965	4.92	5.9
Gd	977.9	225.	51	-	2.990	4.35	4.5
Tb	1240.	255.	60	6	3.093	4.86	4.2
Dy	1485.	362.	77	12	3.172	4.10	4.7
Ho	1754.	459.	108	22	3.244	3.82	4.2
Er	2087.	484.	149	19	3.320	4.31	3.3
Tm	-	-	-	-	-	-	-
Yb	-	-	-	-	-	-	-
Lu	3056.	724.	201	45	3.485	4.22	3.6
Y	1598.	351.	129	9	3.204	4.55	2.7

[a]The values in this table are subject to absolute errors as great as
± 2 % in the case of K_1, and to relative errors as great as ± 10 %,
± 30 %, and ± 50 % in the cases of K_2, K_3, and K_4, respectively.

Karraker, Kolat and Farrell at the Third Rare Earth Research Conference[18].
The constants obtained in this research at 25.0°C fall between the two classi-
fications mentioned above, and fit a much smoother curve than those previously
reported, as can be seen in Figur 1. This curve seems to be sufficiently
reasonable to account for the most ion-exchange behaviors of the rare-earth

α-hydroxyisobutyrates. Consequently, the gadolinium break observed in Figure 1 is less distinct than before, and an apparent neodymium break is observed.

The fact that, the ion-exchange separation of europium and gadolinium using α-hydroxyisobutyric acid can be achieved as efficiently as in the case of other adjacent pairs of rare earths, apparently coincides with the present experimental results. The ion-exchange separation factors for europium and gadolinium α-hydroxyisobutyrates were calculated[20] using the stability constants obtained, together with the presumed free ligand concentrations, and the factor was found to increase to as much as 1.76 at a free ligand concentration of 0.3 $\underline{M}$ or higher. This coincides with the results by cation exchange method[21]. On the other hand, the separation of praseodymium and neodymium should be carried out at somewhat lower concentrations of the ligand at 25.0°C.

As can be seen in Figure 1, the minor discontinuity around praseodymium and neodymium, which may be called the neodymium break, has also been observed by Devine[22]. This break seems to require further investigation through accumulation of accurate formation constants, in connection with the effect of the 4f electron shells.

The position of yttrium in the stability constant sequence has long been discussed. From this research, yttrium falls between dysprosium and holmium, just as would be predicted from the cationic radii. In the practical ion-exchange separation, however, yttrium has been found to elute close to terbium, or between terbium and dysprosium[2-5]. Unfortunately, this fact cannot be properly explained by the present result.

The situation is somewhat different at 40.0°C, although only a few rare

-272-

TABLE III

Stepwise Stability Constants of the Rare-Earth α-Hydroxyiso-
butyrate Species at 40.0°C and μ = 0.10 (NaClO$_4$).

Element	K_1	K_2	K_3	K_4	log K_1	K_1/K_2	K_2/K_3
La	–	–	–	–	–	–	–
Ce	–	–	–	–	–	–	–
Pr	531.0	118.	8.6	–	2.725	4.49	14
Nd	674.3	92.4	29	–	2.829	7.30	3.2
Sm	867.9	160.	27	–	2.939	5.44	6.0
Eu	–	–	–	–	–	–	–
Gd	1027.	179.	31	–	3.012	5.76	5.7
Tb	–	–	–	–	–	–	–
Dy	1494.	341.	74	–	3.175	4.38	4.6
Ho	1689.	418.	106	14	3.228	4.04	4.0
Er	2012.	464.	119	16	3.304	4.34	3.9
Tm	–	–	–	–	–	–	–
Yb	–	–	–	–	–	–	–
Lu	–	–	–	–	–	–	–
Y	1501.	336.	99	6	3.176	4.47	3.4

earth α-hydroxyisobutyrates have been investigated. As can be seen by the
comparison of Tables II and III, the constants increase slightly when the
temperature is increased in the case of the lighter rare earths, but
decrease slightly in the case of rare earths heavier than holmium. The
remarkable fact is that no neodymium break was observed at 40°C. The released
hydrogen-ion concentrations versus ligand concentration curve for neodymium
indicates that the neodymium α-hydroxyisobutyrates are more stable at higher
ligand concentrations at 40° than at 25°C. It is thus probable that ion-

exchange separation of the lighter rare earths would slightly be more clean cut at 40° than at $25^{\circ}C$.

Acknowledgement

References

(1) G. R. Choppin, B. G. Harvey and S. G. Thompson, J. inorg. nucl. Chem., 2, 66 (1956).

(2) K. E. Seyb and G. Herrmann, Z. Elektrochem., 64, 1065 (1960).

(3) L. Wish and S. C. Foti, J. Chromatog., 20, 585 (1965).

(4) S. C. Foti and L. Wish, ibid., 29, 203 (1967).

(5) M. M. Zeligman, Anal. Chem., 37, 524 (1965).

(6) J. Bjerrum, "Metal Ammine Formation in Aqueous Solution", P. Haase and Son, Copenhagen, 1941.

(7) J. Bjerrum, Chem. Revs., 46, 381 (1950).

(8) I. Leden, Z. physik. Chem.(Leipzig), A188, 160 (1941).

(9) I. Leden, "Potentiometrisk undersökning av nagra kadmiumsalters komplexitet", Dissertation, Lund, 1943.

(10) S. Fronaeus, "Komplexsystem hos kopper", Dissertation, Gleerupska Universitets, Bokhandeln, Lund, 1948.

(11) A. Sonesson, Acta Chem. Scand., 12, 165 (1958).

(12) W. R. Stagg and J. E. Powell, Inorg. Chem., 3, 242 (1964).

(13) G. R. Choppin and J. A. Chopoorian, J. inorg. nucl. Chem., 22, 97 (1961).

(14) R. G. Bates, J. Res. Nat. Bur. Stds., 66A, 179 (1962).

(15) J. E. Powell and Y. Suzuki, Inorg. Chem., 3, 690 (1964).

(16) W. Ostwald, Z. physik. Chem., 3, 170 (1891).

(17) H. Deelstra and F. Verbeek, Bull. Soc. Chim. Belg., 72, 612 (1963).

(18) J. E. Powell, R. H. Karraker, R. S. Kolat and J. L. Farrell, "Rare Earth Research II", Proceedings of the Third Conference on Rare Earth Research, Gordon and Breach, New York, 1964, p. 509.

(19) H. Deelstra and F. Verbeek, Anal. Chim. Acta, 31, 251 (1964).

(20) W. R. Stagg and J. E. Powell, USAEC Rept. IS-727, Iowa State University of Science and Technology, Ames, Iowa (1963).

(21) H. Natsume, to be published.

(22) C. D. Devine, Doctoral dissertation, Iowa State University of Science and Technology, Ames, Iowa (1967), unpublished.
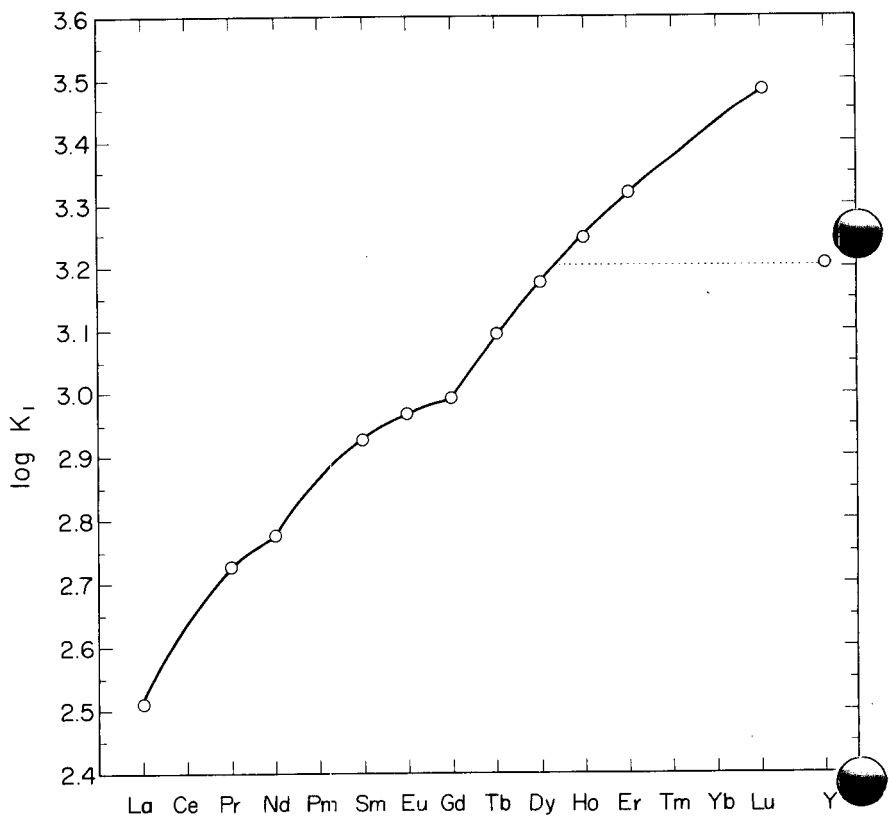
Figure 1. Logarithms of the first—step stability constants of the rare—earth α-hydroxyisobutyrate complex species at 25.0 °C and μ = 0.10 (NaClO$_4$).

DIFFERENT HYDRATED FORMS OF THE ETHYLENEDIAMINETETRAACETATO COMPLEXES OF THE RARE EARTHS*

J. Linn Mackey, David E. Goodney, and James R. Cast

Chemistry Department, Austin College
Sherman, Texas   75090

Abstract

By control of conditions, the reaction between rare earth carbonates and ethylenediaminetetraacetic acid (EDTA) yields different hydrates of the protonated 1:1 rare earth-EDTA chelates. Some of these chelates correspond to those already reported in the literature, while others are new. These chelates have been characterized by chemical analysis, I.R., T.G.A., and X-ray powder diffraction. The stability and structure of the different hydrated forms of these 1:1 chelates are discussed in terms of the ionic radii, coordination numbers of the rare earths and the steric requirements of the chelates.

Introduction

The protonated 1:1 chelates of the rare earths with ethylenediaminetetraacetatic acid (EDTA) were prepared and studied by Moeller and co-workers[1] and by Kolat and Powell[2].

This work indicated that the solid chelates of lanthanum through samarium were monohydrates (HLnEDTA·H₂0) while the rest of the rare earth chelates were anhydrous (HLnEDTA). Recently Hoard and co-workers[3] reported the preparation and X-ray study of a new hydrate form of the lanthanium chelate, HLaEDTA·7H₂0. This rare earth-chelate was shown to have a ten-coordinate lanthanium ion with the EDTA acting as a hexadentate and four water molecules coordinated to the lanthanium.

In this paper, we report the preparation and characterization of other multihydrates of the 1:1 rare earth-EDTA chelates in addition to HLaEDTA·7H₂0 and discuss the relation of these chelates to those reported previously.

Experimental

Preparation. Each of the protonated rare earth-EDTA chelates was prepared by reacting equal molar quantities of the respective rare earth carbonate with ethylenediaminetetraacetic acid in aqueous solution. The rare earth carbonates were prepared by the method of Head[4]. The reaction mixture was stirred until the solution cleared while carefully controlling the temperature. If the temperature is not low enough (below room temperature in some cases) then the respective monohydrate or anhydrous chelate is formed. Crystals of the multihydrate chelates were obtained by cooling the saturated solutions.

Chemical Analysis. The chelates were quantitively
analyzed for rare earth, EDTA and acidic hydrogen. The
quantity of rare earth was determined by firing to the
oxide and weighing. The EDTA was determined by titrating
with bismuth in acidic solution using xylenol orange as an
indicator, and the acidic hydrogen was titrated with a
standard sodium hydroxide solution. Water of hydration
was obtained by difference and also by the Karl Fischer
method for the samarium chelate.

Thermogravimetric Analysis (TGA). The thermograms were
measured with an apparatus consisting of a Cahn RG electro-
balance and a Marshall furnace controlled by a F & M
Scientific 240 temperature programmer. The thermograms
were run in air and in some cases nitrogen atmospheres.
The heating rate was 4° degrees per minute.

Infrared Data. Infrared spectra were recorded on a
Beckman model 8 spectrophotometer. Spectra were of the
solids pressed in KBr pellets.

X-Ray Data. X-ray powder diagrams were obtained using a
114.59 mm diameter Philips camera and Mo $K\alpha$ radiation
with a Zr filter.

Solubility Measurements. The solutions with an excess of
solid added were equilibrated in a constant temperature
bath. Samples were removed over various time periods for

analysis. Equilibrium seems to be obtained within two days. The solutions in equilibrium with the solids were removed and analyzed for non-chelated rare earth-ions by titrating with EDTA using xylenol orange as indicator. Total EDTA was obtained by lowering the pH below two and back titrating with bismuth, again using xylenol orange as indicator. The quantity of rare earth present was obtained by evaporating the solutions and firing to the oxide. A thermogram was run on a sample of the solid in contact with solution.

Results and Discussion

Multihydrate forms of the protonated 1:1 chelates of EDTA with lanthanium, samarium and europium were prepared. The analytical data for these chelates is presented in Table I.

The number of water molecules associated with the chelates varies somewhat with the length of drying. An attempt was also made to prepare a multihydrate form of the holmium chelate, but we were unable to isolate such a product. The only products obtained from the reaction of holmium carbonate and EDTA were the anhydrous HHoEDTA and Ho(HoEDTA)$_3$ under the conditions used.

The temperature stability of the multihydrate chelates in the presence of water was studied as well as the solubility of both the multihydrate chelates and the

-280-

TABLE I.   RESULTS OF CHEMICAL ANALYSIS OF MULTIHYDRATE CHELATES

Sample	mmoles H^+ per g. Cmpd.	mmoles Ln per g. Cmpd.	mmoles EDTA per g. Cmpd.	mmoles H_2O per g. Cmpd.
La	1.744	1.706	1.715	11.77-14.84
Sm	2.071	1.899	1.960	9.12-12.11
Eu	1.509	1.449	1.455	7.36- 9.42

monohydrate or anhydrous chelates. In the presence of water, the multihydrate chelates convert irreversibly to the respective monohydrate or anhydrous chelate over a particular temperature range. For $HLaEDTA \cdot 7H_2O$ the conversion occurs above $45°C$ and is complete by $55°C$. For $HSmEDTA \cdot 6H_2O$ the conversion occurs above $25°C$ and is complete by $35°C$, while for $HEuEDTA \cdot 6H_2O$ the conversion occurs above $15°C$ and is essentially complete by $25°C$. It appears that a decreasing temperature stability occurs for the multihydrates in solution with increasing atomic number across the rare earth series. This trend seems to offer a likely explanation for our inability to isolate a multihydrate form of the holmium chelate.

The data on the solubility of several monohydrate chelates and an anhydrous chelate is presented in Figure 1. A general increase in solubility with temperature is noted for the compounds. There is a considerable difference in solubility between the monohydrate chelates and the anhydrous HHoEDTA.

Data on the solubilities of $HLaEDTA \cdot 7H_2O$ and $HSmEDTA \cdot 6H_2O$ are presented in Table II. There are several striking differences observed between these two chelates. The samarium chelate is much more soluable than the lanthanium chelate and the former disproportionates in solution while the latter does not. This is shown by the

fact that   non-complexed samarium was observed in the
solutions in equilibrium with the solid samarium chelate.
The solid remaining after equilibrium is established is
found to have uncomplexed EDTA present. The material
balance is compatible with the following equilibrium:

$$HSmEDTA \cdot 6H_2O \rightleftharpoons Sm(SmEDTA)_3 + H_4EDTA.$$
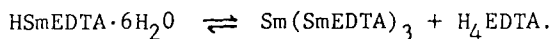
The $Ln(LnEDTA)_3$ salts were observed in the earlier studies
of rare earth-EDTA chelates[1]. The solubility of the multi-
hydrate form of the samarium chelate is nearly ten times
that of the monohydrate form.

TABLE II.   SOLUBILITIES OF $HLaEDTA \cdot 7H_2O$ AND $HSmEDTA \cdot 6H_2O$
            AS MMOLES PER 100 GRAMS OF SOLUTION

| | Temperature | | | |
Species	$15^{\circ}C$	$25^{\circ}C$	$35^{\circ}C$	$45^{\circ}C$
$HLaEDTA \cdot 7H_2O$				
La^{3+}		None present		
$HLaEDTA \cdot 7H_2O$	-	0.11	0.17	0.25
$HSmEDTA \cdot 6H_2O$				
$Sm^{3+} = Sm(SmEDTA)_3$	0.391	1.071	0.024	-
Total EDTA	3.92	6.62	2.26	-
Total Sm	4.31	7.69	2.33	-
HSmEDTA	2.69	3.31	2.26	-

X-ray diffraction data for the multihydrate chelates is summarized in Table III. The samarium and europium compounds show a distinct similarity and appear to be isomorphous, while the lanthanium compound is markedly different. The X-ray data of the multihydrate chelates are also distinctly different from that published for the respective monohydrate or anhydrous chelates[1,2].

TABLE III.   SUMMARY OF X-RAY DIFFRACTION DATA ON
             d-SPACINGS

HLaEDTA·7H$_2$O d-Å	HSmEDTA·6H$_2$O d-Å	HEuEDTH·6H$_2$O d-Å
8.09 (w)[a]	7.97 (m)	-
6.95 (m)	6.56 (s)	6.69 (m)
6.23 (w)	5.81 (s)	5.83 (s)
5.53 (s)	4.80 (vs)	4.83 (vs)
4.87 (s)	3.87 (m)	3.89 (w)
4.26 (m)	3.37 (vs)	3.34 (vs)
3.86 (m)	2.82 (s)	2.82 (s)
3.58 (m)	2.55 (s)	2.58 (m)
3.30 (m)	2.24 (m)	2.27 (w)
3.03 (m)	2.05 (vw)	2.03 (vw)
2.79 (m)	1.92 (vw)	-
2.62 (vw)	1.61 (w)	1.62 (w)
2.41 (vw)		
2.30 (w)		
2.19 (w)		
2.05 (m)		
1.92 (w)		

a   vs - very strong
    s - strong
    m - medium
    w - weak
    vw - very weak

The infrared spectra are presented in Figures 2, 3 and 4. The I.R. spectra of the monohydrate and anhydrous chelates are presented for comparison. A partial inter- pretation of the I.R. spectra of the monohydrate and anhydrous chelates has been presented by Kolat and Powell[2]. Unfortunately, the resolution of our spectra over the carbonyl stretching region is not great enough to make a detailed analysis and comparison with previous studies. Therefore, we will limit the discussion to very general features of the spectra.

The spectra of HSmEDTA·6H$_2$0 and HEuEDTA·6H$_2$0 appear to be identical while there are significant differences in the spectra of HLaEDTA·7H$_2$0. This is seen, for example, in the relative intensities of the bands in the 1280-1340 cm^{-1} and 1220-1260 cm^{-1} regions. The absorptions in this region have been assigned to -COO$^-$ and -CN- respectively by some investigators[5]. There is also a significant difference in the splittings and intensities in these same regions of the spectrum when the monohydrate or anhydrous chelates are compared to the multihydrate forms. The multihydrate chelates all show a broad -OH band which nearly obscures the C-H stretch absorption at 2855 cm^{-1}, while for the monohydrates and anhydrous chelates the band at 2855 cm^{-1} stands out clearly. The 900-1000cm^{-1} region of the spectrum appears to give a characteristic pattern

for the multihydrates as contrasted with other chelates.

The thermograms of HLaEDTA·7H$_2$0 and HLaEDTA·1H$_2$0 are presented in Figure 5, and HSmEDTA·6H$_2$0 and HSmEDTA·1H$_2$0 are presented in Figure 6. The results for the europium chelate are similar to those shown. The thermograms show that the multihydrate chelates retain water well above 100°C, and in fact it appears that some of the water and carboxyl groups decompose over the same temperature range. This is evidence that several waters are coordinated to the metal ion. It is also significant that the thermograms of the multihydrates do not show a weight plateau corresponding to either a monohydrate or anhydrous form. The most striking difference in the thermograms is the decomposition of the carboxyl groups of the EDTA. For the monohydrate or anhydrous chelate, a single rapid decomposition occurs in the 400 to 450°C temperature range, while the carboxyl decomposition appears to be stepwise for the multihydrate chelates. One carboxyl decomposition occurs as high as 600°C for the latter. This type of thermal behavior for EDTA chelates has been attributed to different structural types. We infer from the thermograms that the multi-hydrate chelates of samarium and europium have a structure similar to that of HLaEDTA·7H$_2$0 with a hexadentate EDTA and several waters coordinated to the metal ion to give coordination numbers of eight or nine.

-286-

These results raise a question regarding the structure of the monohydrate and anhydrous chelates. These chelates have been interpreted in terms of a coordination number of six for the lanthanide ions. It was suggested that the ethylenediaminetetraacetato ligand acted as a pentadentate for the lanthanides through samarium with a sixth coordination position filled on the metal ion by water and as a hexadentate for the rest of the lanthanide series[1,2]. However, X-ray studies indicate that the chelation framework of EDTA can reach less than half way around even the smallest lanthanide ion, so that coordination numbers greater than six would be expected for all EDTA-lanthanide chelates[6]. In view of this and the now well established coordination numbers of eight, nine or ten for lanthanide compounds[6,7], we suggest that the monohydrate and anhydrous chelates are polymeric with one or more carboxyl groups bridging different lanthanide ions. This would allow the lanthanide ions to achieve their usual coordination numbers. Some evidence for a polymeric form for the monohydrate chelates may be inferred from the very low solubility and their nonhydroscopic nature as compared to the multihydrate chelates.

References

1. T. Moeller, F. A. J. Moss and R. H. Marshall, _J. Am._
   Chem. Soc., _77_, 3182 (1955).

2. R. S. Kolat and J. E. Powell, _Inorg. Chem._ _1_, 485 (1962).

3. J. L. Hoard, Byungkook Lee, and M. D. Lind, _J. Am. Chem._
   Soc., _87_, 1611 (1965).

4. E. L. Head, _Proceedings of the Seventh Rare Earth_
   Research Conference, Coronado, California,
   Oct. 28-30. p. 731 (1968).

5. D. T. Sawyer and P. J. Paulsen, _J. Am. Chem. Soc._, _80_,
   1597 (1958).

6. J. L. Hoard, Byungkook Lee, and M. D. Lind, _J. Am. Chem._
   Soc., _87_, 1612 (1965).

7. T. Moeller, D. F. Martin, L. C. Thompson, R. Ferrus,
   G. Feistel, and W. J. Randall, _Chem. Rev._, _65_, 1 (1965).
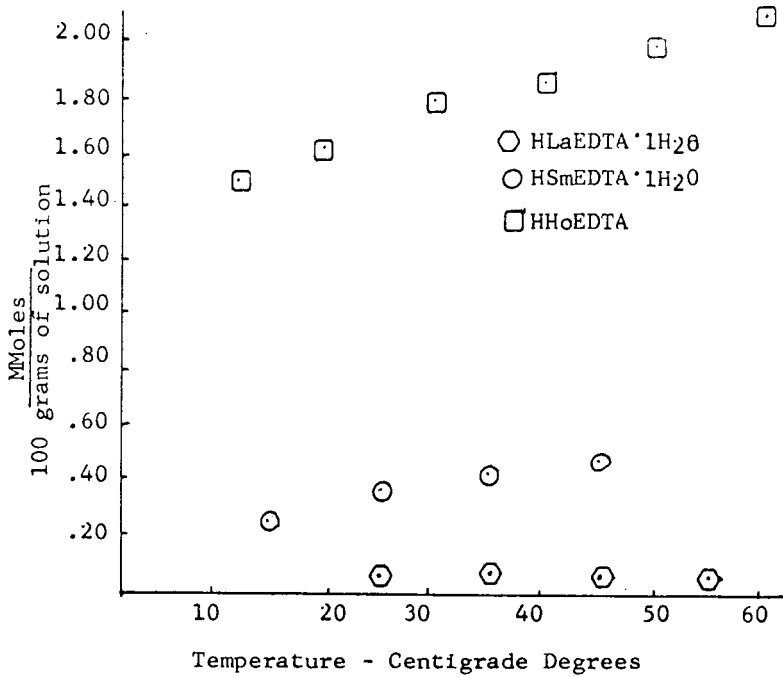
Fig. 1 Solubilities of Monohydrate and Anhydrous
Rare Earth - EDTA Chelates
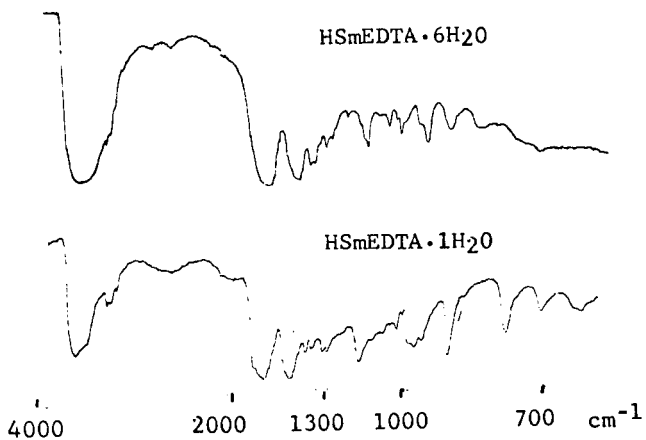
Fig. 2   I.R. Spectra of Samarium - EDTA Chelates
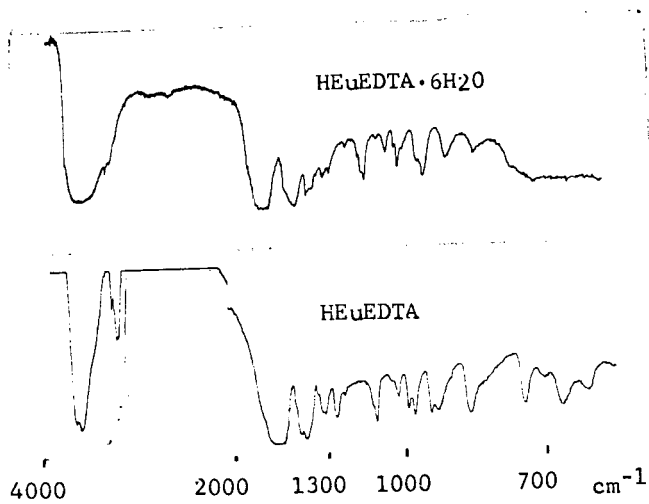
Fig. 3   I.R. Spectra of Europium - EDTA Chelates
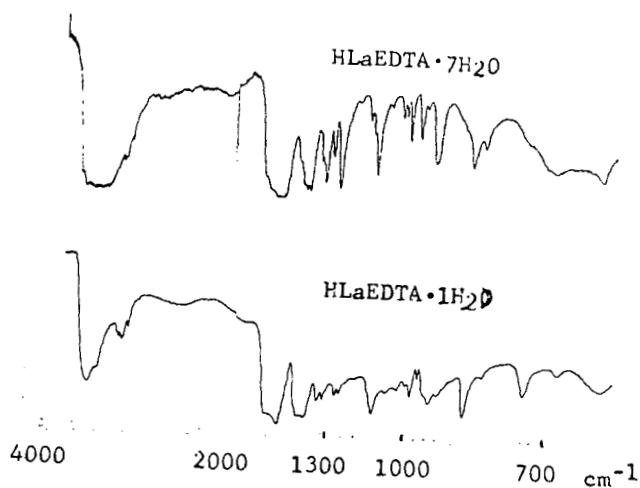
Fig. 4   I.R. Spectra of Lanthanium - EDTA Chelates

Fig. 5

—— HSmEDTA·5H$_2$O
‑ ‑ ‑ HSmEDTA·1H$_2$O

WEIGHT

I 1mg

100 200 300 400 500 600 700 800 900 1000
TEMPERATURE °C

Fig. 6

—— HLaEDTA·7H$_2$O
‑ ‑ ‑ HLaEDTA·1H$_2$O

WEIGHT

I 1mg

100 200 300 400 500 600 700 800 900
TEMPERATURE °C

-292-
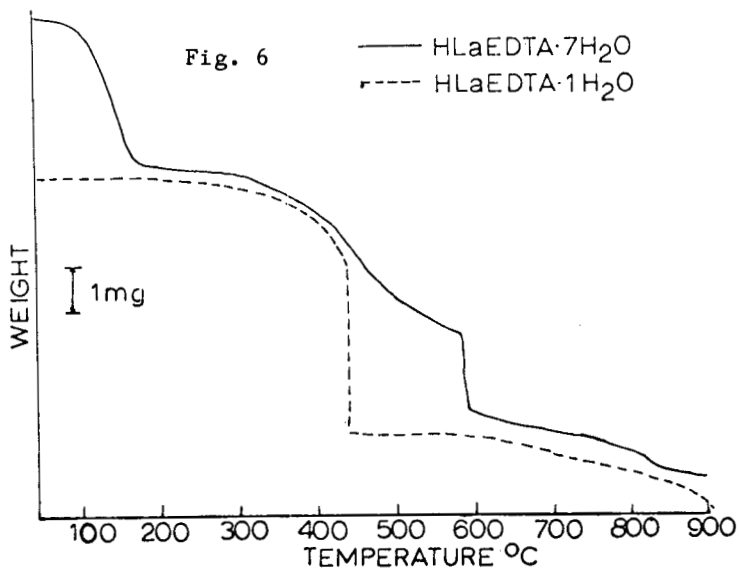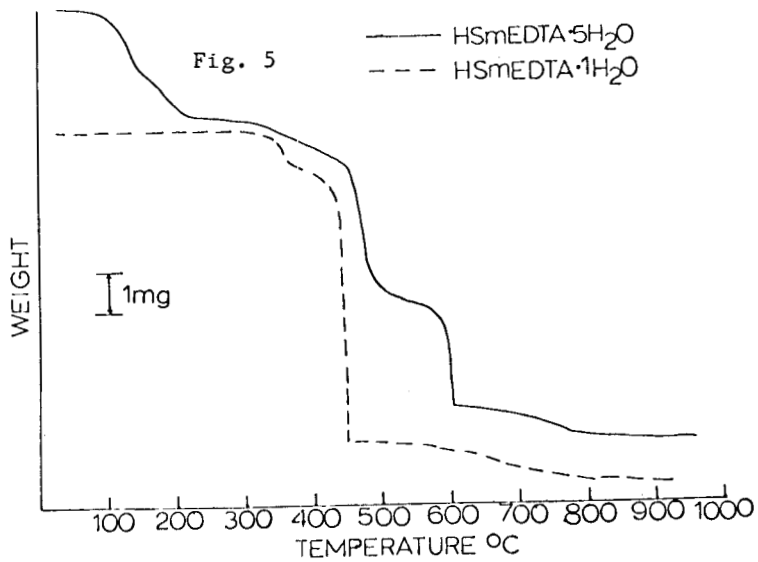
ANALYSIS OF THE ELUTION SYSTEM OF RARE EARTHS
WITH CHELATING AGENT AS ELUENT

Zenzi Hagiwara* and Susumu Sakaguchi**

*Faculty of Engineering, Tohoku University, Sendai 980, Japan
**Shinetsu Chemical Company, Marunouchi, Chiyoda-ku,
  Tokyo, Japan

Abstract

　　Under steady-state conditions, elutions of the Tb-Y and
Dy-Y pairs have been performed at different temperatures using
EDTA involved a metal chelate. After the establishment of a
steady state throughout the exchange system, several series
of the experimental data on the rare-earth eluates from the
ion-exchange column were analyzed on the basis of rate theory,
employing the separation factors measured in similar conditions
to those in the real elution system. It was found that the
present ion-exchange system was controlled by film diffusion
as the rate-determining step and the plate-height values due
to film diffusion (H_f) were found to be a function of the flow
rate. The H_f values were consistent with the HETP values
obtained from the point of countercurrent extraction. Also,
in an attempt to justify the observed α values needed to
analyze the elution results of the rare-earth mixtures at
different temperatures, the separation factors of the Tb-Y and
Y-Dy pairs in the presence of chelating agent have been
discussed.

INTRODUCTION

　　Individual rare-earth elements have been separated by
either ion exchange or solvent extraction. Of these, demand
for yttrium with higher purities has been increased to satisfy
the various purposes in the fields of research and industry.
The ion-exchange production[1]of yttrium proposed by the Ames
Laboratory, USAEC, has been mainly developed using a chelating
agent such as ethylenediamine-N,N,N',N'-tetraacetic acid
(EDTA or H_4Y) in combination with the cation exchange resin.
　　In the ion-exchange separation of Y from other rare
earths with dilute EDTA eluent, the elution position falls
between Tb and Dy in the lanthanide series, as may be expected
from the stability constants [2, 3] of the yttrium- and the
lanthanide-EDTA chelates. For understanding the elution
mechanism, it may be valuable to investigate precisely the
elution behavior of the Tb-Y and Y-Dy pairs at different con-
ditions, since no systematic research has been made for them.
It is also possible from the above fundamental research to
find the optimum elution condition for resolving a Tb-Y-Dy
mixture by ion exchange and to serve in fact to produce each
element in high purity.

-293-304

Generally, for more effective column performance, it is necessary to improve the fundamental items such as the separation factor and the theoretical plate height concerning the exchange system, and these two have the responsibility for the efficiency of the column operation. Starting from the rate theory on the ion-exchange process, one of the authors has derived theoretical relationships[4] related to the plate height contribution due to either film or particle diffusion as the rate-determining step, and the induced equations were confirmed to explain well the ion-exchange systems described in the previous reports[4,5,6].

The principal purpose of this study was to analyze the elution system related to the purification of Y in high purities. Thus, the mixtures of the Tb-Y and Y-Dy pairs were eluted at various conditions using the Ca-NH_4-Y eluent, and the results obtained in elutions at the steady state were treated theoretically using the separation factors[7,8] measured at different temperatures. The Y-concentrate obtained from Xenotime was also employed for the elution experiments in a fairly large scale.

<center>EXPERIMENTAL</center>

The rare-earth oxides such as Tb_4O_7, Y_2O_3, and Dy_2O_3 were supplied from the Shinetsu Chemical Company, and their purities were much greater than 99,95 %. They were dissolved with a slight excess of hydrochloric acid on heating. Further, the Y-concentrate composed of 61.0 % Y_2O_3, 8.4 % Ce-group oxide, 91.4 % Y-group oxide, and small amounts of FeO and ThO_2, was employed for the experiments.

The ion-exchange columns filled with Dowex 50W-X8, 50-100 mesh were conditioned with hydrochloric acid and then with citric acid in order to remove trace amounts of heavy metals in the resin particle. The eluents of a Ca-NH_4-H-Y type were prepared by dissolving a mixture of EDTA and $CaCO_3$ with dilute ammonium hydroxide on heating.

The elution experiments of the rare-earth mixtures were carried out at different temperatures using a similar experimental apparatus to that mentioned in our recent paper[9]. The columns constructed of 22 mm (i.d.) Pyrex glass tube jacketed with 60 mm (i.d.) glass tube, were closed at the bottom with coarse sintered glass disks in order to support the resin bed with a bed dimension of 22 mm (i.d.) $\times$ 1000 mm (H-form basis), and these were used as the retaining bed as well as the loading bed for rare earth. In the experiments, the sorption columns for the rare earth were adjusted to proper lengths, depending on the loaded amount of the rare-earth mixture. Also, the 50 mm (i.d.) jacketed acryl columns with a bed dimension of 50 mm (i.d.) $\times$ 1000 mm (H-form basis) were employed in series. Prior to elution, the columns were

<center>-294-</center>

back-washed with hot water maintaining at a slightly higher
degree than the real elution temperature so that dissolved
gases and fine particles in the resin could be removed.
After pre-treatment, a saturated bed with the rare-earth
mixture and two types of the mixed retaining bed were prepared;
one of the mixed beds consisted of the Zn-NH$_4$-H form ($\overline{Zn^{2+}} \cong$
0.94, $\overline{NH_4^+} \cong$ 0.05, $\overline{H^+} \cong$ 0.01 equivalent fraction), and the other
bed, of the Zn-H form ($\overline{Zn^{2+}} \cong$ 0.92, $\overline{H^+} \cong$ 0.08 equivalent fraction).
In the above expressions, the barred symbols refer to the resin
phase of the indicated species.   With the aid of vinyl tube,
the loaded rare-earth column was first connected with the Zn-
NH$_4$-H bed, and the latter was then connected, in series, with
the Zn-H bed.   The purpose of using the Zn-NH$_4$-H bed between
the rare-earth band and the Zn-H bed is to prevent the depo-
sition of free acid H$_4$Y, due to the reaction of hydrogen ion
in the retaining bed.

After one series of the ion-exchange columns had been kept
at a definite temperature by circulating hot water from a
constant-temperature-bath, elution was started by flowing a
degassed solution of the eluent into the top of the exchange
column with a saturated rare earth mixture.   The variation in
the temperature was held at ± 0.5°C through all the columns.
The number of the ion-exchange column with a mixed form of
Zn and H was increased, corresponding to the amount of the
rare earth charged on the resin.

In the elution experiments carried out at 60°C, the sorption
bed for the rare earth as well as the mixed retaining bed is
enough length to reach a steady state during the column operation.
After the establishment of the steady state, the shape of the
boundary involving a binary mixture is kept unchanged, which
in turn is independent of the distance of further displacement.
In other runs, the rare-earth mixtures were eluted at lower
temperatures in order to investigate the effect of temperature
on the theoretical plate height.

The rare-earth eluates from the elution experiments were
precipitated as oxalates, and then ignited to the oxides for
weighing.   The oxide samples were analyzed by the X-ray
fluorescent method.   Periodically, the analytical values
were re-checked by Analytical Group, Shinestu Chemical Company,
employing the spectroscopic method.

RESULTS AND DISCUSSION

1) Separation Factors for the Tb-Y and Y-Dy Pairs in the
Presence of EDTA.   The accurate separation factor for the
two adjacent rare-earth pair, Ln$_1$ and Ln$_2$, should be used for
a detailed treatment of the elution results, and this is given
in the form.

$$\alpha^{Ln_1}_{Ln_2} = \frac{[\overline{Ln_1^{3+}}]_T [Ln_2^{3+}]_T}{[\overline{Ln_2^{3+}}]_T [Ln_1^{3+}]_T} = \frac{[\overline{Ln_1^{3+}}][Ln_2^{3+}] \left\{ 1 + K_{Ln_2 Y} [Y^{4-}](1 + K_{HLn_2 Y} [H^+]) \right\}}{[\overline{Ln_2^{3+}}][Ln_1^{3+}] \left\{ 1 + K_{Ln_1 Y} [Y^{4-}](1 + K_{HLn_1 Y} [H^+]) \right\}} , \qquad (1)$$

where K's express the stability constants of the indicated
chelates, the superscript barred quantities refer to the resin
phase of the indicated constituents, and T's indicate the total
amounts of the refered rare earths.   In this system involved
EDTA, the presence of trivalent rare-earth ion Ln^{3+} is too small
to appreciate, as compared to the rare-earth chelate LnY^-.   The
latter amount is much greater than the protonated chelate HLnY.
Consequently, the HLnY can be regarded to neglect for the
calculation of the separation factor.   Therefore, the appro-
ximation of Equation (1) becomes in the form.

$$\alpha_{Ln_2}^{Ln_1} = K_{Ln_2}^{Ln_1} \frac{K_{Ln_2 Y}}{K_{Ln_1 Y}} \quad , \tag{2}$$

where $K_{Ln_2}^{Ln_1}$ is the apparent ion-exchange constant for the rare-
earth ions in the absence of EDTA.   As the ion-exchange con-
stants for the adjacent tripositive ions are considered to be
approximately equal to unity in the lanthanide series, the sepa-
ration factor can be expressed in a simplified form of the ratio
of stability constants of the adjacent rare-earth chelates.
However, some precaution might be necessary for calculating the
separation factors for the Tb-Y and Y-Dy pairs involving a
chelating agent.   According to Kettele and Boyd[10], the
adsorbability of the trivalent metal ions for the resin is the
following sequence: Gd > Tb > Dy > Y > Ho. The ionic radii[11]
are 0.94Å for Gd^{3+}, 0.92Å for Tb^{3+}, 0.91Å for Dy^{3+}, 0.88Å for Y^{3+},
and 0.89Å for Ho^{3+}.   In practical elution of the rare earths
with EDTA, Y is actually eluted between Tb and Dy. Thus, one
cannot be allowed to neglect the K_Y^{Tb} value in the calculation of
α, and Equation (2) should be used exactly for these elements.
According to the ion-exchange study of Surls and Choppin[12],
the distribution coefficient K_d for Tb-Dy is 1.156, while the
value for Tb-Y will become somewhat greater than the former
value, as may be estimated from the above fact.   Therefore,
the K_Y^{Tb} cannot tolerate to neglect for computing α accurately,
whereas the K_d for the Dy-Ho pair is only 1.05.   This leads
to an estimation that K_d for Dy-Y will be more close to unity
so that the K_{Dy}^Y can be neglected on the calculation of α_{Dy}^Y
using Equation (2).

     One of the authors has observed the following α values[13]
under similar experimental conditions to those in the real
elution system with EDTA:

$\qquad \alpha_Y^{Tb}$: 1.76 (30°C), 1.84 (60°C)

$\qquad \alpha_{Dy}^Y$: 1.61 (30°C), 1.54 (60°C)

Apparently, a reversal of the temperature dependence of the
separation factor occurs between the above pairs. The observed
value of 1.61 for the Y-Dy pair gives a good agreement with the
calculated value from the ratio of the stability constants of
the Y- and Dy-EDTA chelates.   From Relationship (2), one obtains

-296-

$$a_Y^{Tb} = K_Y^{Tb} \frac{K_{YY}}{K_{TbY}} \qquad (3)$$

Substituting a value of 1.45[8] from the ratio of K_{YY}/K_{TbY} and 1.76 for the a_Y^{Tb} into (3), we have a value of 1.21 as K_Y^{Tb}. Using $K_Y^{Tb} = 1.21$ and K_d for Tb-Dy $= K_{Dy}^{Tb} = 1.156$, the K_Y^{Dy} becomes to 1.04, while K_d for Dy-Ho is equal to 1.05[12], as has been noted earlier. This fact shows that the adsorbability of tripositive yttrium ion for the resin is located in the middle of Dy and Ho, and that Equation (3) must be used for the accurate calculation of a_Y^{Tb}.

The a value is not true constant, depending on the experimental conditions employed, but its variation is kept to a insignificant degree[7,13], since the activities of the related species in the aqueous and resin phases would be compensated each other in the adjacent rare earth elements. In this study, the observed a values for the Tb-Y and Y-Dy pairs are used for the analysis of the results under the assumption that a value is maintained unchanged at any portion of the overlap region in the rare-earth band.

2) Analysis of the Elution Results Obtained at 60°C from the Point of Rate Theory.   In the ion-exchange process, the rates [14] of particle and film diffusions may be expressed as follows:

For particle-diffusion control, one obtains

$$\left(\frac{\partial \overline{X_i}}{\partial t}\right)_2 = \frac{\overline{D}}{0.071 \, r_o^2} \left(\overline{X_i^*} - \overline{X_i} \right), \qquad (4)$$

and for film-diffusion control

$$\left(\frac{\partial \overline{X_i}}{\partial t}\right)_2 = \frac{3 D}{2 \delta r_o} \left(C_i - C_i^* \right). \qquad (5)$$

Starting from Equations (4) and (5), one of the authors has already induced the following relations. The detailed results were described in the previous report [4].

In the case where particle diffusion is the rate-determining step, we have

$$Z(X_{in_2}) = H_p \left\{ - \frac{1}{a-1} \ln X_{in_2} + \frac{a}{a-1} \ln \left(1 - X_{in_2} \right) + 1 \right\}, \qquad (6)$$

where $H_p = V_b \, r_o^2 \,/\, 14 \, \overline{D}$.

For film-diffusion control, we have

$$Z(X_{in_2}) = H_f \left\{ - \frac{a}{a-1} \ln X_{in_2} + \frac{1}{a-1} \ln \left(1 - X_{in_2} \right) - 1 \right\}, \qquad (7)$$

where $H_f = 2 \delta r_o \, V_b \, \overline{X} \,/\, 3 \, D \, C$.

In the above equations, the symbols r_o and δ indicate the radius of resin particle and the film thickness respectively, while $\overline{D}$ and D represent the self-diffusion or interdiffusion coefficient in the resin and aqueous phases. The symbol C_i

refers to the concentration of species i in the interstitial solution, and $\overline{X}_i$, the amount of species i in the resin phase per unit volume of the resin bed.   The asterisks refer to equilibrium; for example, C_i^* denotes the concentration of the interstitial solution in equilibrium with $\overline{X}_i$.   The Z symbol represents the distance from a reference point of the column. In Equations (6) and (7), $Z(X_{Ln_2})$ indicates the distance of the plane with a concentration of X_{Ln_2} from the center of a rare-earth boundary containing Ln_1 and Ln_2 , and α is the separation factor for the adjacent elements.   The symbol $\overline{V}_b$ represents the linear flow rate for the movement of the rare-earth band, $\overline{X}$ the total amount of the species in the resin per unit volume of bed, and C represents the total concentration of counterions. The H_p and H_f symbols express the plate height due to particle diffusion and film diffusion respectively.

With the aid of Equations (6) and (7), the plots of X_{Ln_2} against Z gives a shape of the boundary at a steady-state condition.   In the present analysis of the overlap region, the described α values at 60ºC are used for the Tb-Y and Y-Dy pairs.   Introducing $\alpha_Y^{Tb} = 1.84$ and $\alpha_{Dy}^Y = 1.54$ at 60ºC, the following relations are derived for film-diffusion controlling. For the ion-exchange system involved a mixture of Tb and Y at 60ºC, we have

$$Z\,(X_{Tb}) = H_f\left\{-\,5.04\,\log X_{Tb} + 2.74\,\log(1-X_{Tb}) - 1\right\}, \qquad (8)$$

and for the ion-exchange system involved a mixture of Y and Dy at 60ºC, we have

$$Z\,(X_Y) = H_f\left\{-\,6.56\,\log X_Y + 4.26\,\log(1-X_Y) - 1\right\}. \qquad (9)$$

Using either Equation (8) or (9), the plate-height value due to film diffusion was found by the curve fitting method.

The elution data (Run No. A-1 to A-3) related to the boundary of Y and Dy appear in Figure 1, in which most of them fall on the solid theoretical line based on film-diffusion control.   A characteristic set of the elution data on the Tb-Y region is shown in Figure 2.   In Runs B-2 and B-3 at 60ºC, about 11.5 g of a rare-earth mixture containing 44.35 % Y_2O_3, 48.25 % Tb_4O_7, and 7.4 % Gd_2O_3 were adsorbed on the hydrogen form of resin, and then eluted through the mixed retaining bed ($\overline{Zn}^{2+} \cong 0.94$, $\overline{NH}_4^+ \cong 0.05$, $\overline{H^+} \cong 0.01$ equivalent fraction) using the Ca-NH₄-H-Y eluent.   In these runs, the elution distance was corresponded to approximately 2.5 band lengths, and the flow rates were 10 ml/min for B-2 and 20 ml/min for B-3.   In Run G-6 at 60ºC, with the Ca-NH₄-H-Y eluent ($\overline{Y}_T = 0.022$ M), an equimolar mixture of Y and Dy was displaced at a flow rate of 20 ml/min through the same mixed beds as Run B-2 until the steady state had been established.   On the other hand, in Run H-Z, the Y-concentrate involving 61 % Y_2O_3 was loaded on the 50 mm (i.d.) jacketed columns, and then eluted down the re-

taining columns. The rare-earth eluate obtained from the overlap portion with Tb and Y was collected in small fractions for analysis.

The shapes of the boundaries at steady-state conditions, are represented as the broken lines on the basis of particle-diffusion controlling (Figures 1 and 2), but all the experimental data at 60°C are inconsistent with the theoretical curves on particle diffusion. Therefore, it can be concluded that the present ion-exchange system of the rare earth involving dilute EDTA-species are mainly controlled by film diffusion as the rate-determining step.

In elution[15]of the heavy rare-earth group with 2-hydroxyethyl-ethylenediamine-N,N,N'-triacetic acid (HEDTA), a linear relationship was confirmed between H_f and flow rate, A similar relationship[6]was also found in elution of the light rare earth with EDTA. As Figure 3 shows, the correlation between them is identical in the present elution system. The H_f values obtained at 60°C are almost similar in both experiments A-3 and D-1, where the mixture of different compositions of Tb and Y were adsorbed on the resin, and then eluted at 3.95 cm/min. Inasmuch as the elution condition is identical, whatever the loading ratio of the rare earth, both shapes of the mixed region must be finally fixed to a definite gradient of composition. In other words, the H_f value should be the same in both runs, as confirmed experimentally. Further, the elution experiments (Runs H-A, H-B, H-C, and H-Z) of the Y-concentrate were carried out at 60°C in order to investigate the effect of the flow rate on the H_f value.

3) Relation between H_f and HETP. The HETP values were calculated using equation induced by Spedding and Powell [16], as tabulated in Table 1. Typical plots of $\log[Ln_1]/[Ln_2]$ are shown in Figure 4 , in which slight tailing of Y is seen in a range much greater than the molar ratio of $\log[Y]/[Dy]= 3$, and slight channelling phenomenon in a range much smaller than $\log[Tb]/[Y] = -3$.

In general, film diffusion, particle diffusion, and particle size contribute to the plate-height value. However, as may be clear from the curve fitting method, the contribution of the last two is too small to evaluate in the present system with dilute EDTA and Dowex 50W-X8, 50-100 mesh, and obviously film diffusion plays an important role for the rate-determining step. Thus, the plate-height value due to film diffusion should come near to the HETP value. As Table 1 shows, the H_f values found from the curve fitting method are consistent with the HETP's calculated using Spedding's relation [16] .

4) H_f with Respect to Flow Rate or Elution Temperature.

The H_f value depends on several parameters such as δ, Υ_0, $\sqrt{v_b}$, X, D, and C, most of which are influenced by the temperature. As Figure 5 shows, the elution temperature gives a great effect on the theoretical plate, whose value decreases exponentially with a rise in the elution temperature.

Elevated temperature reduces the Y-Dy separation factor, appreciably negating the increased separation efficiency expected from the decreased plate height due to elution at a high temperature.

5) Calculation of Minimum Length of Overlap Region at a Steady-State Condition. In the case where either particle or film diffusion is the rate-determining step, it is possible from Equations (8) and (9) to calculate a minimum length (L) of the overlap region in the rare-earth band at a steady state; knowing the separation factor and the H_f value at 60°C, the L-values required to isolate Tb, Y, and Dy in 99 or 99.9% purity can be calculated as given in Table 2. Further, using Equations (9) and (12), the required lengths to resolve a Dy-Y mixture in a desired quality at either 30° or 60°C are displayed in Figure 6.

In film-diffusion-controlled exchange at 30°C, similar relations to (8) or (9) are induced from Equation (7). Introducing $\alpha_Y^{Tb} = 1.76$, we obtain the relation for the exchange system with the Tb-Y pair at 30°C.

$$Z(X_{Tb}) = H_f \left\{ - 5.33 \log X_{Tb} + 3.03 \log (1 - X_{Tb}) - 1 \right\}. \quad (11)$$

Introducing $\alpha_{Dy}^{Y} = 1.61$, we obtain the relation for the exchange system with the Y-Dy pair at 30°C.

$$Z(X_Y) = H_f \left\{ - 6.08 \log X_Y + 3.78 \log (1 - X_Y) - 1 \right\}. \quad (12)$$

For the Tb-Y pair, Figure 7 shows the same relations as those appeared in Figure 6. When making the ion-exchange separation of the Y-concentrate with EDTA, the Tb-Y cut would become much sharper than the Dy-Y cut at the same flow rate. This reason can be understood from a comparison of the overlap area in Figures 6 and 7, where the increase in the elution temperature yields the increase in the length of the Y-Dy overlap region, but the decrease in the length of the Y-Tb overlap region. Thus, a sharp boundary composed of Y and Tb is formed at a steady-state condition.

Table 1. Comparison of the plate-height values obtained by different methods (60°C).

Exp. No.	Flow Rate cm/min	Plate Height		Loaded Rare Earth
		H_f cm a)	HETP cm b)	
A-1*	1.18	1.4	1.4	Y-Dy
A-2*	2.63	2.1	2.2	Y-Dy
B-2*	2.63	1.2	1.2	Tb-Y
B-3*	5.26	1.8	1.8	Tb-Y
G-6*	5.26	2.0	2.1	Tb-Y
H-C**	5.18	1.8	1.8	Xenotime(Tb-Y)
H-Z**	6.00	2.1	2.0	Xenotime(Tb-Y)

*22 mm (i.d.)-column   **50 mm (i.d.)-column
a) Calcd. on the basis of film diffusion
b) Calcd. on the basis of countercurrent extraction[16]

Table 2. Comparison of the lengths of overlap region required to isolate individual elements in desired purities (60°C).

Exp. No.	Length(cm) of Overlap Region Calcd. by Eq. (8) or (9)		Length(cm) of Overlap Region Found by Exp.		Ln-Pair
	99.9%*	99%*	99.9%*	99%*	
A-1	45.4	30.3	46.5	31	Y-Dy
A-2	68.2	45.4	67	45	Y-Dy
B-2	28.0	18.6	28	19	Tb-Y
H-Z	49.0	32.6	50	32	Xenotime(Tb-Y)

* purity

Figure Captions.

Fig. 1. Plots of the equivalent fraction of yttrium against Z in film diffusion as the rate-determining step(Y-Dy).

Fig. 2. Plots of the equivalent fraction of terbium against Z in film diffusion as the rate-determining step(Tb-Y).

Fig. 3. Relationship between H_f and flow rate.

Fig. 4. Plots of the ratio of Ln_1 and Ln_2 with respect to L.

Fig. 5. Relationship between H_f and temperature at a definite flow rate.

Fig. 6. Length of the overlap region required to obtain individual elements in desired purities(Y-Dy).

Fig. 7. Length of the overlap region required to obtain individual elements in desired purities (Y-Tb).

Fig. 2

x_{Tb}, eq. fract.

60°C

Z, cm

Hp 1.2 cm

Hf cm
1.2 B-2
2.1 H-2

Fig. 1

x_y, eq. fract.

60°C

Hf cm
1.4 A-1
2.1 A-2
3.0 A-3

Hp-3.0 cm

Z, cm

Fig. 3

60°C

Hf, cm

A-1

A-2

A-3 D-1

A-4

D-2

(Y-Dy)

H-A H-B H-C HZ

B-2

B-3

(Y-Tb)

frow rate, cm/min.

Fig.4

Fig.5

Fig.6

Fig.7
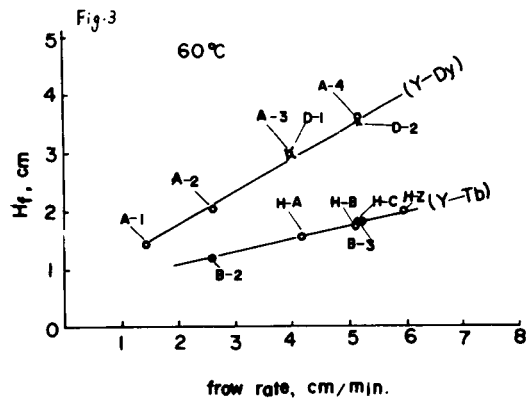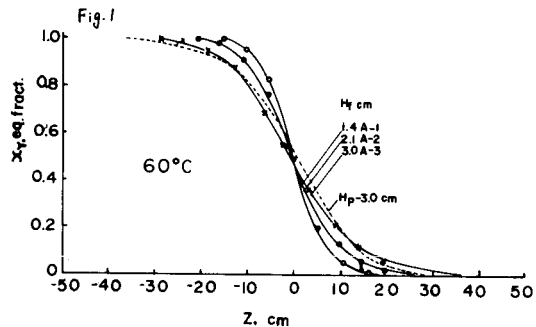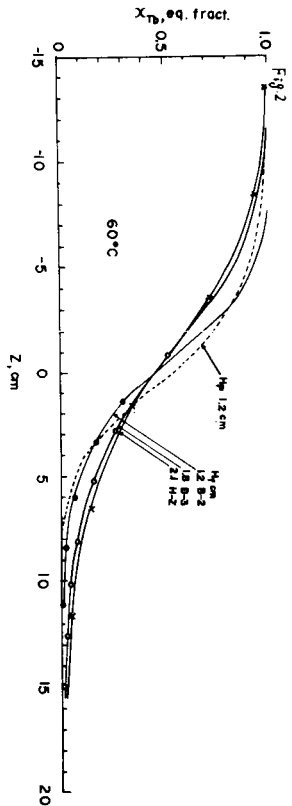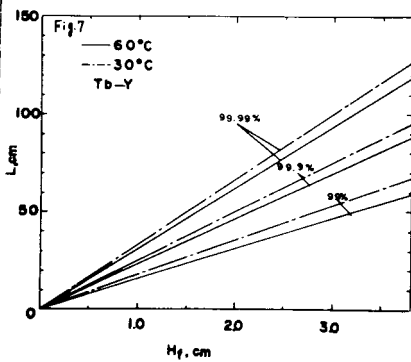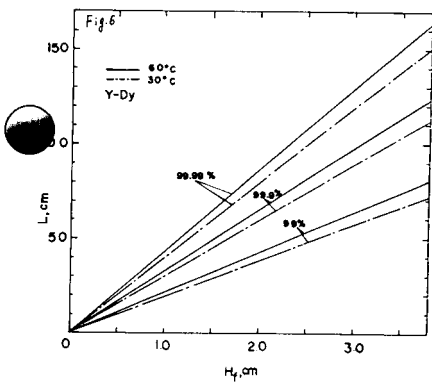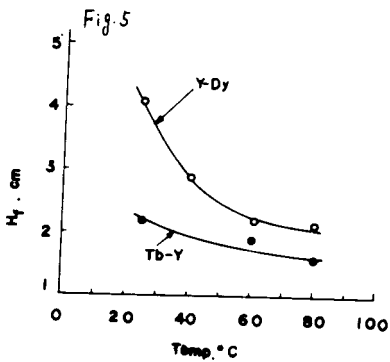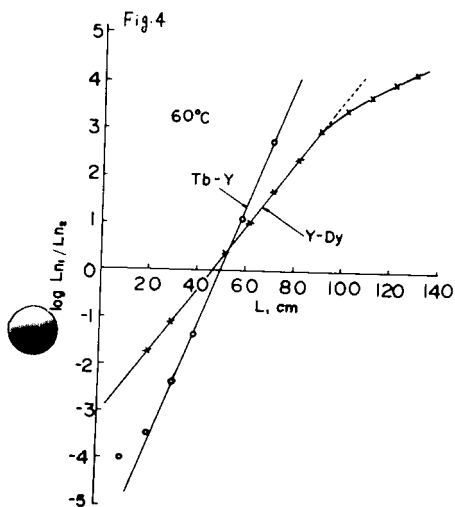
REFERENCES

1) J. E. Powell,and F. H. Spedding, Trans. Met. Soc. AIME,
   $\underline{215}$, 457 (1959) ; Chem. Eng. Progr., Symposium
   Series, No. 24, $\underline{55}$, 101 (1959).

2) E. J. Wheelwright, F. H. Spedding, and G. Schwarzenbach,
   J. Am. Chem. Soc., $\underline{75}$, 4196 (1953).

3) G. Schwarzenbach, R. Gut, and G. Anderegg, Helv. Chim.
   Acta, $\underline{37}$, 937 (1954).

4) Z. Hagiwara, J. inorg. nucl. Chem., $\underline{31}$, 2933 (1969).

5) Z. Hagiwara, and A. Kamei, ibid., $\underline{31}$, 3295 (1969).

6) Z. Hagiwara, J. Phys. Chem., $\underline{73}$, 3102 (1969).

7) M. Noguchi, A. Yoshifuji, and Z. Hagiwara, Bull. Chem.
   Soc. (Japan), $\underline{42}$, 2286 (1969).

8) Z. Hagiwara,and M. Noguchi, Bull. Chem. Soc. (Japan),
   in press.

9) Z. Hagiwara, and H. $\overline{O}$ki, Bull. Chem. Soc. (Japan),
   $\underline{42}$, 3177 (1969).

10) B. H. Kettele, and G. E. Boyd, J. Am. Chem. Soc., $\underline{69}$,2800(1947).

11) G. T. Seaborg, and J. Katz,"The Actinide Elements",
    McGraw-Hill Book Co., Chapter 18 (1954).

12) J. P. Surls. Jr., and G. R. Choppin, J. Am. Chem. Soc.,
    $\underline{79}$, 855 (1957).

13) Z. Hagiwara and M. Noguchi, Bull. Chem. Soc.(Japan), in press.

14) F. Felfferich, Angew. Chem. Intern. Ed., $\underline{1}$, No. 8, 440(1968).

15) Z. Hagiwara, and H. $\overline{O}$ki, Bull. Chem. Soc.(Japan), in press.

16) F. H. Spedding, and J. E. Powell, J. Am. Chem. Soc.,
    $\underline{77}$, 6125 (1955).

MOBILITIES OF RARE EARTH CATIONS BY BROMINE
REDOX ELECTROLYSIS WITH POROUS CARBON ELECTRODES[*]

by

E. I. Onstott

Los Alamos Scientific Laboratory
P.O. Box 1663 *, N. mex.
Los Alamos, New Mexico 87544

Abstract

    The mobility ratios of two pairs of rare earth cations were
measured for chloride electrolytes and for chloride-sulfate electrolytes
in which the chloride-sulfate ratio was equal to one. The mobility
ratio for Pr(III)/Nd(III) was measured to be 1.00 ± 0.02 for both elec-
trolytes. The mobility ratio of Nd(III)/Ho(III) in chloride electrolyte
was measured to be 1.053 ± 0.006, and the ratio in chloride-sulfate
electrolyte was 0.979 ± 0.012. Sulfate had the effect of reversing the
relative mobilities of Nd(III) and Ho(III).

INTRODUCTION

    The method of bromine redox electrolysis with porous carbon elec-
trodes (1) can be utilized to measure the mobility ratio of cations by
measuring the ratio of cations transported from the flowing anolyte
stream to the flowing catholyte stream. This method has been used to
measure the mobility ratio of Eu(III)/Gd(III) (2).

    Success of the method depends on very accurate determination of con-
centration changes in the electrolyte streams; at best the anolyte
changes in concentration under optimum experimental conditions are less
than 35% of the feed concentration.

    It is of considerable interest to measure the mobility ratio of rare
earth cations under electrolysis conditions and to compare the results to
those obtained in conductance measurements. From a practical viewpoint,
this method could possibly be used for specific separations for rare
earth cations with sufficiently large mobility differences, since large
amounts of material can be handled with rather modest equipment.

In this investigation Pr(III)/Nd(III) and Nd(III)/Ho(III) were studied, since all of these cations can be determined accurately by differential spectrophotometry (3).

EXPERIMENTAL

The electrochemical cell which was used had circular electrodes with an effective area of 45 cm^2 and spacing of 0.5 cm. The electrodes were cut from National Carbon Company Grade 60 porous carbon to a thickness of 0.2 cm. and framed with acrylic plastic. A collection chamber was provided behind each electrode to allow separation of anolyte and catholyte. Gas vents were provided for the inlet chamber and outlet chambers to allow filling with electrolyte and to insure uniform stream flows during electrolysis. Feed electrolyte was pumped to the cell from a pneumatic reservoir with a precision peristaltic pump. Anolyte and catholyte stream flows were measured with calibrated volumetric vessels.

The feed in all experiments contained an exact equimolar mixture of the two rare earth cations being studied. The amount of dissolved bromine was 6 g/ℓ (0.038 M Br_2). Electrolyses were done with applied cell voltages of 2.2 to 2.6, and currents were 0.18 to 0.35 ampere. Anolyte and catholyte samples were collected for periods of about one hour. Flows were about 4 mℓ/min each.

Mass transport was measured by quantitative recovery of the mixed rare earth oxides from the feed, anolyte and catholyte samples by oxalate precipitation and ignition at 900°. Changes in concentration due to mass transport and mobility differences were measured by a differential technique with a Cary Model 14 spectrophotometer. Oxides recovered from the feed, anolyte and catholyte were dissolved as perchlorates. The feed sample was placed in the reference beam, and the anolyte sample or catholyte sample was placed in the sample beam. Then the concentration of the anolyte or catholyte sample was adjusted until the absorption due to one rare earth cation disappeared. The remaining absorption due to the difference in concentration of the second rare earth cation was measured and compared to a standard calibration plot. By this procedure the ratio Pr(III)/Nd(III) was determined with a precision of 0.4% with the concen-

tration of each cation at about 0.25 M. The ratio Nd(III)/Ho(III) was
determined with a precision of 0.15% with the concentration of each
cation at about 0.4 M.

RESULTS AND DISCUSSION

A schematic representation of the method is depicted below with
the flow streams shown as arrows:

$$Ln_1 \ S(1-E_1)$$
$$Ln_2 \ S(1-E_2)$$
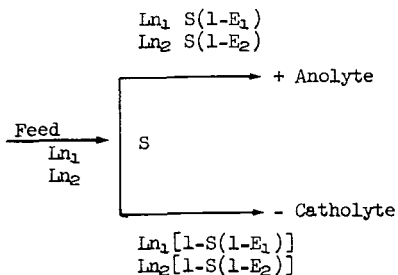
Ln_1 = flow of rare earth cation 1 into cell, mols/min.

Ln_2 = flow of rare earth cation 2 into cell, mols/min.

S = dividing fraction of feed for anolyte flow.

$1-S$ = dividing fraction of feed for catholyte flow.

E_1 = fraction of rare earth cation 1 removed from anolyte by electrolysis.

E_2 = fraction of rare earth cation 2 removed from anolyte by electrolysis.

$Ln_1 \ S(1-E_1)$ = flow of rare earth cation 1 out of anode side, mols/min.

$Ln_2 \ S(1-E_2)$ = flow of rare earth cation 2 out of anode side, mols/min.

$Ln_1[1-S(1-E_1)]$ = flow of rare earth cation 1 out of cathode side,
mols/min.

$Ln_2[1-S(1-E_2)]$ = flow of rare earth cation 2 out of cathode side,
mols/min.

E_1/E_2 = mobility ratio, rare earth cation 1/rare earth cation 2.

Steady-state operating conditions must be imposed for the above model
to hold. Steady-state is easily checked since the loss in mass from the
anolyte stream must equal the gain in mass in the catholyte stream. In
two experiments steady-state conditions were tested. In one experiment
the loss of rare earth cations from the anolyte was 2.92×10^{-3} g/min
(as oxide), while the gain in the catholyte was 2.93×10^{-3} g/min. In the

other experiment the loss and gain, respectively, were 3.11×10^{-3} and 3.14×10^{-3} g/min. Thus, steady-state operating conditions were verified quantitatively, and the mobility ratios which were measured and are listed in Table I are meaningful.

Table I

Cation Pair	Electrolyte	Mobility Ratio
Pr(III)/Nd(III)	0.01 M $PrCl_3$ 0.01 M $NdCl_3$	1.00 ± 0.02
Pr(III)/Nd(III)	0.01 M $Pr(SO_4)Cl$ 0.01 M $Nd(SO_4)Cl$	1.00 ± 0.02
Nd(III)/Ho(III)	0.01 M $NdCl_3$ 0.01 M $HoCl_3$	1.053 ± 0.006
Nd(III)/Ho(III)	0.01 M $Nd(SO_4)Cl$ 0.01 M $Ho(SO_4)Cl$	0.979 ± 0.012

The mobility ratios for chloride electrolytes in Table I can be checked by comparison to mobility ratios computed from conductance measurements for individual pure rare earth chlorides. For $PrCl_3$, $\lambda^+ = 104.9 - 68.5 = 36.4$ at 25° and 0.02 M concentration (4); for $NdCl_3$, $\lambda^+ = 104.8 - 68.5 = 36.3$ (5); the mobility ratio for Pr(III)/Nd(III) = $36.4/36.3 = 1.003$. For $HoCl_3$, $\lambda^+ = 102.7 - 68.5 = 34.2$ (5); the mobility ratio for Nd(III)/Ho(III) = $36.3/34.2 = 1.061$. Both of these values computed from conductance measurements check well with the values in Table I.

When sulfate ion is substituted for two chloride ions, the mobility ratio of Nd(III)/Pr(III) does not change significantly. However, it does change significantly for Nd(III)/Ho(III). The mobility of Ho(III) becomes greater than Nd(III), whereas the reverse is true for chloride electrolytes. The inversion of the mobility ratio of Nd(III/Ho(III) on substituting sulfate is not surprising, since it is known that Ho(III) in sulfate electrolytes has higher mobility than Nd(III) (6).

The differences in mobilities of rare earth cations with chloride and/or sulfate anions are not great enough to project even an easy group separation based on bromine redox electrolysis. A large number of stages would be required. It is of academic interest to note, however, that

separation of the heavy rare earth cations from the light cations could
be reversed simply by using sulfate to substitute for chloride, which
would deplete the heavy cations in the anolyte instead of in the
catholyte.

As a research tool this method is very useful for measuring
mobility ratios of cations in mixed electrolytes, while conductance
measurements are meaningful only for pure individual salts.

REFERENCES

1. E. I. Onstott, J. Electrochem. Soc. 111, 966 (1964).

2. Proceedings, Seventh Rare Earth Research Conference, Coronado,
   California, October 28-30, 1968, p. 751.

3. Charles V. Banks, John L. Spooner and Jerome W. O'Laughlin,
   Anal. Chem. 30, 458 (1958).

4. F. H. Spedding and I. S. Yaffe, J. Am. Chem. Soc. 74, 4751 (1952);
   D. A. MacInnes, Principles of Electrochemistry, Reinhold Pub.
   Corp., New York, 1939, p. 340.

5. F. H. Spedding and J. L. Dye, J. Am. Chem. Soc. 76, 879 (1954).

6. F. H. Spedding and S. Jaffe, ibid. 76, 884 (1954).

AN ELECTRONIC TRANSITION IN CERIUM HYDRIDE

G. G. Libowitz, J. G. Pack, D. H. Howling and W. P. Binnie
Ledgemont Laboratory, Kennecott Copper Corporation
Lexington, Massachusetts 02173

453 0800

Abstract

Resistivity measurements of cerium hydride single crystals as a function of hydrogen content in the range CeH_2 to CeH_3 have shown that there is a metal to semiconductor transition at a composition corresponding to approximately $CeH_{2.8}$. Measurements of resistivity as a function of temperature in metallic samples whose compositions $(CeH_{2.74}-CeH_{2.77})$ are in proximity to that at the compositional transition have revealed a sharp change in resistivity at about $245^\circ K$. In NMR studies of a polycrystalline sample of $CeH_{2.75}$ as a function of temperature, a sudden change in intensity of the proton resonance peak at approximately the same temperature was observed. A neutron diffraction investigation of the corresponding deuteride, $CeD_{2.75}$, above and below the transition temperature showed no change in structure. It is proposed that cerium hydride, of approximate composition $CeH_{2.75}$, transforms from the metallic state to a semiconducting state at about $250^\circ K$.

Introduction

All of the rare earth metals combine with hydrogen to form dihydrides[1]. Except for europium and ytterbium, these dihydrides have the fluorite-type structure and they exhibit wide deviations from stoichiometry. For dihydrides of the first four rare earth metals, the compositional variation ranges from $MH_{1.9}$ to MH_3. It has been shown[2-4] that when H/M > 2, the excess hydrogen enters the octahedral interstices of the fluorite-type structure such that all the interstices are occupied at the limiting composition, MH_3.

Previous investigations[5] on cerium hydride single crystals have established that this compound undergoes a compositional metal-to-semiconductor transition as shown in Figure 1. The open triangles represent earlier resistivity measurements on polycrystalline cerium hydride by Heckman[6]. It can be seen that at a H/Ce atom ratio of approximately 2.75 to 2.8, there is a sharp rise in the resistivity of
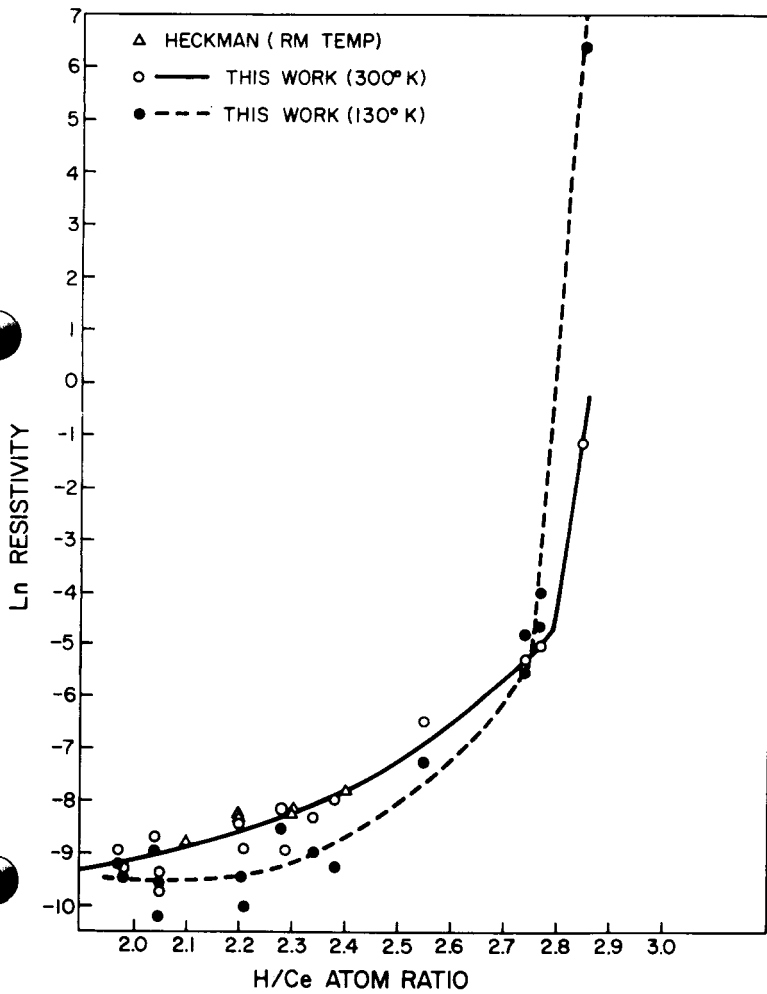
Fig. 1. Resistivities of cerium hydride as a function of hydrogen content.

the hydride. Measurements on samples whose H/Ce atom ratio is less than 2.7 show an increase of resistivity with temperature characteristic of metallic behavior as seen in Figure 2. The nonlinear increase in resistivity with temperature for the higher composition samples ($CeH_{2.2}$) is indicative of a degenerate semiconductor in which the Hall mobility decreases nonlinearly with temperature[7]. Resistivity measurements on a sample of $CeH_{2.85}$ revealed the linear increase with reciprocal temperature typical of semiconductors as seen in Figure 3. (The two activation energies may be explained[5] by the presence of oxygen impurity.)

In this paper the behavior of samples whose compositions are in the neighborhood of the compositional transition is examined.

Resistivity Measurements

Resistivities of two single crystals, of compositions $CeH_{2.77}$ and $CeH_{2.74}$, were measured as a function of temperature in an inert atmosphere glove box using the four-point probe technique. Experimental details are described elsewhere[8]. The results for $CeH_{2.77}$ are shown in Figure 4. The two curves represent measurements on two separate parts of the crystal. As the temperature is decreased from room temperature ($\sim 300^{\circ}K$), the resistivity changes only slightly with temperature, at first. At about $247^{\circ}K$ there is a sharp increase in temperature indicative of a transition. With further cooling, the resistivity peaks out and appears to decrease at lower temperatures. Above $220^{\circ}K$, the curve is fairly reproducible. Below this temperature, however, there is a great deal of scatter in the data.

Similar results were obtained for the crystal of $CeH_{2.74}$ as illustrated in Figure 5a. The transition occurs at about $245^{\circ}K$, and again there is much scatter of the data at lower temperatures. In another run on a different portion of the $CeH_{2.74}$ crystal, the temperature was lowered and raised through two cycles and the change in resistivity was carefully followed. The results, shown in Figure 5b, suggest that some sort of hysteresis mechanism is responsible for the scatter in
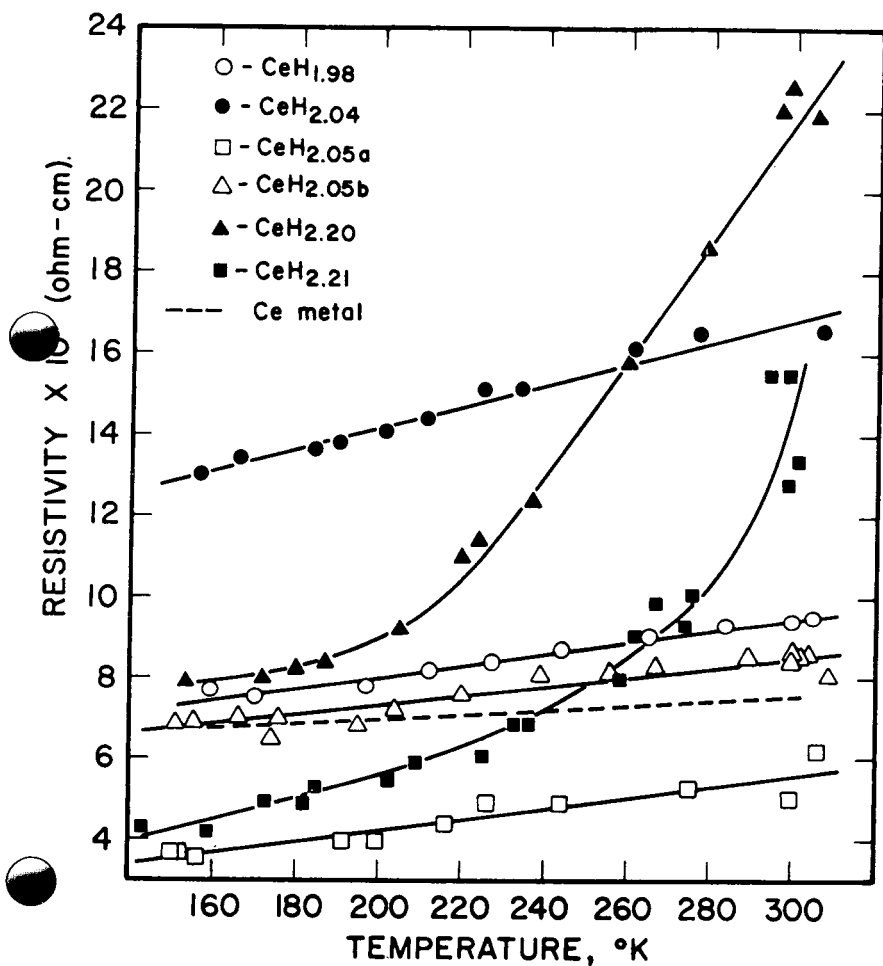
Figure 2. Resistivities of cerium hydride single crystals as a function of temperature in the metallic range.

Figure 3. Resistivity as a function of reciprocal temperature for a $CeH_{2.85}$ single crystal.
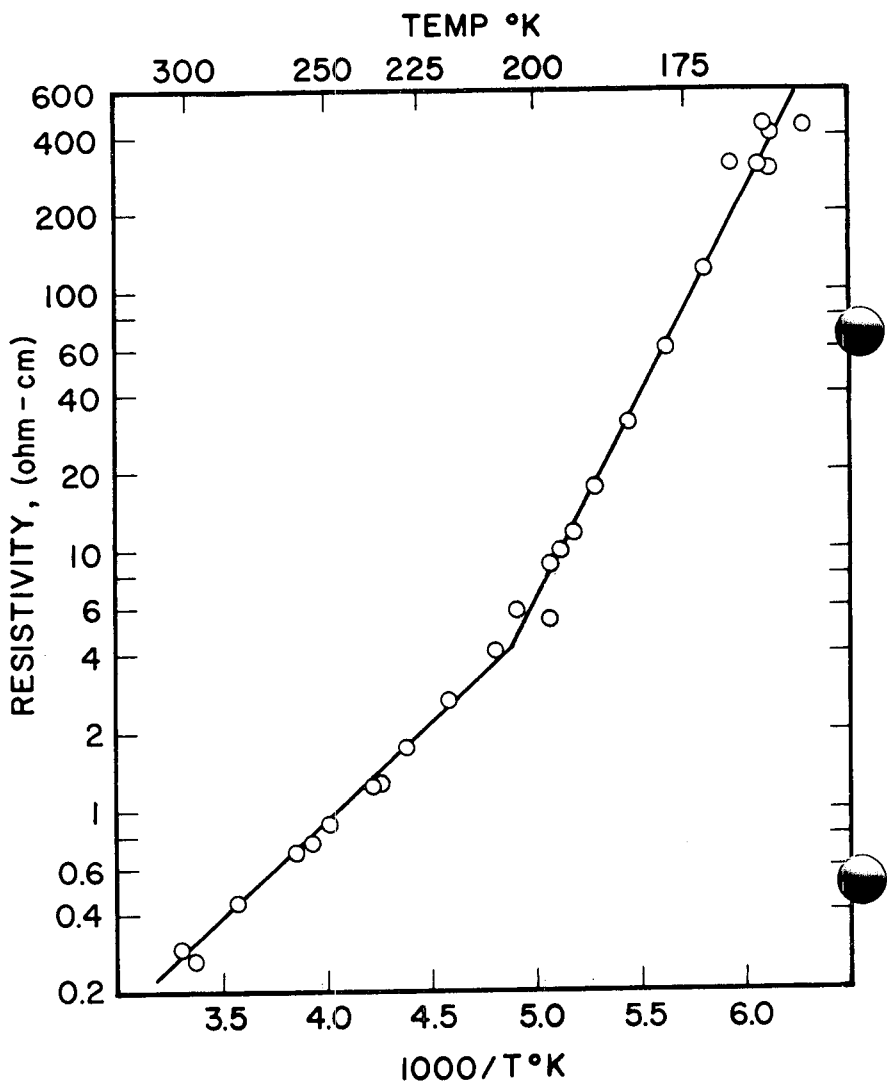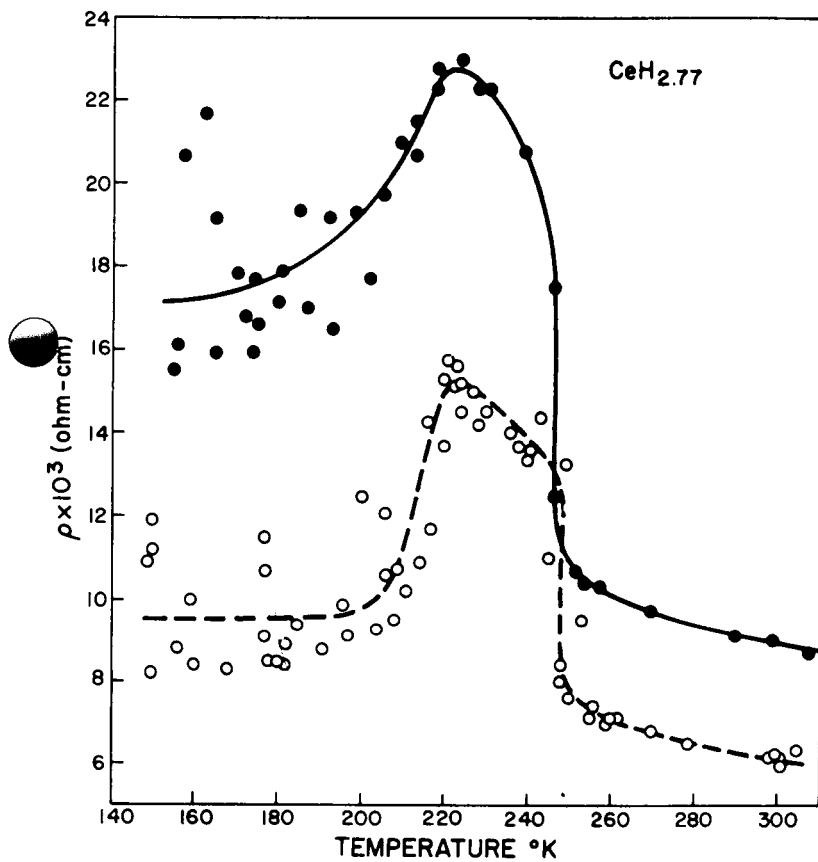
Fig. 4. Resistivity as a function of temperature for a $CeH_{2.77}$ single crystal. The two curves represent different portions of the same crystal.
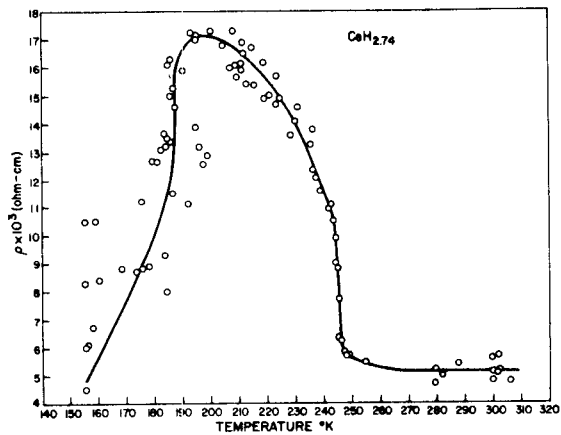
(a)
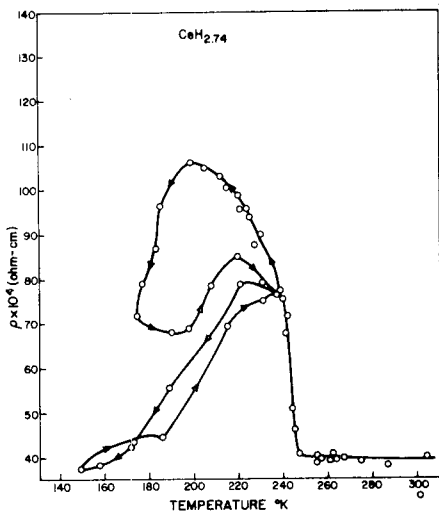
(b)

Fig. 5. (a) Resistivity as a function of temperature for a $CeH_{2.74}$ single crystal. (b) A different portion of the same crystal on which measurements were taken during two cycles of temperature.

-316-

the resistivity data below $235^{\circ}K$. The average transition temperature from the four resistivity curves shown is $245^{\circ}K$.

Bieganski, Fesenko, and Stalinski[9] observed a specific heat anomaly at $255^{\circ}K$ in a sample of $CeH_{2.86}$. The authors state that the sample was annealed at $300^{\circ}C$ for several days. However, according to the data of Hardcastle and Warf[10], the equilibrium pressure of $CeH_{2.86}$ at $300^{\circ}C$ is about 80 atm. Therefore, it is likely that the hydrogen content of Bieganski et al's sample was considerably less than H/Ce = 2.86. Thus, it is quite possible that specific heat anomaly observed by these authors corresponds to the transition discussed in this paper.

NMR Studies

Measurements of the temperature dependence of the nuclear magnetic resonance line widths and amplitudes of the hydrogen peak were made on powdered samples of $CeH_{2.75}$, $CeH_{2.92}$, and $CeH_{2.50}$. The amplitude of the hydrogen resonance peak of the $CeH_{2.75}$ sample decreased sharply at about $250^{\circ}K$ as shown in Figure 6. No significant change of line amplitude with temperature was observed with the other samples. The transition shown in Figure 6 undoubtedly corresponds to the transition shown in Figures 4-5.

Neutron Diffraction Investigation

No significant changes in magnetic susceptibility or x-ray diffraction patterns were observed[9] at the transition temperature (245-255°K), thus precluding a magnetic transition or a phase transition involving the rearrangement of cerium atoms.

At H/Ce = 2.75, 75 percent of the octahedral interstices in the fluorite lattice are occupied by hydrogen atoms and 25 percent are vacant. Room temperature neutron diffraction studies[2] indicate that the excess hydrogen atoms (above H/Ce = 2.0) are randomly distributed over the octahedral interstices. In order to determine if the transition were due to ordering of the hydrogen atoms in the octahedral interstices

-317-
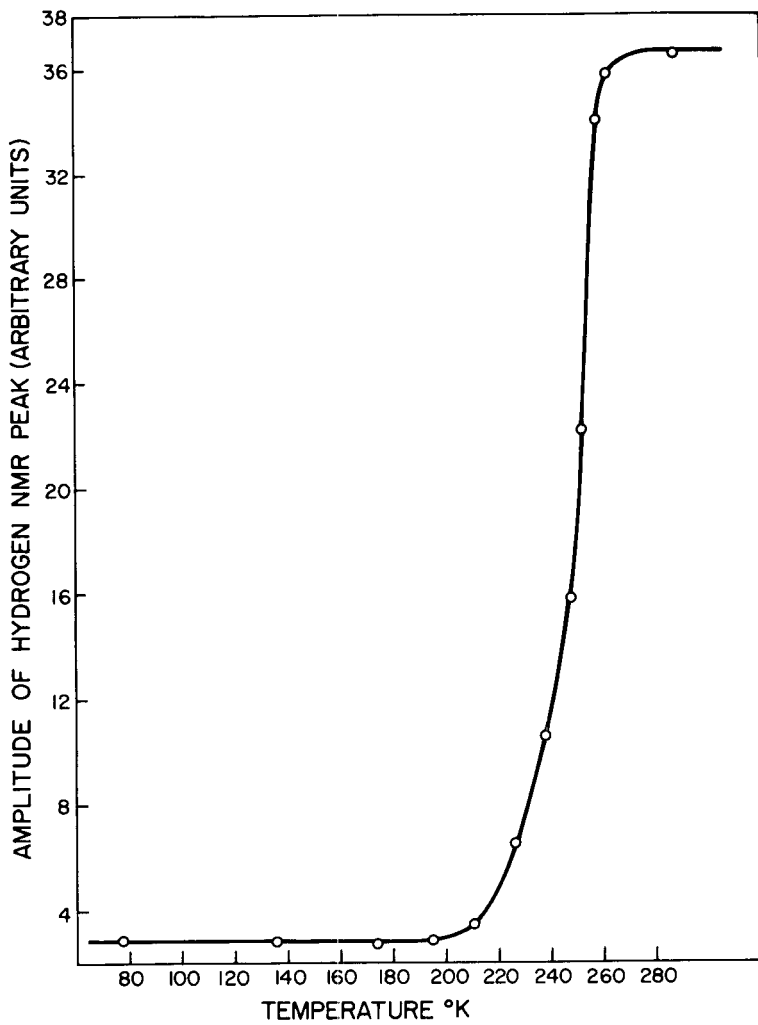
Fig. 6. Amplitude of proton magnetic resonance peak in $CeH_{2.75}$ as function of temperature.

below 245^OK, a neutron diffraction study of polycrystalline $CeD_{2.75}$ was carried out. Diffraction patterns were obtained above ($\sim 300^O$K) and below (210^OK) the transition temperature. As seen in Figure 7, the patterns are identical at the two temperatures, and they contain only the peaks to be expected for the fluorite lattice with randomly occupied octahedral interstices. Thus, there does not appear to be any ordering of the hydrogen at the lower temperature.

The possibility was considered that the super-lattice peaks due to ordering of the hydrogen atoms may be too weak to be observed. The two most likely cases of hydrogen ordering would be (1) the body-centered position in the unit cell is regularly vacant leading to a primitive cubic lattice or (2) a layered structure in which the body-centered position is occupied by hydrogen, but the other octahedral sites in that layer on the cube edges are vacant, leading to tetragonal symmetry. Theoretical intensities were computed for each of these cases, and it was found that some of the peaks in each ordered struc-ture should be of sufficient intensity to have been observed in the present investigation. Consequently, it can be concluded that the tran-sition is not due to an order-disorder transition of hydrogen atoms.

Conclusion

Electrical resistivity and NMR studies in the present investigation and a previous specific heat study[9] have disclosed a transition at about $245\text{-}255^O$K in cerium hydride of composition near $CeH_{2.75}$. Since the transition is not due to a structural phase change nor to magnetic ordering, it must be concluded that it is a temperature dependent metal-to-semiconductor transition corresponding to the compositional transition shown in Figure 1.

The metal-to-semiconductor transition in cerium hydride may be considered an example of the Mott transition[11]. The composition CeH_3 would be an insulator since the valence of trivalent cerium is com-pletely satisfied. It is proposed that as hydrogen is removed from the trihydride, donor levels are formed in the band gap and the material becomes a semiconductor. Further removal of hydrogen with the
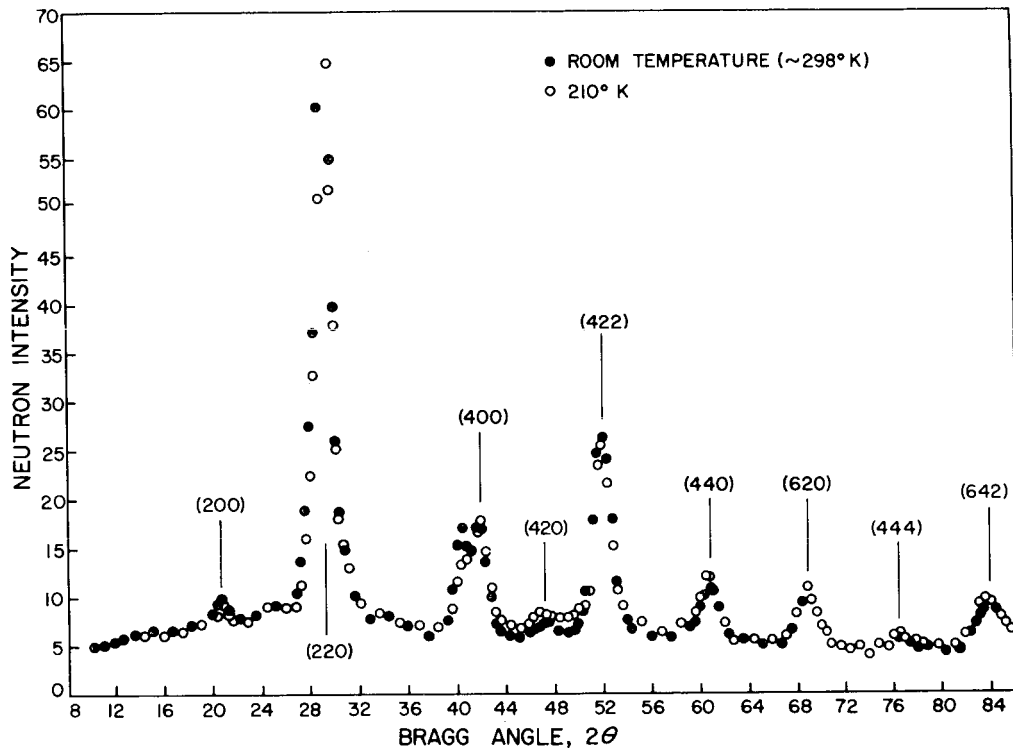
Fig. 7. Neutron diffraction patterns of $CeD_{2.75}$ at room temperature and $210^\circ K$. Wavelength of neutrons is 0.980 Å.

commensurate increase in donors leads to overlap of the wave functions of the electrons associated with the donor levels at $H/Ce \simeq 2.8$, and to formation of a "defect band" (analogous to an impurity band), in which metallic conduction occurs. For $CeH_{2.75}$, the defect band is narrow at room temperature. As the temperature is lowered, separated donor states "condense" from the electron gas and the material becomes a semiconductor.

Further electronic and NMR investigations are being carried out to obtain a better understanding of the electronic structure of this compound.

References

1. G. G. Libowitz, Binary Metal Hydrides, W. A. Benjamin, New York, 1965.

2. C. E. Holley, R. N. R. Mulford, F. H. Ellinger, W. C. Koehler, and W. H. Zachariasen, J. Phys. Chem. 59, 1226 (1955); I. Karimov, M. G. Zemlyanov, M. E. Kost, V. A. Somenkov, and N. A. Chernoplekov, Soviet Physics - Solid State 9, 1366 (1967).

3. D. S. Schreiber and R. M. Cotts, Phys. Rev. 131, 1118 (1963).

4. G. G. Libowitz and J. B. Lightstone, Proc. Sixth Rare Earth Research Conf., Gatlinburg, Tenn., May, 1967, pp. 132-44.

5. G. G. Libowitz and J. G. Pack, J. Chem. Phys. 50, 3557 (1969).

6. R. C. Heckman, J. Chem. Phys. 40, 2958 (1964).

S. K. Bahl and K. L. Chopra, J. Appl. Phys., to be published April 1970.

8. J. G. Pack and G. G. Libowitz, Rev. Sci. Instr. 40, 420 (1969).

9. Z. Bieganski, W. Fesenko, and B. Stalinski, Bull. Acad. Polon. Sci., Ser. Chim. 13, 227 (1965).

10. K. I. Hardcastle and J. C. Warf, Inorg. Chem. 5, 1728 (1966).

11. N. F. Mott, Proc. Phys. Soc. (London) A62, 416 (1949); Phil. Mag. 6, 287 (1961).

ELECTRICAL RESISTIVITY AND MAGNETIC SUSCEPTIBILITY OF DEFINITE COMPOUNDS IN THE TIN SAMARIUM SYSTEM

Annick PERCHERON
Laboratoire des Terres Rares du C. N. R. S.
92-BELLEVUE - FRANCE

P. LETHUILLIER, J. L. FERON
Laboratoire d'Electrostatique et Physique du Métal
du C. N. R. S. -38-GRENOBLE - FRANCE

O. GOROCHOV
Laboratoire de Chimie Minérale
Faculté de Parmacie - PARIS - FRANCE

ABSTRACT

Electrical resistivities of polycrystalline definite compounds in the tin-samarium system, $SmSn_3$, Sm_2Sn_3, and Sm_5Sn_3 have been measured between 77° K and room temperature. These values have been compared with samarium and tin resistivities.

The temperature dependence of the electrical resistivities can be expressed by the following equations:

$$\rho_{SmSn_3} = 11.5 + 0.054\ T \qquad\qquad 10^{-6}\ \Omega\ cm$$

$$\rho_{Sm_2Sn_3} \approx 280 + 2.18\ T - 2.51 \cdot 10^{-3}\ T^2 \qquad 10^{-6}\ \Omega\ cm$$

$$\rho_{Sm_5Sn_3} \approx 210 + 0.234\ T \qquad\qquad 10^{-6}\ \Omega\ cm$$

The magnetic behavior of these compounds has been investigated over the temperature range 2° to 900° K. CURIE WEISS behavior was not observed. NEEL points were observed for $SmSn_3$ and Sm_2Sn_3, respectively, at 9 and 11° K. Sm_5Sn_3 showed an anomaly of susceptibility between 120 and 160° K. Above 300° K, the susceptibility of the three compounds decreases with temperature with a minimum near 400° K.

We have studied the temperature dependence of the electrical resistivity and the magnetic susceptibility of some compounds in the tin-samarium system to define the nature of bonding in the investigated compounds. In fact, the vary exothermic enthalpy of formation (1) of these compounds has indicated very strong interactions between tin and samarium atoms and a strong covalent or polar character of the bonding.

We investigated here among the definite compounds of the system (2) only $SmSn_3$, Sm_2Sn_3, and Sm_5Sn_3.

Alloys were prepared from samarium of 99. 9% purity and of 99. 99% purity. They were melted under pure argon atmosphere and annealed to obtain a good homogeneity. Their stoichiometry was checked by chemical analysis and X-ray diffraction. The definite compounds are vary reactive and must be handled under an argon atmosphere.

The crystal structures and lattice parameters of these compounds are:

$SmSn_3$ cubic $AuCu_3$ type   a $= 4.677 \overset{o}{A}$

Sm_2Sn_3 tetragonal   a $= 9.1 \overset{o}{A}$; c $= 15.4 \overset{o}{A}$

Sm_5Sn_3 hexagonal Mn_5Si_3 type   a $= 9.089 \overset{o}{A}$

$c = 6.610 \overset{o}{A}$

ELECTRICAL RESISTIVITY

The variable temperature apparatus used for this investigation is shown in Fig. 1 (3). Liquid nitrogen was used as a cooling agent between 77 and 300° K. Temperatures were changed by using pulses of electrical power in the heater coil to obtain the temperature desired. Temperatures of the sample were measured with a copper-constantan thermocouple, and time allowed for thermal equilibrium at each measurement. The measuring device was maintained under a helium atmosphere.

The sample resistance was determined by the usual four probe method using current reversal, described by PISTOULET (4). A constant current power supply was used and potential was measured by a potentiometric method.

We have obtained an absolute value of the electrical resistivity
$\rho = \frac{V}{I} \cdot f$ where f (5) is a corrective factor depending on dimensions of
samples and characteristics of apparatus.

All of the samples were machined in parallelepiped form with the
following dimensions:

8 < length   <20 mm
2 < width   <4 mm   They were polished on diamond paste
1 < thickness <4 mm   before measurements.

The electrical resistivities observed on samarium, tin and the various
compounds are shown on fig. II-1, 2, 3, 4 and are discussed below:

Tin - The electrical resistivity of tin was measured at various
temperatures and we obtain: $\rho_O = 11 \cdot 10^{-6}$ Ω cm with a thermal co-
efficient of resistivity equal to $4.4 \cdot 10^{-3}$ K^{-1}. This result is in good
agreement with values of PIETENPOL (6).

Samarium (fig. II, 1) - The electrical resistivity of samarium
changes almost linearly with temperature below 300° K. At about
110° K, the resistivity decreases much more rapidly with decreasing
temperature. This behavior suggests (7) that above 110° K, the mag-
netic moments, resulting from the localized 4 f electrons in samarium
are disordered and give rise to considerable moment disorder resistivity
ρ md. The electrical resistivity at room temperature is:

$$\rho_{300} = 86 \cdot 10^{-6} \Omega \text{ cm}$$
$$\rho_O + \rho_{md} = 46 \cdot 10^{-6} \Omega \text{ cm}$$

The present measurements agree satisfactorily with known previous
values (8-10).

SmSn$_3$ (fig. II, 2) - The electrical resistivity of this compound
changes linearly with temperature between 77 and 300° K. The curve
can be expressed by the equation:

$$\rho = 11.5 + 0.054 \text{ T} \quad 10^{-6} \Omega \text{ cm}$$

This variation with temperature follows MATHIESSEN'S rule (11), and
the specific value at room temperature ρ_{300} $27 \cdot 10^{-6}$ Ω cm is the same
order of magnitude as the one for metals.

Sm$_2$Sn$_3$ (fig. II, 3) The electrical resistivity of Sm$_2$Sn$_3$ did not follow
a linear relationship with temperature between 80 and 300° K. The curve
can be expressed by the equations:

Sample 1. $\rho = 320 + 2.21 \text{ T} - 2.16 \; 10^{-3} \text{ T}^2 \quad 10^{-6} \Omega \text{ cm}$

Sample 2. $\rho = 258 + 2.15 \text{ T} - 1.58 \; 10^{-3} \text{ T}^2 \quad 10^{-6} \Omega \text{ cm}$

-324-

The difference between residual resistivities of samples was due to imperfections. In fact, these compounds were very brittle, and we had encountered great difficulties in obtaining a sample without cracks. But the dependences of temperature were almost the same.

Room temperature resistivity was found to be greater than for any of the investigated compounds, and it was at the upper limit in the range of magnitude of metallic resistivities $\rho_{300} = 715 \cdot 10^{-6} \, \Omega\text{-cm}$.

These results were significant of partial localization of conduction electrons.

$Sm_5 Sn_3$ (fig. II, 4)
The same sample was used for the three runs. The electrical resistivity of $Sm_5 Sn_3$ changes linearly with temperature, and the curve (1) shows a weak anomaly near 150° K. The linear variation was expressed by:

$$\rho = 210 + 0.234 \ T \quad 10^{-6} \, \Omega\text{ cm}$$

Room temperature resistivity $\rho_{300} = 278 \cdot 10^{-6} \, \Omega$ cm was higher than the calculated value using the law of mixtures.

Values of the various characteristics of investigated compounds and pure elements are given in table I.

	Sm	$Sm_5 Sn_3$	$Sm_2 Sn_3$	$SmSn_3$	Sn
$\rho_0 \ 10^{-6} \, \Omega\text{-cm}$	45	210	289	11,5	
$\rho_{273} \ 10^{-6} \, \Omega\text{-cm}$	82	270	692	26	11
$a \ 10^{-6} \, \Omega\text{-cm}°^{-1}$	0,14	0,22	2,18	0,054	0,049
$\beta \ 10^{-6} \, \Omega\text{-cm}°^{-2}$	-	-	$1,87 \cdot 10^{-3}$	-	-
Temperature $°^{-1}$ Coefficient	0,0017	0,00085	0,00262	0,00207	0,0044

Table I

These compounds follow the LECHATELIER-GUERTLER rule (11). The temperature coefficient of resistivity of compounds has the same order of magnitude as the one for pure metals.

MAGNETIC SUSCEPTIBILITY

The magnetic susceptibility measurements have been performed by means of translation balances of Weiss-Forrer type. Between 2 and 300 Kelvin, the strength of the magnetic field applied on the sample is 12,000 Oe; at high temperatures, it is 9,650 Oe. The magnetic susceptibilities of the studied samples are quite small. At low temperatures the paramagnetism of oxygen may perturb our results; we must get a secondary vacuum of 10^{-6} torr inside the balance.

The values of the molar reciprocal susceptibilities of the compounds $SmSn_3$, Sm_2Sn_3, and Sm_5Sn_3 are plotted versus temperature on the figures III 1, 2, 3. For the compounds $SmSn_3$ and Sm_2Sn_3, the presence of a quite large minimum on the curves (X^{-1}, T) is characteristic of an antiferromagnetic order at low temperatures. The NEEL temperatures T_N of these compounds are respectively 9 Kelvin and 11 Kelvin. For Sm_5Sn_3, we did not observe a minimum in the reciprocal susceptibility curve until 2 Kelvin. For this compound, we observe, between 120 and 160 Kelvin, an anomaly of the susceptibility curve; we may compare this anomaly to the one observed on the susceptibility curve of pure samarium measured by LOCK (12). For all the studied compounds, we never observed a linear behavior of the reciprocal susceptibility versus temperature, as predicted by the Curie-Weiss law.

The high temperature magnetic behavior of our samarium–tin compounds is the same as the magnetic behavior of other samarium intermetallic compounds (13), (14). The susceptibility decreases with temperature, exhibits a flat minimum around 400 Kelvin, and increases slowly afterward (4).

In the pure metal or in intermetallic compounds, samarium is in an ionic state Sm^{3+} as most rare earth elements.

The energy separation between the ground $J = 5/2$ and the first excited $J = 7/2$ multiplet states of Sm^{3+} ion is only 1,000 Kelvin.

For the other rare earth elements (except europium), this energy separation is two or three times higher. On the other hand, the LANDE factor g_J of the ground state multiplet $(J = 5/2)$ is only $2/7$. These two reasons make the temperature–independent VAN VLECK–type paramagnetism (15) of considerable magnitude relative to the Curie type paramagnetism of the ground state multiplet $J = 5/2$.

The crystal field, acting on the Sm^{3+} ions, splits the manyfold ground state multiplet; in particular in $SmSn_3$ the crystal field is cubic and the ground state multiplet is split in a doublet and a quadruplet. The energy separation between the levels, belonging to the ground state multiplet is quite small. For temperatures higher than 300 Kelvin, the contribution due to the crystal field effect may be neglected.

The thermal variations of atomic susceptibilities of $SmSn_3$, Sm_2Sn_3, and $Sm_5 Sn_3$ compounds and these of pure metallic samarium measured by ARAJS (16) are shown on figure IV. We also reported the theoretical thermal variation for two values of the screen constant $\sigma = 35$ and $\sigma = 36$; the corresponding energy separations between the ground $J = 5/2$ and the first excited $J = 7/2$ multiplet states are respectively 1,160 Kelvin and 1,020 Kelvin. The agreement between the theoretical curves relative to Sm^{3+} ions and the experimental susceptibility variations is quite good. This fact confirms, in particular, that samarium is in the Sm^{3+} ionic state in investigated compounds.

We have not taken into account the exchange interactions between Sm^{3+} ions. They surely exist in $SmSn_3$ and Sm_2Sn_3 compounds which exhibit, at low temperatures, a long range magnetic order. We may have a better fit between experimental and theoretical curves if we take into account these exchange interactions.

Magnetic measurements permit us to conclude that the samarium is in the trivalent ionic state in the investigated compounds.

From electrical resistivities we can deduce the metallic nature of the bonding in the first compound $SmSn_3$ and for Sm_2Sn_3 and $Sm_5 Sn_3$, the partial localization of conduction electrons by sharing in covalent bonding that could be expected by strong electrochemical factor.

These conclusions were in agreement with previous determinations (1), (2). Fig. IV shows high values of melting points, enthalpies of formation, and electrical resistivities of compounds which are also criteria of the localization of electrons.

REFERENCES

1 - A. PERCHERON, J. C. MATHIEU, F. TROMBE
    C. R. Acad. Sc., 266, série C, 1968, p. 2150.

2 - A. PERCHERON
   Colloque International du C. N. R. S. sur les Eléments des
   Terres Rares, Paris, Mai 1969.

3 - O. GOROCHOV
   Contribution à l'étude de quelques combinaisons sulfurées,
   séléniées et ellures de l'argent et des éléments du groupe
   IV. b, Thesis Fac. Sc. Paris (1968).

4 - B. PISTOULET
   L'onde électrique, 334, 1955, p. 71.

5 - J. LAPLUME
   L'onde électrique, 335, 1955, p. 113.

6 - PIETENPOL et MILEY
   Phys. Rev. , 34, 1929, p. 1588.

7 - S. ARAJS, G. R. DUNMYRE
   Z. Naturforschg, 21 a, 1966, p. 1856.

8 - M. A. CURRY
   Electrical resistivity of Sm, Eu, Tm, Yb and Lu, M.S. Thesis
   Iowa State University of Science and Technology, Ames Iowa,
   U. S. A. 1958.

9 - C. E. OLSEN
   The Electrical resistivity of samarium between 1. 4° K and
   300° K, Report LA-2406 Los Alamos New Mexico U. S. A.
   (1960).

10.- J. K. ALSTAD, R. V. COLVIN, S. LEGVOLD and F. H. SPEDDING
   Phys. Rev. 121. (1961), p. 137.

11 - J. K. STANLEY
   Electrical and magnetic properties of metals, A. S. M. (1963).

12 - J. M. LOCK
   Proc. Roy. Soc. , B. 70, 1957, p. 566.

13 - H. W. de WIJN, A. M. VAN DIEPEN, K. H. J. BUSCHOW
   J. Chem. Phys. 50, 1969, p. 142.

14 - H. W. de WIJN, A. M. VAN DIEPEN, K. H. J. BUSCHOW
     Phys. Rev. Vol. 161, n° 2, 1967, p. 253.

15 - J. H. VAN VLECK
     The theory of electrical and magnetic susceptibilities
     Oxford university press 1932.

16. S. ARAJS
     Phys. Rev. 120, 1960, p. 756.
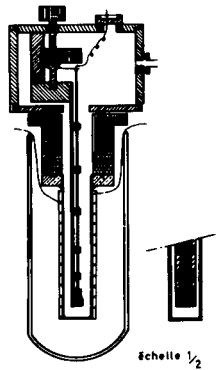
Fig. I - Low temperature heat leak chamber
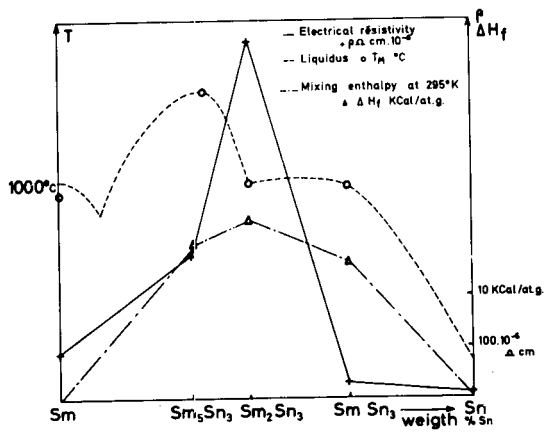
-Fig. V - Melting point, enthalpy of formation and electrical resistivity of definite compounds versus Sn weight %.
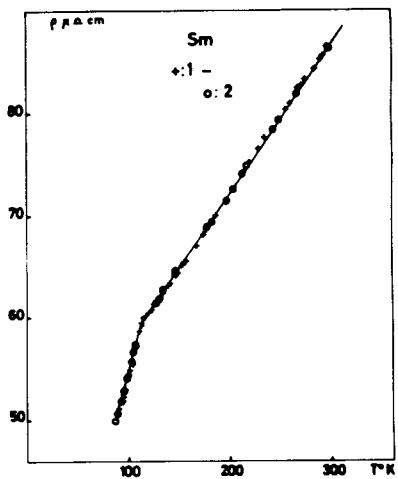
Fig. II, 1
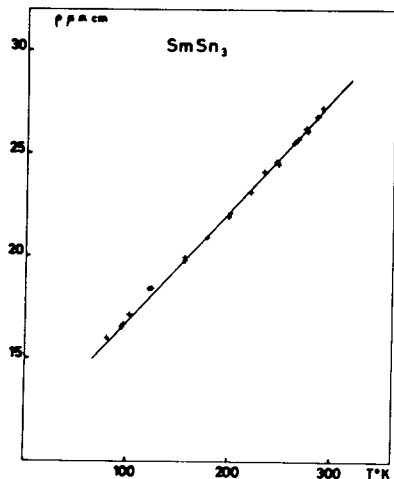
Fig. II, 2
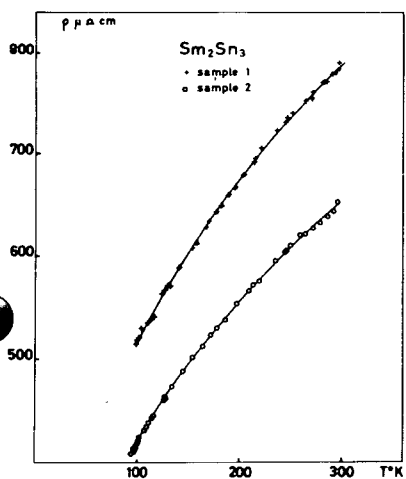
Fig. II, 3
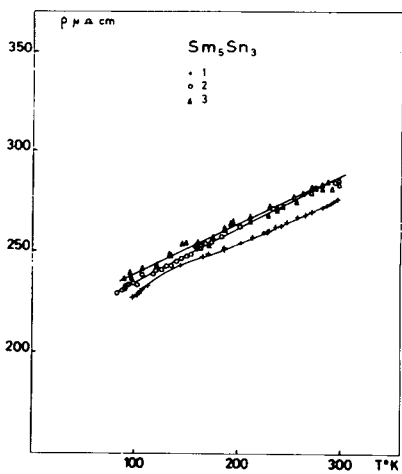
Fig. II, 4

Fig. II: Electrical resistivities versus temperature between 80 and 300° K.
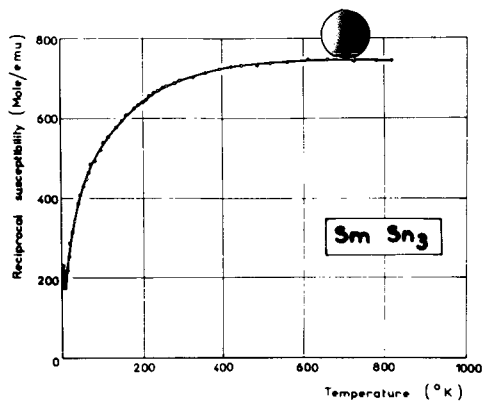
Fig. III, 1
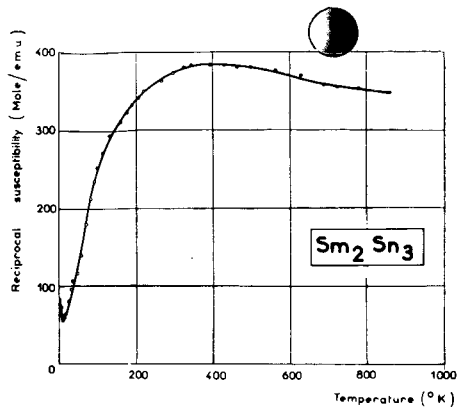
Fig. III, 2
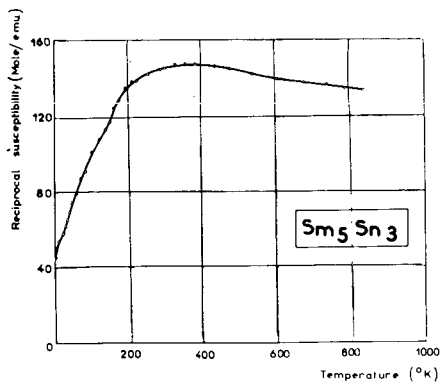
Fig. III, 3
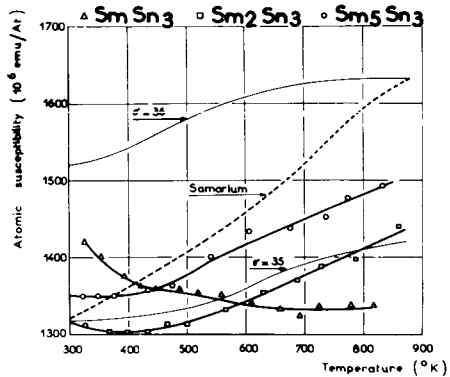
Fig. IV

PRESSURE-INDUCED CHANGES IN THE ELECTRONIC AND

LATTICE PROPERTIES OF THULIUM MONOTELLURIDE AND

THEIR SIGNIFICANCE

by

A. Jayaraman, E. Bucher and D. B. McWhan
Bell Telephone Laboratories, Incorporated
Murray Hill, New Jersey

ABSTRACT

The monotelluride of Tm has been prepared with Tm in the divalent state. It has the NaCl-type structure and a lattice constant of 6.34 A. The magnetic susceptibility measurements yield an effective moment of 4.96 μ_B. High pressure X-ray studies show that the material undergoes an electronic phase transition in which Tm^{2+} transforms to Tm^{3+}, with no change in the crystal structure. The resistivity of TmTe (~ 0.75 ohm cm) decreases by a factor of 3×10^3 ($\sim 25 \times 10^{-5}$ ohm cm) in the 1-30 kbar pressure region and thereafter exhibits very little change. It is believed that the resistivity variation is due to the electronic transition in which electrons from the 4f state are promoted into the conduction band, as the energy separation between them decreases with pressure. From the saturation resistivity, an energy separation of 0.21 ev is estimated, which is in agreement with the PΔV of transition evaluated from high pressure X-ray data.

INTRODUCTION

The monochalcogenides of the rare earth metals

exhibit interesting electrical and magnetic properties and

for this reason have received much attention in recent years.

They all crystallize in the NaCl-type structure[1] and are

either semiconducting or metallic,[2,3] depending on whether

the cation is dipositive or tripositive. With the exception

of Eu, Yb and Sm all the other rare earth monochalcogenides are reported to be metallic.[4] In the case of Eu, Yb and Sm the strong exchange interaction of electrons in the half filled, completely filled and nearly half filled 4f shell leads to stable divalent state. Hence their monochalcogenides in their ground state have no electrons in the conduction band and are therefore semiconductors.

There is strong experimental evidence[5,6,7] that in the beginning of the half periods the $4f^x5d^0$ and $4f^{x-1}5d^1$ electronic states have energies quite close to each other and can be inverted by external constraints. For this reason pressure or temperature causes 4f-5d electron promotion in Ce metal.[8,9] Recently it has been shown that high pressure induces an electronic transition in EuTe[6] and SmTe[7] in which a 4f electron is promoted into the conduction band. A rather large volume decrease and metallic behavior accompanies the transition but the structure remains the same in the high pressure phase. Also, recent studies on the temperature activated conductivity[10,4] in the monosulfide of Sm has been interpreted as due to the ionization of electrons from the 4f level located at only 0.22 ev below the bottom of the conduction band.

Thulium occupies an analogous position with respect to Yb, as Sm to Eu and can therefore be divalent with an almost fully occupied 4f shell. Therefore, the Tm monochalcogenides may be expected to behave like the Sm compounds,

-334-

but they are all reported to exhibit metallic conductivity and magnetic behavior consistent with a tripositive Tm ion.[1,4] Iandelli and Palenzona[11,12] have, however, noted that TmTe could be non-metallic and Tm ion could be divalent in the telluride.

We have made TmTe in the nonmetallic state. Magnetic susceptibility measurements and the lattice constant is consistent with Tm ion in the 2^+ state. Further, we have carried out resistance and X-ray studies at high pressure, which show that there is an electronic phase transition involving the promotion of a $4f$ electron. These will be discussed in the present paper.

EXPERIMENTS AND RESULTS

TmTe was prepared by reacting high purity Tm chips in Te vapor, followed by fusion and annealing. For this purpose appropriate amounts of high purity Tm and semiconductor grade Te were sealed in an evacuated quartz tube which had provisions to keep the Tm chips separated from molten Te. The quartz tube was sealed inside another quartz tube to prevent any oxygen contamination. The reaction in the vapor was carried out for 72 hours at 750°C and then at 900°C for 24 hours. Although the Te was completely used up, the reacted material at this stage was not single phase and had to be melted to obtain single phase TmTe. For this purpose the reacted material was encapsulated in tantalum and heating (1600°C to 1700°C) was accomplished electrically

-335-

by passing current through the pinched ends of the Ta tubing. After melting, the sample was annealed for several weeks at 450°C in a sealed quartz tube. The ingots thus obtained were polycrystalline but the individual crystallites were quite large (~ 0.5 cm) and therefore it was possible to cleave single crystal specimens for the studies.

X-ray powder photographs showed that the material was single phase, and had the NaCl-type structure with a lattice constant of 6.34 Å. This is consistent with Tm in the divalent state. For TmTe with Tm^{3+}, the lattice constant is given as 6.042 Å.[13] One of our unannealed samples had two NaCl phases and the lattice constants were 6.30 Å and 6.19 Å.

Magnetic susceptibility measurements[14] were made on a single crystal sample, down to liquid He temperatures. The susceptibility as a function of temperature is shown in Fig. 1. From the high temperature paramagnetic susceptibility the effective moment is calculated as 4.96 μ_B. For divalent Tm the effective moment should be 4.5 μ_B and for trivalent Tm 7.6 μ_B. The magnetic measurements are thus consistent with the Tm being predominantly in the divalent state in our TmTe sample.

RESISTIVITY UNDER PRESSURE

For resistivity measurements freshly cleaved single crystal bar samples about 1 mm in cross section and 3-4 mm long were used. Ohmic contacts were obtained with

-336-
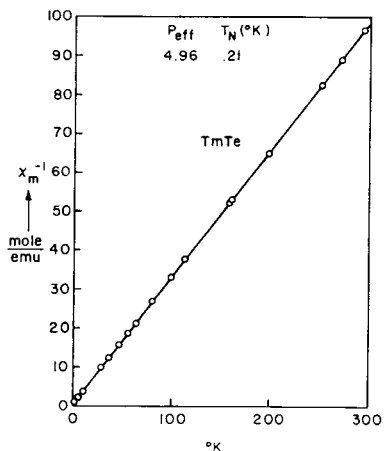
FIG. 1
Temperature dependence of the magnetic susceptibility in TmTe.
Magnetic ordering at 0.21°K.

indium (indium sticks especially well to freshly cleaved
surface) and four leads were soldered on to the bar. At
atmospheric pressure, the room temperature resistivity varied
from 0.5 to 1 ohm cm. and the temperature coefficient of
resistivity was negative. The effect of pressure on resis-
tivity was investigated up to 40 kbar.

        Hydrostatic pressure was generated in a piston-
cylinder device using the Teflon cell technique.[15] The
pressure medium was isoamyl alcohol. The resistance measure-
ments were usually carried out at room temperature except
in one case at 260°K. In Fig. 2 is shown a plot of the
log of resistivity against pressure. The resistivity
decreases by a factor of 3×10^3 in 30 kbar pressure and
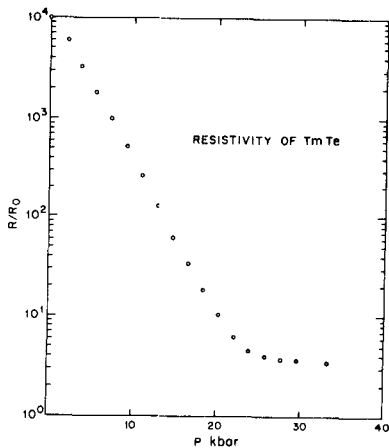
FIG. 2
Pressure dependence of the resistivity of TmTe at room
temperature.

thereafter shows only a small decrease with pressure. The

resistivity of the sample at a pressure of about 35 kbar is

about 25×10^{-5} ohm cm. and the atmospheric pressure resis-

tivity of this particular sample was about 0.75 ohm cm. On

releasing pressure the resistivity returns to the initial

value with no observable hysteresis.

X-RAY STUDIES

X-ray powder patterns were taken in a high pressure

camera described by McWhan and Bond.[16] The sample was

diluted with boron and mounted in an epoxy-boron disc which

served as the pressure medium. Powder patterns were taken

at approximately 10 kbar pressure intervals. From the

observed pattern the lattice constant was calculated and this

is plotted against pressure in Fig. 3.
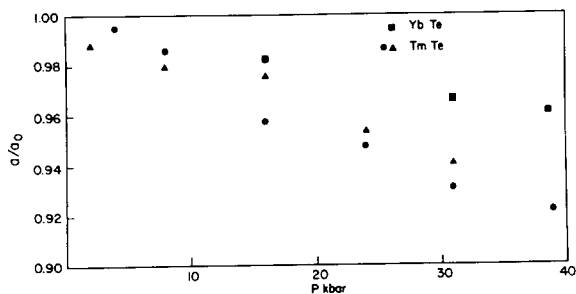
FIG. 3
Pressure variation of the lattice constant of TmTe and YbTe
for comparison. a/a_o is plotted as a function of pressure.

The observed change in the lattice constant with pressure

reflects an abnormally large compressibility.

DISCUSSION

The structure of TmTe at atmospheric pressure and

at 40 kbar is NaCl-type, but at the high pressure end the

change in the lattice constant reflects a striking increase

in the density. The calculated density from the X-ray data,

($a = 6.34$ Å) at zero pressure is 7.7 gms/cc and at 30 kbar

$a = 5.94$ Å) 9.4 gm/cc. This change represents a $\Delta V/V$ of

18% which is at least three times larger than the normal

compressibilities quoted for EuTe or SmTe; $K \approx 10^{-3}$/kbar.[7,17]

If we assume the above value for TmTe the volume change ΔV

due to normal compression should be about 5-6%. When this is

subtracted, the lattice contraction at 40 kbar amounts to a

-339-

$\Delta V/V$ of 12-13%. We ascribe this large volume change to an electronic transition in TmTe, of the type reported in the case of Ce[5,9] and more recently in the case of EuTe[6] and SmTe.[7] However, the transition in TmTe is spread over a broad pressure range and appears to take place continuously, near room temperature. As in the case of EuTe and SmTe, the transitions involve the promotion of a 4f electron in which the change $Tm^{2+}Te^{2-} \rightarrow Tm^{3+}Te^{2-} + 1e$ occurs. The excess electron goes into the conduction bands formed mostly by the 6s and 5d states. The Tm^{3+} ion is considerably smaller in size than the Tm^{2+} ion and hence the substantial contraction of the lattice upon transition. The observed volume change is similar in magnitude to what has been reported for the analogous electronic transition in EuTe[6] and SmTe.[7]

In one of the samples which was quenched from the melt, we were able to see two NaCl-type phases of which the one closer to the $Tm^{3+}Te^{2-}$ was the dominant phase. The fact that $Tm^{3+}Te^{2-}$ can be obtained by rapidly quenching from the melt indicates that at high temperatures the Tm ion exists in the trivalent state in the compound. The energy difference between the electronic states characterizing the $Tm^{2+}Te^{2-}$ and $Tm^{3+}Te^{2-} + 1e$ must be relatively small, so that modest high pressures or high temperature is able to invert them.

The promotion of one electron into the conduction band per TmTe should result in a semiconductor-metal transition, since the number of 4f electrons promoted is of the

-340-

order of 2×10^{22} cm^{-3}. The resistivity vs. pressure data
shown in Fig. 1 is in accordance with this. A similar
change in resistivity with pressure has been reported in
the case of EuTe. In the case of TmTe the resistivity
decreases by a factor of 3×10^3 in 30 kbar and at about 35
kbar the sample has a resistivity of 25×10^{-5} ohm cm. If it
is assumed that the logarithmic decrease in resistivity is
due to activation of electrons from the 4f state into the
conduction band and this is a consequence of decreasing
energy separation between the latter with pressure, one can
estimate the zero pressure energy separation between the
4f state and the conduction band from the resistance data,
using

$$\rho_{sat.}/\rho_o \approx \exp - E_D/kT$$

where $\rho_{sat.}$ is the saturation resistivity at high pressure
and ρ_o is the zero pressure resistivity. We obtain for the
energy separation 0.21 ev using 3×10^3 for the resistivity
ratio. In the case of SmS, the energy separation between
the 4f state and the conduction band has been determined[3,4,10]
as 0.22 ev from temperature activated conductivity data. In
our samples no doubt there is extrinsic conductivity with
much smaller activation energy.

The possibility remains that the observed pressure
variation of resistivity in TmTe is just due to the decreasing
energy separation with pressure of the conduction band from

a donor impurity level 0.21 ev below. However, since the
X-ray data clearly shows that the electronic promotion occurs
in the same range of pressure, we are led to believe that
the resistivity variation is most likely to be due to electron
promotion. Further we find that PΔV of transition evaluated
at about 35 kbar yields a gain in energy of 4500 cal/gm mol,
which is $\approx$ 0.20 ev. This value is in good agreement with the
gap estimated from the resistivity data.

  The nature of the transition at room temperature
raises many interesting questions. Firstly, would it become
a discontinuous transition below some critical temperature?
Since the transition is also a semiconductor-metal transition
with no change in the long range order of the crystal, what
model, among the various models currently in vogue for the
metal-semiconductor transitions, would best describe the
situation presented in a substance such as TmTe and perhaps
in other analogous monochalcogenides. More experiments are
clearly necessary to answer these questions and these are
presently in progress.

REFERENCES

1. A. Iandelli, Rare Earth Research (Ed. Kleber, E. V.) page 135, The MacMillan Company, New York (1961).

2. F. J. Reid, L. K. Matson, J. F. Miller and R. C. Himes, J. Phys. Chem. Solids 25, 969 (1964).

3. R. Didchenko and F. P. Gortsema, J. Phys. Chem. Solids 24, 863 (1963).

4. J. W. McClure, J. Phys. Chem. Solids 24, 873 (1963).

5. A. W. Lawson and T. Y. Tang, Phys. Rev. 76, 301 (1949).

6. C. J. M. Rooymans, Solid State Comm. 3, 421 (1965).

7. C. J. M. Rooymans, Berichte der Bunsengeselchaft fur Physik Chemi. 70, 1036 (1966).

8. M. K. Wilkinson, H. R. Child, C. J. McHargue, W. C. Koehler and E. D. Wollan, Phys. Rev. 122, 1409 (1961).

9. A. F. Schuch and J. H. Sturdivant, J. Chem. Phys. 18, 145 (1950).

10. A. V. Golubkov, E. V. Goncharova, V. P. Zhuze and I. G. Manoilova, Sov. Phys. Sol. State 7, 1963 (1966).

11. A. Iandelli and A. Palenzona, Proprietes des derives Semi-metalliques (Ed. CNRS, Paris, 1967), 397.

12. F. Hulliger, Hel. Phys. Acta. 41, 945 (1968).

13. L. H. Brixner, J. Inorg. Nucl. Chem. 15, 199 (1960).

14. E. Bucher, Eighth Rare Earth Research Conference (1970).

15. A. Jayaraman, A. R. Hutson, J. H. McFee, A. S. Coriell and R. G. Maines, Rev. Sci. Instr. 38, 44 (1967).

16. D. B. McWhan and W. L. Bond, Rev. Sci. Instr. 35, 626

(1964).

17. C. J. M. Rooymans, Doctoral Thesis, University of Amsterdam, 1967.

SEMICONDUCTION IN RARE EARTH OXIDES

C.N.R. Rao and G.V. Subba Rao
Department of Chemistry
Indian Institute of Technology
Kanpur-16, India.

Abstract

We have examined the defect structure and electrical transport properties of several rare earth sesquioxides and non-stoichiometric oxides. These oxides have conductivities in the range $10^{-9} - 10^{-6}$ ohm^{-1} cm^{-1}. The non-stoichiometric oxides, LnO_x, with $1.50 \leq x < 1.75$ are p-type semiconductors, while the oxides with $1.75 < x \leq 2.00$ are n-type semiconductors. Fully or partly ionized cation vacancies seem to be predominant defects contributing to the defect structure in these oxides. On the basis of the conductivities and Seebeck coefficients, we have explained the mechanism of conduction in terms of the hopping model and the polaron theory.

We have examined the electrical conductivities (as a function of temperature and oxygen partial pressure) and Seebeck coefficients of several compositions of the solid solutions, $CeO_2-Y_2O_3$ and $CeO_2-Nd_2O_3$. Considerable ionic contribution to the total conductivity was noticed at all compositions; the electronic conductivity was p- or n-type depending on the composition. Both the ionic and the electronic conductivity appear to go through a maximum around 30% $YO_{1.5}$ (or at 12.5% $NdO_{1.5}$). The results are interpreted in terms of ordered defect complexes.

INTRODUCTION

Rare earth oxides with filled or partially filled

inner 4f-shells of the lanthanide ions are likely to be narrow

band materials and electrical conduction in these oxides would

undoubtedly involve the 4f-electrons[1]. In the literature there

are a few reports on the electrical conductivity of rare earth

oxides. Noddack and Walch[2] measured the resistivities of a few

rare earth oxides and found the conduction to be predominantly

electronic. Eyring and Baenziger[3] have reported preliminary

measurements of the resistivities of a few praseodymium oxides,

while Honig and coworkers[4] have studied both the electrical resistivities and Seebeck coefficients of a few oxides. Some evidence has been presented by Tare and Schmalzried[5] for the presence of ionic conductivity in rare earth sesquioxides.

We have presently examined the semiconduction of several rare earth sesquioxides and the non-stoichiometric oxides of praseodymium and terbium in some detail. We have measured the conductivities, σ, of a few oxides at different partial pressures of oxygen in order to establish the defect equilibria. Seebeck coefficients, β, have been measured to find out the sign of the charge carriers. We were particularly interested in studying the variation of σ and β with $\underline{x}$ in LnO_x. Employing the experimental σ and β, we have attempted to explain the mechanism of conduction with the aid of the hopping model and the polaron theory.

We have determined the σ and β of a few compositions of $CeO_2-Y_2O_3$ and $CeO_2-Nd_2O_3$ in order to understand the mechanism of conduction and the defect structure of these solid solutions. We were interested to see if these solid solutions exhibit conductivity maxima at compositions corresponding to the $LnO_{1.75}$ or $LnO_{1.71}$.

RESULTS AND DISCUSSION

Sesquioxides

The conductivities of rare earth sesquioxides, Ln_2O_3, at two temperatures along with the activation energies for conduction, E_a, are given in Table I. The conductivities are generally low particularly in the heavier rare earth sesquioxides.

-346-

Most of the sesquioxides, especially those of the heavier rare earths show breaks in the log σ vs $1/T$ plots in the 300-600°C range. These breaks in the conductivity curves do not correspond to any phase transformations. Whereas the conductivity decreases down the rare earth series, the activation energy above the break temperature, T_B, increases. The change in slope was seen at all values of p_{O_2} studied (0.10 - 760 mm Hg); further, the actual values of σ were more sensitive to p_{O_2} below T_B. We therefore believe that the change in slope in the conductivity plots does not arise from the loss of oxygen, but is likely to be due to the increased ionic conductivity around T_B.

In order to examine the defect chemistry of these sesquioxides, the conductivities of Eu_2O_3 and Ho_2O_3 were measured at different oxygen pressures in the range 2-100 mm Hg at a few temperatures; σ was proportional to $p_{O_2}^{+1/6}$ and $p_{O_2}^{1/5.3}$ respectively in the two oxides. Schwab and Bohla[6] have recently found $p_{O_2}^{+1/5.5}$ dependence of conductivity of Eu_2O_3 in the pressure range that we have examined. In Y_2O_3, Tallan and Vest[7] have observed a $p_{O_2}^{+1/5.33}$ dependence of conductivity. All these results show that rare earth sesquioxides are p-type semiconductors. The observed oxygen pressure dependence can be explained by a mechanism involving cation vacancies most of which are ionized.

When oxygen is initially let into the evacuated conductivity cell containing the pellet of Eu_2O_3 or Ho_2O_3, there was a marked decrease in the conductivity. It appears that at low p_{O_2}, Eu_2O_3 and Ho_2O_3 may act as n-type semiconductors.

This observation is consistent with some of the literature reports[6,7]. Except for Pr_2O_3, no Seebeck coefficient data are available for the rare earth sesquioxides. We have presently measured a few sesquioxides in the range 400–800°C at $p_{O_2} \approx 150$ mm Hg. As expected, these oxides are p-type semiconductors in this temperature range. The β values are small below 600°C, but increase markedly above this temperature.

Non-stoichiometric oxides

Among the non-stoichiometric oxides, the intermediate phase close to the composition $LnO_{1.75}$ (Ln = Pr or Tb) exhibits the highest σ and the lowest E_a. It is interesting that the conductivities of all the LnO_x compositions fall on the $\sigma - x$ curves showing maxima at $x \approx 1.75$, immaterial of whether they are ordered (with narrow homogeneity ranges) or disordered (and biphasic) phases. Apparently, the main factor that governs the conductivity maximum at $x \approx 1.75$ is the stoichiometry (Ln^{+3} and Ln^{+4} concentrations) rather than the defect structure. Obviously, the non-stoichiometric oxides are hoppers, wherein σ is proportional to the product $[Ln^{3+}][Ln^{4+}]$. Thus, in LnO_x, σ should go through a maximum around $x = 1.75$ at a given temperature as found experimentally.

In the oxides where x is not far from 1.5, holes can jump from one cation site to another of different valency giving rise to p-type conductivity. In compositions near LnO_2, the charge carriers are electrons and we expect the material to be n-type. Midway between $LnO_{1.5}$ and LnO_2 we would expect a change from p- to n-type behavior. This prediction is in agreement with the Seebeck

coefficient data on PrO_x reported by Honig and coworkers[4] and on TbO_x obtained presently. β is positive for $TbO_{1.5}$ typical of a p-type semiconductor and negative when $\underline{x} > 1.75$ indicating n-type behavior. In the case of $TbO_{1.5}$ (when the stoichiometry was exact), the β value was very small ($\sim 2\mu$ V/°C around 200°C), but when $\underline{x}$ becomes slightly higher ($1.50 < \underline{x} < 1.52$), β increases markedly ($\sim 200\mu$ V/°C at 200°C). Within experimental error, β was independent of temperature for a given composition; $TbO_{1.81}$, however, shows a slight maximum around 350°C, the cause of which is not clear. The variation of β with temperature in LnO_x is similar to that found in electron-transfer materials. We find that the value of S^*/k is of the order of 0.2 in TbO_x; S^*/k in PrO_x has been reported to be 0.2 by Honig and coworkers[4].

The composition $LnO_{1.75}$ can be assumed to have a random distribution of Ln^{3+} and Ln^{4+} ions with a maximum of electronic disorder. It is possible to conceive of a slightly different model according to which the conductivity maximum would be at the composition $\underline{x} = 1.71$ instead of $\underline{x} = 1.75$. The phase $LnO_{1.71}$ may be described as consisting of parallel 'strings' of irregular LnO_6 octahedra in the $\langle 111 \rangle$ direction surrounded by contiguous sheaths of seven-coordinated cations[8]. According to this model, the seven-coordinated cations with an average charge of +3.5 would be responsible for the conductivity. This would result in the conductivity maximum and zero β at $LnO_{1.71}$ rather than at $LnO_{1.75}$. Although the second model appears to be reasonable, it is difficult to make such subtle distinctions on the basis of the available experimental data. In order to understand the defect equilibria in the PrO_x system, σ was

measured at different p_{O_2} values. Pr_6O_{11} in the low pressure range (p_{O_2} = 2-15 mm Hg) indicated a $p_{O_2}^{-1/6}$ dependence of conductivity at 200°C; the $p_{O_2}^{-1/6}$ dependence can be interpreted in terms of anion vacancies. The conductivity of the non-stoichiometric oxides in the composition range $1.68 < x < 1.72$, on the other hand, showed a dependence of $p_{O_2}^{+1/6}$; this is consistent with a neutral cation vacancy mechanism.

Since the band widths in rare earth oxides are small, we have examined the conduction in these compounds in terms of the polaron theory[9,10]. The measure of the electron-phonon interaction in polaron materials is given by the dimensionless Fröhlich coupling constant, α_F^*. We have calculated α_F^*, polaron mass and dimension, transition probability, drift and Low-Pines mobility and other transport parameters. For $TbO_{1.81}$, we have calculated the transport parameters as a function of temperature which permits us to examine the applicability of the hopping model more closely.

The charge carrier density is higher in non-stoichiometric oxides; in $TbO_{1.81}$ it is almost independent of the temperature in the range studied. The effective mass of the charge carriers, m^*, is usually 20 to 40 time the free electron mass, indicating considerable interaction between the charge carriers and phonons; m^* is slightly lower for non-stoichiometric oxides. For $TbO_{1.81}$, m^* and α_F^* show decreasing trends with rise in temperature.

Both τ^{-1} and μ_D are greater in the non-stoichiometric oxides compared to the stoichiometric oxides. In the oxides studied presently, μ_D is in the range 10^{-3} to 10^{-8} $cm^2/V.sec$, which is in the region normally found in oxide semiconductors.

In $TbO_{1.81}$, μ_D increases with temperature exponentially, the
activation ~~ef~~ energy being 0.5 eV. This monotonic increase
in mobility can be taken to indicate hopping mechanism rather
than 'polaron band' formation. The value of 0.5 eV is comparable
with the 0.6 eV obtained from the conductivity data. The polaron
dimension is of the same order as the lattice parameter indicating
that the charge carriers are localized at lattice sites. The
polaron mass (m^{**}) is higher than the effective mass of the
charge carriers (when $\alpha_F^* \leqslant 6$); for $TbO_{1.81}$, m^{**} decreases from
44m to 20m in the temperature range 200–500°C and then slightly
increases to 24m at 600°C. This is because of the decrease of
both m^* and α_F^* with temperature. The same behavior is exhibited
by the self-energy of the polaron. These results are in agreement
with the theoretical predictions.

$CeO_2-Y_2O_3$ and $CeO_2-Nd_2O_3$

Studies of the crystallography, σ (as a function of
temperature and oxygen partial pressure) and β of various
compositions of the $CeO_2-Y_2O_3$ and $CeO_2-Nd_2O_3$ systems indicate
that simulation of the non-stoichiometric rare earth oxide phases
is not feasible since both cation and anion ordering seem to be
present. Considerable ionic contribution to the total conductivity
was noticed at all compositions in these mixed oxides and the
electronic conductivity was n- or p-type depending on the
composition. Both the ionic and electronic conductivity appear
to go through a maximum around 30 mole % $YO_{1.5}$ (or at 12.5 % $NdO_{1.5}$).
The results can be interpreted in terms of 'defect complex formation

and ordering of the vacancy strings consistent with the known crystallography of these solid solutions[11,12].
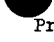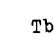
In the $CeO_2-YO_{1.5}$ system, the conductivity in the range 0-57% $YO_{1.5}$, is mainly due to the electrons released by the ionisation of the vacancies which jump from one site to another by a hopping mechanism. The mobility at 700°C calculated from the dopant concentration and the known unit cell volume is of the order of 10^{-7} $cm^2/V.sec$. Significant contribution to the conductivity also arises out of the migration of oxygen ions _via_ anion vacancies.

In the range, 75-100% $YO_{1.5}$ (C-type phase region of the system) the conductivity is _p_-type probably involving an anion interstitial mechanism. The holes created by these anion interstitials may move from one cation site to another by a hopping process.

At small concentrations of $YO_{1.5}$, anion vacancies that are created start interacting within themselves and around 12% $YO_{1.5}$, defect complexation starts; around 30%, the complexation is complete and vacancy strings will be formed leading to long range order. This produces a decrease in conductivity. At higher concentrations, oxygen may enter the lattice to fill up the anion vacancies and at 75% $YO_{1.5}$ the anion vacancies will be filled almost completely. At still higher concentrations, oxygen may go into the interstitials creating holes and causing a _p_-type behavior. We should expect a minimum in the electronic conductivity at the composition where the system changes from _n_- to _p_-type behavior; the conductivity data on $CeO_2-YO_{1.5}$ solid solutions appear to confirm this prediction.

-352-

Electrical conductivity data of rare earth sesquioxides (Ln_2O_3) [a]

Ln	T_B, °C	E_1, eV [b] $(T < T_B)$	E_2, eV $(T > T_B)$	$\sigma_{400°C}$ ($\times 10^9$ ohm^{-1} cm^{-1})	$\sigma_{650°C}$ ($\times 10^9$ ohm^{-1} cm^{-1})
La	270	0.7	1.05	230	1700 [c]
Pr [d]	320	0.4	0.95	300	3450
Nd	–	–	1.15	25	1450
Sm	560	0.6	1.28	20	880
Eu	570	0.6	1.35	5	150
Gd	560	0.5	1.57	5	130
Tb [d]	280	0.4	0.95	3	200
Ho	575	0.7	1.61	5	160
Yb	605	0.5	1.61	3	50
Y	–	–	1.10	–	55

(a) DC conductivity measured at $p_{O_2} \approx 150$ mm Hg.

(b) Approximate values only since the conductivity is small at $T < T_B$.

(c) Values are for the hexagonal (A) form. In all the other cases, the oxides are in the cubic (C) form (defect fluorite structure).

(d) Measured in dry hydrogen to prevent oxidation.

REFERENCES

1. R.R. Heikes, "Rare Earth Research", 1, 247 (1961) (MacMillan Co., New York, NY).

2. W. Noddack and H. Walch, Z. Physik., 211, 194 (1959); Z. Electrochem., 63, 269 (1959).

3. L. Eyring and N.C. Baenziger, J. Appl. Phys., 33, 428 (1962).

4. J.M. Honig, A.A. Cella and J.C. Cornwell, Rare Earth Res., 2, 555 (1964) (Gordon and Breach, New York).

5. V.B. Tare and H. Schmalzried, Z. Physik. Chem. (NF), 43, 30 (1964).

6. G.M. Schwab and F. Bohla, Z. Naturforsch., 23a, 1549 (1968).

7. N.M. Tallan and R.W. Vest, J. Am. Ceram. Soc., 49, 401 (1966).

8. B.G. Hyde and L. Eyring, Rare Earth Res., 3, 623 (1965). (Gordon and Breach, New York).

9. "Polarons and Excitons", (Ed: C.G. Kuper and G.C. Whitfield, Plenum Press, New York, 1962).

10. T.D. Lee, F. Low and D. Pines, Phys. Rev., 90, 297 (1953).

11. D.J.M. Bevan, W.W. Barker, R.L. Martin and T.C. Parks, Rare Earth Res., 3, 441 (1965) (Gordon and Breach, New York).

12. W.W. Barker and A.F. Wilson, J. Inorg. Nucl. Chem., 30, 1415 (1968).

KONDO EFFECT AND THE INFLUENCE OF CRYSTALLINE ELECTRIC FIELD

ON THE ELECTRICAL RESISTIVITIES OF THE INTERMETALLIC

COMPOUNDS $CeAl_3$ AND $CeAl_2$

V. U. S. Rao,[*] W. Suski,[**] R. S. Craig and W. E. Wallace

Department of Chemistry
University of Pittsburgh
Pittsburgh, Pa. 15213

Abstract

A method is proposed to evaluate the effect of the crys-
talline electric field on the spin-disorder resistivity of rare-
earth intermetallics and the procedure is used to interpret the
resistivity vs. temperature behaviour of $CeAl_2$. Resistivity
measurements performed on $CeAl_3$ in the temperature range 3 to
450°K indicate a peak at 33°K and a broad minimum at 310°K in
the resistivity vs. temperature curve. The results are explained
as arising from the presence of the Kondo effect in addition to
the influence of the crystalline electric field on the spin-
disorder resistivity of $CeAl_3$.

Introduction

The effect of localized moments on the electrical resis-

tivity via the exchange scattering of conduction electrons has

been a subject of considerable interest in recent years. When

evaluated in the first Born approximation, this interaction gives

rise, in the paramagnetic state, to a temperature independent con-

tribution which is usually termed as the spin-disorder resistivity.[1]

---

[*] On leave from Tata Institute of Fundamental Research,
Bombay, India.
[**] On leave from Institute of Low Temperature and Structure
Research, Polish Academy of Sciences, Wroclaw, Poland.

If, however, the evaluation is carried out to the second Born approximation,[2] in the case when the s-d or s-f interaction has a negative sign, an additional contribution arises at temperatures below a certain critical temperature, giving rise to the well-known resistivity minimum (Kondo effect) in certain alloys. Among rare-earth systems, the Kondo effect has been observed in a number of cerium alloys.[3,4,5]

In this paper we wish to demonstrate that the spin-disorder contribution cannot be regarded as being independent of temperature when the crystal field splitting of the ground multiplet of the rare-earths is comparable to the temperatures at which the resistivity is measured. To take a typical example, heat capacity measurements on $CeAl_2$ performed in our Laboratory[6] have indicated that the ground multiplet ($J = \frac{5}{2}$) of the Ce^{3+} ion in the cubic field is split into a doublet (Γ_7) and a quartet (Γ_8) with a separation of the order of $100°K$. We have evaluated the effect of this crystal field on the spin-disorder resistivity of $CeAl_2$ and have been able to explain an unusual feature in the ρ versus T behavior reported earlier by van Daal and Buschow.[7]

Also reported in this paper is the resistivity measurement on $CeAl_3$ in the temperature range 3 to $450°K$. A tentative explanation is provided for the unusual ρ versus T curve in terms of the Kondo effect and the influence of the hexagonal crystal field on the spin-disorder resistivity.

Outline of the Calculation of the Effect of Crystal Field on

the Spin Disorder Resistivity of $CeAl_2$

We shall assume in the usual manner that the exchange inter-
action between a conduction electron of spin $\vec{s}$ at $\vec{r}$ and a rare-earth
atom of spin $\vec{S}_n$ at $\vec{R}_n$ can be written as

$$H_n = -2G\delta(\vec{r} - \vec{R}_n)\vec{s} \cdot \vec{S}_n \tag{1}$$

here G is a quantity with the dimensions of energy times volume.
As a result of spin-orbit coupling, equation (1) can be rewritten in
terms of the total angular momentum $\vec{J}_n$ as

$$H_n = -2G(g-1)\delta(\vec{r} - \vec{R}_n)\vec{s} \cdot \vec{J}_n \tag{2}$$

$$= -2G(g-1)\delta(\vec{r} - \vec{R}_n)\left\{ s_z J_z + \frac{1}{2}(s_+ J_- + s_- J_+) \right\}$$

where g is the Landé factor.

When there is no crystal field interaction, the $(2J+1)$
eigenstates of the ground J-multiplet are degenerate in the paramag-
netic state and can be labelled by the eigenvalues (m_J) of J_z. A
conduction electron in a state $\vec{k}$ is scattered by the potential (2)
into a new state $\vec{k}'$. The scattering occurs without spin flip if the
initial and final states are connected by the term $s_z J_z$ in the Hamil-
tonian and with spin flip if they are connected by the terms $s_\pm J_\mp$.
The scattering cross-section is proportional to the square of the
relevant matrix element and summing up over all the scattering paths
one obtains for the spin-disorder resistivity[1]

-357-

$$\delta_s^o = (3\pi Nm/2\hbar e^2 E_F) G^2 (g-1)^2 J(J+1) \tag{3}$$

where N is the number of magnetic centers per unit volume. From Equation (3), it can be seen that δ_s^o is independent of temperature.

When the effect of the crystal field interaction is included, the above procedure has to be modified in the following manner. First, the eigenstates are no longer pure m_J states but are admixtures of them. Secondly the probability (p_i) of a given rare-earth atom being present in a certain crystal field state, i, depends on the extent of the crystal field splitting and on the temperature. Finally, cognizance must be taken of the change in the energy of the conduction electron in certain scatterings since the cross-section then depends upon the occupation probability of different states in the Fermi sea.

The eigenfunctions of the ground multiplet $(J = \frac{5}{2})$ of the Ce^{3+} (f^1) ion are given by[3] the following linear combinations of the unperturbed m_J states.

$$\Gamma_7 \rightarrow 0.4083 \left| \pm \frac{5}{2} \right\rangle - 0.9129 \left| \mp \frac{3}{2} \right\rangle$$

$$\Gamma_8 \rightarrow 0.9129 \left| \pm \frac{5}{2} \right\rangle + 0.4083 \left| \mp \frac{3}{2} \right\rangle$$

and

$$\left| \pm \frac{1}{2} \right\rangle$$

With the above considerations in mind, it can be easily shown that the spin-disorder resistivity now becomes

$$\rho_s(T) = \frac{3\pi Nm}{he^2 E_f} \; G^2(g-1)^2 \sum_{m_s,m_s',i,i'} \left\langle m_s',i' \left| \vec{s}\cdot\vec{J} \right| m_s,i \right\rangle^2 \; p_i f_{ii'} \quad (4)$$

where the $f_{ii'}$ are given by[9]

$$f_{ii'} = \frac{2}{1+\exp(-E_{ii'}/kT)} \quad\quad\quad (5)$$

with $E_{ii'} = E_i - E_{i'}$, and $p_i = \exp(-E_i/kT)/\sum_i \exp(-E_i/kT)$. In the high temperature limit, $\rho_s(T)$ becomes equal to ρ_s^o of equation (3).

In Fig. 1, the ratio $\rho_s(T)/\rho_s^o$ has been plotted as a function of kT/E, the ratio of the temperature to the crystal field separation E between the doublet and the quartet. It is seen that when the doublet is lower $\rho_s(T)$ approaches a much lower value as $T \to 0$ than when the quartet is lower.

The experimental ρ versus T curve obtained by van Daal and Buschow[7] is shown in Figure 2. Measurements on $CeAl_2$ were repeated in our laboratory and were found to be in satisfactory agreement with those of the above authors. The upturn in the ρ-T curve at low temperatures is now regarded as due to a Kondo anomaly.[3] The point of interest to us is the unusual broad "knee" in the ρ-T curve at about 70°K. We ascribe this behaviour to the influence of the crystal field on the spin-disorder resistivity. The general shape of the ρ-T curve is well predicted by our analysis as may be seen by a comparison of Figures 1 and 2. To make a quantitative comparison between theory and experiment one would have to subtract the lattice contribution $\rho_L(T)$ from the observed resistivity. If one assumes the

-359-
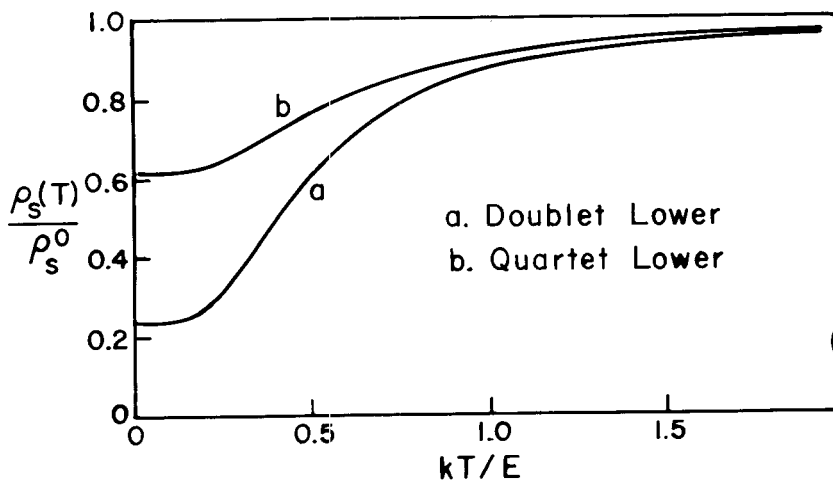
Fig. 1. Theoretical curves for the variation of spin-disorder resistivity of $CeAl_2$ with temperature under the influence of a cubic crystal field for (a) doublet lower and (b) quartet lower. $\rho_s(T)$ and ρ_s^0 are given by equations (3) and (4).
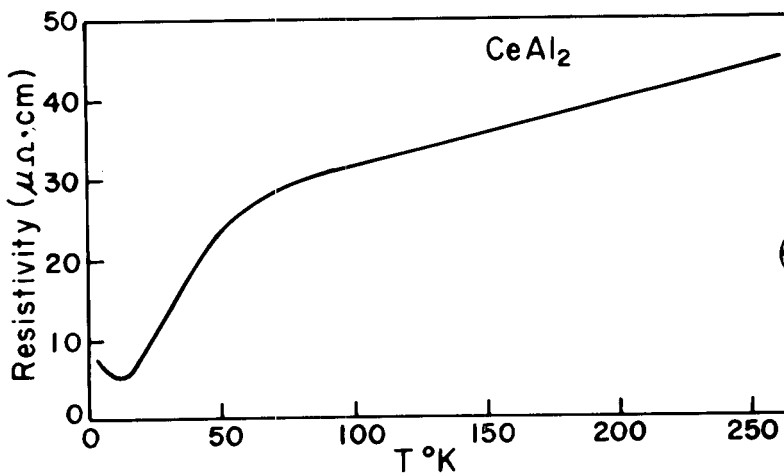
Fig. 2. Temperature variation of the resistivity of $CeAl_2$. (Ref. 7)

$\rho_L(T)$ of $CeAl_2$ to be similar to that of $LaAl_2$, the spin-disorder contribution is found to fall by a factor of at least three. This should be considered a lower limit for $\rho_s(T=o)/\rho_s^o$ since the residual resistivity has not been subtracted from the measured resistivity of $CeAl_2$. A second complication is the Kondo anomaly below about 15°K. In view of these undetermined contributions to the measured resistivity, the spin-disorder part might well fall to .23 of its high temperature value as predicted when the doublet is lower, rather than to a fraction of .61 which is predicted when the quartet is lower (see Fig. 1). The conclusion is therefore that the doublet is lower in agreement with the recent heat capacity results of Hill and da Silva[10] in the temperature range 0.5 to 15°K.

<center>Resistivity of $CeAl_3$</center>

Experimental Results

The resistivity of $CeAl_3$ was measured in the temperature range 3 to 450°K using a conventional four probe technique. The ρ versus T curve is shown in Fig. 3. The ρ-T curve of $CeAl_3$ exhibits a maximum at 33°K and a broad shallow minimum near 310°K.

Discussion

The crystal structure[11] of $CeAl_3$ is of the hexagonal Ni_3Sn type with a = 6.545 Å and c = 4.609 Å. The variation of magnetic susceptibility with temperature was studied earlier by Mader and Swift.[12] The χ versus T variation was found to deviate appreciably

<center>-361-</center>
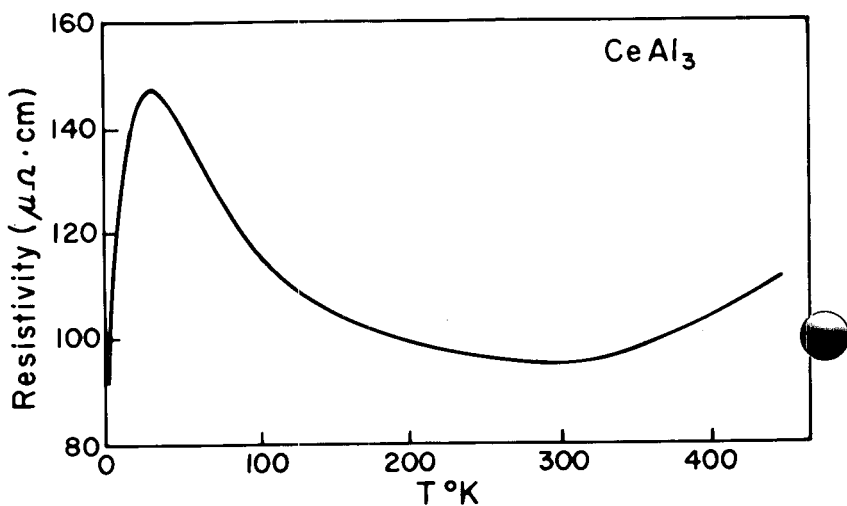
Fig. 3. Temperature variation of the resistivity of CeAl$_3$.
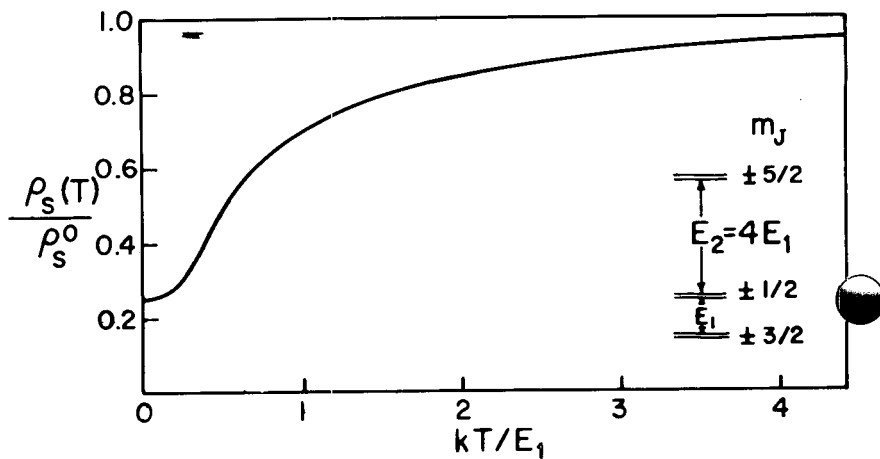
Fig. 4. Theoretical curve for the temperature variation of the spin-disorder resistivity of CeAl$_3$ under the influence of a hexagonal crystal field splitting of [3] the type shown in the inset.

from free-ion behaviour especially at low temperatures. No evidence for a magnetic transition was found down to a temperature of 2.2°K. Mader and Swift interpreted the χ-T behavious on the basis of the effect of the hexagonal crystal field potential of the form

$$V_{cf} = B_2^O O_2^O + B_4^O O_4^O \tag{6}$$

which splits the ground multiplet of Ce^{3+} into three doublets as shown in Fig. 4. (inset). Since the operator equivalent form of V_{cf} contains terms involving only powers of J_z^2, there is no admixture of the pure m_J states. Taking $B_2^O/B_4^O \simeq 30$, which yields $E_2/E_1 \simeq 4$ (see Fig. 4) they were able to fit the χ-T curve with $E_1/k \simeq 56°K$.

We have evaluated the effect of the above type of crystal field on the spin-disorder resistivity using the procedure described earlier. The calculations predict a variation of $\rho_s(T)/\rho_s^O$ with T as shown in Fig. 4. It seems reasonable to attribute the precipitous fall of the measured ρ with decreasing T below 33°K to an effect of the crystal field.

The decrease of ρ with increasing T above 33°K and the minimum at 310°K may be due to the formation of a Kondo state. If this be the case, it would mean a very high Kondo temperature ($\sim 300°K$) for $CeAl_3$. This is not impossible since T_K depends sensitively on both G and $N(0)$, the density of states at the Fermi level through the well-known expression $T_K \simeq T_F \exp[-1/3 |G| N(0)]$. However, the above interpretation should be regarded as tentative and its confirmation must await heat capacity measurements on $CeAl_3$, now underway in our laboratory.

REFERENCES

1. See for e. g. A. J. Dekker, J. Appl. Phys. 36, 906 (1965) and references therein.

2. J. Kondo, Prog. Theoret. Phys. (Kyoto) 32, 37 (1964).

3. K. H. J. Buschow and H. J. van Daal, Phys. Rev. Letters 23, 408 (1969).

4. H. H. Hill, R. O. Elliott and W. N. Miner, Proc. Seventh Rare Earth Research Conf. (Coronado, 1968) p. 847.

5. T. Sugawara and S. Yoshida, J. Phys. Soc. Japan 24, 1399 (1968).

6. W. E. Wallace, R. S. Craig, A. Thompson, C. Deenadas, M. Dixon, M. Aoyagi and N. Marzouk, Colloquium of CNRS, Paris and Grenoble, May, 1969, to appear.

7. H. J. van Daal and K. H. J. Buschow, Solid State Comm. 7, 217 (1969).

8. K. R. Lea, M. J. M. Leask and W. P. Wolf, J. Phys. Chem. Solids 23, 1381 (1962).

9. T. van Peski-Tinbergen and A. J. Dekker, Physica 29, 917 (1963).

10. R. W. Hill and J. M. Machado da Silva, Phys. Letters 30A, 13 (1969).

11. J. H. N. van Vucht and K. H. J. Buschow, J. Less-Common Metals 10, 98 (1965).

12. K. H. Mader and W. M. Swift, J. Phys. Chem. Solids 29, 1759 (1968).

Chemistry and Physics of Lower Valence States
of Lanthanides in Ionic Crystals

By

Francis K. Fong

Department of Chemistry, Purdue University,
LaFayette, Indiana

ABSTRACT

Techniques of the preparation of divalent and monovalent rare earths in ionic
host crystals are described. Reduction of trivalent rare earths (R. E. $^{3+}$) to
the divalent state in alkali earth halides by gamma radiation leads to the
production of unstable defect complexes, which upon heating, give rise to
multipeak thermoluminescent glo curves. An analysis of these glo curves
reveals that the oxidation of the divalent ion occurs through thermoexcitation
of an f electron to the d band. Reduction of R. E. $^{3+}$ through additive treatment
or solid state electrolysis gives rise to R. E. $^{2+}$ ions that are optically and
thermally stable, but otherwise identical in spectroscopic properties. The
reduction of R. E. $^{2+}$ to the monovalent state in alkali halides yields unexpected
results; while Sm^{1+} ions in KCl obtained by gamma radiation give rise to
broad-band optical spectra which have been identified as $4f^66S^1 \rightarrow 4f^56S^2$
transitions, those obtained through pressure-additive treatment with liquid K
give rise to narrow lines, 4. 2° K spectra which are most likely of d → f
origin. Determination of symmetry of the rare-earth ion sites through
Zeeman and anisotropy fluorescence spectroscopy is described in connection
with the numerous solid state chemical transformations of the rare-earth ions.

STUDIES OF THE DIVALENT OXIDES OF THE RARE EARTHS

by

Gregory J. McCarthy, William B. White and Rustum Roy

Materials Research Laboratory

The Pennsylvania State University

University Park, Pennsylvania 16802

Abstract

The stability of divalent compounds of the rare earths are examined in relation to the crystal chemical parameters of field strength and electronegativity. Europium compounds of AX stoichiometry form over the full range of electronegativity but oxides and fluorides of Sm^{++} and Yb^{++} are destabilized. Ternary compounds of Eu^{++} form over the full range of field strength and electronegativity difference. Divalent samarium and ytterbium are stabilized only by covalently bonded anions of high field strength and **low** electronegativity difference.

Introduction

The rare earth elements which have the best documented examples of

the divalent oxidation state in compounds are europium, samarium, and

ytterbium. Each forms divalent halides, sulfides, selenides, tellurides,

sulfates, and carbonates (1). Silicates of each have also been reported

(2). There are many binary and ternary oxides of divalent europium (3).

During the last few years, however, several investigators (4,5) have

questioned the existence of the lower oxides of samarium and ytterbium

as stable solid phases. In our studies of the ternary oxide systems

R.E.-Ti-O (6,7,8) we found five divalent europium titanates but no

analogous divalent samarium or ytterbium titanates. In (8) we proposed

-366-

that no ternary oxides* containing divalent samarium could be prepared. In this report we describe several other attempts to prepare divalent samarium and ytterbium oxides and examine the parameters which might explain why these oxides cannot be prepared.

Search for Lower Oxides of Sm and Yb

The method described by Shafer (3) for the preparation of EuO was employed in an attempt to prepare SmO and YbO. It involves the reduction of the sesquioxide by the metal according to the reaction:

$$RE + RE_2O_3 \rightarrow 3REO .$$
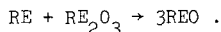
A large excess of metal was added to allow for some oxidation and hydration of the metal during handling. Pressed pellets of this mixture were placed in a tantalum capsule inside a silica tube and opened to vacuum of 10^{-2} torr. The temperature was slowly raised to $800° - 1000°C$, depending on the melting point of the rare earth, and held there for 12 hours. The temperature was then raised to $1200° - 1300°C$ and the pressure lowered to 10^{-4} torr in order to vaporize off the excess metal. EuO was readily prepared, but the products from the attempted SmO and YbO preparations were grey-white and gave X-ray powder patterns of B-type Sm_2O_3 and C-type Yb_2O_3 respectively. Thus very little or no reduction had taken place. The reaction listed above therefore represents a metastable

---

*In calling a ternary compound an oxide we mean not only that it contains oxygen as one of its components but also that the bonding throughout is predominantly ionic. Thus $SmTiO_3$ is an oxide and $SmSO_4$ is a sulfate.

-367-

equilibrium at the temperature of these experiments. The oxygen fugacity in the system is extremely low.

R. Valletta (9) has described another unsuccessful attempt to prepare SmO. He heated pellets of a stoichiometric mixture of Sm metal and Sm_2O_3 at 1000° - 1100°C in a tantalum crucible sealed by arc welding. Only Sm_2O_3 and Sm metal were found in the products.

The Silicates of Divalent Sm and Yb

Shafer (3) and Bondar, Toropov and Koroleva (2,10) have described the preparation of silicates of divalent europium. Bondar et al.(2,10) also claimed to have prepared silicates of divalent ytterbium and samarium. Since we had been unable to prepare any other single or mixed oxides of divalent samarium or ytterbium, there was some doubt that the silicates could be prepared. Therefore, the silicate preparation as described by these authors was repeated. A single composition $(RESiO_3)$ for samarium and ytterbium silicate was chosen for study.

Finely pulverized silica gel and sesquioxide in the molar ratio 1:2 were ground in an agate mortar, pressed into pellets and placed in a tungsten crucible. The crucible was heated at 1300°C in a vertical tube resistance furnace, through which high-purity grade hydrogen was flowing. The heatings took place for a total of five days with three intermediate coolings and regrindings. In order to check that the experiment was operating as expected, a pellet of 1:2 molar mixture of Eu_2O_3 and SiO_2 was heated in the hydrogen along with the $Sm_2O_3 \cdot 2SiO_2$ and $Yb_2O_3 \cdot 2SiO_2$ pellets. The pellets were quenched while they were still in the hydrogen atmosphere by withdrawing them to a cold part of the furnace.

-368-

Divalent europium silicate was formed as expected, but the products of the samarium and ytterbium mixtures were known trivalent silicates $Sm_4(SiO_4)_3$ and $Yb_2Si_2O_7$. The stoichiometric silicate $Sm_2Si_2O_7$ was not stable at 1300°C and dissociated into $SiO_2 + Sm_4(SiO_4)_3$. The samarium mixture pellet showed no hint of reduction, but the grey color of the ytterbium mixture pellet indicated some slight reduction.

It is possible that the conditions of the experiment of Bondar et al. re more reducing than these conditions just described, but this seems unlikely due to the care that was taken to keep a tight, clean system. We therefore doubt that the silicates described by Bondar et al. are stable phases at the temperatures given.

Stability of Halides and Chalcogenides

Divalent halides and chalcogenides of samarium, europium and ytterbium can be prepared with relative ease (1). Two exceptions are the difluorides of samarium and ytterbium. These tend to contain considerable trifluoride. In a recent study, Asprey, Ellinger and Staritzky (11) found that the compositions $SmF_{2.29}$ and $YbF_{2.24}$ were the limiting concentrations of difluoride.

Electronegativity is a measure of an atom's ability to attract electrons. The electronegativity of an anion could affect whether an associated cation would be divalent or would lose an additional electron and become trivalent. In Table I are listed the electronegativities of oxygen, the halides and chalcogenides.

Table I

Electronegativities of Some Anions*

O	F	Cl	Br	I	S	Se	Te
3.5	4.0	3.0	2.8	2.5	2.5	2.4	2.1

*From Pauling (13)

Oxygen and fluorine, the two anions with which difficulty is encoun-
tered in preparing divalent samarium and ytterbium compounds, have the
highest electronegativity. That the difluorides and not the monoxides
of these two elements can be prepared may be due to a greater stabili-
zation of the divalent cations by the fluorite structure than by the
rocksalt (SmO, YbO) structure.

Ternary Compounds of the Divalent Rare Earths

Shafer (3) has shown that many ternary compounds may be prepared
with divalent europium as one of the cations. There are also several
well characterized ternary compounds containing divalent ytterbium and
samarium: carbonates, phosphates and sulfates (1,11). Yet in earlier
studies we were unable to prepare divalent samarium or ytterbium titan-
ates. The determining factor appears to be the degree of anisodesmicity
(nonhomogeneity) of the bonding in these compounds.

We have made two attempts at rating "anion radicals" (sulfates,
silicates, titanates, etc.) according to the degree of anisodesmicity of
the bonding when these "radicals" form ternary compounds with the dival-
ent rare earths. One scale starts with ionic bonding and adds covalent

character to the radical according to its field strength. This para-
meter is defined by the equation $F.S. = Z/A^2$ where Z is the charge of
the cation and A is the sum of the radii of the cation and oxygen (12).
A larger field strength is a measure of a greater degree of covalency
in the radical since small, highly charged ions polarize oxygen more
effectively and thus increase the covalent character of the bond. (See
"Fajans' Rules", 1). The second rating system starts with pure covalent
bonding and adds ionic character by considering the electronegativity
differences between the two atoms in the radical (13). The larger the
difference in electronegativity, the greater the tendency of the elec-
trons to associate with one atom, and thus the greater the ionic charac-
ter. Table II lists a number of common oxygen radicals in order of
decreasing covalency. This is proportional to the degree of anisodesmi-
city when the radicals are in compounds with divalent samarium, europium
and ytterbium. There is relatively good agreement between the two cri-
teria. The radicals at the top of the table have a distinct identity
as molecules while those near the bottom when in compounds have nearly
pure ionic bonding.

Divalent europium compounds are known to form with virtually all
these radicals. However, only when the radicals are quite covalent do
we find divalent samarium and ytterbium compounds. In very qualitative
terms we might say that the tendency of oxygen to "rob" samarium of its
third electron is lessened because the oxygen is so "tied-up" with the
covalently bonded radical.

If we were to predict where to look for other divalent samarium and
ytterbium compounds, the molybdates and tungstates might be a good

Table II

Stability of Divalent Rare Earth Salts According to

Covalency of Anion

Anion	Field Strength	Electronegativity Difference	Eu^{2+}	Yb^{2+} or Sm^{2+}
Sulfate	2.29	1.0	Yes	Yes
Carbonate	1.83	1.0	Yes	Yes
Phosphate	1.79	1.4	Yes	Yes
Molybdate	1.60	1.4	?	?
Tungstate	1.60	1.4	?	?
Vanadate	1.37	1.7	?	?
Silicate	1.32	1.7	Yes	No
Tantalate	1.25	2.1	?	?
Niobate	1.24	1.9	?	?
Germanate	1.23	1.8	?	?
Titanate	1.00	1.9	Yes	No
Aluminate	0.90	2.0	Yes	?
Zirconate	0.88	2.1	Yes	?

possibility. The F.S. and Δe values for these radicals are not too far

removed from those of the phosphate, sulfate and carbonate. However,

the availability of lower oxidation states in these elements complicates

the problem. The energy required to reduce hexavalent molybdenum (or

tungsten) to a lower oxidation state could probably be easily supplied

by samarium or ytterbium oxidizing from the divalent to the trivalent

state. That is, the valences $[Mo^{6+} + Sm^{2+}]$ in a ternary compound could

well be unstable with respect to $[Mo^{4+} + Sm^{3+}]$. Silica has no readily

available lower valences and silicate occupies an intermediate position, and thus the existence of divalent samarium and ytterbium silicates cannot be ruled out by these criteria. Titanate, with which no divalent samarium or ytterbium compounds could be formed, falls near the bottom of the list.

Acknowledgments

References

1. F.A. COTTON and G. WILKINSON, "Advanced Inorganic Chemistry," Ch.31, Interscience, New York (1962).

2. I.A. BONDAR, N.A. TOROPOV, and L.N. KOROLEVA, Izves. Akad. Nauk. SSSR, Neorg. materialy 1, 561 (1965).

3. M.W. SHAFER, J. Appl. Phys. 36, 1145 (1965).

4. T.L. FELMLEE and L. EYRING, Inorg. Chem. 7, 660 (1968).

5. G. BRAUER, H. BAERNIGHAUSEN, and N. SCHULTZ, Z. Anorg. Allg. Chem. 356, 46 (1967).

6. G.J. McCARTHY, W.B. WHITE and R. ROY, J. Inorg. Nucl. Chem. 31, 329 (1969).

7. G.J. McCARTHY, W.B. WHITE and R. Roy, Mat. Res. Bull. 4, 251 (1969).

8. G.J. McCARTHY, W.B. WHITE and R. ROY, Inorg. Chem. 8, 1236 (1969).

9. R. VALLETTA (Private communication).

10. I.A. BONDAR, N.A. TOROPOV, and L.N. KOROLEVA, Izves. Akad. Nauk. SSSR, Neorg. Materialy 3, 2034 (1967).

11. B. ASPREY, F.H. ELLINGER and E. STARITZKY, Proc. Third Rare Earth
        Research Conference, Clearwater, Florida, April 21-24, pp 11-20
        (1963).

12. A. DIETZEL, Z. Electrochem. $\underline{48}$, 9 (1942).

13. L. PAULING, "The Nature of the Chemical Bond." Cornell University
        Press, Ithaca, New York (1960).

ON THE EXISTENCE OF DIVALENT YTTERBIUM

IN SOME OXIDE SYSTEMS

J.C. ACHARD, O. de POUS

Laboratoire des Terres Rares du C.N.R.S.

92-BELLEVUE - FRANCE

ABSTRACT

No evidence has been found yet for the existence of the pure lower oxide YbO, and its existence without impurities has been questioned.

CaO has the same crystal structure and a lattice parameter very close to the one expected for YbO. Consequently, we tried to substitute Yb into a matrix of the f.c.c. CaO in order to stabilize Yb^{2+}. In fact, by heating mixtures of calcium metal and ytterbium sesquioxide including additions of ytterbium metal in some experiments we have found a f.c.c. phase. Its lattice parameter changes with the Yb concentration and is found to be in between the value for CaO and the one expected for YbO.

On the other hand, a f.c.c. phase with a lattice parameter equal to $4,875 \pm 0,003$ Å was also obtained by careful oxidation of the metal ytterbium.

The valence of ytterbium in the f.c.c. phase of the Yb-Ca-O system is discussed, and a comparison is made with other ternary systems.

AN INVESTIGATION OF THE Eu-Eu$_2$O$_3$ SYSTEM
AND THE EQUILIBRIA BETWEEN THE EUROPIUM OXIDES
AND THE Eu-Pt SYSTEM, WITH RELATED STUDIES
OF THE Sm-Sm$_2$O$_3$ AND THE Yb-Yb$_2$O$_3$ SYSTEMS*

R. G. Bedford and E. Catalano

Lawrence Radiation Laboratory, University of California

Livermore, California 94550

ABSTRACT

The binary system Eu-Eu$_2$O$_3$ has been examined in detail over the composition range EuO to Eu$_2$O$_3$ at 1500°C. Only one intermediate oxide phase, Eu$_3$O$_4$, was found. Both EuO and Eu$_3$O$_4$ exhibit very narrow composition limits, while the monoclinic sesquioxide is stable over the composition range EuO$_{1.46}$ to EuO$_{1.50}$ at 1500°C.

The melting points found for the three phases were 1900°C for EuO, 2000°C for Eu$_3$O$_4$ and 2300°C for Eu$_2$O$_3$.

Europium was quantitatively extracted from EuO by reaction with Pt in sealed capsules at 1500°C, which resulted in the formation of an intermetallic phase plus a higher oxide of Eu. The most Eu-rich intermetallic phase found in these studies, EuPt$_{2+x}$, has the MgCu$_2$ structure and is stable over the composition range EuPt$_{2.0}$ to EuPt$_{2.8}$ at 1500°C. There may be one additional phase besides the previously reported EuPt$_5^*$ at Pt-Eu ratios above 3:1.

No crystalline phases other than the sesquioxides were found in the Sm-Sm$_2$O$_3$ or the Yb-Yb$_2$O$_3$ systems.

INTRODUCTION

Brauer[1] has reviewed the structural and solid-state chemistry of the lanthanon oxides, and Westrum[2] has reviewed the thermodynamics and magnetic properties.

When this work began, the Eu-Eu$_2$O$_3$ system had not been clearly defined. Although the oxides Eu$_2$O$_3$, Eu$_3$O$_4$, and EuO had been reported and their structures described, the possibility of other intermediate phases in the system still remained.[3-7] It has since been established, however, that no other phases exist in this system.[8]

Significant ranges of stoichiometry have been reported for EuO[9] and Eu_2O_3 (cubic).[10] The results reported here confirm the findings of Ref. 8 and present new data on the composition ranges of these oxides.

Optical and x-ray examination of samples prepared by metathetical synthesis in sealed containers indicated that EuO, Eu_3O_4 and Eu_2O_3 were the only stable oxides in the $Eu-Eu_2O_3$ system. However, there had been some uncertainty about this conclusion due to interference to Ta contamination in some of our early experiments. An investigation involving controlled quantitative extraction of Eu from EuO single crystals was devised which unambiguously established the number of phases present in the range $EuO-Eu_2O_3$ and provided data on the stoichiometries of these phases. Europium was removed from EuO through the vapor phase by equilibration with Pt in sealed containers at 1500°C. These experiments also provided new information on the Eu-Pt system.

It seemed appropriate to apply the techniques and facilities used in studying the reduced europium oxides to investigate the possible stability of divalent or other reduced oxidation states of Sm or Yb in oxide systems. SmO, Sm_2O and YbO had all been reported.[11-15] We were interested in characterizing these phases if possible and in comparing the Sa, Eu, and Yb systems. Brauer et al.[16] have recently published results that showed reduced oxidation states of Sm and Yb could not be prepared in binary oxides at temperatures up to 800°C and that divalent Sm could not be formed even in solution with CaO. Femlee and Eyring[17] have reported that the substances previously identified as Sm_2O and SmO were actually SmH_2 and $SmN_{1-x}O_x$. McCarthy and co-workers[18] have also reported that divalent Sm cannot be formed in titanates and is probably not stable in any oxide system. Our results which include observations from reactions carried out at temperatures up to 2100°C confirm that in the binary oxide systems, reducing conditions lead to no new phases in which Sm or Yb are in reduced oxidation states. Reduced sesquioxides Sm_2O_{3-x} and Yb_2O_{3-x} were found. Similar reduced lanthanon sesquioxides have been reported and the oxygen deficiencies shown to be due to vacancies in the oxygen

sublattice.[19] Our measurements show that the oxygen deficiency in Yb_2O_{3-x} is approximately the same as that reported for the other reduced lanthanon sesquioxides.

MELTING OF Eu_2O_3

Eu_2O_3 was melted in both tungsten and iridium crucibles. We estimate the melting point to be in the range 2250 to 2350°C.

Our observations of the melting of Eu_2O_3 were not precise enough to confirm either the value of 2240 ± 10°C given by Schneider[20] or of 2330°C given by Foex.[21] Schneider determined the melting point in air using an iridium container. Foex's measurement was also in air, using a solar furnace.

Except for the presence of Eu_3O_4 inclusions, the optical properties and x-ray diffraction results for the melted Eu_2O_3 were identical to those for the starting material. The x-ray powder patterns corresponded to the ASTM data.[22]

SYNTHESIS AND MELTING OF EuO

EuO was prepared by reducing Eu_2O_3 with an excess of Eu metal in sealed, evacuated Mo crucibles. We obtained single crystals of approximately 1 cm^3.

We estimate the melting point of EuO to be 1900°C ± 50, in agreement with the value suggested by Shafer.[9] However, we believe that as yet there is not enough evidence to conclude that EuO melts peritectically, as Guerci and Shafer[23] suggest, rather than congruently.

X-ray powder diffraction analysis of this material gives a lattice parameter, a = 5.14_4 ± 0.005 Å for the NaCl-type structure, in agreement with prior reports.

EuO crystals are dark reddish-violet in color and are opaque to visible light, even in thin sections with the most intense illumination available in our microscope (a mercury discharge lamp).

SYNTHESIS AND MELTING OF Eu_3O_4

Eu_3O_4 was prepared by heating equimolar mixtures of EuO and Eu_2O_3 to 2050°C in a sealed Ir container and cooling slowly. The product had completely melted. It consisted of relatively large Eu_3O_4 grains (~1 mm^3) with traces of Eu_2O_3 concentrated at the grain

boundaries. Although there was no visible sign of reaction between the sample and the container, there may have been some loss of Eu by vaporization, yielding a product slightly more O-rich than the starting material. Part of the product was ground and reheated to 1920°C in a sealed Ir capsule; no sign of melting was observed. Reheating in a sealed Mo container for eight hours at 1625°C had no detectable effect on the sample. These observations indicate that the Eu_2O_3 resulted from a slight excess of O in the sample rather than from disproportion by a peritectic reaction.

We estimate the melting point of Eu_3O_4 to be 2000 ± 100°C. Part of the uncertainty in this figure is because in some of the heatings the shielding was deliberately rearranged to establish a large temperature gradient (~80° from top to bottom) to facilitate crystal growth. Results from preparations in Ta indicated the possibility of peritectic melting. The experiments in Ir and Mo do not support this conclusion, but neither do they provide direct contradictory evidence.

INVESTIGATION OF OTHER COMPOSITIONS
BETWEEN EuO AND Eu_2O_3

Several compositions intermediate between EuO and Eu_2O_3 were heated to 2000°C in sealed Ir or Mo containers in conjunction with the preparation and study of Eu_3O_4. The x-ray powder diffraction patterns of Eu_3O_4 were identical within our precision for samples prepared with either excess O or excess Eu, as were the qualitative optical properties. The x-ray powder diffraction patterns agreed with the results reported by Bärnighausen and Brauer[5] and Rau[6,24] for Eu_3O_4 (orthorhombic). The existence of Eu_3O_4 in the presence of either EuO or Eu_2O_3 and the failure to observe any other phases is in agreement with other recent reports on this system.[6-8]

The presence of Eu_2O_3 in samples very close to the ideal composition for Eu_3O_4 and the concentration of the Eu_2O_3 in the grain boundaries of Eu_3O_4 preparations indicates that the deviation from stoichiometry is very small on the O-rich side. The appearance of the crystallized samples indicated that the stable composition range for Eu_3O_4 is probably narrow even near the melting point. Even in the rapidly cooled samples, the Eu_3O_4 crystals did not appear to contain inclusions of EuO or Eu_2O_3.

STUDY OF THE EuO-Eu_2O_3 BY REMOVAL OF Eu BY
Pt FROM EuO AT HIGH TEMPERATURES

To confirm the absence of compounds other than Eu_3O_4 between EuO and Eu_2O_3 as well as to investigate in more detail the stoichiometry of these three oxides, we studied the distribution of Eu between the oxide phases and intermetallic phases in the Eu-Pt system at 1500°C.

EuO single crystals were sealed by EBW into Mo capsules, along with pieces of chemically pure Pt wire. The Pt wire was suspended from Mo wire holders to avoid physical contact between the Pt and the oxide. Subsequently, several runs were made with the configuration shown in Fig. 1, where a tungsten-lined Mo cup was used instead of the Mo wire to contain the Pt. The sealed capsules were heated at 1500°C for about five hours and then cooled quickly.

The product oxide phases were recovered intact and had the same size and shape as the starting EuO crystals. There was no evidence of vapor transport of oxide within the capsules nor of mechanical losses of oxide in transfers or recovery. After weighing and examination with a low-power microscope, the oxide products were cleaved and examined further. The two-phase oxide products consisted of a central core of the lower oxidation state phase surrounded by an outer shell of the higher oxidation state phase. The boundaries were very sharp, with no gradation in properties detectable. Samples were taken from the inner and outer phases for x-ray diffraction and examination with the polarizing microscope. The x-ray and optical properties of the products of these experiments were identical to those described above for EuO, Eu_3O_4 and Eu_2O_3. Where the Pt-to-EuO ratio was such that more than one-fourth of the Eu was extracted from the oxide, the product was a homogeneous, dense, polycrystalline core of Eu_3O_4 with an outer layer of Eu_2O_3. However, the outer layers were not pure Eu_2O_3. Small red crystals of Eu_3O_4 were uniformly dispersed in these layers. When enough Pt was added to give an oxide product with an O-to-Eu ratio of 1.46 or more, the Eu_3O_4 core was absent and the product was Eu_2O_3 containing small crystals of Eu_3O_4 uniformly dispersed throughout.

The results showed unambiguously that the only stable oxides in this system at 1500°C are the three mentioned above.

The metallic phase products were weighed and examined with a microscope and by x-ray diffraction. For runs in which the Pt-to-Eu ratio of the product was 3.45:1 or less, the surfaces of the products were very rough, and relatively large (0.05-mm) plate-like crystals had developed. There was no evidence of liquid formation and the Pt-phase—Mo or W interfaces were sharp, with the interaction confined to very small regions at the points of contact between the sample and holder. The samples with Pt:Eu of 3.69 and 5.21 had completely melted. Samples with higher Pt-to-Eu ratios had only partly melted, and retained the basic form of the original wire, smooth with coils stuck together by the crystallized liquid phase. The liquid phase is probably due to a binary eutectic reaction below 1500°C between Pt and the Pt-rich intermetallic compound.

X-ray powder diffraction analysis of the Pt-phase products gave the following information: The most Eu-rich phase formed in these experiments has the fcc $MgCu_2$ structure. The lattice parameter reported for $EuPt_2$ by Elliott[25] is 7.731 Å. The lattice parameter of $EuPt_{2+x}$ decreases linearly with increasing Pt concentration to a value of 7.62_0 Å for $EuPt_{2.8}$. Compositions with Pt:Eu ratios of 3.17 and 3.45 appeared to be two-phase mixtures of $EuPt_{2.8}$ and another phase whose structure and stoichiometry are undetermined. Powder diagrams of the products with Pt:Eu ratios of 3.69 and 5.21 showed identical patterns of another unidentified phase plus some very weak Pt lines in the 5.21 pattern. The structure or stoichiometry of the phase producing these patterns has not been determined in this study either, but it is probably $EuPt_5$ which has been prepared by Bronger.[26] Of the possible candidates for the phase between $EuPt_{2.8}$ and $EuPt_{3.69}$, Eu_2Pt_7 seems to be the most reasonable, and preliminary single-crystal results on specimens from the $EuPt_{3.45}$ sample appear to be consistent with one of the Ln_2Ni_7 structure types.[27-29] Results from single-crystal studies of material from the samples with Pt:Eu ratios of 3.69 and 17.29 were consistent with single-crystal results for $EuPt_5$

reported by Bronger.[26] Although we do not have firm evidence, we believe that the reason the $EuPt_{3.69}$ sample appeared to be monophasic is that the "$EuPt_5$" phase is stable over a wide range of stoichiometries extending from the ideal Pt:Eu ratio of 5:1 to compositions which are substantially Pt-deficient, and that the concentration of Eu_2Pt_7 in that sample was too low to be observed by x-ray diffraction analysis. Products with Pt:Eu ratios of 9:1 and 17:1 contained mixtures of $EuPt_5$ and Pt. The Pt lines in these patterns were identical to those for pure Pt, with no detectable change in lattice parameter. The d-spacings taken from patterns from the Pt:Eu = 3.45 and 5.21 samples are listed in Table I.

The quantitative results of the equilibrations are analysed by plotting the O-to-Eu ratios for the oxide phases versus the Pt-to-Eu ratios for the equilibrium metallic phases. The lines are drawn using the information from optical and structural (x-ray) examinations of the samples as well as the composition data. The product compositions were calculated using the assumption that the weight loss of the oxide phase resulted only from Eu loss, and that all of this Eu was transferred to the Pt phase. For several of these runs, the composition of the oxide-phase product was determined by igniting the sample in air to constant weight (about 60 hr at 1200 to 1300°C) and measuring the weight gained on oxidizing to Eu_2O_3.

A limit to the range of stoichiometry for single-phase EuO at 1500°C can be established from the run with the lowest Pt-to-EuO ratio. The starting EuO crystals were prepared in excess Eu, as described above. The run with Pt:EuO = 0.02 gave a product with a uniform layer of Eu_3O_4 covering the EuO crystal. The calculated overall composition of the oxide product, assuming a starting composition of $EuO_{1.000}$, is $EuO_{1.010}$. Therefore, the range of stoichiometry of EuO at 1500°C is <0.01. This result is contradictory to the findings of Shafer.[9] The lattice parameter of EuO in the equilibration products which were O-rich was 5.14_4, identical to the parameter for Eu-rich products. The color and appearance in bulk and under the microscope were also the same for hypo- and hyper-stoichiometric EuO.

The absence of dispersed second-phase precipitates in the bulk Eu_3O_4 after quenching from equilibrations at 1500°C either with EuO or with O-deficient Eu_2O_{3-x} indicates that the composition range of Eu_3O_4 does not change significantly as temperatures are decreased from 1500°C to lower temperatures where diffusion rates are too slow to show disproportionation. As with EuO, the hypo- and hyper-stoichiometric materials have identical x-ray and optical properties. We conclude that at 1500°C the range of stoichiometry in Eu_3O_4 is very small. A ternary diagram for part of the system Pt-Eu_2O_3-Eu at 1500°C can be constructed using the above information.

THE Sm-Sm_2O_3 AND Yb-Yb_2O_3 SYSTEMS

Attempts were made to prepare Sm_2O, SmO, Yb_2O, YbO and other reduced oxides of Sm and Yb. Samples of Sm + Sm_2O_3 were heated to 2100°C in sealed Mo capsules and cooled quickly. All samples had been completely melted and cooled to a uniformly dark gray product. X-ray powder diffraction and microscopic analysis showed that the products in all cases were Sm_2O_3 with finely dispersed Sm metal. In order to check for the possible existence of Sm compounds stable only at lower temperatures, the samples were again sealed in Mo capsules and heated for eight hr at 1500°C. The products of this run were identical to the starting material.

The results indicate that at temperatures above 2100°C, the system is one liquid phase for compositions from Sm metal to ones with O:Sm ratios of 1.33 or higher and that no crystalline oxide of Sm other than Sm_2O_3 exists.

The Yb + Yb_2O_3 samples were heated for several hours at 1800°C in sealed Mo capsules. The composition Yb_2O had completely melted and appeared to consist of a mixture of dark red crystals and excess metal. With the YbO and Yb_3O_4 compositions, only the metal phase melted. In these samples, the oxide sintered and consisted of very dark red crystals about 0.01 mm across.

Examination with the polarizing microscope showed the material to contain a mixture of dark red crystals and colorless crystals, in addition to the excess metal. There was no birefringence. X-ray powder diffraction analysis showed only Yb_2O_3(bcc) and Yb(fcc).

The excess metal was dissolved from one sample with HCℓ and the composition of the oxide phase was determined by ignition in air at 1200°C, as described by Miller and Daane.[19] The composition of the reduced sesquioxide was $YbO_{1.495}$ which agrees well with the

compositions of reduced sesquioxides of *other rare-earth elements* reported by Miller and Daane.[19]

Since our products were obviously two-phase at room temperature, the reduced sesquioxide apparently disproportionated into Yb_2O_3 + Yb as it cooled from 1800°C. We have assumed that the metal from this reaction is dispersed within the crystalline material and is not dissolved when the bulk excess metal is removed. If some of this metal was lost in the HCℓ treatment, then the oxygen deficiency in Yb_2O_{3-x} at 1800°C is somewhat greater than the value we have reported.

Another sample of composition YbO was heated to 1450°C for three hours and cooled slowly (three hours to 1000°C). The reaction temperature for this sample was in the range used by Achard[15] for preparations of YbO. The product was a sintered pellet of oxide similar to the previous samples, but the excess metal was concentrated at the bottom of the capsule rather than dispersed through the oxide pellet.

We conclude that Yb_2O_3 is the only stable oxide of Yb and that the material Achard[15] reported as YbO was probably a solid solution of oxygen in YbN similar to the Sm oxide-nitride which had been confused with SmO.[17] Since Achard's preparations were made by reducing the sesquioxide with carbon, an oxide-carbide is also a possibility.

CONCLUSIONS

We have established that EuO and Eu_3O_4 are the only stable reduced oxides of Eu and that they both have very narrow ranges of stoichiometry. We have also shown that O-deficient Eu_2O_{3-x} is stable to $Eu_2O_{2.92}$ at 1500°C. In the Eu-Pt system, the range of stoichiometry for the fcc (MgCu$_2$) phase $EuPt_{2+x}$ has been determined to be $EuPt_2$ - $EuPt_{2.8}$ at 1500°C and two additional intermetallic phases were observed.

In contrast to the fluorides for which there is rather close correspondence between the Sm, Eu, and Yb systems,[30] there are no stable oxides of Sm or Yb corresponding to EuO or Eu_3O_4. The factors that lead to the marked differences between the Eu oxides and the other lanthanon element oxide systems, in contrast to the similarities between the fluoride systems, are still not understood.

ACKNOWLEDGMENTS

us to pursue the equilibration studies and predicted for us in 1965, before any Sm or Eu intermetallic compounds with Pt or Ir had to our knowledge been reported, the stability and structures of LnM_2 and LnM_5 for Ln = Sm and Eu and M = Pt and Ir. The time and effort of the people who reviewed early versions of the manuscript are appreciated. The comments of Dr. R. Taylor, Dr. L. Himmel and Dr. A. W. Searcy were particularly helpful.

REFERENCES

1. G. Brauer, Progress in the Science and Technology of the Rare Earths, L. Eyring, ed. (Pergamon Press, 1964) vol. I, pp. 152-165; ibid. vol. II, pp. 312-339, 1966; ibid. vol. III, pp. 434-459, 1968.
2. E. F. Westrum, ibid. vol. I, pp. 310-349, 1964; ibid. vol. II, pp. 35-89, 1966; ibid. vol. III, pp. 459-514, 1968.
3. V. M. Goldschmidt, F. Ulrich, and T. Barth, Skrifter Norske Videnskaps-Akad., Oslo, I, Mat.-Naturv, Kl., No. 5, 5 (1925). [Chem. Abs. 19, 2764 (1926).]
4. R. S. Roth and S. J. Schneider, J. Res. Natl. Bur. Std. 64A, 309 (1960).
5. H. Bärnighausen and G. Brauer, Acta Cryst. 15, 1059 (1962).
6. R. C. Rau, Rare Earth Research II, K. S. Vorres, ed. (Gordon and Breach, New York, 1964), pp. 117-134.
7. G. Garton and D. A. Hukin, Rare Earth Research II, K. S. Vorres, ed., ibid., pp. 3-20.
8. H. Bärnighausen, J. Prakt. Chem. 34, 1 (1966).
9. M. W. Shafer, J. Appl. Phys. 36, 1145 (1965).
10. M. F. Barrett and T. I. Barry, J. Inorg. Nucl. Chem. 27, 1483 (1965).
11. F. H. Ellinger and W. H. Zachariasen, J. Am. Chem. Soc. 75, 5650 (1953).
12. H. A. Eick, N. C. Baenziger, and L. Eyring, J. Am. Chem. Soc. 78, 5147 (1956).
13. J. O. Achard, Compt. Rend. 245, 1064 (1957).
14. T. L. Felmlee and L. Eyring, Proc. Fifth Rare Earth Res. Conf., Ames, Iowa, 1965, pp. 13-24.
15. J. C. Achard and G. Tsoucaris, Compt. Rend. 246, 285 (1958).
16. G. Brauer, H. Bärnighausen, and N. Schultz, Z. Anorg. Allgm. Chemie 356, 46 (1967).
17. T. L. Felmlee and L. Eyring, Inorg. Chem. 7, 660 (1968).
18. G. J. McCarthy, W. B. White and R. Roy, Inorg. Chem. 8, 1236 (1969).
19. A. E. Miller and A. H. Daane, J. Inorg. Nucl. Chem. 27, 1955 (1965).
20. S. J. Schneider, J. Res. Natl. Bur. Std. 65A, 429 (1961).
21. M. Foex, Compt. Rend. 260, 6389 (1965).
22. X-Ray Powder Data File 12-384, P. W. Brindley, ed., ASTM, Philadelphia, Pa. (1962).
23. C. F. Guerci and M. W. Shafer, J. Appl. Phys. 37, 1406 (1966).

24. R. C. Rau, Acta Cryst. 20, 716 (1966).
25. R. P. Elliott, Proc. Fourth Rare Earth Res. Conf., Phoenix, Ariz., 1964, pp. 215-245.
26. W. Bronger, J. Less-Common Metals 12, 63 (1967).
27. D. T. Cromer and A. C. Larson, Acta Cryst. 12, 855 (1959).
28. K. H. J. Buschow, J. Less-Common Metals 16, 45 (1968).
29. A. V. Virkar and A. Raman, J. Less-Common Metals 18, 59 (1969).
30. E. Catalano, R. G. Bedford, V. G. Silveira, and H. H. Wickman, J. Phys. Chem. Solids 30, 1613 (1969); and R. G. Bedford and E. Catalano, Phase Studies of Sm, Eu and Yb Fluorides, to be published.

Table I. d-Spacings for $EuPt_{3.45}$ and $EuPt_{5.21}$

Pt:Eu = 3.45			Pt:Eu = 5.21	
d	I/Io		d	I/Io
4.55	15		4.57	10
*4.40	10		*2.66	15
2.83	5		2.5	—
*2.69	10		2.42	—
2.53	5		2.26	65
2.40	—		2.19	100
2.31	60		2.14	—
*2.29	100		2.06	—
2.22	15		**1.96	—
*2.18	70		1.69	5
2.15	75			
1.95	10		1.53	—
*1.91	—			
*1.75	7		1.45	10
1.69	5		**1.38_5	5
1.58	—		1.32_5	10
*1.56	—		1.28_5	35
1.52	—		1.27	5
1.50	—		1.25_5	—
1.47	7		**1.18	—
1.46	35		**1.13_8	10
*1.43	10		1.10	15
1.42	—			
1.36	7			
*1.34	30			
1.30_5	20			
*1.28	15			
1.17_3	7			
1.14_5	40			

* Spacings corresponding to fcc $EuPt_{2.8}$.

** Spacings corresponding to Pt.
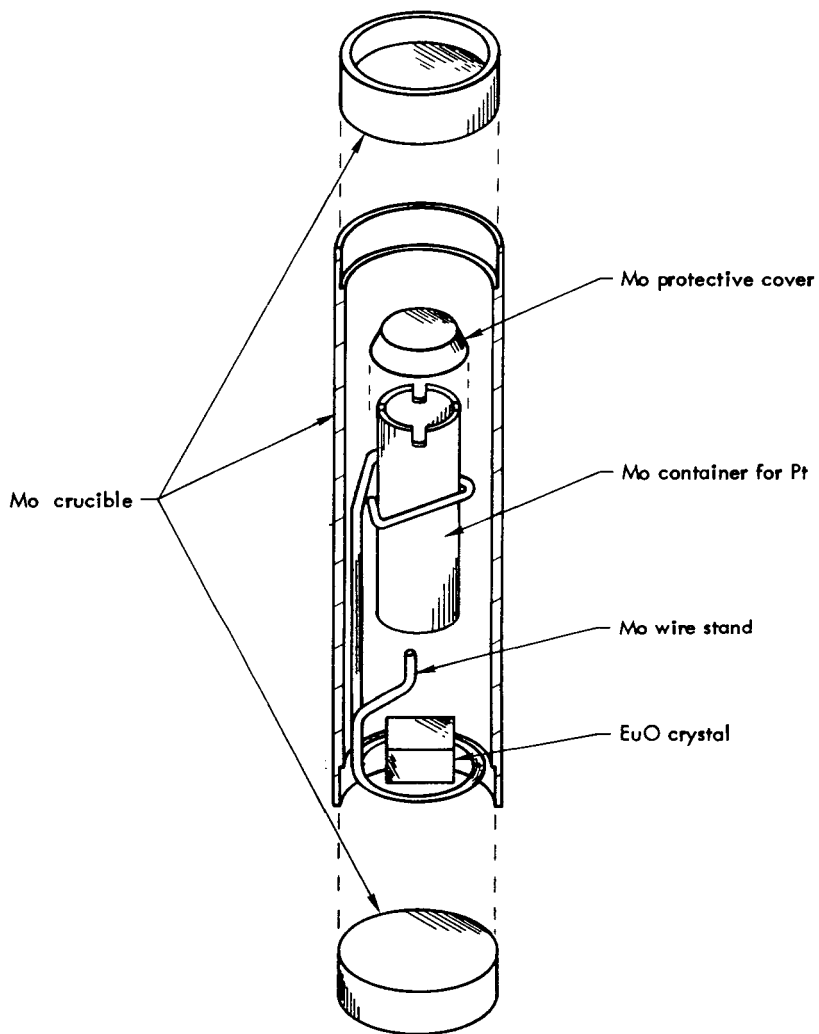
Fig. 1. Sample configuration for extraction of Eu from EuO by Pt.
The protective cover prevents Mo particles from falling into
the container when the capsule is opened. Early runs were
made with Pt wire hung directly on the Mo wire stand.

A STUDY OF THE BINARY SYSTEMS
SmF_2-SmF_3, EuF_2-EuF_3, AND YbF_2-YbF_3
AND THEIR EQUILIBRIA WITH CORRESPONDING Ln-Pt SYSTEMS[*]

R. G. Bedford and E. Catalano

Lawrence Radiation Laboratory, University of California

Livermore, California 94550

ABSTRACT

Phase relationships in the binary systems SmF_2-SmF_3, EuF_2-EuF_3 and YbF_2-YbF_3 have been investigated using differential thermal analysis, Debye-Scherrer x-ray analysis, observation of optical properties with a polarizing microscope, and by establishing equilibria in the ternary systems Pt-Ln-LnF_3. Tentative phase diagrams most consistent with the data are given.

For the three binary systems Pt-Ln with Ln = Sm, Eu, and Yb, some structural information and phase relationships were derived from x-ray powder diffraction data obtained on platinum-phase products of the Pt-Ln fluoride equilibrations.

INTRODUCTION

A number of systems exhibiting non-stoichiometric behavior based on fluorite-structure solid solutions with anion defects have been reported.[1-5] Such solutions are formed by dissolving a fluoride or an oxide of an altervalent cation in an appropriate difluoride or dioxide. A similar class of systems is produced by dissolving lanthanon trifluorides in lanthanon oxyfluorides.[6-9] At high temperatures, many of these systems include fluorite-structure solid solutions which extend from the ideal composition MX_2 to mixtures with up to 20% anion defects. At lower temperatures, the systems become more complex. Phases with ordered structures closely related to the fluorite structure become stable, and the cubic solid solutions become limited to compositions that do not deviate greatly from the ideal MX_2 composition.

The LnF_2-LnF_3 systems are uniquely simple examples of the general type described above. Systems involving LnF_3 or UF_3 dissolved in alkaline earth fluorides (interstitial anions) and Ln_2O_3 dissolved in ThO_2 (anion vacancies) are complicated by the presence of two kinds of cations. The M-O-F systems (interstitial anions) are complicated by the presence of two kinds of anions. In these systems, phase changes involve equilibration of three different elements. The necessary diffusion introduces kinetic problems which may make observation of the true equilibrium situation very difficult, if not impossible.[8] Interpretation of the three-element systems is complicated by the increased number of variables, as well as by the kinetic problems. The LnF_2-LnF_3 systems are among the simplest of this basic type, and so offer a most promising avenue to begin understanding the interactions involved. Even the non-cubic structures in these systems are closely related to the fluorite structure, and they retain nearly ideal cation sublattices. Phase changes in the LnF_2-LnF_3 systems are likely to require diffusion only for the anions. Changes in the cation sublattice can occur primarily by diffusionless rearrangements and charge transfers.

In this investigation we extend the previous x-ray and optical studies of the samarium and europium systems to include the ytterbium fluorides.[4] We have also applied the techniques of differential thermal analysis (DTA) and equilibration of reduced fluorides with platinum to derive enough information to present fairly complete phase diagrams for the three fluoride systems.

<div align="center">EXPERIMENTAL</div>

A. Preparation of Samples. Samples were prepared by sealing appropriate mixtures of lanthanon element metal or lanthanon difluoride with the corresponding lanthanon trifluoride in crucibles by electron beam welding (EBW) and heating to about 1600°C. Molybdenum crucibles were used for all compositions except the fluorine-rich Eu fluorides and the pure trifluorides. The latter were prepared in

platinum. The starting materials and other details of the preparations
and chemical analyses of the products are discussed in Ref. 4.

B. Differential Thermal Analysis. The differential thermal
analysis experiments were carried out in apparatus constructed in our
Laboratory for these studies. Two DTA systems were used, one for
operation in air and another for use with argon around the sample block.
The first system was used for samples in Pt containers. The reduced
fluorides react with Pt, so another system was constructed in order to
run these materials in Mo containers. It was necessary to seal the
samples in the DTA capsules by EBW to prevent composition changes
due to vaporization or reaction with the environment. Identical cap-
sules containing Al_2O_3 were used for references. Platinum versus
platinum—10% rhodium thermocouples were used for all temperature
and differential measurements. Nearly all of the data were taken at
heating and cooling rates of approximately 10°/min. To avoid frequent
furnace element replacement, we decreased the heating rates to about
6°/min at temperatures above 1400°C in the argon system. Tempera-
ture calibrations of the thermocouples were checked by running sam-
ples of optical-quality single-crystal CaF_2. The onset of melting for
CaF_2 was observed at 1392 ± 1°C in both the air and argon systems,
with an apparent melting range of 6°C in both systems.

C. Reactions of Divalent Fluorides with Platinum. The distri-
butions of lanthanon elements between a lanthanon fluoride and a
lanthanon-platinum intermetallic compound or solid solution were mea-
sured at about 1260°C for Sm, Eu, and Yb. Equilibrations were car-
ried out in the capsules shown in Fig. 1 of Ref. 10. Dense pieces of
polycrystalline difluoride were weighed and placed at the bottom of the
capsules. Appropriate weights of Pt wire were placed in the Mo cups
and weighed. After loading, the capsules were sealed by EBW in a
vacuum of about 10^{-5} torr and heated in an induction furnace at 1260°C
for 12 to 15 hours. They were cooled rapidly by turning off the power
and quenching with He gas. After equilibration, the capsules were
broken open and the two phases were recovered, weighed and exam-
ined by x-ray diffraction and optical microscopy. Because of the vola-
tility of the fluorides, significant vapor transport occurred inside the
capsules. Since it was impossible to achieve perfectly isothermal con-
ditions in the furnace a small gradient was established, the top being
hotter. This reduced the amount of fluoride distributed on the capsule
walls and lid and eliminated direct condensation on the cup which held
the platinum. In spite of the precautions taken, some of the fluorides
were found condensed in a finely divided state on the lower parts of the
capsules and in the interstices where the bottoms were welded on.
This made quantitative recovery of the fluorides impossible, so all
final compositions were based on weight gains of the Pt phases.

D. Crystallographic and Optical Examination. The bulk pieces
of the fluoride products retained the form of the original difluoride
samples. These were cleaned and examined with a microscope under

reflected light. Powdered samples of the fluoride products were suspended in immersion oil or Canada balsam and examined by transmitted light using a polarizing microscope. The Pt phases were examined at low power under reflected light to determine whether a liquid phase might have been present, and to estimate the extent of reaction with the container. Debye-Scherrer powder patterns were obtained using Cu K_α radiation with a Ni filter and Fe K_α radiation with a Mn filter.

RESULTS AND DISCUSSION

A. <u>X-ray and Optical Properties of Reduced Ytterbium Fluorides</u>. Results of the x-ray and optical examinations of the Yb fluorides were similar to those from examination of the Sm and Eu fluorides described in Ref. 4. Samples with compositions from $YbF_{2.0}$ to $YbF_{2.18}$ had the fcc fluorite structure with lattice parameters decreasing from 5.59_9 to 5.58_3 Å as the fluorine content increased. X-ray diffraction patterns from samples with compositions from $YbF_{2.2}$ to $YbF_{2.4}$ have not been resolved. Patterns from samples with fluorine contents greater than that of $YbF_{2.4}$ had lines corresponding to YbF_3 (orthorhombic), plus unidentified lines.

Material with F:Yb ratios of 2.0 and less was transparent, dark green, and non-birefringent. All samples had small brightly birefringent inclusions which looked something like bubbles. Samples with F:Yb ratios below 2.0 contained opaque inclusions, probably Yb metal. Samples prepared by synthesis in sealed containers at about 1600°C with compositions from $YbF_{2.0}$ to $YbF_{2.2}$ were non-birefringent with brightly birefringent inclusions, and changed in color from green to greenish yellow to greenish brown as the fluoride concentration increased. Samples in this composition range from the equilibration studies were identical to samples of like composition which had been prepared by heating to 1600°C, except that compositions between $YbF_{2.05}$ and $YbF_{2.1}$ contained a tan, moderately birefringent phase not seen in the samples cooled from above their melting point. Samples from the equilibrations of compositions near $YbF_{2.25}$ were yellow and brightly birefringent, appearing brownish gold under crossed polarizers, and they appeared to be completely homogeneous, without the

inclusions seen in the other materials. Samples with fluoride concentrations higher than $YbF_{2.25}$ were not obtained from the equilibration experiments. Directly synthesized samples of $YbF_{2.25}$ and $YbF_{2.30}$ appeared to be mixtures of a greenish yellow non-birefringent phase with bright birefringent inclusions and a yellowish brown brightly birefringent phase. $YbF_{2.35}$ was yellowish brown, brightly birefringent and contained inclusions of a different birefringent material. $YbF_{2.38}$ was yellow and non-birefringent with very few brightly birefringent inclusions. Samples in the composition range $YbF_{2.45}$ to $YbF_{2.9}$ were mixtures of the yellow non-birefringent material and colorless brightly birefringent material, YbF_3.

  B. Differential Thermal Analysis. All three lanthanon element fluoride systems examined here exhibited complex thermal behavior, having thermal effects indicating up to six different solid state reactions in addition to the melting effects. For example, Figs. 1 and 2 are direct tracings of thermograms for samples of $SmF_{2.40}$ and $YbF_{2.90}$.

  Part of the offset between peaks on the heating and cooling curves is due to heat transfer effects. The peak shapes are affected by these same effects. However, most of the samples showed substantial hysteresis due to supercooling, as illustrated in Fig. 2. Therefore, cooling curves were used only as an aid in resolving the number of different thermal effects contributing to the thermograms, and quantitative data were taken from heating curves. The beginning temperature for a thermal effect is taken as the temperature at which the differential signal deviates from the baseline, and the end of the effect is taken as the temperature at which the signal begins to drop back to the baseline.

  The information derived from the thermograms is shown as points plotted on the phase diagrams shown in Figs. 3-5. Open circles are used to indicate the beginning temperatures of thermal effects. Open triangles are used to indicate beginning temperatures for thermal effects due to multiple reactions not resolved in the heating curves. Crosses show the end of the effects. In the samarium fluoride system, no reaction has been attributed to the effects observed in the temperature range 900 to 1000°C. These effects were very small compared to

those observed at other temperatures, as seen in Fig. 1, and did not vary in intensity over the composition range of samples in which they were seen.

C. Equilibrations of Lanthanon Fluorides with Platinum. The DTA data for the Eu and Sm systems in the composition range $LnF_{2.04}$ to $LnF_{2.1}$ showed small endothermic peaks 50 to 100°C below the melting effects, which suggested the possibility of additional phases. In the Sm system, dramatic color changes from blue to violet to red across the composition range $SmF_{2.0}$ to $SmF_{2.25}$ also indicated the possible existence of additional compounds.[4] Experiments to determine the distribution of the lanthanon element between Pt intermetallic phases and fluorides were made for Sm, Eu, and Yb to gain more information about the number of phases occurring in these systems at elevated temperatures, and about the compositions of the stable phases. The experiments and interpretations are similar to the europium oxide-platinum studies described elsewhere.[10] To minimize the time required to achieve equilibrium, the temperature for the equilibrations was chosen to be as high as possible and still not melt the fluorides.

Results from the equilibration experiments are shown in Figs. 6-8, where the ratios of fluorine to lanthanon element in the fluoride are plotted versus the ratios of Pt to lanthanon element in the metallic phase equilibrated at 1260°C. The phase diagrams, Figs. 3-5, were constructed to be consistent with the equilibration results.

The optical and x-ray diffraction analyses of the fluoride products of these experiments did not produce results as definitive as the results from the europium oxide-platinum equilibrations. In no case did we achieve products layered from outside-in with the fluorides as we had with oxides. The fluoride products appeared to be either single-phase or intimate mixtures of two phases. The appearance of all of these products was of material that had been single-phase at the equilibration temperature, which is contradictory to the mass transfer results.

In general, the appearance of the equilibrated products under microscopic examination was similar to that of material of the same composition from other preparations.[4] A notable exception is the case

of samarium fluorides from SmF_2 to $SmF_{2.05}$. Previous samples, which has been made by heating $Sm + SmF_3$ or $SmF_2 + SmF_3$ to about 1500°C in sealed containers, had appeared to be homogeneous single-phase materials changing in color from blue to violet as the fluorine concentration increased.[4] Products in this composition range from the equilibrations at 1260°C were seen to be two-phase mixtures of blue crystals and red crystals, both non-birefringent. Also, ytterbium fluoride products from the equilibrations with compositions from $YbF_{2.05}$ to $YbF_{2.1}$ contained a tan, moderately birefringent phase not observed in the samples prepared by metathetical reactions.

The x-ray diffraction analyses were not as valuable as those from the europium oxide work since we were unable to isolate fluoride-rich and fluoride-poor samples from the products. In all cases, results were consistent with data from samples of similar compositions prepared by direct synthesis (Ref. 4).

The intermetallic phase in equilibrium with samarium fluorides from SmF_2 to $SmF_{2.05}$ at 1260°C had the composition approximately $SmPt_{1.2}$. These products had all melted and because of the small samples for these compositions we did not get material for x-ray analysis. Products between $SmPt$ and $SmPt_2$ had partly melted, and gave x-ray powder patterns that appeared to result from $SmPt_2$ ($MgCu_2$ structure) with lattice parameter a = $7.68_6 \pm 0.005$ Å, plus another unidentified phase. At 1260°C, the solid solution $SmPt_{2+x}$ was found to exist over the composition range $SmPt_2$ to $SmPt_{2.75}$. At room temperature, the lattice parameter of $SmPt_{2.75}$ is a = $7.62_0 \pm 0.005$ Å. The equilibria indicate the existence of a compound with composition near Sm_2Pt_7, similar to the Eu compound discussed in Ref. 10, but we do not yet have any crystallographic evidence for the Sm compound. Powder patterns of phases with Pt concentrations above that for $SmPt_{2.75}$ have not been resolved. Samples with Pt content greater than that for $SmPt_{3.5}$ appear to have lines that can be attributed to a hexagonal phase such as $SmPt_5$, with a structure related to the $CePt_5$ type.

Europium fluorides from $EuF_{2.0}$ to $EuF_{2.05}$ are in equilibrium with an intermetallic with composition approximately $EuPt_{5.1}$ at 1260°C.

The powder patterns obtained from this material indicate a structure closely related to the $CePt_5$ structure with hexagonal parameters a = 5.36_9 and c = 4.38_5 Å. The patterns did not exactly correspond to either the patterns of $EuPt_5$ from our oxide equilibrations at 1500°C or those of Bronger (see Ref. 10). Compositions containing more Pt than $EuPt_5$ gave patterns which appeared to result from $EuPt_5$ plus fcc phase with a lattice parameter of about 7.72 Å. These lines had not been seen in products from the oxide equilibria. Also contrary to the results from the oxide studies, Pt lines were not seen in patterns from samples with Pt:Eu ratios below 95:1.

Ytterbium fluorides from YbF_2 to $YbF_{2.05}$ are in equilibrium with $YbPt_{1.05}$ and fluorides from $YbF_{2.05}$ to $YbF_{2.1}$ are in equilibrium with $YbPt_{1.4}$ at 1260°C. A liquid phase did not appear to have been present in either of these materials, or in any of the more platinum-rich products. Our experiments were not precise enough to resolve discrete phases in either the fluoride or platinum system for more fluoride-rich and platinum-rich compositions. None of the x-ray powder patterns from the metallic products could be resolved. The patterns seemed to be characteristic of three different phases. One pattern was obtained from samples of composition $YbPt_{1.05}$, another from samples of composition $YbPt_{2.2}$ to $YbPt_{2.7}$ and a third from samples of $YbPt_4$ to $YbPt_5$. Samples with compositions between $YbPt_{1.05}$ and $YbPt_2$ appeared to be mixtures of the end-point compositions and gave patterns similar to the Sm-Pt mixtures of like compositions.

CONCLUSIONS

As frequently occurs, the number of new questions raised as a result of these studies is larger than the number of questions answered. However, we believe that we have added useful information to the foundation that will eventually lead to an understanding of non-stoichiometric compounds based on fluorite-structure systems. Phase diagrams have been drawn for three lanthanon element fluoride systems based on thermal analysis data, equilibrium data at 1260°C, and information from x-ray diffraction and optical examinations of samples across the

the composition range LnF_2 to LnF_3. Equilibration data at lower temperatures is needed to more completely resolve the phase diagrams. Electrolytic studies using fluoride electrolytes, vaporization measurements, and x-ray diffraction data from room temperature to about 1200°C are the obvious kinds of information that might fill the gaps.

It is noteworthy that the phase diagrams are significantly more complex than had been predicted on the basis of previous x-ray diffraction and optical data.[4] The reduced fluoride systems appear to be more closely analogous to the lanthanon oxyfluoride systems than would have been suspected.

Information from examining the metallic phase products of the equilibrations has shown that the Sm-Pt system is closely analogous to the Eu-Pt system, as expected. Additional evidence supporting the existence of a phase between $LnPt_{2+x}$ and $LnPt_5$ in these systems was obtained, as well as evidence pointing to the possible stability of LnPt phases in the Sm-Pt and the Yt-Pt systems. Dwight et al.[11] have reported SmPt to have the FeB structure. Data indicating the existence of phases in the Yt-Pt system which have similar compositions to those of the lower lanthanon element — Pt compounds, but different structures, was also obtained.

ACKNOWLEDGMENTS

REFERENCES

1. L. E. J. Roberts, Non-Stoichiometric Compounds, R. F. Gould, ed. (Am. Chem. Soc., Washington, D. C., 1963), pp. 66-73.
2. J. Short and R. Roy, J. Phys. Chem. 67, 1860 (1963).
3. R. W. M. D'Eye and F. S. Martin, J. Chem. Soc. 1847 (1967).
4. E. Catalano, R. G. Bedford, V. G. Silveira, and H. H. Wickman, J. Phys. Chem. Solids 30, 1613 (1969).
5. A. M. Diness and R. Roy, J. Mater. Sci. 4, 613 (1969).
6. W. H. Zachariasen, Acta Cryst. 4, 231 (1951).
7. P. J. M. Bevan, R. S. Cameron, A. W. Mann, G. Brauer, and U. Roether, Inorg. Nucl. Chem. Letters 4, 241 (1968).

8. G. Brauer and U. Roether, *Proc. Seventh Rare Earth Res. Conf.*, Coronado, Calif., 1968, p. 253 (distributed to attendees only).
9. W. Klemm and H. A. Klein, Z. Anorg. Chem. 248, 167 (1941).
10. R. G. Bedford and E. Catalano, "An Investigation of the Eu-Eu$_2$O$_3$ System and the Equilibria Between the Europium Oxides and the Eu-Pt System," in *Proc. Eighth Rare Earth Res. Conf.*, Reno, Nev., April 1970.
11. A. E. Dwight, R. A. Connor, Jr., and J. W. Downey, Acta Cryst. 18, 835 (1965).
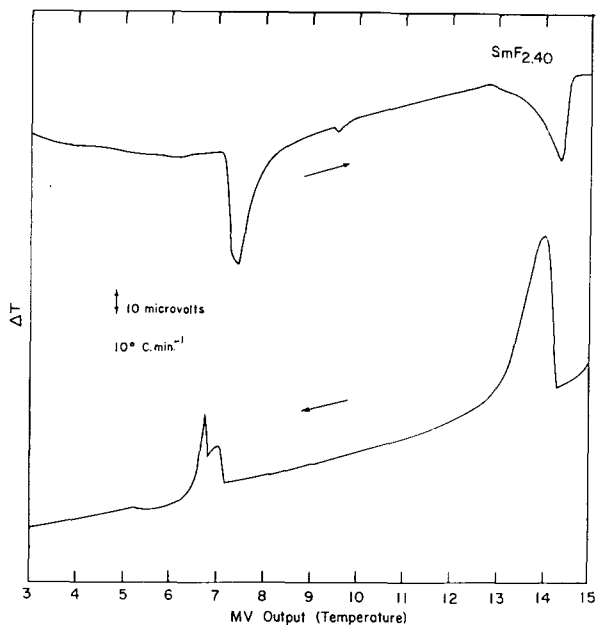
Fig. 1. Differential thermogram for SmF$_{2.40}$.
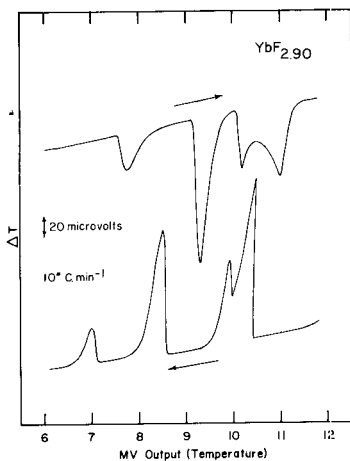
Fig. 2.   Differential thermogram
for YbF$_{2.90}$.
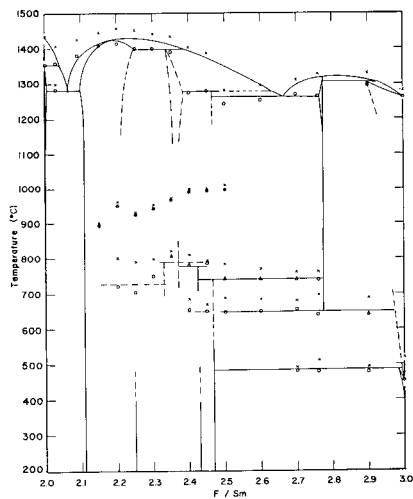
Fig. 3.   Phase diagram for the
SmF$_2$-SmF$_3$ system.
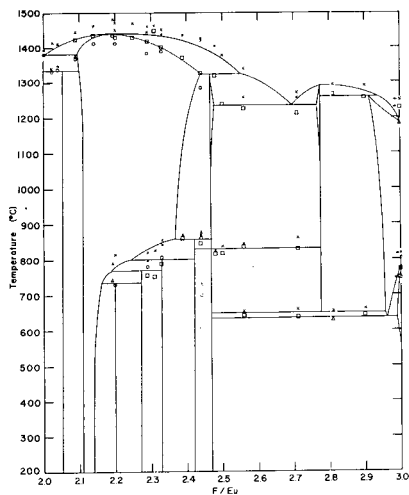
Fig. 4.   Phase diagram for the
EuF$_2$-EuF$_3$ system.
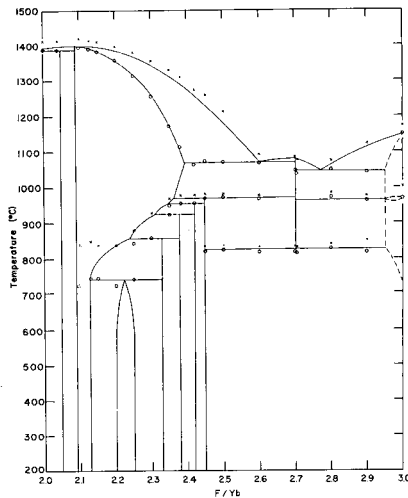
Fig. 5.   Phase diagram for the
YbF$_2$-YbF$_3$ system.
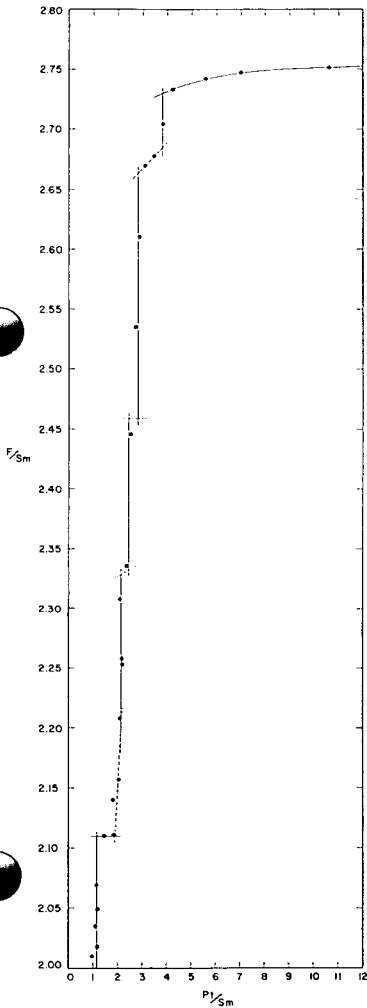
Fig. 6. F:Sm ratios vs Pt:Sm ratios for samples equilibrated at 1260°C.
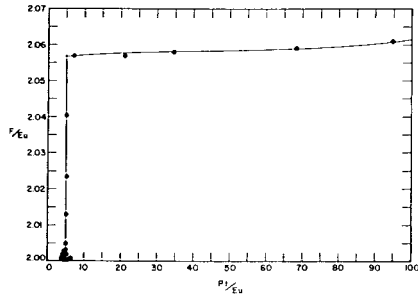
Fig. 7. F:Eu ratios vs Pt:Eu ratios for samples equilibrated at 1260°C.
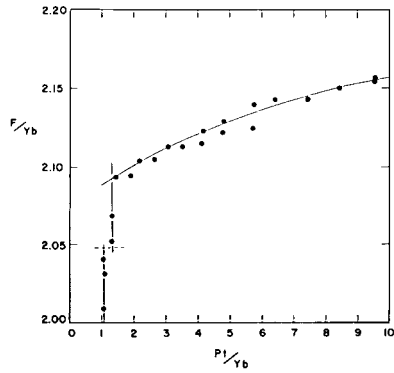
Fig. 8. F:Yb ratios vs Pt:Yb ratios for samples equilibrated at 1260°C.

GROWTH AND PROPERTIES OF LANTHANUM OXYSULFIDE CRYSTALS[*]

L. E. Sobon, K. A. Wickersheim, R. A. Buchanan and R. V. Alves
Lockheed Palo Alto Research Laboratory
Palo Alto, California 94304

Abstract

In order to better determine the optical properties of the rare earth oxysulfide phosphors and to lay the foundation for their application in single crystal form, we have grown for the first time single crystals of these materials. A description of the growth techniques for lanthanum oxysulfide will be presented. Materials problems and our progress towards their solutions will be discussed. Single crystal properties such as optical transmission range, hardness, indices of refraction and thermal conductivity will also be reported.

I. Introduction

Because of their exceptional luminescent efficiencies, the rare earth oxysulfides are rapidly achieving technological importance. Early investigations of lanthanum oxysulfide centered around its use as the host compound for a variety of infrared-stimulable storage phosphors[1]. Europium--activated yttrium oxysulfide has been commercialized for color television use[2]. The terbium-activated oxysulfides of lanthanum and gadolinium both show promise as x-ray conversion phosphors[3].

The oxysulfides are unusual among rare earth phosphor systems in that virtually all rare earth activators exhibit high luminescent efficiencies in one or another of the several host compounds[4]. They are unusual among rare earth compounds in that all trivalent rare earth oxysulfides exist and possess the same crystallographic structure regardless of ion size[5]. For these reasons the oxysulfides form an excellent laboratory system for the investigation of rare earth luminescence.

It is also interesting to think beyond present rare earth oxy-sulfide uses to those applications requiring single crystals - e.g. scintillators and lasers. The first practical step is to learn to produce single crystals of the several host compounds, and then to grow crystals suitably doped with appropriate rare earth ions. In the exploratory stage one needs single crystals in order to obtain the absorption and emission spectra of selected rare earth activators complete with polarizations and magnetic field dependences and to obtain other critical optical, thermal and mechanical properties. Ultimately one needs crystals of sufficient size and quality to be useful in practical device configurations.

In this paper we describe (1) the technique we have developed to produce crystals of lanthanum oxysulfide[6], (2) some of the more interesting physical properties of the crystals obtained and (3) the problems remaining to be solved before materials of the desired quality can be produced routinely.

II. Crystallography and Other Background Information

Before we discuss the crystal growth technique, let us review briefly what is known of the rare earth oxysulfides. The space group has been determined by x-ray diffraction[7] to be D_{3d}^3 - $P\bar{3}m$. There is one formula unit per unit cell. The structure is very closely related to the A-type rare earth oxide structure, the difference being that one of the three oxygen sites is occupied by a sulfur ion. An examination of a model of the structure reveals the fact that the sulfur ions form discrete planes perpendicular to the c-axis of the crystal. Each metal ion is bonded to four oxygen ions and three sulfur ions.

Over the years a wide variety of techniques have been developed for the preparation of the rare earth oxysulfides in powder form[1,7-15]. Of these only one[15] involves a liquid phase reaction. Thus the chemistry involved in this background work on powder preparation has little bearing on the liquid state environment of prime importance in

crystal growth. There are likewise no detailed phase equilibria studies of the rare earth-oxygen-sulfur system available to guide the crystal growth efforts.

La_2O_3 and La_2O_2S both exist as discrete stoichiometric phases. Our present data indicate surprisingly little solid solubility between these two apparently similar compounds. In powder preparation work we have been able to vary the sulfur to oxygen ratio of La_2O_2S by less than 1% despite wide variations in preparation conditions.

The substitution of one sulfur for an oxygen ion produces marked differences in the physical and chemical characteristics of La_2O_2S and La_2O_3. Whereas La_2O_3 hydrolyzes rapidly in moist air, La_2O_2S is remarkably stable by comparison. As we will note later in this paper, crystalline La_2O_2S has a much less pronounced cleavage than La_2O_3 and generally exhibits conchoidal fracture. The spectra of given activator ions are similar in La_2O_2S and La_2O_3, but the lines are markedly broadened in the oxide, even when the material has been freshly prepared and protected from moisture. Luminescent efficiencies of specific rare earth activators appear to be markedly higher in La_2O_2S than in La_2O_3.

III. Crystal Growth

Lanthanum oxysulfide oxidizes when heated above $600^\circ C$ in air. It melts at about $2000^\circ C$ with decomposition and sulfur loss when melted in a vacuum or inert atmosphere. Given these facts the most logical approaches to crystal growth seemed to us to be: (1) to attempt to grow from the melt at appropriate pressures under a suitable atmosphere; (2) to attempt to find a suitable flux from which to grow or (3) to look for a vapor transport technique. Despite the high melting point, the first alternative appeared the most straightforward. The technique we have developed involves melting the oxysulfide in sealed tungsten crucibles[16], and then growing crystals by the Bridgeman-Stockbarger technique.

The starting powders are produced by one of the powder preparation procedures referenced earlier. 10 to 30 grams of powder is loaded into the crucible, and the crucible is then evacuated and sealed by electron beam welding. Present crucibles are either 3" or 6" in length and have a 1/2" inner diameter, a 0.03" wall thickness and a 1/2-inch taper to a point at the bottom[17]. The crucible is loaded into a graphite holder which is then inserted into an Astro high temperature furnace. The furnace is graphite resistance heated, packed with graphite insulation, has a water-cooled shell and can be operated either under flowing helium or evacuated. In Figure 1 we show the furnace assembly and fixturing used. The combination of graphite spacers, crucible holder and lower hearth produces the necessary temperature gradient in which the crucible is positioned. In initial crystal growth attempts the crucible was held from above and lowered slowly through the temperature gradient at a fixed furnace temperature setting. At the present time the crucible is held stationary in the gradient and the furnace temperature is lowered slowly.

We have established the melting point of La_2O_2S to be $2070 \pm 30°C$. The crucible and charge are raised to a temperature somewhat above this for about an hour before the programmed lowering or cooling are started. In the earlier arrangement the crucible was lowered at a rate of from 0.5 to 2 cm per hour. In the present method, the temperature is lowered at a rate of from $10°$ to $20°C$ per hour.

In all experiments there is evidence of high internal pressure. The crucible lids assume a domed shape. Occasionally the side wall of the crucible will bulge. Very rarely the crucible will rupture. All such crucible failures have been non-violent, tungsten being quite ductile at the melting temperatures of the oxysulfides.

Under the right conditions - e.g. proper location in the gradient, proper starting temperature and melting time and proper lowering or cooling rate - clear single crystalline ingots are obtained. These vary in color from yellowish to nearly colorless. When conditions are

not quite right, polycrystalline ingots are obtained. Regions of purplish discoloration, thought to be the result of color centers produced by small variations in sulfur content, are observed rarely. A yellowish-brownish skin and a region of greenish discoloration is frequently seen near the upper surface of the crystal (the meniscus of the melt). It is thought that this results from either the sweeping of trace impurities to the upper surface during crystallization (zone-refining) or from a gross variation in sulfur content near the surface. Bubbles or voids are occasionally observed. When the crucible fails at high temperature, a black ingot is obtained.

Some crystals show a hazy grey precipitate which has now been identified as tungsten metal. It appears that if the temperature of the melt is raised too high or held too long before growth is started, tungsten dissolves in the oxysulfide, only to precipitate out on cooling. When viewed under a microscope, the precipitate is seen to consist of long strings of beads running along specific crystallographic directions, suggesting strongly decorated dislocations.

In summary then we have been able to produce good single crystalline ingots up to 1/2" by 1-1/2", occasionally obtaining discolored or polycrystalline materials. We have also grown a number of crystals activated with low concentrations of various rare earth ions. The crystals obtained exhibit a variety of minor defects. It is our feeling that the tungsten solution and precipitation problem is not serious provided we do not raise the melt temperature much above the melting point for very long. This however requires extremely good temperature control and possibly a smaller gradient than presently used. Some thought should also be given to other crucible materials. Bubbles and voids can probably be eliminated by using precrystallized starting materials rather than powders and by reducing the temperature gradient. It is also clear that starting material purity should be as high as possible.

V. Physical Properties

Mechanically the crystals are relatively hardy. They are inert to attack by atmospheric constituents and show no apparent solubility in water. They do not exhibit pronounced cleavage and frequently fracture conchoidally. The hardness measured by the diamond pyramid technique is 750. This translates into a Knoop hardness of 780, only slightly lower than the reported value of 820 for quartz. Thus the crystals are mechanically durable and yet soft enough for easy optical working. We have prepared a variety of optical shapes - e.g. prisms, sections, cubes and rods - and have encountered no problems in either fabrication or handling.

We have begun to measure thermal properties. Thermal conductivity is a very important parameter for laser applications. We obtain a room temperature conductivity of 350 ± 70 milliwatts/cm$^\circ$K in the direction perpendicular to the c-axis of the crystal. This is to be compared, for example, with a value of 140 milliwatts/cm$^\circ$K reported[18] for laser grade YAG:Nd. Thermal expansion coefficient measurements are now in progress. The effects of temperature change on other parameters such as the index of refraction are as yet unknown.

Since the applications of greatest interest are optical, we have explored the optical properties most extensively. The indices of refraction have been measured at room temperature using small prisms of La_2O_2S cut with the optic axis perpendicular to the prism base. The two indices were calculated after finding the angles of minimum deviation for each of the principal visible emission lines of mercury and for the 1.06 micron line from a YAG:Nd laser. The indices are plotted as a function of wavelength in Figure 2. As can be seen the crystal is optically positive for wavelengths longer than 5600 A and optically negative for wavelengths shorter than 5600 A. The indices are fairly high, ranging from about 2.16 at one micron to about 2.3 at 4000 A.

Lanthanum oxysulfide is an excellent optical host, exhibiting high transparency from 3500 A in the ultraviolet to beyond 8 microns in the infrared. The absorption coefficient, neglecting reflection losses, is plotted in Figure 3.

Additional optical measurements, including detailed absorption and emission spectra of Eu^{3+} and Tb^{3+} in La_2O_2S, and measurements of optical gain and loss, decay times, and laser performance for $La_2O_2S:Nd$, have also been made and will be reported elsewhere[19].

VI. <u>Future Work</u>

Several areas are in need of additional effort. The crystal growth procedures need to be developed further to the point where they are routine and reproducible. This means, in part, better temperature measurement and control. It would also be advantageous to be able to work in an open system. This means considering growth by pulling inside of a pressurized furnace or possibly growth from flux if a suitable one can be found. Better control of oxygen-sulfur stoichiometry and purity of starting materials are also areas of potential concern. While rare earth compounds are available in fairly high purity, trace contaminants may still affect crystal growth. We may have to consider subsequent purification of starting materials as by zone refining. As mentioned earlier, the tungsten solution and precipitation problem, while not severe, forces us again to work on refined temperature control and to consider as well alternate crucible materials.

Up until now we have concentrated almost exclusively on La_2O_2S. Crystals of the other host compounds, namely Y_2O_2S, Gd_2O_2S and possibly Lu_2O_2S, are also of interest. It is felt that growth procedures similar to the ones reported here should apply as well to the other hosts with relatively minor modification. From our work on selected rare earth dopants in concentrations up to several mole percent, it appears that changing the rare earth activator has relatively little effect on growth conditions except for varying the melting temperature slightly. Because of the structural homogeneity of the entire rare earth sequence

of oxysulfides, any ratio of rare earths in the final crystal seems possible. However growth of the other hosts and of crystals containing still higher concentrations of specific activators needs to be explored further.

Acknowledgements

References and Footnotes

1. J. J. Pitha, et al., J. Am. Chem. Soc. 69, 1870 (1947).

2. As early references, see M. R. Royce and A. L. Smith, Abstract No. 34 and R. E. Shrader and P. N. Yocum, Abstract No. 35, the Electrochemical Society Meeting, Boston, May 1968.

3. S. P. Wang, et al. and K. A. Wickersheim, et al., IEEE Nuclear Science Symposium, San Francisco, October 1969. To be published in the Symposium Proceedings.

4. P. N. Yocum and R. E. Shrader, Proceedings of the Seventh Rare Earth Research Conference, 601 (October 1968).

5. I. Flahaut, Progress in the Technology of the Rare Earths, Volume 3, 1968, Pergamon Press, Oxford, p. 267.

6. Discussions of earlier crystal growth efforts are contained in a paper by L. E. Sobon presented at the ACCG Conference on Crystal Growth, Gaithersburg, Md., August 1969, and in "Study of Rare Earth Activated Materials for Radiation-Sensing Applications," U. S. Atomic Energy Commission, Division of Biology and Medicine Contract AT(04-3)-674, K. A. Wickersheim, et al., Third Annual Report, June 1969.

7. W. H. Zachariasen, Acta. Cryst. 2, 60 (1949).

8. E. D. Eastman, et al., J. Am. Chem. Soc. 73, 3896 (1951).

9. J. Flahaut, et al., Compt. Rend. 245, 2291 (1957).

10. J. Flahaut, et al., Bull. Soc. Chem. France 990 (1958).

11. H. A. Eick, J. Am. Chem. Soc. 80, 43 (1958).

12. V. P. Surgutskii and V. V. Serebrennikov, Zh. Neorgan, Khim. 9, 786 (1964).

13. G. Collen and J. Loriers, Compt. Rend. 260, 5043 (1965).

14. P. Khodadad, et al., Compt. Rend. 260, 2235 (1965).

15. M. R. Royce, et al., Abstract 86, Electrochemical Society Meeting, New York, May 1969.

16. Dr. Thomas Reed of Lincoln Laboratories originally suggested to us this approach.

17. The crucibles are prepared by chemical vapor deposition. They are purchased from San Fernando Laboratories, a Division of Fansteel Corp.

18. P. H. Klein and W. J. Croft, J. Appl. Phys. 38, 1603 (1967) reported a value of 110 mw/cm°K but J. R. Thornton, et al., Applied Optics 8, 1087 (1967) gave the value of 140 mw/cm°K quoted here.

19. R. V. Alves, K. A. Wickersheim and R. A. Buchanan, to be published. See also other papers presented at this conference.

WATER-COOLED SHELL

CARBON INSULATION

TUNGSTEN ROD

GRAPHITE LINER

GRAPHITE CRUCIBLE HOLDER

TUNGSTEN CRUCIBLE

GRAPHITE HEATING ELEMENT

BOTTOM HEARTH

AUXILIARY SIGHT PORT

RADIOMETER SIGHT PORT
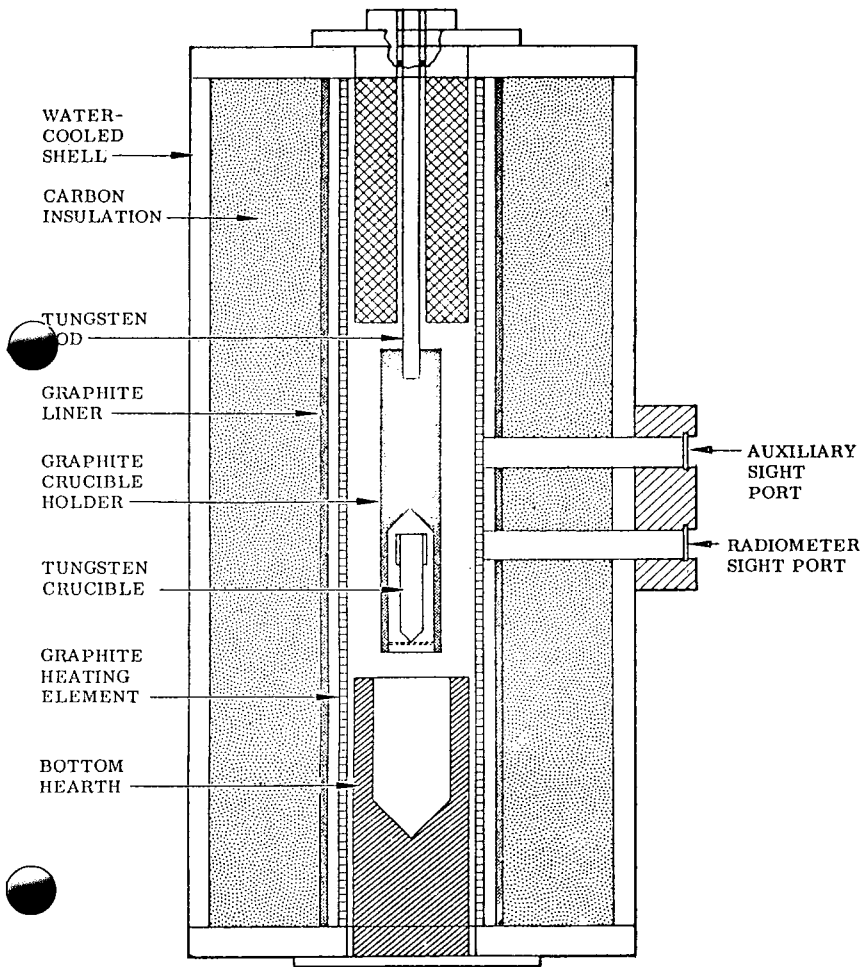
Figure 1: Furnace assembly used for the growth of lanthanum oxysulfide crystals
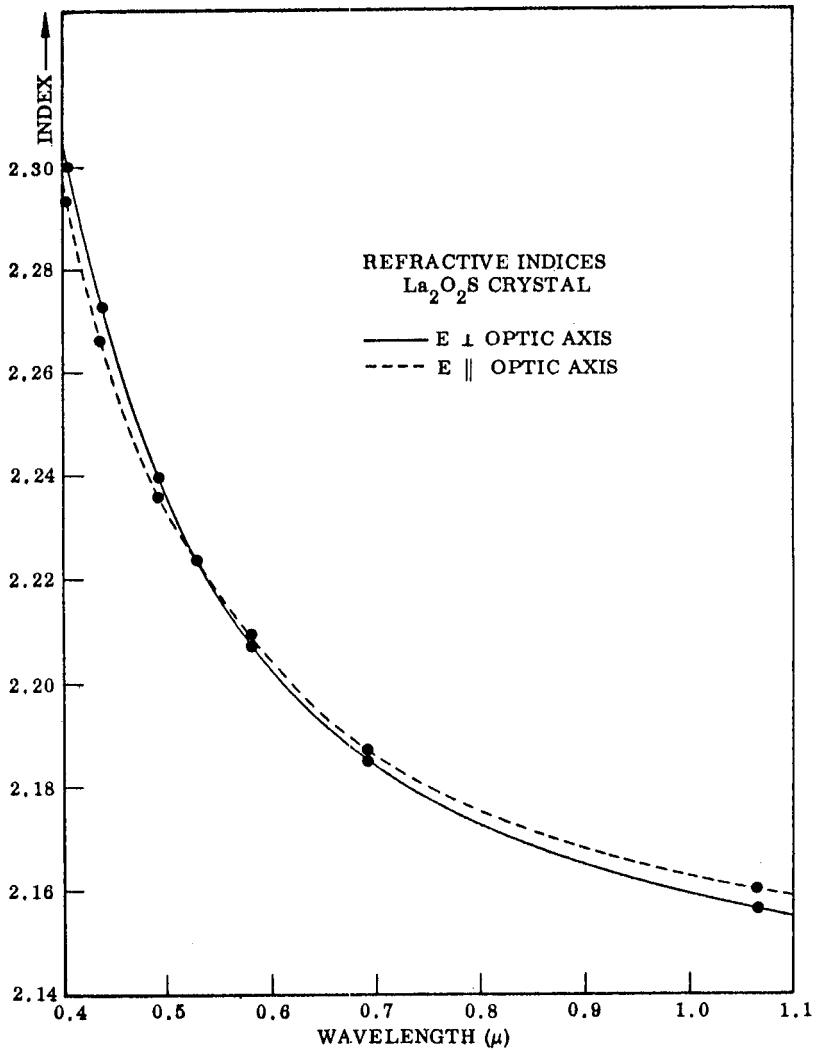
Figure 2: Plot of the refractive indices of lanthanum oxysulfide versus wavelength
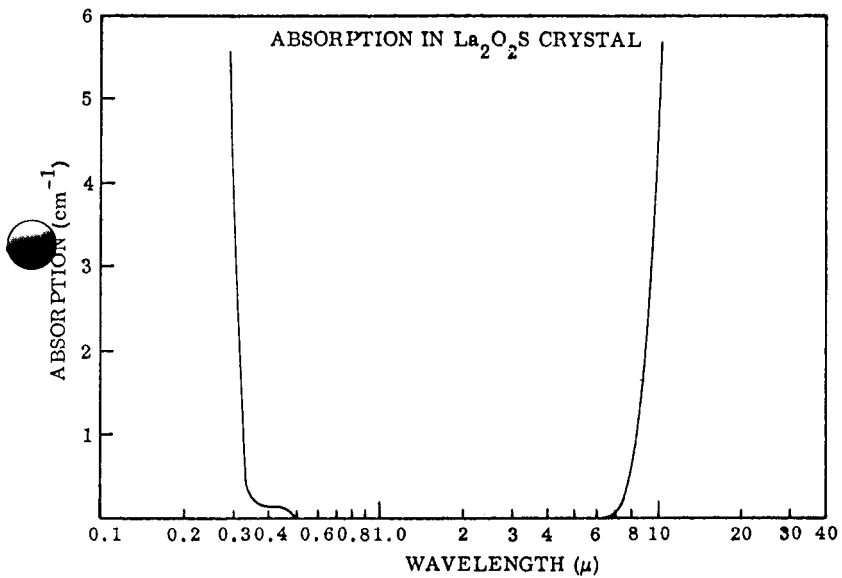
Figure 3: Plot of the absorption coefficient of crystalline lanthanum oxysulfide versus wavelength

VACANCY AND CHARGE ORDERING IN THE Th_3P_4 STRUCTURE

Forrest L. Carter and Margaret O'Hara
Naval Research Laboratory, Washington, D.C. 20390

5718000

ABSTRACT

Vacancy ordering in the lanthanide sesquichalcogenides having the Th_3P_4 structure has been a long standing problem. In such materials with 1/9 of the metal sites unoccupied, vacancy pairing statistically has a high probability, but chemically such pairing appears unlikely. Models of the ordering of vacancies have been sought which correspond to their maximum separation. Using a Wigner-Seitz cell approach the all space-filling dodecahedron associated with the metal sites in the Th_3P_4 structure has been determined. The linking of these dodecahedron via their smaller triangular faces corresponds to a diamond-like structure of next-nearest metal neighbors and leads to two tetragonal space groups, $I\bar{4}2d$-D_{2d}^{12} and $I\bar{4}$-S_4^2 as models for partial vacancy ordering. The first space group is suggested as corresponding to charge ordering in the Sm_3S_4 and Eu_3S_4 type semiconductors and the second suggests new classes of Th_3P_4 type compounds. While x-ray evidence for vacancy ordering in Ce_2S_3 etc. is lacking, transport phenomena in Eu_3S_4 support a charge ordered model. Madelung constant calculations for the various ordered structures are in progress.

INTRODUCTION

The growing literature on rare earth compounds having the Th_3P_4 structure testify to the great versatility of this high temperature phase in accommodating large quantities of metal site vacancies and cation substitutions. For the pure compounds the composition generally varies between R_2X_3 and R_3X_4 where R represents a light rare earth metal and X indicates either sulfur, selenium or tellurium.[1-4] The R_2X_3 compositions in the Th_3P_4 structure are insulating or semiconducting and correspond to a vacancy concentration of 1/9 of the metal sites[5]. When these vacancies are filled with trivalent metals

-412-

such materials as Ce_3S_4, Gd_3Se_4, and Nd_3Te_4 are semimetallic and demonstrate no lattice parameter increase over those of the R_2X_3 composition. The vacancies in the R_2X_3 composition can also be wholly or partly filled with divalent alkaline earths,[6-8,4] divalent transition metals,[9] or divalent lanthanides[10] with the maintainence of the semiconducting character of the R_2X_3 composition all the way to the filled structures including $CaCe_2S_4$, $SrGd_2Se_4$, $YbDy_2S_4$, Eu_3S_4, and Sm_3Se_4. In the latter two compounds semiconductivity is achieved by the localization of the itinerant electrons responsible for electrical conductivity in the trivalent compounds to give trivalent and divalent Sm and Eu atoms in the ratio of 2:1 (see Ref. 4). Thus the versatility of the structure to accommodate a variety of substitutions and hence various electron/atom ratios, has encouraged many phase studies, especially by Flahaut and his coworkers, as well as many studies involving transport phenomena, such as thermoelectricity,[11,12] electron mobility control,[7,8] electron transport,[13] Mossbauer effects,[14] and superconductivity,[15] as well as optical[16] and magnetic effects.[17,18]

In the above compounds it is generally considered that the trivalent and divalent metals, as well as the vacancies, all occupy the same set of crystallographically equivalent sites on a purely statistical basis.[5] This is in contrast to the situation involving the heavier rare earth chalcogenides where such compounds as $BaHo_2Se_4$ have the same orthorhombic structure type[19] as $CaFe_2O_4$ involving non-equivalent divalent and trivalent sites. As noted earlier,[7] the assumption of only statistical occupancy is somewhat more extreme for the pure lanthanide and actinide sesqui-sulfides for which Zacharisasen originally proposed that 1-1/3 vacancies are randomly distributed among the 12 metal sites. Now, since each metal atom has eight near metal neighbors in the Th_3P_4 structure, the

-413-

probability of the pairing of vacancies is sufficiently high (8/81) that pairing cannot be ignored in even a zero order discussion. In addition, the absence of two large metal atoms associated with adjacent vacancies would lead to serious collapse of the structure in that area and would appear to be highly unlikely on the scale called for by the statistics alone. Since the ordering of vacancies does not appear to have been discussed in the literature and since such ordering, if it exists, could have important ramifications in the single crystal properties of these materials the question of vacancy and charge ordering (as in $Eu^{+2}Eu_2^{+3}S_2^{=}$) is the subject of this paper. The ordering of vacancies among the metal sites has been sought by consideration of a Wigner-Seitz type cell about each metal atom. This readily leads to a model in which the vacancies are no nearer than second-nearest metal neighbors and could be third-nearest metal neighbors. The corresponding structures are tetragonal and represent successive reductions in symmetry from the cubic Th_3P_4 structure. In addition, the effect of the ordering on the metalloid (P) atom is considered and the relation of the model to the experimental evidence is examined. We also note here that occurrence of ordering should increase interest in compounds having the non-centrosymmetric Th_3P_4 structure since the possibilities for non-linear optical and magnetic phenomena are expanded by the presence of the uniaxial tetragonal structures in this series of compounds of demonstrated versatility.

Vacancy Model - In the search for a possible ordering of vacancies, use was made of a Wigner-Seitz type cell about each metal atom followed by the paper-scissors construction of the resulting polyhedra. These allspace-filling polyhedra are obtained as follows: The intersections of the planes which are the perpendicular bisectors of the interatomic metal-metal distances from a single

-414-

metal site define a series of polyhedra of increasing volume. The
smallest such polyhedron containing the central metal site is the
desired one. For the Th_3P_4 structure one obtains dodecahedra
with a volume of 1/12 the unit cell and which, when duplicated at
each metal site with the correct orientation, fill all space. Each
dodecahedron has eight identical faces which can be considered as
obliquely truncated isoceles triangles associated with the nearest-
neighbor metal-metal interactions and four additional isosceles
triangles associated with the next-nearest metal-metal distances.
These faces are arranged to give $\bar{4}$ symmetry to the polyhedra
(see Fig. 1). By linking together that set of dodecahedra corres-
ponding to the next-nearest interactions only, one forms an open
(but distorted) diamond-like structure (Fig. 2) in which all $\bar{4}$ axes
of the dodecahedra are parallel to each other and to one of the
cubic axes. There are three interpenetrating networks such that
each metal site (or dodecahedron) has as nearest neighbors only
those dodecahedra with their $\bar{4}$ axes perpendicular to its own. By
randomly distributing the vacancies among the metal sites cor-
responding to just one of the diamond-like structures (called here,
D_z) one obtains a tetragonal structure with the space group $I\bar{4}2d$-
D^{12}_{2d}. In such a case the vacancies are no nearer than second-
nearest metal-metal neighbors.

Further ordering is obtained by restricting the vacancies to half
the D_z sites. This results in a wurtzite-like structure in which each
site V (for vacancy) is tetrahedrally surrounded by four F (filled)
sites and vice-versa. This wurtzite-like structure with cell edges,
A_w, B_w and C_w has a severe tetragonal distortion such that $\sqrt{2}\, C_w =$
$A_w = B_w = \sqrt{2}\, a_o$ where a_o is the cubic unit cell edge. Now the
vacancy sites (V) are only third-nearest metal-metal neighbors in
a structure of even lower tetragonal symmetry (space group $I\bar{4}$-S_4^2).

-415-
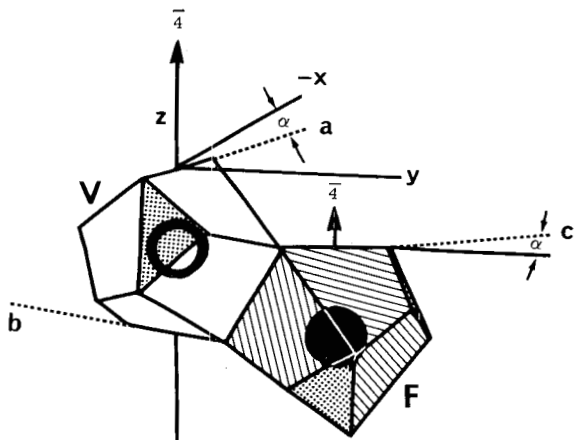
Fig. 1. Two of space filling dodecahedra about the twelve metal sites in the Th_3P_4 structure are shown. Next nearest metals share the four small isosceles triangles and have parallel $\bar{4}$ axes. The dodecahedron of nearest neighbor metals have one of the eight quadrilateral faces in common and have perpendicular $\bar{4}$ directions. The dodecahedra edges marked a, b, and c are perpendicular to the $\bar{4}$ or z-axis and make an angle of 26.56° with the [100] or [010] direction.
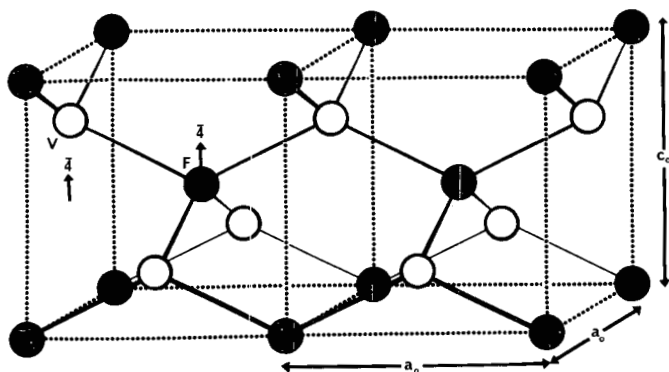
Fig. 2. The D_z substructure of the metal sites with $\bar{4}$ symmetry is illustrated for two unit cells with the relative positions of the sites marked V and F the same as in Fig. 1. A charge ordered structure proposed for Eu_3S_4 would have divalent metal atoms in both the V and F positions with the trivalent ions in the 2 fold positions (not shown). A highly ordered Ce_2S_3 structure would have the eight D_x, D_y sites and the F positions fully occupied with two-thirds of the V positions vacant.

-416-

This structure is seen in Fig. 2 which shows neither the filled D_x or D_y metal sites nor the 16 metalloid positions.

The relation between the various space groups is illustrated in Table I which shows the symmetry of the sites germane to the Th_3P_4 type structure along with the approximate atomic parameters. The direction of further shifts in the metalloid parameters are indicated by δ terms assuming zero metal shifts but an increased size for the occupants of the D_z sites. In calculating the approximate parameters we note that between the Th_3P_4 structure type and the tetragonal space groups there is an origin shift of 0, 1/4, -1/8.

Three possible models for the ordering of vacancies in the rare earth sesquichalcogenides are now readily described. 1) The vacancies can be distributed among the 12a positions of the Th_3P_4 structure which include the D_x, D_y, and D_z substructures. In agreement with Zachariasen's proposal,[5] the probability of finding a vacancy in a metal site is 1/9 and the probability of finding two adjacent vacancies is 8/81. 2) The vacancies are distributed among the 4a sites of the $\bar{I}42d-D_{2D}^{12}$ space group corresponding to the D_z sites only. The probability of finding a vacancy in such a site is 1/3 for the R_2X_3 compositions and vacancies are no closer than second-nearest metal neighbors. This would appear to be a reasonable model for the sesquisulfides, as usually prepared, and for charge ordered semiconductors like Eu_3S_4 at low temperature. 3) By restricting vacancies to just one of the $\bar{4}$ sites in the $I\bar{4}-S_4^2$ structure the probability of the site being vacant is 2/3; now vacancies are no closer than the third-nearest metal neighbors. In the figures the site selected is the 2c or V site. Such ordering might occur for a well annealed sesquisulfide. These examples are included in Table II along with other possible new semiconducting compounds based on the Th_3P_4

-417-

TABLE I. BODY CENTERED TETRAGONAL STRUCTURES AND
THEIR RELATION TO THE TH_3P_4 STRUCTURE

SPACE GROUP	Metal Site			Metalloid Site		
	Position	Symmetry	u v w[a,b]	Position	Symmetry	u v w[a,b]
$I\bar{4}3d-T^6_d$ No. 220 (Th_3P_4)	12a (D_x,D_y,D_z)	$\bar{4}$	$\frac{3}{8}$ 0 $\frac{1}{4}$	16c	3	x x x $x \cong \frac{1}{12}$
$I\bar{4}2d-D^{12}_{2d}$ No. 122	4a (D_z)	$\bar{4}$	0 0 0	16e	1	x,y,z $\begin{cases} x \cong \frac{1}{12} + 2\delta \\ y \cong \frac{1}{3} + \delta \\ z \cong \frac{23}{24} - 4\delta \end{cases}$
	8d (D_x,D_y)	2	$x,\frac{1}{4},\frac{1}{8}$ $x \cong \frac{3}{8}$			
$I\bar{4}-S^2_4$ No. 82	2a (F)	$\bar{4}$	0 0 0	8g	1	x y z $\begin{cases} x \cong \frac{1}{12} + 2\delta \\ y \cong \frac{1}{3} + \delta \\ z \cong \frac{23}{24} - 4\delta \end{cases}$
	2c (V)	$\bar{4}$	0 $\frac{1}{2}$ $\frac{1}{4}$			
	8g (D_x,D_y)	1	x y z $\begin{cases} x \cong \frac{1}{8} \\ y \cong \frac{1}{4} \\ z \cong \frac{5}{8} \end{cases}$	8g'	1	x'y'z' $\begin{cases} x' \cong \frac{1}{12} + 2\delta \\ y' \cong \frac{1}{6} - \delta \\ z' \cong \frac{7}{24} + 4\delta \end{cases}$

Footnotes
a   Typical atomic parameters are given; equivalent positions are obtained from the unit cell symmetry elements.
b   When δ equals zero both Th and P type atoms are in the filled Th_3P_4 structure with x(P) = 1/12. The shift δ (positive) is for large atoms on the D_z sites.

TABLE II. POSSIBLE ORDERED SEMICONDUCTING

COMPOUNDS BASED ON TH_3P_4-TYPE STRUCTURES

COMPOUND	METAL SITES D_z		D_x,D_z	SPACE GROUP NO.
	F	V		
Ce_2S_3	$(\frac{8}{9}Ce^{+3},\frac{1}{9}\square)$	$(\frac{8}{9}Ce^{+3},\frac{1}{9}\square)$	$(\frac{8}{9}Ce^{+3},\frac{1}{9}\square)$	220
Ce_2S_3	$(\frac{2}{3}Ce^{+3},\frac{1}{3}\square)$	$(\frac{2}{3}Ce^{+3},\frac{1}{3}\square)$	Ce^{+3}	122
Ce_2S_3	Ce^{+3}	$(\frac{1}{3}Ce^{+3},\frac{2}{3}\square)$	Ce^{+3}	82
Sm_3S_4	Sm^{+2}	Sm^{+2}	Sm^{+3}	122
$EuGd_2Se_4$	Eu^{+2}	Eu^{+2}	Gd^{+3}	122
$FeBaLa_4Te_8$	Fe^{+2}	Ba^{+2}	La^{+3}	82
$Th_5P_4S_4$	Th^{+4}	$\square$	Th^{+4}	82^a
$MnBaTh_4P_4S_4$	Mn^{+2}	Ba^{+2}	Th^{+4}	82^a
$BaTbCe_4S_8$	Ba^{+2}	Tb^{+2}	Ce^{+3}	82
VCe_4Se_8	V^{+4}	$\square$	Ce^{+3}	82

a   Nonequivalent metalloid atoms are permitted in space group No. 82.

type structure. Note that some of these suggest the possibility of both n- and p-type conductivity with suitable cationic doping. Reports of the latter type conductivity are rare.[2]

Ordering and the Chalcogen Position. - In the rare earth chalcogenides having the Th_3P_4 structure, the metal site is surrounded by eight chalcogens in the form of two tetrahedra, one which is long in the direction of the $\bar{4}$ axis and the second which is quite flat and almost lies in the plane normal to the $\bar{4}$ axis. With reference to the metal sites the chalcogen atom sits on the axis of a twisted trigonal prism slightly closer to one set of three metal atoms. The symmetry of this site (P position) in the Th_3P_4 structure is threefold and has the general coordinates x, x, x, where $x \lesssim \sim 1/12$. As x increases it moves toward the top triangle of the twisted prism and shortens the distances corresponding to the long tetrahedra about the metal site while lengthening the chalcogen-metal distances of the base triangle corresponding to the flat tetrahedra. (For more complete descriptions of the structure with a valence bond interpretation see Refs. 7 and 20).

If the semiconducting Sm_3S_4 compound were to have an ordered structure with the divalent ions in the D_z sites (4a positions of the $\bar{1}\bar{4}2d$-D_{2d}^{12} space group) then each sulfur atom would be adjacent to two Sm^{+2} ions, one each in the triangular base and top of the trigonal prism. The cation arrangement would distort the threefold symmetry of the sulfur atom; however, crystallographically there is still only one kind of metalloid in the ordered tetragonal Sm_3S_4 structure as is indicated by the 16e positions for the space group in Table I.

If, for the sesquisulfides, the vacancies were statistically distributed over all the D_z sites, the above discussion for Sm_3S_4 would

be applicable; if however, they were restricted to the V sites then two thirds of these positions would be vacant. If the vacancies were random among the V sites, then the $I\bar{4}-S_4^2$ space group would apply and there would be equal numbers of two different kinds of sulfur atoms, with the vacancy in either the base or top triangle of metal sites. Going beyond Table I and ordering the vacancies in the V positions so that every third V site along a stack of trigonal prisms ([111] direction in Th_3P_4) is occupied by a metal atom, then there are six kinds of chalcogens, four of them with five metal neighbors and two of them with six neighbors. Other differences between them involve their distance from an occupied V site and whether the vacant V site is in the top triangle (long tetrahedra) or in the bottom triangle (flat tetrahedra). For the originally proposed[5] statistically distributed vacancies in Ce_2S_3 there are a large number of various kinds of S-atoms, with fair fraction of them (16/81) having a pair of vacancies in a single triangular base.

For the sake of completeness we note that the space-filling cell for the sixteen metalloid positions in Th_3P_4 was obtained for $x = 1/14$ and is a trigonal hendecahedron composed of two equilateral triangles and three sets of three quadrilateral faces.

Experimental Evidence. - The experimental evidence for the ordering of vacancies or charge in the Th_3P_4 structure is meager. The authors know of no lattice parameter or single crystal x-ray studies suggesting ordering. The observation of vacancy ordering would appear to be most likely in the light rare earth sesquisulfides grown at the lowest possible temperature. One of us (FLC) has grown[21] tiny crystals of Ce_2S_3 by I_2-transport at 925°C. While the size of the crystal (less than 0.1 mm) prevented a definitive study there were no obvious intensity or space group violations of the Th_3P_4 structure. On the other hand the refractory nature of these materials and the

lack of lattice parameter variations from cubicity suggest that the single crystal could have an equal number of tetragonal domains with their c axes distributed along the "pseudo" cubic cell edges. A very careful x-ray study involving statistical analysis of equivalent reflections may be required and/or disorder studies may be indicated.

Recent transport studies in bulk Eu_3S_4 provide some evidence for charge ordering in these compounds. The presence of localized tri- and divalent cations in the ratio of 2 to 1 in samarium and europium chalcogenides with the Th_3P_4 structure has since been established by magnetic susceptibility measurements and by their semiconducting properties. Mössbauer studies[14] in 1967 by Berkooz, Malamud, and Shtrikman show the existence of Eu^{+3} and Eu^{+2} ions in the expected ratio below 210°K but above that temperature the isomershift peaks broaden and then merge into a single intermediate peak consistent with a hopping electron transport model involving Eu^{+2} "extra" electrons. In the same material Bransky, Tallan, and Hed have observed[22] an electrical transition at about 175°K as an abrupt change in activation energy from 0.16 to 0.21 ev., in reasonable agreement with 0.24 ev. obtained by Berkooz et al.

The loss of symmetry from $\bar{4}$ to 2 fold or to none in two-thirds of the metal sites suggests the observation of charge or vacancy ordering might be possible via EPR, optical, or NMR experiments on single crystals. However, the local distortions from $\bar{4}$ symmetry may be rather small. On the other hand, the effect on the chalcogen is appreciable. For example, in the disordered Zachariasen Th_3P_4 structure there would be many kinds of S in Eu_3S_4, corresponding to the various combinations of distributing Eu^{+3} and Eu^{+2} ions at the corners of a twisted trigonal prism. In the ordered structure, at low temperature, only one kind of sulfur is present as indicated

in Table I. X-Ray support for charge and vacancy ordering in the
Th_3P_4 structures may be long in coming since an averaging process
is involved. Accordingly, other methods of detecting local site
symmetry changes are highly recommended. Finally we note that
the calculation of the Madelung constants by the method of Bertaut[23]
are in progress for the various models of ordering and will be com-
pared to the above experimental results as well as to that obtained
previously[20] for the average Zachariasen structure. The receipt of
a preprint[22] on Eu_3S_4 from Dr. N. Tallan is gratefully acknowledged.

REFERENCES

1. E. D. Eastman, L. Brewer, L. A. Bromley, P. W. Gilles, and
    N. L. Lofgren, J. Am. Chem. Soc. 72, 2248 (1950).

2. J. F. Miller, L. K. Matson, and R. C. Himes, "Rare Earth
    Research" (Ed. by J. F. Nachman and C. E. Lundin, Gordon
    and Breach, New York, 1961) p. 233.

3. J. Flahaut, M. Guittard, M. Patrie, M. P. Pardo, S. M. Golabi,
    and L. Domange; Acta Cryst. 19, 14 (1965).

4. M. Guittard, A. Benacerraf, and J. Flahaut, Ann. Chim 9,
    25 (1964).

5. W. H. Zachariasen, Acta Cryst. 2, 57 (1949).

6. E. Banks, K. F. Stripp, H. W. Newkirk, and R. Ward, J. Am.
    Chem. Soc. 74, 2450 (1952).

7. F. L. Carter, R. C. Miller, and F. M. Ryan, Advanced Energy
    Conversion 1, 165 (1965).

8. S. W. Kurnick, R. L. Fitzpatrick, and M. F. Merriam,
    "Rare Earth Research" (Ed. by J. F. Nachman and C. E.
    Lundin, Gordon and Breach, New York, 1961), p. 249.

9. M. Patrie, J. Flahaut, and L. Domange, Rev. Hautes Temper
    Et Refract. 2, 187 (1965).

10. V. Tien, J. Flahaut, and L. Domange, Compt. Rend. 262,
    278 (1966).

11. F. M. Ryan, I. N. Greenberg, F. L. Carter, and R. C. Miller,
    J. Appl. Phys. 33, 864 (1962).

12. J. Appel, S. W. Kurnick, and P. H. Miller, Jr., "Metallurgy of Semiconductor Materials" (Ed. by J. B. Schroeder, Interscience Publishing Co., New York, 1961) p. 245.

13. M. Cutler, J. F. Leavy, and R. L. Fitzpatrick, Phys. Rev. 133, A1143 (1964);

   M. Cutler and J. F. Leavy, Phys. Rev. 133, A1153 (1964).

14. O. Berkooz, M. Malamud, and S. Shtrikman, Solid State Commun. 6, 185 (1968).

15. F. Holtzberg, P. E. Seiden, and S. Von Molnar, Phys. Rev. 168, 408 (1968).

16. S. W. Kurnick and C. Meyer, J. Phys. Chem. Solids 25, 115 (1964).

17. F. Holtzberg and S. Methfessel, J. Appl. Phys. 37, 1433 (1966).

18. F. Holtzberg, T. R. McGuire, S. Methfessel, and J. C. Suits, J. Appl. Phys. 35, 1033 (1964).

19. M. Patrie, S. M. Golabi, J. Flahaut, and L. Domange, Compt. Rend. 259, 4039 (1964).

20. F. L. Carter, "Rare Earth Research III" (Ed. by L. Eyring, Gordon and Breach, New York, 1965), p. 495.

21. F. L. Carter, "Metallurgy of Semiconductor Materials", (Ed. by J. B. Schroeder, Interscience Publishing Co., New York, 1961), p. 245.

22. I. Bransky, N. M. Tallan, and A. Z. Hed, submitted to J. Appl. Phys.

23. F. Bertaut, J. Phys. Radium 13, 499 (1952).

34:17380

THE YTTERBIUM-CARBON SYSTEM: VAPORIZATION OF $YbC_{1.25 + y}$

John M. Haschke
and
Harry A. Eick

520 5600

Department of Chemistry
Michigan State University
East Lansing, Michigan

Dept. of Chemistry.

Abstract

The ytterbium carbon system, YbC_x, has been investigated over the composition range $0.33 < x < 2.00$; samples were prepared by direct reaction of the elements in sealed tantalum bombs. Tetragonal $YbC_{2.00}$, monoclinic $YbC_{1.25 + y}$ $(0 \leq y \leq 0.16)$, $YbC_{0.95}$, and dimorphic (fcc and rhombohedral) $YbC_{0.50 \pm z}$ have been identified by X-ray diffraction and elemental analysis. A linear variation of the carbon-rich $YbC_{1.25 + y}$ phase boundry and the monoclinic b parameter with temperature have been observed. The equilibrium vapor pressure of gaseous ytterbium in the $YbC_{1.25 + y}$ - $YbC_{2.00}$ two-phase region has been measured by a target collection Knudsen effusion technique. A partial phase diagram for the Yb-C system is proposed, third law enthalpy data for $YbC_{1.25 + y}$ are presented, and the variation of composition and lattice parameter is discussed.

Introduction

From a structural investigation of the lanthanide carbides, Spedding *et al.*[2] reported for ytterbium the dicarbide, a tri-metal monocarbide, and "an intermediate carbide" of undetermined composition. More recent studies on this system have been concerned with the carbon-rich phases. Krikorian *et al.*[3] investigated the dicarbide-carbon eutectic and searched for a tetragonal-cubic dicarbide transition. Haschke and Eick[4]

-424- 35

presented evidence for a two-phase region between $YbC_{1.5}$ and
YbC_2, and consequently for the existence of a sesquicarbide.
The present investigation was initiated to examine the metal-
rich portion of the ytterbium-carbon system, and in particular
to characterize the phase near the sesquicarbide composition.

Experimental

Ytterbium metal (Research Chemicals, Phoenix, Ariz., 99.9%,
impurities: Ca, Mg and Cu each < 0.01%) and CP graphite (Fisher
Scientific Co., Pittsburg, Pa.) which had been degassed in
vacuum at 1800°, were combined in the desired stoichiometric
ratios and sealed into outgassed tantalum ampoules by arc welding
in an argon atmosphere. Mixtures of the stoichiometry YbC_x,
$0.33 \leq x. \leq 2.00$, were heated at 1400-1500° by induction for
2-3 hrs in a 10^{-6}-10^{-7} torr vacuum. The samples were then
annealed at 800-1100° for approximately 1 hr before being
quenched. The surface temperature of the ampoules was measured
with a NBS-calibrated Leeds and Northrup disappearing filament
pyrometer, and was corrected for the emissivity of tantalum[5]
(0.49). A series of preparations with $x = 1.50$ were reacted at
the higher temperature, and then annealed for 1 hr at a carefully
measured lower temperature (817-1457°) prior to quenching.

The products were analyzed microchemically for both metal
and carbon content by conversion to the sesquioxide and carbon
dioxide. The CO_2 was determined gravimetrically by collection
ascarite. Samples were also examined by X-ray fluorescence
for possible tantalum contamination.

X-Ray powder diffraction patterns were obtained with a
Haegg-type Guinier camera. Samples, which were prepared in an
inert atmosphere glove box purged of water and oxygen, were
coated with a thin layer of paraffin oil to prevent hydrolysis
during transfer and exposure.

The vaporization reaction for the intermediate carbide, $YbC_{1.25 + y}$, was characterized by X-ray examination of the vaporization residues and by mass spectrometric analysis of the effusate species. The vapor species emanating from a sample contained in a molybdenum cell at 900-950° were examined with a Bendix time-of-flight mass spectrometer (Model 12-107) with a 10-70 eV ionizing electron beam. Target collection Knudsen effusion measurements were made as described previously[6]. Molybdenum effusion cells with orifice areas of 8.7×10^{-4} (run E), 21.4×10^{-4} (runs A, B), 42.6×10^{-4} (run D), and 60.4×10^{-4} (run F) cm^2 were charged with 0.3-0.4 g of $YbC_{1.25 + y}$ and 0.05-0.10 g YbC_2. Pressure measurements, which were made at successively increasing and decreasing temperatures in the range 783-1064°, were conducted to 75% sample depletion. The condensed effusates, which were collected on aluminum targets, were analyzed quantitatively by X-ray fluorescence.

Results

The four ytterbium-carbon phases: YbC_2, $YbC_{1.25 + y}$, $YbC_{0.95}$, and $YbC_{0.50 + z}$, which were observed by analytical and X-ray diffraction techniques, are considered individually below.

$YbC_{2.00}$. The golden-colored dicarbide was present in all reaction products in which $1.50 \leq x \leq 2.00$, but a mixture of dicarbide and a silver-grey phase was always present for $x < 2.00$. Because of their color difference, these phases could often be separated physically for elemental analysis. Samples with $x = 1.5$ which were quenched from various temperatures were also mixtures of dicarbide and grey phase. The composition

of the dicarbide separated from a $x = 1.50$ mixture quenched from 1475° was $YbC_{2.003} \pm 0.005$. The tetragonal lattice parameters ($a = 3.639 \pm 0.003$, $c = 6.110 \pm 0.008$ Å) remained invariant with temperature and bulk stoichiometry.

$\underline{YbC_{1.25 + \eta}}$. The composition of the previously mentioned silver-grey phase varied from $YbC_{1.25}$ to $YbC_{1.41}$ (55.5-58.5 at % C). The interplanar d-spacings of a preparation quenched from 1450°K were indexed on monoclinic symmetry ($a = 7.070 \pm 0.005$, $b = 7.850 \pm 0.004$, $c = 5.623 \pm 0.005$ Å, and $\beta = 90.99 \pm .09°$). In the $YbC_{1.25 + \eta}$ - YbC_2 two-phase region, the composition and the monoclinic b parameter of $YbC_{1.25 + \eta}$ varied linearly with quenching temperature (Figure 1). The refined cell parameters and compositions of crystallographically pure $YbC_{1.25 + \eta}$ samples are listed in Table I. In the $YbC_{0.95}$ - $YbC_{1.25 + \eta}$ two-phase region, the b parameter was invariant at 7.75 ± 0.01 Å (estimated error). Since this parameter also varies linearly across the variable composition region, the intersection of a graph of this parameter $vs.$ composition with the $b = 7.75$ Å line indicates the lower phase boundry is $YbC_{1.25 \pm 0.01}$.

$\underline{YbC_{0.95}}$. A second intermediate, silver-grey carbide has been observed near the monocarbide composition. The X-ray diffraction data (Table II) indicate a complex structure which we could not index on either orthogonal or trigonal symmetry. The diffraction pattern was independent of both annealing temperature and bulk composition. Analysis of a crystallographically pure product from a $x = 0.90$ stoichiometry indicated a composition of $YbC_{0.95 \pm 0.02}$.

-427-

$\underline{YbC_{0.50 \pm z}}$. The lowest observed carbide possesses a
metallic luster and appears in a region at the diytterbium
monocarbide (hypocarbide) composition. The X-ray diffraction
data were interpreted on the basis of a diphasic mixture of fcc
($a = 5.001 \pm 0.003$ Å) and hexagonal ($a = 3.541 \pm 0.004$,
$c = 17.46 \pm 0.02$ Å) structures. When the latter structure is
defined on rhombohedral symmetry, it yields $a = 6.167$ Å and
$\alpha = 33.33°$. Both phases were observed in all samples containing
the hypocarbide. The composition range ($\pm z$) of the hypocarbide
was not determined, but a crystallographically pure carbide
from a $x = 0.33$ mixture quenched from $1080°K$ indicated
$C:Yb = 0.43 \pm 0.02$. At the $x = 0.33$ composition, the carbide
was in equilibrium with unreacted metal.

The Phase Diagram. The results of the phase investigation
can be presented graphically in a temperature-composition phase
diagram (Figure 2). Whereas the cross-hatched regions about
Yb_2C and $YbC_{1.25 + y}$ demonstrate variable composition, that
about $YbC_{0.95}$ is only indicative of the uncertainty in com-
position of the phase. The experimental data points are
indicated by open circles; the data for solid, liquid, and
gaseous ytterbium are from Hultgren[7].

Vaporization. The combination of X-ray and mass spectro-
metric results indicates that $YbC_{1.25 + y}$ vaporizes according
to reaction one.

$$8YbC_{1.25 + y} \text{ (s)} \rightarrow (5 + 4y)YbC_2 \text{ (s)} + (3 - 4y)Yb \text{ (g)} \qquad (1)$$
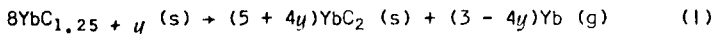
X-Ray diffraction data for the solid residues showed the presence
of only $YbC_{1.25 + y}$ and YbC_2, and the mass spectrum contained
only Yb^+.

The log P *vs.* 1/T results of five independent vaporization
experiments are presented in Figure 3. Since at each temperature
a different composition of $YbC_{1.25 + y}$ is in equilibrium with

-428-

the dicarbide, the data were treated by third law calculations.
For each vaporization temperature, the composition of $YbC_{1.25 + y}$
was determined from the correlation of quenching temperature and
composition. The heat capacity equation for each composition was
estimated by a modified Kopp's Rule procedure[8] employing heat
capacity data for ytterbium sesquioxide[9]. A free energy function
for each $YbC_{1.25 + y}$ composition was obtained by combination of the
heat capacity function with an estimated S°_{298} (19 eu), which was
assumed constant over the composition range ($YbC_{1.37} - YbC_{1.41}$).
The calculations, which were effected with free energy functions
for the dicarbide[4] and gaseous ytterbium[7] show that ΔH°_{298} for
reaction one varies monotonically from 114 kcal/gfw for $YbC_{1.41}$
($1050^{\circ}K$) to 106 kcal/gfw for $YbC_{1.37}$ ($1337^{\circ}K$). Enthalpies of
formation were calculated for each composition from the third law
results and the enthalpies of formation of $YbC_2(s)$[4] and $Yb(g)$[7].
These $\Delta H^{\circ}_{f\,298}$ values, which were averaged over composition
increments of the order of magnitude of analytical uncertainty
follow: $YbC_{1.400} - YbC_{1.409}$, $\Delta H^{\circ}_{f\,298} = -16.1_1 \pm 0.1_5$ kcal/gfw;
$YbC_{1.390} - YbC_{1.399}$, $\Delta H^{\circ}_{f\,298} = -15.8_7 \pm 0.2_3$ kcal/gfw; $YbC_{1.380} -$
$YbC_{1.389}$, $\Delta H^{\circ}_{f\,298} = 15.3_9 \pm 0.2_0$ kcal/gfw; and $YbC_{1.370} - YbC_{1.379}$,
$\Delta H^{\circ}_{f} = -14.3_0 \pm 0.1_5$ kcal/gfw. By assuming that the entropy of
vaporization of $YbC_{1.25 + y}$ per mole of gaseous ytterbium is
essentially identical to that observed per mole for YbC_2 (25 eu)[4],
the following $\Delta G^{\circ}_{f\,298}$ values were estimated for several com-
positions from the third law enthalpies and the free energies of
formation of $YbC_2(s)$[4] and $Yb(g)$[7]; $\Delta G^{\circ}_{f\,298}YbC_{1.41} \approx -16.8$ kcal/gfw;
$\Delta G^{\circ}_{f\,298}YbC_{1.39} = -16.2$ kcal/gfw; and $\Delta G^{\circ}_{f\,298}YbC_{1.37} = -14.7$
kcal/gfw.

Discussion

The ytterbium carbon system is very different from those of lighter lanthanide elements which exhibit well defined dicarbides, Pu_2C_3-type sesquicarbides, and fcc hypocarbides[2]. Only the tetragonal dicarbide has been observed across the entire lanthanide series[2,3,10], and for ytterbium, appears to occupy a narrow composition range up to 1750°K. As Spedding *et al.*[2] have noted, ytterbium forms an intermediate carbide, but apparently not at the Yb_2C_3 composition. The $YbC_{1.25 + y}$ phase occurs in the same region as the 55-58 at % solid solution reported for the ytterium-carbon system[11]. The Y-C phase boundry apparently does not exhibit a composition variation with temperature, and the X-ray data suggest that it is not isostructural with $YbC_{1.25 + y}$.

An intriguing feature of the Yb-C system is the apparent regular variation of the monoclinic b parameter and of the composition of $YbC_{1.25 + y}$ with annealing temperature. It is interesting to speculate concerning this behavior. The intermediate carbides (sesquicarbides) of the heavy lanthanides (Er-Lu) are not only structurally different from those of the lighter elements[2], but have different hydrolysis products[12] (equimolar mixtures of methane and propyne and essentially no C_2 hydrocarbons). Although no hydrolysis data are available for $YbC_{1.25 + y}$, it would be expected to hydrolyze like the carbides of Tm and Lu. The hydrolysis results suggest that carbon is present in the lattice as an essentially equimolar ratio of C^{-4} and C_3^{-4} ions; even if the propyne arose from association of C^{-4} and C_2^{-2} during hydrolysis, relatively large amounts of acetylene should also have been observed. For trivalent ytterbium, an equimolar mixture of either methanide and propynide or of methanide and acetylide ions gives the sesquicarbide stoichiometry. If the alkyne bond ($C\equiv C$) of either C_3^{-4} or C_2^{-2} is collinear with the b axis, replacement of the polyatomic group with a methanide ion (C_3^{-4} replaced by $2C^{-4}$ in one case, and C_2^{-2}

replaced by C^{-4} in the other) would account for both the variation of composition and lattice parameter. An increase in the fraction of C^{-4} groups requires that the stoichiometry shift to a more metal rich composition and that the b parameter decrease. The variation of methanide to alkynide ratio with temperature could easily arise from a shift in thermodynamic stability of the carbide ions. This interpretation is consistent with the invariance of a, c and β, whereas one employing di-trivalent substitution or a vacancy-interstitial model would predict variation of these parameters.

A unique feature of the Yb-C system is the existence of a phase near the monocarbide composition. Analytical results and preparative data suggest that the phase has a C:Yb ratio < 1.00. Since the stoichiometric 1:1 phase would be expected to exhibit the fcc lattice characteristic of other monocarbides[13], the $YbC_{0.95}$ composition is reasonable. It is possible that the phase is either an oxide carbide or an ytterbium tantalum carbide, but in all cases the sum of ytterbium and carbon percentages $\geq 99.85\%$ and tantalum could not be detected by X-ray fluorescence.

The diphasic mixture observed at the hypocarbide composition indicates the ytterbium phase is dimorphic, and is consistent with results reported for corresponding yttrium[14] and holmium[15] phases. As Atoji and Kikuchi[14] have noted for the yttrium system, the high temperature cubic phase of variable composition and the low temperature rhombohedral Yb_2C phase always coexist. The lattice parameter for the NaCl-type phase agrees with the value reported for Yb_3C[2]; however, the composition is more consistent with that reported for yttrium[16]. The rhombohedral anti-$CdCl_2$-type structure for Yb_2C is consistent with the data for the M_2C phases of other heavy lanthanides (Gd, Dy, Ho, Er), ytterium, and scandium[14].

No evidence was observed for the cubic YbC_{1-x} ($4.85 \leq a \leq 4.97$ Å) phase reported recently by Laplace and Lorrenzelli[17]. Since these workers prepared their samples by reacting YbH_2 with $(1-x)$ moles of carbon at 600°, their phase is probably an ytterbium carbide hydride.

The variation of the $YbC_{1.25 + y}$ composition with temperature has provided a unique opportunity to collect thermodynamic data across a wide composition region. The anomolous increase in the equilibrium ytterbium pressure with temperature is in agreement with the shift in the $YbC_{1.25 + y}$ phase boundry to more metal-rich compositions at higher temperature, and the thermodynamic data are consistent with the results for ytterbium dicarbide. The relative stability of the carbides requires that the enthalpy of vaporization of $YbC_{1.25 + y}$ per mole of Yb(g) must be less than that for the dicarbide (54.3 kcal/gfw)[4]; for $YbC_{1.25 + y}$ this $\Delta H°_{298}$ varies from 41.9 kcal/gfw to 48.3 kcal/gfw.

Although numerous questions about the ytterbium carbon system remain unanswered, this investigation has indicated clearly that its behavior is markedly different from that of the light lanthanides.

Tables and Figures

Table I: Lattice Constants and Composition of $YbC_{1.25 + y}$ Samples
Quenched from Various Temperatures (est. error *$\pm$ 0.01 $Å$,
**0.005 $Å$)

Quench Temp. ($°K$)	$a(Å)$**	$b(Å)$*	$c(Å)$**	$B(°)$	Yb:C
1091	6.067	7.91_0	5.621	90.88	—
1183	6.070	7.88_9	5.621	90.88	1.389 ± 0.015
1285	6.065	7.86_9	5.620	90.88	—
1398	6.065	7.85_8	5.621	90.97	1.360 ± 0.015
1490	6.070	7.85_4	5.624	90.94	—
1730	6.073	7.80_1	5.624	91.18	1.319 ± 0.006

Table II: Observed d-values and Relative Intensities of $YbC_{0.95}$

I	$d(Å)$	I	$d(Å)$
w-m	9.460	s	2.822
w-m	6.529	s	2.744
w-m	4.742	s	2.609
w	3.893	m	2.596
w	3.859	w	2.504
w-m	3.524	s	2.491
w	3.295	w	2.465
m-s	3.091	w-m	2.436
m	2.990	w	2.382
s	2.978	m-s	2.342

Figure I: Variation of b Parameter and Composition of YbC
with Quenching Temperature
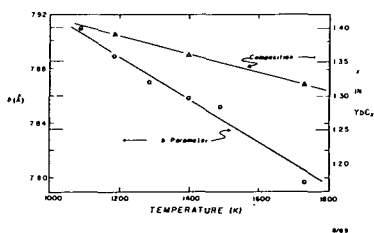
Figure 2: The Ytterbium-Carbon Phase Diagram
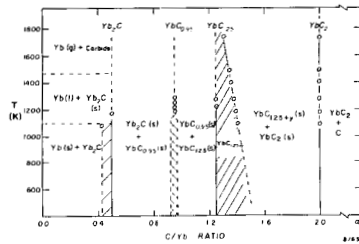
Figure 3: The Vapor Pressure of Ytterbium in Equilibrium with
YbC$_2$ and YbC$_{1.25 + y}$
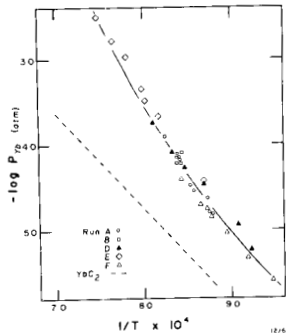
References

1. Abstracted in part from a manuscript accepted for publication
by J. Amer. Chem. Soc.

2. F. H. Spedding, K. Gschneidner, Jr., and A. H. Daane, J. Amer.
Chem. Soc., 80, 4499 (1958).

3. N. H. Krikorian, T. C. Wallace, and M. G. Bowman, Proceedings,
Collague International Sur les Derives Semi-metallique du Centre
National de la Recherche Scientifique et Universite du Paris
(Orsay), Paris, October 1965.

-434-

4. J. M. Haschke and H. A. Eick, *J. Phys. Chem.*, 72, 1697 (1968).

5. R. C. Weast, Ed., "Handbook of Chemistry and Physics" 45th Ed., The Chem. Rubber Publishing Co., Cleveland, Ohio (1964) p. E110.

6. J. M. Haschke and H. A. Eick, *J. Phys. Chem.*, 73, 374 (1969).

7. R. Hultgren, "Supplement to the Selected Values of Thermodynamic Properties of Metals and Alloys", Private Communication.

8. J. M. Haschke, Ph.D. Thesis, Michigan State University, East Lansing, Michigan, 1969.

9. L. B. Pankratz and E. G. King, U.S. Bureau of Mines Report of Investigations 6175, U.S. Department of Interior, Washington, D.C., 1963.

10. R. E. Gebelt and H. A. Eick, *Inorg. Chem.*, 3, 335, (1964).

11. O. N. Carlson and W. M. Paulson, *Trans. Met. Soc. AIME*, 242, 846 (1968).

12. H. J. Svec, J. Capellen and Saalfeld, *J. Inorg. Nucl. Chem.*, 26, 721 (1964).

13. E. K. Storms, "The Refractory Carbides", Academic Press, New York, N.Y., 1967.

14. M. Atoji and M. Kikuchi, U.S. Atomic Energy Commission Report, ANL-7441, Argonne, Ill., May 1968.

15. G. L. Bacchella, P. Meriel, M. Pinot and R. Lallement, *Bull. Soc. Fr. Mineral. Cristallogr.*, 89, 226 (1966).

16. R. Lallement, Centre d'Etude Nucleaires de Fontenay – Aux – Roses Rapport, CEA-R 3043 (1966).

17. A. Laplace and R. Lorrenzelli, Colloques Internation aux du Centre National de la Recherche Scientifique, Centre National de la Recherche Scientifique, NO 180, Paris-Grenoble, May, 1969.

# VAPOR PRESSURE MEASUREMENTS IN THE SmC_2-C AND TmC_2-C SYSTEMS

Robert L. Seiver*
and
Harry A. Eick*

520 86000

Abstract *Michigan State Univ., East Lansing. Dept. of Chemistry.*

Samarium and thulium dicarbides have been prepared by direct reaction of the elements in sealed tantalum bombs and an extensive study of their vaporization behavior has been completed. Container interaction which was observed was demonstrated to have negligible effect on the measured decomposition pressures. The cause of the large discrepancies in previous reports of the SmC_2 decomposition pressure was found to be oxygen contamination; most workers inadvertently have been studying the reaction:

$$Sm_2O_3(s) + 3 C(s) \rightarrow 2 Sm(g) + 3 CO(g) \qquad (1)$$
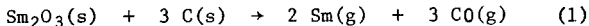
The oxide probably resulted from hydrolysis by atmospheric water vapor. Samples in this laboratory were observed to hydrolyze significantly even in a P_2O_5 charged glove-box. Handling procedures necessary to prevent this hydrolysis are discussed. The correct value of the decomposition pressure of samarium in equilibrium with $SmC_2(s)$ is

$$\ln P_{Sm(atm)} = [(-32,740 \pm 460)/T] + (8.84 \pm 0.25)$$

and that of thulium in equilibrium with $TmC_2(s)$ is

$$\ln P_{Tm(atm)} = [(-35,570 \pm 340)/T] + (8.98 \pm 0.18)$$

Results of second- and third-law data reductions are reported, and ΔH°_{f298} is 18.4 ± 1.3 kcal/gfw for $SmC_2(s)$ and, 20.0 ± 2.0 kcal/gfw for $TmC_2(s)$. The data extend the correlation between enthalpy of vaporization of the lanthanide dicarbides and vapor pressure of the pure metal.

Introduction

In recent years a number of investigations[1-5] of the samarium-carbon system have been reported. All workers agree that the most

---

* Department of Chemistry, Michigan State University, East Lansing, Michigan.

-436- 47

carbon-rich phase is the dicarbide, and that it has a very narrow
composition range and vaporizes exclusively by reaction one.

$$SmC_2(s) \rightarrow Sm(g) + 2C(s) \tag{1}$$
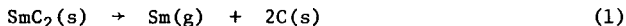
However, the reported values of the equilibrium samarium decomposition
pressures vary widely, even among different groups in the same labora-
tory[1-3]. *For example, at 1850 K reported pressures vary from* 1.0×10^{-4}
to 6.4×10^{-4} *atm.*

Close examination of the data revealed a trend with amount of
free carbon present, as shown in Figure 1. Comparison with Storms'
work on the uranium-carbon system[7] gives the following interpretation.
The "dicarbide" single phase region extends to a C/Sm atom ratio of
about 2.3, beyond which there is a two phase region to C/Sm = 5.
Either there exists a compound SmC_5 or up to 20 mole per cent samarium
dissolves in graphite. This interpretation is inconsistent with dir-
ect observations on the system.

Haschke and Eick[6] have reported a correlation of the enthalpy and
mode of vaporization of the lanthanide and alkaline earth dicarbides
with the vapor pressures of the pure metals at a fixed temperature.
Since samarium and thulium have the lowest vapor pressures of the
metals whose dicarbides are expected to decompose according to
reaction one, accurate values for the enthalpies of decomposition of
these carbides would be very useful in extending this correlation.

The present investigation was initiated to explain the apparent
*composition dependence of enthalpy in the Sm system and to provide
meaningful values for the correlation mentioned above.*

Experimental

Samarium or thulium metal (Michigan Chemical Corp., St. Louis,
Michigan, 99.9%) was combined with CP graphite (Fisher Scientific Co.,
Pittsburgh, Pa., degassed in vacuum at 2000° before use) in stoichio-
metric dicarbide composition and sealed into outgassed tantalum ampou-
les by arc welding in an argon atmosphere. Mixtures were heated to

1400-1600° by induction for 2-6 hours in vacuum. The ampoules were opened and the product stored in an argon filled glove-box.

Samples were analyzed for metal content both by direct combustion to the sesquioxide and by precipitation as oxalate, followed by firing to the sesquioxide. In direct combustion the CO_2 was collected on ascarite and determined gravimetrically. X-Ray powder diffraction patterns were obtained before and after the vapor pressure measurements with a Haegg-type Guinier powder camera. Samples for X-ray analysis were coated with a thin layer of paraffin oil to prevent hydrolysis during transfer and exposure.

Vapor pressure measurements were made by target collection Knudsen effusion as described previously[8]. Knife-edged molybdenum effusion cells with orifice areas of 7.2×10^{-4} (runs 15, 16A, 16B, 16C), 25.8×10^{-4} (runs 11, 12, 1Mo, 2Mo) and 39.2×10^{-4} (runs 4, 6, 7) cm^2 for Sm-C measurements and of 11.8×10^{-4} (run 5), 18.15×10^{-4} (run 12), 35.8×10^{-4} (runs 13, 14) and 64.0×10^{-4} (runs 1, 2, 8) cm^2 for Tm-C measurements were used. These cells were charged with 0.25-0.65 g samples. To study high carbon compositions, the dicarbide either was mixed with outgassed graphite before it was loaded into the Knudsen cell (runs 11, 15, 16A, 16B, 16C for Sm; 13, 14 for Tm) or was inserted into a graphite lined cell (run 12 Sm), and in two cases (runs 1Mo and 2Mo) an equimolar mixture of SmC_2, graphite, and powdered Mo (325 mesh, Fansteel Corp., North Chicago, Illinois) was used to charge the cell.

Pressure measurements were made at successively increasing and decreasing temperatures in the range 1630-2050 K for Sm and 1660-2130 K for Tm. Temperatures were measured by sighting on a black-body hole in the base of the cell with an NBS-calibrated Leeds and Northrup disappearing filament pyrometer. The effusate was condensed onto aluminum targets which were analyzed quantitatively by X-ray fluorescence.

Results

All preparations of SmC_2 yielded the golden-colored tetragonal form reported by Spedding,[10] while preparations of TmC_2 yielded this form when quenched or the black low-symmetry form reported by Krupka[11] on slow cooling. Analytical results were generally metal-rich, ranging from $C/M = 1.78$ to 2.02. Oxygen contamination, determined by difference, was typically around 0.8% by weight.

The vaporization behavior of samples with little excess carbon was qualitatively similar to that reported previously. No unusual behavior was noted for samples with $C/M < 3$. Metal rich samples showed high erratic pressure at first, then stabilized. Calculation from weight loss data showed that stable pressures were achieved very close to the $MC_{2.00}$ composition.

When excess graphite was added to the effusion samples, however, behavior was quite different from that reported by earlier workers. Pressures were first high, then decreased sharply after 2-3 hours heating. The first part showed a lower temperature dependence, as predicted in Figure 1, but not the lower pressure that was also reported. The second part of the run, however, gave pressures identical to those measured with little excess carbon present. A typical example of such a run is shown in Figure 3a. The data points are numbered in the order in which they were taken. Further experiments showed that the behavior was dependent on elapsed time, not ascending or descending temperature.

Two other features were observed about the first part of such runs. First, residual pressure in the vacuum system was somewhat higher than expected. Second, for TmC_2-C samples, the duration of the first part of the run was related to the duration of storage of the sample, and this initial high pressure burst could nearly be eliminated by using freshly prepared $TmC_2(s)$ and graphite. It had been observed that $TmC_2(s)$ is not quite as susceptible to hydrolysis as $SmC_2(s)$.

To check for possible container interaction, an effusion experiment was effected in a cell fitted with a graphite liner (run 12). The behavior was almost identical to that of run 11 (Figure 4a). The two experiments in which molybdenum powder was added to the sample did not show the initial high pressures. Careful examination of the X-ray diffraction patterns of the samples after effusion showed in two instances the three strongest lines of the Mo_2C pattern, but even when 50% of the sample had been depleted these were among the weakest lines observed. Thus, container interaction does not affect the vapor pressure of the metal significantly.

In one experiment with a high carbon content sample, a Tesla coil was used to excite a discharge in the residual gas. The color of the discharge was a light blue--a color attributed to a carbon monoxide discharge.

In experiment 16, a sample of $SmC_2(s)$ was mixed with graphite and vaporized (16A) in the normal manner. It was then stored, using handling techniques described below, for only the time required to prepare the apparatus for a new run (16B). It was then stored again using the same precautions, but with 17 mg calcined Sm_2O_3 added before the next run (16C).

The drybox was modified for this latter experiment so that the argon atmosphere was recirculated through columns of activated alumina regenerated at 425°, instead of being exposed to open dishes of phosphorus pentoxide. Oxygen was removed using the catalyst BASF R3-11. Also, the Knudsen cell was bathed in a dry argon stream during the transfer to the target collection apparatus. The time between runs 16A and B, and between 16B and C, was less than 4 hours.

The results are shown in Figure 4b,c,d. Run 16A gave the expected behavior; although the scatter was somewhat higher than usual, points 5, 6, 7 and 8 are within 2.5σ, or 99% confidence level, of the line finally assigned to condensed SmC_2. Points 1, 2, 3 and 4 are high by

3.5-4.5σ. A high system pressure was observed during the exposure of targets 1-4. Run 16B did not show this initial behavior, although there was a brief pressure surge as the cell was being heated. The pressure was high throughout run 16C, and all points from it are high, five of them by >2.5σ. Thus the effect noted in the first part of the high-carbon experiments is identical to that which results from addition of oxide. In view of the known hydrolysis behavior of the dicarbides it can be concluded that traces of oxide caused the anomalous behavior in the high carbon content runs.

All SmC_2 data points where oxygen contamination was absent are shown in Figure 2. The linear least-squares equation describing the 62 data points in the temperature range 1630-2050 K is

$$\ln P_{Sm}(atm) = [(-32,7_{40} \pm 4_{60})/T] + (8.8_4 \pm 0.2_5) \qquad (2)$$

where the uncertainties are calculated standard errors. Likewise for TmC_2, as shown in Figure 3, the linear least-squares line through the 46 data points in the temperature range 1660-2130 K is

$$\ln P_{Tm}(atm) = [(-35,5_{70} \pm 3_{40})/T] + (8.9_8 \pm 0.1_8) \qquad (3)$$

From these equations, the following thermodynamic data, together with their standard deviations, are calculated: For SmC_2, (reaction one), $\Delta H^{\circ}_{1840} = 65.0_7 \pm 0.9_1$ kcal/gfw, $\Delta S^{\circ}_{1840} = 17.5_7 \pm 0.5_0$ eu; and for TmC_2 in the analogous reaction 4, $\Delta H^{\circ}_{1895} = 70.6_8 \pm 0.6_8$ kcal/gfw, $\Delta S^{\circ}_{1895} = 17.8_5 \pm 0.3_6$ eu. These second-law values have been corrected to 298 K using published heat content and entropy data[13-15] and the following assumptions. The heat content of SmC_2 and TmC_2 was assumed to be that of CaC_2 of the same crystal modification. The ΔH_{trans} for the tetragonal to cubic conversion (1.33 kcal/gfw)[14] of CaC_2 at 720 K was used but correction was made for the fact that the transition occurs at 1170 K for SmC_2 and 1355 K for TmC_2[16]. The results of this data reduction with the listed error indicating the composite of standard deviation and estimated error in thermodynamics values are: $\Delta H^{\circ}_{v298}(SmC_2) =$

$= 68._4 \pm 1._3$ kcal/gfw; ΔS°_{v298} (SmC$_2$) $= 22._4 \pm 1._2$ eu; ΔH°_{v298} (TmC$_2$) $=$
$77._7 \pm 1._3$ kcal/gfw, ΔS°_{v298} (TmC$_2$) $= 26._2 \pm 1._2$ eu.

Third law ΔH°_{v298} has been calculated using free energy functions
approximated for MC$_2$(s) as follows[15,17,18]: fef$_{MC_2}$ = fef$_{CaC_2}$ $-$
fef$_{Ca}$ + fef$_M$. These were combined with published free energy func-
tions for graphite, gaseous samarium, and gaseous thulium to obtain
Δfef values for reaction one. The third law values are ΔH°_{v298} (SmC$_2$)
$= 67._2 \pm 1._2$ kcal/gfw and ΔH°_{298} (TmC$_2$) $= 73._3 \pm 1._2$ kcal/gfw. No
temperature trend was observed for either third-law treatment. The
second- and third-law enthalpies for TmC$_2$ are not in particularly
good agreement. It is not known whether this lack of agreement is due
to failure to consider the low temperature, low symmetry modification
of TmC$_2$ reported by Krupka, et al.[11]

The averaged values of ΔH°_{v298} have been combined with the enthalpy
of formation of the gaseous metals at 298 K to give ΔH°_{f298} (SmC$_2$) $=$
$18._4 \pm 1._3$ kcal/gfw and ΔH°_{f298} (TmC$_2$) $= 20._0 \pm 2._0$ kcal/gfw.

Discussion

It is proposed that the cause of anomalous behavior in high-
carbon samples is oxide contamination. The reaction actually being
studied is

$$Sm_2O_3(s) \quad + \quad 3C(s) \quad \rightarrow \quad 2Sm(g) \quad + \quad 3CO(g) \tag{5}$$
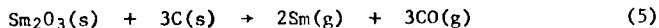
or a similar reaction involving an oxidecarbide, which gives a higher
samarium pressure and also accounts for the higher residual system
pressure. Vickery has used[12] a similar reaction (6) to prepare con-
densed SmC$_2$;

$$Sm_2O_3(s) \quad + \quad 7C(s) \quad \rightarrow \quad 2SmC_2(s) \quad + \quad 3CO(g) \tag{6}$$
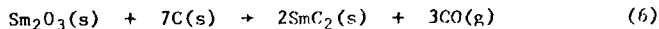
he states that elemental samarium was observed upon micrographic
examination of quenched reaction mixtures. This reaction probably
proceeds in two steps, the first of which is reaction five. The
observation of the CO color in the discharge supports this hypothesis.

Runs 1Mo and 2Mo did not show initial high pressures probably because the oxygen was lost as volatile molybdenum oxides.

All reported lower pressures and enthalpies of vaporization from high carbon content samarium dicarbide samples have concerned experiments conducted with a mass spectrometer. Because of the speed with which mass-spectrometric measurements can be made, the experiments were probably complete before residual oxygen had been evolved completely as CO(g), and the change in pressure was not observed. Likewise, absolute pressure measurements with a mass spectrometer are at best uncertain; and without the above mechanism it is very difficult to rationalize higher Sm pressures over Sm-depleted samples. Calibration data were probably weighted to remove this effect. This weighting yielded as a result the very high pressures reported for stoichiometric samples.

There is only one value for the vapor pressure of Sm and Tm in the entire two-phase MC_2-C region. The value for samarium is very close to that reported by Faircloth[3], whose work was done by target collection on almost stoichiometric samples. Our work extends and confirms his data. Oxygen contamination was probably present both in Faircloth's work and in the portions of this study done on nearly stoichiometric samples, but its effect was masked by the similar effect of sesquicarbide usually present in dicarbide preparations. The failure to observe an oxide species in X-ray diffraction patterns is not disturbing. First, it would not be present after a vaporization experiment; second, run 16C shows that the sesquioxide contamination required is so small it would be unobservable by X-ray diffraction; and third, oxide formed by hydrolysis has very poor crystalline struc- ture and would have to be annealed before it could be observed, even if it is present in large amounts.

The values of ΔH°_{298} for vaporization of SmC_2 and TmC_2, when plotted against the pure metal $\log P_{1500}$ of -1.60 and -2.36 respectively,

extend very well Haschke's correlation[6] for the lanthanide and alkaline earth dicarbide enthalpies of vaporization.

Acknowledgment. Partial support of the U.S. Atomic Energy Commission Contract AT(11-1)-716 is gratefully acknowledged.

References

1. J. Cuthbert, R. L. Faircloth, R. H. Flowers, and F. C. W. Pummery, Proc. Brit. Ceram. Soc., 8, 155 (1967).

2. D. F. Avery, J. Cuthbert, and C. Silk, Brit. J. Appl. Phys., 18, 1133 (1967).

3. R. L. Faircloth, R. H. Flowers, and F. C. W. Pummery, J. Inorg. Nucl. Chem., 30, 499 (1968).

4. N. D. Stout, C. L. Hoenig, and P. C. Nordine, J. Amer. Ceram. Soc., 52, 145 (1969).

5. P. A. Pilato, Ph.D. Thesis, Michigan State University, East Lansing, Michigan, 1968.

6. J. M. Haschke and H. A. Eick, J. Phys. Chem., 72, 1697 (1968).

7. E. K. Storms, "The Refractory Carbides," Academic Press, New York, N.Y., 1967. Especially p. 208.

8. J. M. Haschke and H. A. Eick, J. Phys. Chem., 73, 374 (1969).

9. J. M. Haschke, R. L. Seiver, and H. A. Eick, U.S. Atomic Energy Commission Report, COO-716-033 (1968).

10. F. Spedding, K. Gschneidner, Jr., and A. H. Daane, J. Amer. Chem. Soc., 80, 4499 (1958).

11. M. C. Krupka, N. H. Krikorian and J. C. Wallace, presented at the Seventh Rare Earth Conference, Coronado, Calif. (October 1968).

12. R. C. Vickery, R. Sedlacek and A. Ruben, J. Chem. Soc., 103, 498 (1959).

13. R. C. Feber and C. C. Herrick, "Ideal Gas Thermodynamic Functions of Lanthanide and Actinide Elements," Los Alamos Scientific Laboratory Report LA-3184, 1965.

14. K. K. Kelley, Bureau of Mines Bulletin 584, U.S. Government Printing Office, Washington, D.C., 1960.

15. C. E. Wicks and F. E. Block, Bureau of Mines Bulletin 605, U.S. Government Printing Office, Washington, D.C., 1963.

16. N. H. Krikorian, J. C. Wallace, and M. G. Bowman, Proceedings, Collaque International Sur les Derives Semimetallique du Centre National de la Rescherche Scientifique et Universite du Paris, Orsay, 1965.

17. R. Hultgren, R. L. Orr, P. D. Anderson, and K. K. Kelley, "Selected Values of Thermodynamic Properties of Metals and Alloys," John Wiley and Sons, New York, N.Y., 1963.

18. R. Hultgren, "Supplement to the Selected Values of Thermodynamic Properties of Metals and Alloys," Private Communication.

Figure I. Apparent Dependence
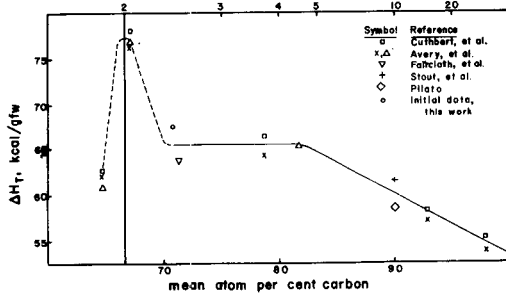of Enthalpy on Bulk Composition

Figure 2. Equilibrium Pressure
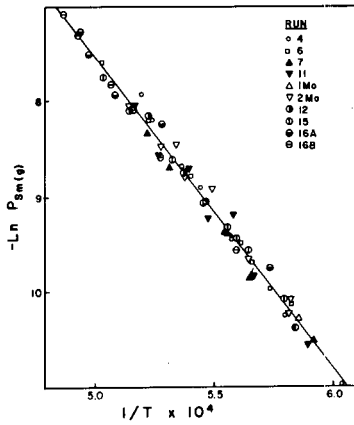of Samarium Vapor over
Samarium Dicarbide

Figure 3. Equilibrium Pressure
of Thulium Vapor over
Thulium Dicarbide
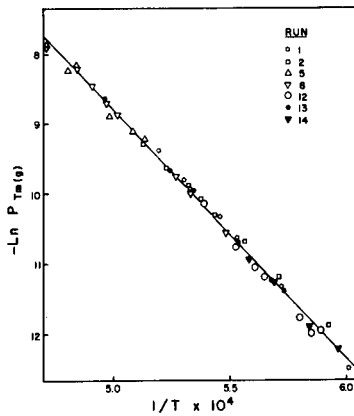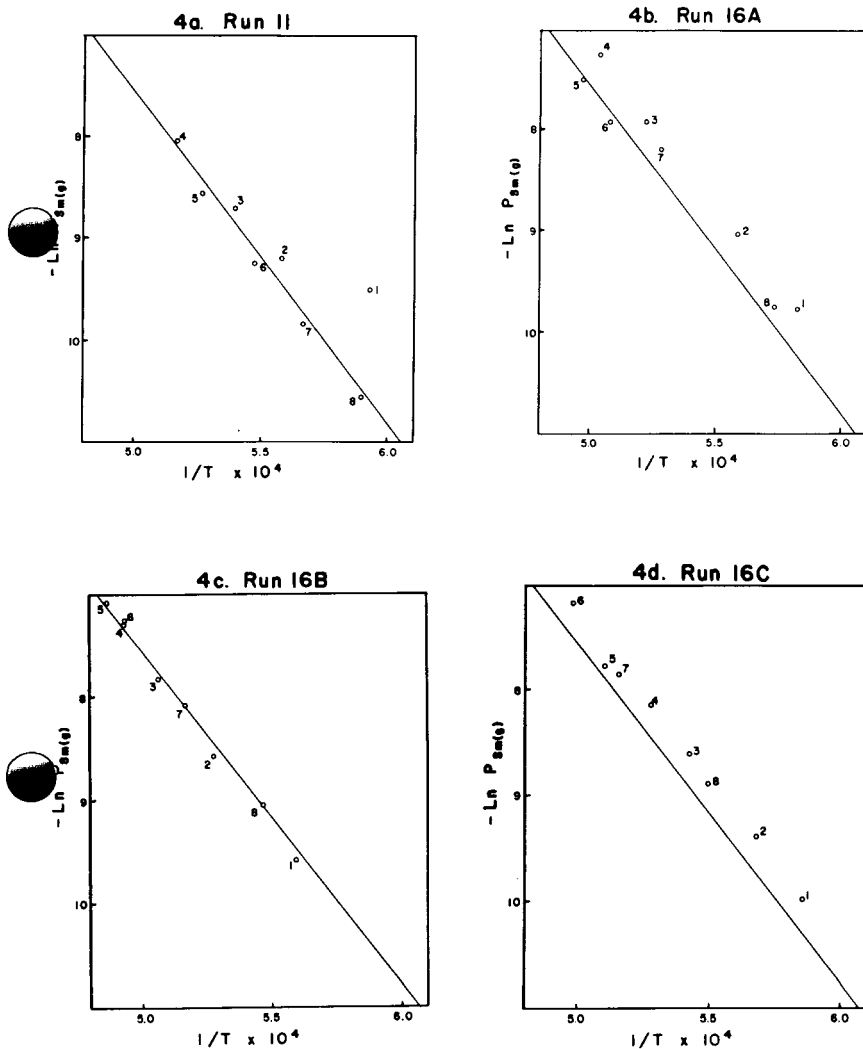
FIGURE 4. Vaporization Behavior of High Carbon Content Samples

ISOTOPIC ENRICHMENT OF THE PRODUCT OF A LANTHANIDE
NEUTRON CAPTURE REACTION*

David O. Campbell
Oak Ridge National Laboratory
Oak Ridge, Tennessee

617 1000

ABSTRACT

A procedure is described which results in a substantial enrichment of the product isotope resulting from neutron capture by a lanthanide isotope. The lanthanide is loaded by ion exchange into a faujasite zeolite (Linde X or Y), given an appropriate heat treatment, irradiated in a nuclear reactor, and finally eluted with a concentrated salt solution. Typically, the eluate contains about 50% of the neutron capture product and less than 1% of the target isotope. The reaction has been demonstrated with praseodymium, neodymium, erbium and thulium, as well as with zeolites containing two rare earths.

INTRODUCTION

The motivation for this work was the need to prepare multigram amounts of isotopes like ^{247}Cm and others which may have great value but which exist only in low concentrations in products from high exposures in nuclear reactors. The work reported here is primarily concerned with studies of lanthanide elements, which were used as stand-ins for actinides during initial studies. The lanthanides, however, are of interest in themselves, and they also offer potential large scale applications. For example, ^{170}Tm and ^{171}Tm have been considered for heat sources.

-448- 59

For several decades there has been research directed toward the separation and enrichment of the product isotope resulting from a nuclear reaction, with respect to the target isotope. The well-known Szilard-Chalmers reaction[1] presented a solution to the problem, but there are cases in which application of this reaction is difficult. In particular, if significant production of a nuclear reaction product is desired, as compared to tracer levels, then radiation damage may seriously limit application of this method.

Such an enrichment reaction is necessary only if the product and target are isotopes of the same element, as in a neutron capture (n,γ) reaction, since a chemical separation is possible if they are different elements. If they are isotopes of the same element a chemical separation is generally not practical, and separation depends on the physical effects of the nuclear reaction which created the product, or on a physical method such as electromagnetic separation.

The physical effects result from recoil of the nucleus. In the case of neutron capture by a lanthanide or actinide the recoil energy arises from prompt gamma emission following neutron capture. Although the total energy dissipated is in the region of 5 to 10 Mev, the product nucleus receives only 100 to 200 ev at most. If there are two or more gammas emitted, the product may receive very much less recoil energy.

In the Szilard-Chalmers reaction the recoil energy breaks a chemical bond; the product is ejected from a molecule in which it was bound and with which it will not readily recombine (for example, iodine in ethyl iodide). In the case of lanthanide elements such a reaction is less available because these trivalent metals do not readily form covalent compounds like ethyl iodide. They do form some rather stable chelates, however, and such compounds are being studied elsewhere. Such chelates are organic, and organic compounds are not suited for extended irradiation in nuclear reactors.

In view of these factors we considered the possible behavior, under irradiation, of various inorganic materials which could contain lanthanides or actinides. Certain

-449-

zeolites were selected for study because of their promising combination of both chemical and physical properties.[2] Zeolites are inorganic, so they might have adequate radiation stability to permit significant production. They are composed of aluminum, silicon and oxygen, all of which have small neutron capture cross-sections. They contain exchangeable cations which permit one to introduce various metals into the structure. Finally, they contain a remarkable system of interconnected pores.

ZEOLITE PROPERTIES

One class of zeolites was selected for initial study, consisting of the mineral faujasite and the structurally similar synthetic zeolites, Linde X and Linde Y. All experiments to date have been done with Linde X or Y. The sturcture of this zeolite is known (see reference 2 for review), and the important feature is the dual pore system, consisting of two sizes of interconnected pores (Fig. 1). Zeolites consist of tetrahedra formed by the four oxygen atoms coordinated about a central metal atom, silicon or aluminum; these SiO_4 and AlO_4 tetrahedra are interconnected by the oxygen atoms, each of which is shared between two such tetrahedra. In Fig. 1, each intersection of lines represents a metal atom, Si or Al, and the lines represent the bridging oxygen atoms about each metal.

The small pore system (shaded in Fig. 1) consists of truncated octahedra, called sodalite cages, interconnected at alternate hexagonal faces by hexagonal prisms. The octahedra are approximately 6.5 Å in free diameter--large enough to contain four water molecules; and the hexagonal faces have a free diameter of about 2.5 Å, near the size of many ions. This network of small pores also defines a second system of much larger pores, called supercages. The supercages are about 12 Å in free diameter and interconnected by 12-sided openings of 8 to 9 Å diameter. The supercages and the small pore system communicate via the hexagonal faces with 2.5 Å free diameter.

The ion exchange property arises from the presence of aluminum in the structure, in place of silicon. Aluminum lacks one positive charge to satisfy the four shared oxygens around it, so there is one equivalent of some cation in the vicinity of each AlO_4 tetrahedron in the structure.

Commercial Linde X or Linde Y consists of small crystals of this structure, usually agglomerated into larger shapes with a clay and alumino-silicate binder. The resulting material has an ion exchange capacity of a few milliequivalents per gram of zeolite, depending on the particular material.

Lanthanide exchanged Types X and Y zeolites are valuable catalysts for certain industrial chemical processes, and as a result they have received consider-able study during the last few years. When these zeolites are contacted with an aqueous lanthanide solution the lanthanide ions are strongly absorbed, readily displacing alkali and alkaline earth ions.[3] The lanthanide ions enter the large supercages. When such an exchanged zeolite is heated to dehydrate the system (350 to 700°C) the lanthanide ions move into the small pore system;[4,5] and they are not readily exchanged back out of the crystal.

This structure offers the possibility for separation of the product of a nuclear reaction. The target material, lanthanide or actinide, is fixed in the small pore structure, and the large pores are essentially unoccupied. Gamma recoil will eject product atoms from the small pores, and some fraction of them should end up in the supercages where they may be accessible to exchange.

EXPERIMENTAL

Nearly all work has been done with Linde 13X zeolite exchanged with several lanthanides, including praseodymium, neodymium, erbium and thulium. The prepara-tion of a praseodymium loaded zeolite (PrX) is typical: contact 1 gram Linde 13X for 15 minutes with excess $Pr(NO_3)_3$ solution (the pH should be near 5), repeat, wash, dry, and ignite to 500°C to drive the lanthanide into the small pore structure;

repeat the loading procedure to assure a high degree of exchange; after ignition elute (or leach) the zeolite several times with 10 $\underline{M}$ LiCl solution to remove any lanthanide which is readily exchangeable; contact with $Ca(NO_3)_2$ solution to displace most of the lithium ions, wash, dry, and again ignite to 500° to yield a dry product for reactor irradiation.

The zeolites were irradiated in a pneumatic tube facility in the Oak Ridge Research Reactor at a thermal flux of 4 to 5×10^{13} n/cm^2·sec for times from a few seconds to ten minutes. The irradiated zeolites were eluted by contacting with 10 $\underline{M}$ or 11 $\underline{M}$ LiCl solution (or other concentrated salt solutions). The yield of the neutron capture product was determined from the intensity of the characteristic gamma ray in both the zeolite and the eluate, measured with a 3×3 in. NaI crystal spectrometer with 512 channels, or, for low energy gammas, a 5 cm^3 lithium drifted germanium detector with a 400 channel analyzer. Conditions were chosen to provide adequate resolution to avoid interferences such as manganese, copper, sodium and chlorine. The amount of target material eluted along with the product was determined by activation analysis; the product was recovered by precipitation with aluminum carrier and reirradiated, generally for a time longer than the initial zeolite irradiation. Appropriate corrections were made for decay.

RESULTS AND DISCUSSION

Typical results are shown in Table 1 for Linde X zeolite exchanged with natural praseodymium, neodymium, erbium, and thulium, respectively. Generally, 40 to 60% of the neutron capture product was eluted, along with about 1% of the target material. Thus, enrichment factors (the ratio of specific activity of the eluate to the average specific activity of all material) are in the vicinity of 50.

In two cases (A and C) the target zeolite was recovered after the first irradiation, reirradiated, and eluted again. Yields were similar in the second cycle, showing that the same zeolite may be re-used, at least with short irradiations such as these.

There were several variations in elution procedure. Sodium sulfate was generally a somewhat less effective eluant than lithium chloride. Similar results were observed at temperatures of 25° and 90°C. Time of elution is clearly an important variable, but it was not studied systematically. Most of the product recovered was eluted in the first fraction, even with elution times of five minutes or less (C). Subsequent elution, even for hours, removed little product (Tables 1 (D), 2 and 3).

These results indicate that both light and heavy rare earths may be used, with results which are generally similar. There appears to be some difference in yields, with praseodymium usually giving higher yields than the others. This could result from physical effects (the recoil energy distribution of the product) or from chemical effects (the extent and nature of loading with different rare earths).

The amount of stable target material in the activated product was usually less than 1%, but sometimes more. High values would result from inadequate elution of the zeolite before irradiation, or from entrainment of some of the zeolite with the eluate. However, we have been unable to reduce target elution to less than a few tenths of a percent, and this places an ultimate limit on attainable enrichment.

The effect of partial exchange (or loading) of the zeolite is shown for two different loadings in Table 2. Only enough praseodymium was used to exchange 25% or 40% of the total zeolite capacity; the rest of the exchangeable ions were calcium and a little sodium and lithium. At the lower loading the yield was only a few percent, even after elution over a weekend. At 40% loading the yield was much higher, but still less than that of highly loaded zeolites. In both cases, what did elute was enriched. These results show that yield depends markedly on the extent of loading of lanthanide in the zeolite.

A high yield is obtained, however, if the total lanthanide loading is large; not necessarily just the target element. This is shown in Table 3 for three zeolites,

all partially loaded to the same praseodymium content. When the rest of the exchange capacity was calcium, the yield was low as in Table 2. When the zeolite was highly loaded by adding erbium or yttrium the yield was high. In fact, the ^{142}Pr yield from the PrYX zeolite was the highest we have obtained.

With the PrErX zeolite it was practical to determine the behavior of both ^{142}Pr and ^{171}Er. It is interesting that the yield of erbium was lower; and, in fact, both elements behaved very much as they do alone. Perhaps the lower yield of erbium in this case reflects a lower fraction of neutron capture reactions in which the product atom has enough recoil energy to be freed.

Similar studies are being made with actinide elements, particularly americium and curium. In general, results are similar, and best results have been obtained with Linde X partially loaded with actinide and then subsequently loaded with excess yttrium or praseodymium. There is a tendency for elution of target actinides to be higher than for lanthanides. This may result from damage by the alpha radiation of the actinides, but it is not related in an obvious way to the alpha intensity.

FUTURE APPLICATIONS

The isotope enrichment process has been demonstrated for production of enriched neutron capture isotopes at tracer and somewhat higher levels useful for many experimental purposes. A yield of about 50% of the neutron capture product is usually obtained, along with less than 1% of the target isotope. The process appears to be applicable generally to trivalent lanthanide and lanthanide-like ions. It is obviously applicable to reactions yielding a different product element from the target.

In regard to production of significant quantities of enriched isotopes, the primary uncertainty is the effect of high radiation exposures. No significant effects have been observed at exposures of ten minutes at 5×10^{13} $n/cm^2 \cdot sec$, but production of a heavy isotope like ^{247}Cm benefits from exposures hundreds of times

greater than this. Long irradiations have not yet been made. Linde X is reported[6] to maintain its gas absorption and ion exchange properties at exposures up to the range of 10^{19} fast n/cm^2, but fast neutron damage will certainly place an ultimate limit on this process.

The product obtained by conventional neutron irradiation of ^{246}Cm contains about 2% ^{247}Cm at equilibrium. With enrichments similar to those reported here for rare earths, one could ideally achieve a product containing about 40% ^{247}Cm. However, if one limits the neutron exposure to a fast fluence of 10^{19} in a highly thermal reactor (an exposure far below the optimum for ^{247}Cm production), then the ^{247}Cm content of the enriched product would be 10 to 15%. Such a product would be vastly superior to any now obtainable as a feed for electromagnetic separation.

REFERENCES

1. L. Szilard and T. A. Chalmers, Nature 134, 462 (1934).
2. P. V. Venuto and P. S. Landis, Advances in Catalysis, Vol. 18, p. 263, Academic Press, New York (1968).
3. H. S. Sherry, J. Colloid and Interface Science 28, 288 (1968).
4. D. H. Olsen, G. T. Kokotail, and J. F. Charnell, ibid. 28, 305 (1968).
5. J. V. Smith, J. M. Bennett, and E. M. Flanigen, Nature 215, 241 (1967).
6. L. V. C. Rees and C. J. Williams, Trans. Far. Soc. 61, 1481 (1965).

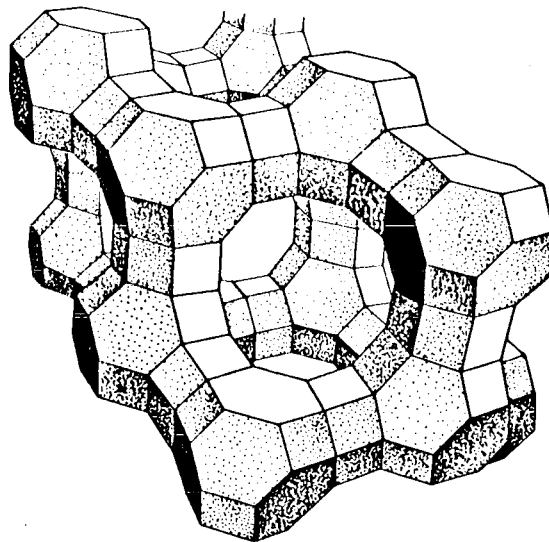Fig. 1.   Structure of Faujasite (Linde X).

Table 1. Neutron Capture Product Enrichment by Zeolite Elution

Description	% of Isotope in Fraction	
(A) Irradiate 100 mg PrX 0.5 min	^{141}Pr	^{142}Pr*
Elute with:		
1 ml 11 M LiCl, 10 min, 25°	0.76	49.
1 ml 11 $\overline{M}$ LiCl, 15 min, 90°	0.54	13.
Remaining in PrX	98	38.
Wash PrX, ignite to 450°, reirradiate 1 min		
Elute with:		
1 ml sat. Na$_2$SO$_4$, 10 min, 25°	0.52	40.
1 ml 11 M LiCl, 15, 90°	0.59	18.
Remaining in PrX	#	42.
(B) Irradiate 52 mg NdX 15 sec	^{148}Nd	^{149}Nd*
Elute with:		
1 ml sat. Na$_2$SO$_4$, 10 min, 90°	0.75	17.
1 ml 10 M LiCl, 5 min, 90°	0.8	25.
1 ml 10 $\overline{M}$ LiCl, 5 min, 90°	0.5	6.
Remaining in NdX	#	52.
(C) Irradiate 100 mg ErX 15 sec	^{170}Er	^{171}Er*
Elute with:		
1 ml 10 M LiCl, 5 min, 25°	1.5	36.
1 ml 10 $\overline{M}$ LiCl, 10 min, 90°	0.8	10.
1 ml 10 $\overline{M}$ LiCl, 20 min, 90°	3.6	8.
Remaining in ErX	94.	46.
Wash ErX, ignite to 500°, reirradiate 2 min		
Elute with:		
1 ml 10 M LiCl, 1.5 min, 25°	0.8	25.
1 ml 10 $\overline{M}$ LiCl, 15 min, 25°	0.6	11.
Remaining in ErX	#	64.
(D) Irradiate 50 mg TmX 10 min	^{169}Tm	^{170}Tm*
Elute with:		
3 ml 10 M LiCl, 15 min, 25°	#	36.
3 ml 10 $\overline{M}$ LiCl, 15 min, 25°	#	4.
3 ml 10 $\overline{M}$ LiCl, 18 hr, 25°	#	3.
Remaining in TmX	#	57.

not determined.

* radioactive neutron capture product.

Table 2. ^{142}Pr Yield from Partially Loaded Zeolite

Description	% of Isotope in Fraction	
	^{141}Pr	^{142}Pr*
(A) Linde X 25% saturated with Pr		
Irradiate 100 mg for 1 min		
Elute with:		
1 ml 10 M LiCl, 4 min, 25°	0.2	3.2
1 ml 10 $\overline{M}$ LiCl, 2 min, 25°	0.2	1.6
1 ml 10 $\overline{M}$ LiCl, 66 hr, 25°	0.1	3.2
Remaining in PrX	#	92.
(B) Linde X 40% saturated with Pr		
Irradiate 100 mg for 1 min		
Elute with:		
1 ml sat. Na$_2$SO$_4$, 5 min, 25°	0.34	14.1
1 ml 10 M LiCl, 5 min, 25°	0.36	9.7
Remaining in PrX	#	76.2

not determined.

* neutron capture product.

Table 3.   Effect of Mixed Loading on Yields

PrX   - 30% Pr--70% Ca loaded Linde 13X
PrErX - 30% Pr--70% Er loaded Linde 13X
PrYX - 30% Pr--70% Y loaded Linde 13X

     Irradiate 50 mg each for 1 min
     Elute with:
        L1 - 1 ml 10 M LiCl, 5 min, 25° followed by
        L2 - 1 ml 10 $\overline{M}$ LiCl, 16 hr, 25°

| | % of Isotope in Each Fraction | | | |
	^{141}Pr	^{142}Pr*	^{170}Er	^{171}Er*
PrX - L1	0.7	15.1	–	–
L2	0.6	15.5	–	–
zeolite	–	69.4	–	–
PrErX - L1	0.5	50.8	0.8	34.6
L2	0.4	13.2	0.8	16.1
zeolite	–	36.	–	49.3
PrYX - L1	1.2	57.4	–	–
L2	0.5	9.2	–	–
zeolite	–	33.4	–	–